THE UNIVERSITY OF CHICAGO

TOWARDS LIFE-LIKE BIOINTERFACES FOR BIOELECTRONICS AND REGENERATIVE MEDICINE

A DISSERTATION SUBMITTED TO

THE FACULTY OF THE DIVISION OF THE PHYSICAL SCIENCES

IN CANDIDACY FOR THE DEGREE OF

DOCTOR OF PHILOSOPHY

DEPARTMENT OF CHEMISTRY

BY

JIUYUN SHI

CHICAGO, ILLINOIS

MARCH 2024

To my parents and family

In the middle of difficulty lies opportunity.

- *Albert Einstein*

TABLE OF CONTENTS

List of Figures

List of Tables

List of Abbreviations

AA	Acrylamide
ABLE	Active biointegrated living electronics
AC	Alternating current
ADC	Analog-to-digital converter
AGH	Aspirin-modified granule-releasing hydrogel
AMI	Acute myocardial infarction
ANOVA	Analysis of variance
APS	Ammonium persulfate
APTS	8-Aminopyrene-1,3,6-trisulfonic acid trisodium salt
AS	Aspirin-modified chitosan/starch granules
ASA	5-aminosalicylic acid
ATP	Adenosine triphosphate
B-mode	Brightness mode
CdS	Cadmium sulfide
CMOS	Complementary metal–oxide–semiconductor
CO	Cardiac output
CPD	Critical point drying
CT	Computed tomography
CV	Cyclic voltammetry
Cys	Cystine
dB	Decibel
DC	Direct current
DDAB	Didodecyldimethylammonium bromide
DGH	Dynamic granule-releasing hydrogels
DMPC	1,2-dimyristoyl-sn-glycero-3-phosphocholine
Dopa	3,4-dihydroxyhydrocinnamic acid

DSS	Dextran sulfate sodium
E. coli	*Escherichia coli*
ECG	Electrocardiography
EDC	N-(3-Dimethylaminopropyl)-N′-ethylcarbodiimide hydrochloride
EDS	Energy dispersive X-ray spectroscopy
EF	Ejection fraction
EIS	Electrochemical impedance spectroscopy
EMG	Electromyography
FBR	Foreign-body response
FDA	U.S. Food and Drug Administration
FITC	Fluorescein isothiocyanate
FPCB	Flexible printed circuit board
FPKM	Fragments per kilobase of transcript per million mapped reads
FS	Fractional shortening
FTIR	Fourier-transform infrared
GA-UA	Glutaraldehyde and urinal acetate
GI	Gastrointestinal
GO	Gene ontology
H&E	Hematoxylin and eosin
H_2S	Hydrogen sulfide
HDMS	Hexamethyldisilazane
HgS	Mercury sulfide
HIF1A	Hypoxia-inducible factor-1 alpha
HPF	High-pass filter
I/R	Ischemia-reperfusion
I2C	Inter-integrated circuit
IBD	Inflammatory bowel disease
ICG	Indocyanine green

ICP-MS	Inductively coupled plasma mass spectrometry
IFN	Interferon
IHC	Immunohistochemistry
IL	Interleukin
IM	Inner membranes
IMQ	Imiquimod
IPA	Isopropyl alcohol
IQR	Interquartile range
IVIS	In vivo imaging system
KO	Knockout
LAD	Left anterior descending artery
LEfSe	Linear discriminant analysis effect size
LV	Left ventricle
LVP	Left ventricular pressure
MBAA	N,N′-Methylenebisacrylamide
MD	Molecule dynamics
M-mode	Motion mode
NAD	Nicotinamide adenine dinucleotide
NFC	Near-field communication
NGH	Non-granule-releasing hydrogels
NIR	Near-infrared
NMP	N-Methyl-2-pyrrolidone
NMR	Nuclear magnetic resonance
OD	Optical density
OM	Outer membranes
OTU	Operational taxonomic unit
PAAm	Polyacrylamide
PAMPs	Pathogen-associated molecular patterns

PAS	Periodic acid–Schiff
PbS	Lead sulfide
PBS	Phosphate-buffered saline
PC	Pyruvate carboxylase
PCoA	Principal coordinates analysis
PCR	Polymerase chain reaction
PDMS	Polydimethylsiloxane
PECAM-1	Platelet endothelial cell adhesion molecule-1
PEDOT: PSS	Poly(3,4-ethylenedioxythiophene) polystyrenesulfonate
PEIS	Potentiostatic electrochemical impedance spectroscopy
PI	Polyimide; red staining for dead cells
PLAX	Parasternal long axis view
PPS	Phosphoenolpyruvate synthase
PR	Polyrotaxane
PSAX	Parasternal short axis view
PSI	Psoriasis severity index
PVA	Polyvinyl alcohol; non-releasing hydrogel
RIE	Reactive ion etching
RNA	Ribonucleic acid
RNA-Seq	RNA sequencing
ROS	Reactive oxygen species
RV	Right ventricle
S. epidermidis	*Staphylococcus epidermidis*
SAED	Selective area electron diffraction
SAXS	Small angle x-ray scattering
SC	Non-modified starch/chitosan granules
sECG	Surface electrocardiography
SEM	Scanning electron microscope

sEMG	Surface electromyography
SNR	Signal-to-noise ratio
STEM	Scanning transmission electron microscopy
SVD	Singular value decomposition
TEM	Transmission electron microscopy
TEMED	N,N,N′,N′-Tetramethyl ethylenediamine
TLR2	Toll-like receptor 2
TNF	Tumor necrosis factor
TSB	Tryptic soy broth
XRD	X-ray powder diffraction
ZIF	Zero-insertion-force

Acknowledgements

The past five years at the University of Chicago have been both unforgettable and invaluable to me. I may never again have the opportunity in my lifetime to dedicate such a long period to focusing on one area and continuously refining the content and structure of my perspective. Throughout my Ph.D. journey, I dedicated myself to the research and, luckily, this dedication led to some research findings presented in this thesis. But all these accomplishments are not solely mine; they belong to all those who have supported me and helped me. I would like to express my sincerely thanks to all those people.

First and foremost, I would like to express my most sincere gratitude to my academic advisor, Prof. Bozhi Tian. The most fortunate and valuable aspect of my Ph.D. experience has been the opportunity to conduct research within his group. There are many reasons for saying this. First, Prof. Tian provides tremendous support and insightful guidance to my research. His unique research ideas and forward-thinking vision continually inspired and guided me toward achieving remarkable goals. Looking back at my first manuscript for publication, I was astonished to realize that Prof. Tian had dramatically changed the content and structure of the initial manuscript. I could see his careful revision (even for typo in figures) and also his intelligent effort in pushing the work forwards. The pursuit of perfection always involves countless refinements and improvements. But it is only with all his dedicated support in manuscript iterations which make the quality of the work has reached its current status. It is no exaggeration to say that he is a scientific research genius. Second, Prof. Tian gave me a lot of freedom in exploring the field I am interested in, which was not the area with his previous experts. As a scientist, Prof. Tian is curious about any new problems and is fearless when it comes to solving challenges. When working with me on new stuff, he can leverage all the available resources for it which usually creates unexpected new opportunities in

my project. To facilitate communication, he always responds promptly to emails for every piece of massages, making you feel that he is always there with you when you are working. We frequently discussed research ideas and experimental progress together, whether it was in his office, in front of my bench, or even outside the lab. Under his unwavering support, I was fortunate and successful in developing my research abilities not only in chemistry but also in engineering and biomedical research. Without his help, I would not have been able to work in such an interdisciplinary field, which I am actually passionate about. Third, Prof. Tian has a positive mindset and philosophy. He has the ability in divergent thinking and keep optimism towards any challenges, failure, and setback in the research and life. He always reminds me to stay positive and tell me "No worries" and "大器晚成". He also taught me that "明道若昧, 进道若退, 夷道若颣", which means that the way into the light often looks dark; the way that goes ahead often looks as if it went back; and the way that is least hilly often looks as if it went up and down. Instead of following others, having an innovative and unique starting point always leads to the achieving significant accomplishments. His philosophy and positive energy infected me to overcome many setbacks during the Ph.D. Last, Prof. Tian is an incredible person with an extremely supportive personality. From the first day I joined the lab, I was continuously impressed by his kindness and supportive attitude towards his students, friends, and family. With his empathetic personality, Prof. Tian always has a knack for understanding the strengths of his students and helping them shine. I learned a lot from his concept of karma. Although it is not directly related to academic growth, it taught me many valuable lessons and also shaped my personality. There are still many aspects in which he excels compared to others, including his ability to generate artwork within scientific research (with elegant aesthetic taste!). However, due to space constraints, I cannot provide an

exhaustive description of all these aspects. But I hope that I can become someone he will be proud of and have the opportunity for a casual chat with him in the distant future.

I would like to thank my committee members, Prof. Sihong Wang and Prof. Dmitri V. Talapin, for their valuable time to review my dissertation and provide constructive advice and comments on my oral defense and dissertation.

I was also extremely lucky to have Dr. Jiping Yue as both a friend and a mentor during my Ph.D. It was he who helped me discover my passion for biomedical science and clinical research. Before I joined this lab, I only had limited knowledge in conducting biological research by myself. I learned a great deal from him, especially in the realm of in-vivo animal experiments and all aspects of biological methodology. As you will see, this thesis contains a significant amount of biomedical research and analysis. Without his assistance, this achievement would never have been possible. His suggestions and comments regarding science are constructive and technically possible. Additionally, he is a good friend in daily life, with a great personality. We had many casual conversations during our daily experiments and lunches. I am thrilled to have had the privilege of collaborating with you on completing these research projects.

I would also like to thank Dr. Yiliang Lin, Pengju Li and Saehyun Kim in the Tian lab that I have overlapped most. The research journey during my Ph.D. was often filled with challenges and issues, but I gained valuable insights from Yiliang and Pengju, both in terms of mindset and skillset. Additionally, I am thankful for the millions of enjoyable conversations we had, which were a great source of relief during times of stress or when issues arose in the lab. These friendships not only aided me in my research development but also played a crucial role in maintaining my mental well-being in the lab. Furthermore, I would like to express my appreciation to Saehyun

Kim for his collaboration on the living bioelectronics projects. His productivity and reliability made our collaboration very effective and efficient.

My gratitude further extends to my colleagues in the Tian group who helped me overcome all the hurdles and shared in the moments. I would like to thank Dr. Lingyuan Meng and Dr. Aleksander Prominski for their help in my graduate student life. I would like to acknowledge Dr. Chuanwang Yang, Dr. Xiang Gao, Dr. Jing Zhang, Dr. Jingcheng Ma, Changxu Sun, Zhe Cheng, without whom all the works in this thesis would not have been possible. I would also like to thank other member including but not limited to Dr. Zifan Ye, Dr. Vishnu Nair, Dr. Yin Fang, Dr. Fei Pei, Dr. Tiantian Guo, Dr. Kun Hou, Wen Li for their stimulating discussion and expand my vision of science. I would also like to thank all my collaborators at the University of Chicago, UIC, Rutgers University, and Argonne National Lab. My acknowledgement goes to Prof. Eugene B. Chang, and Dr. Jiwang Chen for their help in the animal work, Prof. Petr Král and Phil Mickel for their tremendous help on the molecular dynamic simulation, Dr. Yanqi Luo and Dr. Si Chen for their help in material X-ray characterization, Dr. Brennan Ashwood for the FTIR characterization. I also enjoyed the casual talk and discussion with Prof. Yuanwen Jiang and Prof. Simiao Niu. Their help and insights are incredible to me to finish all these works. Additionally, I would like to thank all the shared facility members and scientists at the university of Chicago, especially Dr. Philip Griffin at SMCF, Dr. Qiti Guo and Dr. Justin Jureller at MRSEC, Ms. Yimei Chen at Advanced Electron Microscopy, Dr. Guangchang Zhou at the Mass spectrometry facility, Dr. Terri Li, Xin Jiang, Can Gong, Haiqing Luo at the Human Tissue Resource Center. Outside the University of Chicago, I would also like to thank Dr. Fengyuan Shi at UIC, and Dr. Gajendra S Shekhawat at Northwestern, who provided numerous supports for solving technical issue.

I would express my thanks to four of my undergraduate mentees, Kavita Parekh, Bryan Nam, Elaine Liang, and Jj Abu-Halimah. Although I am the official mentor to guide them, I have learned a great deal from their working styles and personalities. I especially appreciate Kavita and Bryan for their dedicated hard work in the research, which has significantly increased research efficiency. Both of them possess a deep understanding of their respective research systems and a curiosity about the natural world, which I feel is really essential in scientific research.

Work and life are a symbiotic pair. I would like to express my gratitude to several of my friends with whom I have shared many enjoyable moments in the Windy City, Chicago. I want to thank my roommate during these years, Xiao Luo, for his constant help and support in our daily lives. I would also like to extend my thanks to my close friends for the first two years, Hantian Zhang, Ken Chen, and Yufei Zhao. Their kindness and support welcomed me on my very first day in Chicago, which made my transition from my hometown to a foreign place become much easier and happier. It is also very fortunate that we enjoyed similar entertainment which make the time after dinner become relaxing and pleasurable. Additionally, I am grateful to my friends, Ziwan Xu, Tong Lan, and Zhao Xu, with whom I had the opportunity to explore various beautiful landscapes across America. I am also thankful to Yu Jin and Weilai Yan, who give me a lot of advice in my life during these years.

Finally, but most importantly, I would like to dedicate this dissertation to my parents and my family. I was born and raised in a family fully of the academic thinking, which became the major motivation behind my pursuit of a Ph.D. In other words, this thesis would never have existed without the influence of my family. I want to express my deep gratitude to my father, whose dedication and self-discipline have greatly shaped my mindset and my persistence throughout this long Ph.D. journey. Besides, they always share understanding and love no matter where and what

I am doing. Their generous support through these years not only remove my financial concern in my life, but also allows me to fully explore the area I am interested in. Their advice for my career pathway is always constructive and insightful. This dissertation is also dedicated to my grandma, who brought me up during my childhood. I hope that I will have more enjoyable moments together with all my beloved family in the near future.

Abstract

Biointerface is the area where a biological entity interacts with a biomaterial. Properly designing a biointerface enhances the functionalities of biomaterials in recording biological signals and modulating biological behavior. To solve this issue, My Ph.D. thesis research proposed three different strategies at biointerfaces which could bridge the biomaterials with biological tissue. My thesis research demonstrated that by rationally designing the biointerfaces for bioelectronics and biomaterials, we can facilitate bioelectrical signal recording, modulate biological behavior, and also enhance their therapeutic effects in treating complex diseases.

Chapter 2 and Chapter 3 discuss the rational design of the monolithic-to-focal biointerface that combines the benefits of both monolithic and focal biointerfaces. This biointerface employs a phase-transition hydrogel which is responsive to environmental temperature and pH. A comprehensive study of the hydrogel transition process is performed through a variety of simulation and materials characterization tools. Additionally, I will present a novel dynamic adhesion technique for focal biointerface through chemical modification to the polymer backbone. This technique stabilizes the focal biointerface and enhances the therapeutic effect of treating inflammatory colitis. Chapter 2 primarily outlines the fabrication of the monolithic-to-focal biointerface, underscoring its significance in bioelectronics integration. The benefits of this biointerface in recording electrocardiography signals and treating myocardial infarction will also be demonstrated. Chapter 3 evaluates the enhanced therapeutic efficacy of the monolithic-to-focal biointerface compared with existing biointerface methods. The result emphasizes the importance of monolith-to-focal biointerface and the dynamic adhesion technique in the realm of regenerative medicine, spotlighting its promising potential for clinical applications.

Chapters 4 and 5 introduce the concept of a tissue-like living biointerface that seamlessly integrates biomechanical, bioelectrical, biochemical, and biological properties. This biointerface is built by living hydrogels, which innately possess these multifaceted features. Inspired by natural biofilm, the discussion will center on how a material engineering approach can be employed to create an environment suitable for the long-term sustainment of living components inside the hydrogel. Chapter 4 will focus on the construction of the living biointerface. The potential and the functionality of the living biointerface in bridging the tissue and bioelectronics will be shown. Chapter 5 will investigate the applications of the living bioelectronic system in disease management, exploring its capabilities in both recording and therapy. The living biointerface also paves the way for research on the convergence of bacterial and mammalian interactions. Additionally, I will demonstrate its effectiveness in treating skin inflammatory disorders like psoriasis, highlighting its potential for clinical implementation.

Chapter 6 demonstrates a new method for constructing the semiconductor biointerface for bacterial biological modulation. The discussion will cover the in situ construction of the semiconductor biointerface at the periplasmic area of the bacteria. The material properties of the formed semiconductor will be characterized through various advanced material characterization methods. Additionally, the biological pathway underlying the biointerface formation and how the periplasmic biointerface regulates the behavior and metabolism of bacteria will be highlighted through comprehensive transcriptomics analysis. It will also be demonstrated that the periplasmic semiconductor enhances the bioproduction of malate through photo-stimulation.

Chapter 1. Introduction

1.1 Biointerface

The biointerface refers to the region or area between a biological entity and a material or device. A rationally designed biointerface allows for proper interrogation or modulation of the biological entity. At the cellular level, biointerfaces connect external biomaterials with cellular activities using various techniques, such as mechanical[1], electrical[2], thermal[3,4], optical[5], acoustic[6], pharmaceutical[7,8] or even a combination of these[9]. With proper signal transduction behavior in biointerface, the cellular behavior including spreading, proliferation, differentiation can be readily controlled[10]. At the human level, biointerfaces facilitate techniques used in healthcare monitoring and therapeutic interventions for diseases[11]. They aid in the biological integration of current bioelectronics into the body, offering real-time monitoring and timely regulation of bodily functions[12].

Regenerative medicine stands out as one of the most promising translational applications for the development of enhanced biointerfaces[13,14]. The shift towards an aging demographic across the globe has amplified the importance of regenerative medicine in the recent year[15]. The designed regenerative biomaterials are usually mimic certain functional roles through biointerface construction. The properties at the biointerface usually involve biochemical[16], structural[17], and mechanical[18]. For example, one of the fascinating aspects of biointerfaces is for the biochemical surface design[19]. Specifically, using hydrophobic materials, one can encourage the adsorption of albumin, a prevalent serum protein that actively inhibits cell adhesion. In contrast, slightly hydrophilic materials might be more conducive for fibronectin adsorption, a protein known for its cell-binding properties. Another interesting design is the geometry of the interface which also plays a pivotal role in dictating cell-material interactions[20]. For instance, biomaterials with a three-

dimensional (3D) architecture, such as three-dimensional hydrogel and aerogel scaffold[21], are widely believed to offer a cellular environment that is more reminiscent of natural biological settings compared to their two-dimensional counterparts[22]. Furthermore, the mechanical properties of the biointerface are also widely studied[23]. Cells are actively responsive to the mechanical cues in their environment through the activation of mechanosensitive ion channels[24,25]. For example, researchers have found that cells from inherently softer tissues, such as neural tissues, have demonstrated enhanced biological reactions when interfaced with softer biomaterials[26]. This recognition has spurred interest in the development of biointerface with mechanical properties that match those of the tissues they interface with[27].

Besides, dynamic properties are one of the intriguing properties in biointerface design[28,29]. Biointerface that can transition between different phases have found extensive applicability, as seen in innovative techniques like drug delivery[30], biodegradation[31], and injection techniques[32]. For example, controlling the degradation of biomaterials can coordinate with the growth rate of the cells[33]. The space created by the degradation facilitates the nutrient diffusion and cellular matrix regeneration[34]. Another intriguing application lies in biomaterials cross-linked with a trigger element that can be cleaved by biological system[35]. This biointerface design make the biomaterial can be real-time responsive to in vivo conditions, such as inflammation. By this way, the predetermined degradation timelines will be close-looped controlled for tissue engineering applications to achieve intelligent medicine. Thus, the biointerface should not be static and immutable, dynamic design of the biointerface can provide more opportunities in the biointerface for regenerative medicine.

Moreover, the immune response elicited in regenerative interventions has also attracted more and more attention[36]. The immunogenicity of a biomaterial can be modulated by through its

biointerface properties, such as its porosity, surface chemistry, and even its shape[37]. Traditional strategies have predominantly revolved around designing treatments that can subtly bypass or mitigate the host immune response, ensuring that the introduced therapeutic component can function with minimal interference[38]. While further systematic research is required, studies have indicated that the biointerface can significantly influence the phenotype of macrophages and T cells[39]. However, regenerative medicine research usually requires an extensive journey before it is ready for marketing and clinical use (Figure 1-1). In summary, biointerface design is already positioned to make a direct impact on patient care and offers a novel approach to regenerative medicine.

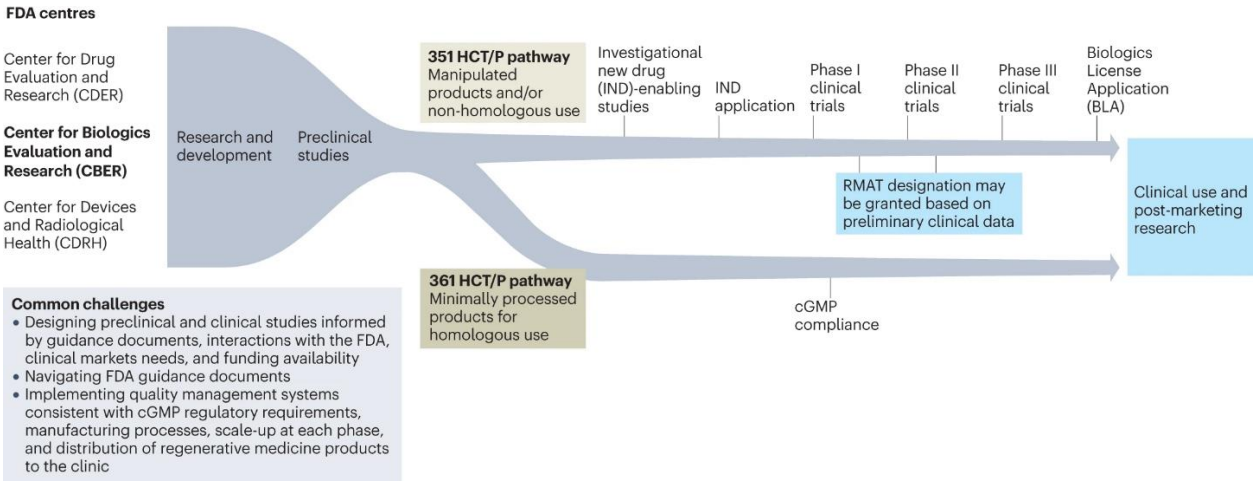

Figure 1-1 The FDA regulatory pathway for regenerative-medicine therapies. Reproduced with permission[13]. Copyright 2023, Nature Publishing Group.

Among different biointerfaces, bioelectrical biointerfaces have emerged as one of the most promising areas of research in recent years[40,41]. A significant reason for this increase in interest is their dual capability: they can offer therapeutic interventions to local tissues while also enabling closed-loop monitoring and recording of the same tissues[42]. Indeed, Bioelectrical interfaces have

a rich history. As early as the late 18th century, Galvani conducted pioneering experiments on frogs that distinctly demonstrated the connection between electricity and physiological activity[43]. This groundbreaking work paved the way for a multitude of investigative tools focused on bioelectrical interfaces. What Galvani initially witnessed is now understood as the excitation and propagation of action potentials in neurons and muscle cells. This phenomenon was systematically modeled by British biophysicists Alan Hodgkin and Andrew Huxley in their groundbreaking 1952 paper[44]. Their significant contributions earned them the Nobel Prize in Physiology or Medicine in 1963.

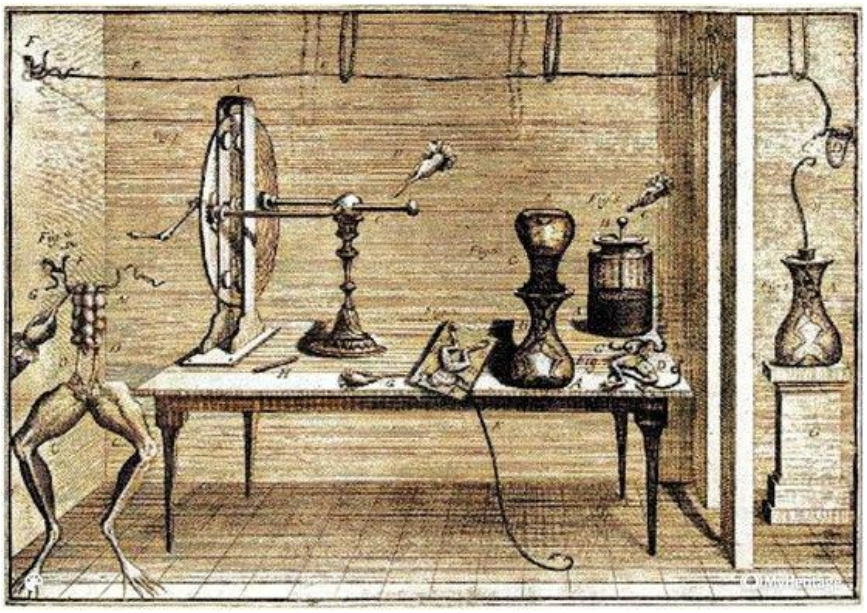

Figure 1-2 The setup with the frog and the electrical device refers to Galvani and his collaborators' spark experiments. Reproduced with permission[44]. Copyright 1997, Cell press.

More recently, due to the development of the microfabrication and chemistry synthesis toolset in the past decades, the bioelectrical interface has a new change. Bioelectronics, a kind of biomaterial at bioelectrical interfaces, can now be fabricated at micro or even nano-scales, dramatically

enhancing the resolution and precision of monitoring and recording. Nanowires epitomize this nano-sized bioelectrical interface evolution, offering promising outcomes in deciphering biological communications (Figure 1-3)[45]. The primary strength of these nanoscale building blocks lies in their ultra-sensitive nature, capable of detecting individual molecules. This heightened sensitivity and enhanced resolution of nanowires stem from their minimal volume and surface area[46]. Additionally, at the nanoscale, even rigid materials become more deformable[47]. The bending stiffness diminishes with the decreasing nanowire diameter, making these structures notably biocompatible with most soft tissues. While the overall device might still be macroscopic, its nanoscale components ensure a seamless integration with biointerfaces[48]. This diminishes mechanical mismatches and can potentially bypass immune system detection[49]. Moreover, nanowires boast a high aspect ratio, accommodating the specific geometry of cells[50]. This is pivotal for unique applications like intracellular force measurements and localized photothermal or photoelectrochemical modulation. By aligning in size with the structures they modulate, semiconductor nanowires not only enhance our grasp of foundational biological theories but also pioneer cutting-edge sensory tools for practical applications.

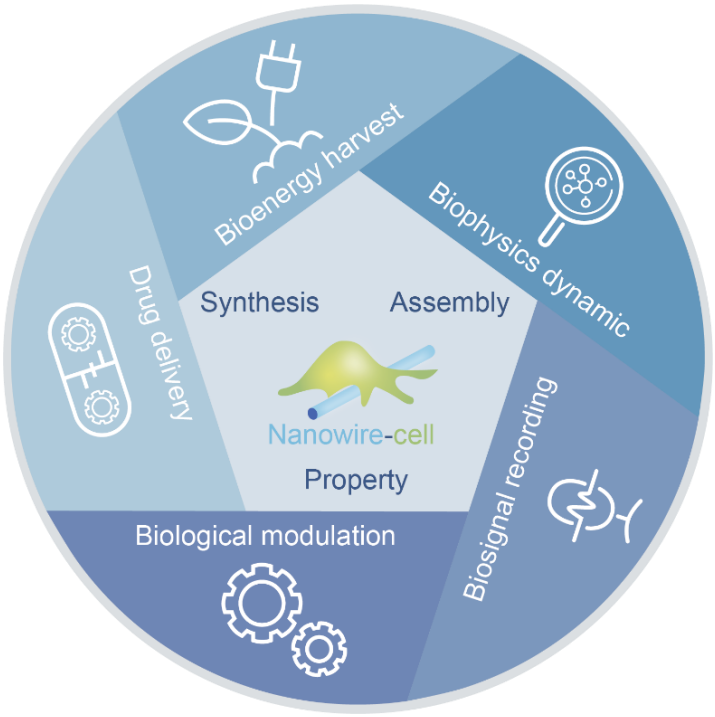

Figure 1-3, Nanowires stand out with their unique properties as an advanced toolset capable of exploring diverse biointerfaces. Specifically, semiconductor nanowires have shown favorable results in deciphering biological communications and translating this cellular language through the nanowire-based biointerfaces.

In addition to nanowires, the realm of bioelectrical biointerfaces is witnessing the incorporation of various nanotechnologies. For instance, integrating ultra-thin quantum dots within a multi-layered photovoltaic structure allows the conversion of near-infrared (NIR) light into safe capacitive ionic currents. This innovation has successfully induced reproducible action potentials in primary hippocampal neurons with impressive efficacy[51]. Looking ahead, we anticipate an expanded role for nanoparticles in this domain. By engineering these particles with lipid bilayers, ion channels, and cytoskeletons, we can direct molecular transport, trigger bioelectric responses, or modulate enzymatic reactions in response to external stimuli (Figure 1-4)[48].

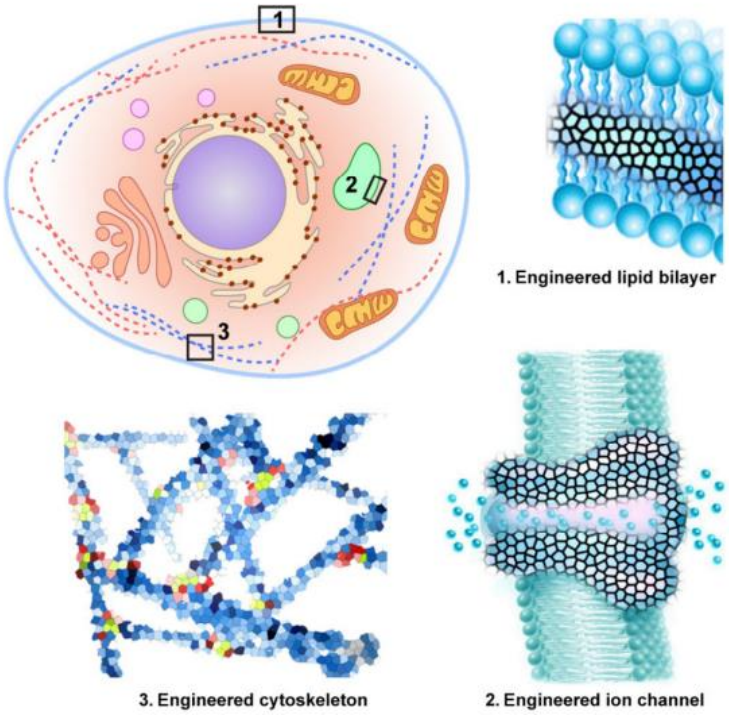

Figure 1-4 Semiconductor-enabled synthetic biology. In the future, semiconductors can also be engineered with lipid bilayer, ion channel, and cytoskeleton to guide molecular transport, elicit bioelectric response, or regulate enzymatic reactions upon external stimuli.

Besides the nanoscale example, the mesh electronics based on the photolithography fabrication also is a good example in constructing micron-scale bioelectrical biointerface for tissue-level biointerfaces[52]. The fabrication and potential of mesh electronics will be comprehensively discussed in the following chapter. Additionally, advancements in the fabrication of integrated circuits over the past decades have made it possible to produce bioelectronic devices on a large scale efficiently. The current semiconductor industry can endow the functionality such as close-loop control in a tiny single chip, which enable the bioelectronics adjust their function based on individual patients or different stage of the disease progress.

Another primary benefits of bioelectrical biointerfaces lies in its ability to offer non-pharmacological intervention[53]. Traditional small molecular drugs often grapple with challenges

related to non-specificity and side effects[54]. In contrast, bioelectronics can address conditions like heart disease with diminished systemic side effects. Crucially, devices like neuromodulation instruments can be programmed to target specific neural pathways or organs[55]. Such precision enables the alleviation of ailments such as chronic pain, epilepsy, or particular psychiatric disorders. This is achieved by modulating the activity of designated nerves or brain regions without the need to introduce foreign substances into the body. Furthermore, the controllable nature of bioelectronics means they can be adjusted remotely, allowing healthcare professionals to fine-tune treatments without necessitating a clinic visit for the patient, ensuring a more convenient and timely approach to intervention[56].

1.2 Limitation and challenges

Despite the significant advancements in both biology and materials science in this century, there remains a notable gap in technology that can seamlessly integrate these two disciplines[57]. This gap has hindered the translation of new technologies from sectors like semiconductors, energy, and the polymer industry into biomedical applications[58]. Moreover, fundamental insights from biological and biomedical science, as well as clinical practice, have not been effectively relayed back to material development. This disconnect significantly limits the potential success of numerous medical and biotechnological innovations.

There are several limitations in traditional bioelectronics devices. First, the mechanical mismatch between tissue and bioelectronics presents significant challenges for seamless integration[59,60]. This mismatch is characterized by potential discrepancies in stiffness (Young's moduli), tensile strength, toughness, viscoelasticity, adhesion properties, and structural parameters such as geometry (Figure 1-5). For instance, the Young's moduli of typical soft tissue ranges from 1 kPa

to 1 MPa (e.g., brain: 1 kPa; heart: 50 kPa; skin: 150 kPa; stomach: 100 kPa), while traditional materials for bioelectronics fall between 1 GPa to 1TPa (e.g., gold: 79 GPa; polyimide: 4 GPa; Silicon: 140 GPa)[61]. This large mechanical mismatch can cause damage to the surrounding tissue. This issue is especially severe for tissues that undergo complex motions, such as heart and muscles[62]. When devices containing electrodes are not mechanically matched to their target neural tissues, they can cause damage and inflammation[63]. This, in turn, can lead to a decline in the quality of electrophysiological signals during chronic recordings. Furthermore, scarring resulting from inflammation can hinder effective signal transmission[64]. Additionally, because of the discrepancy in bending stiffness, an interfacial gap can form between the bioelectronics and the tissue, potentially limiting electrical signal transduction at the biointerfaces[65].

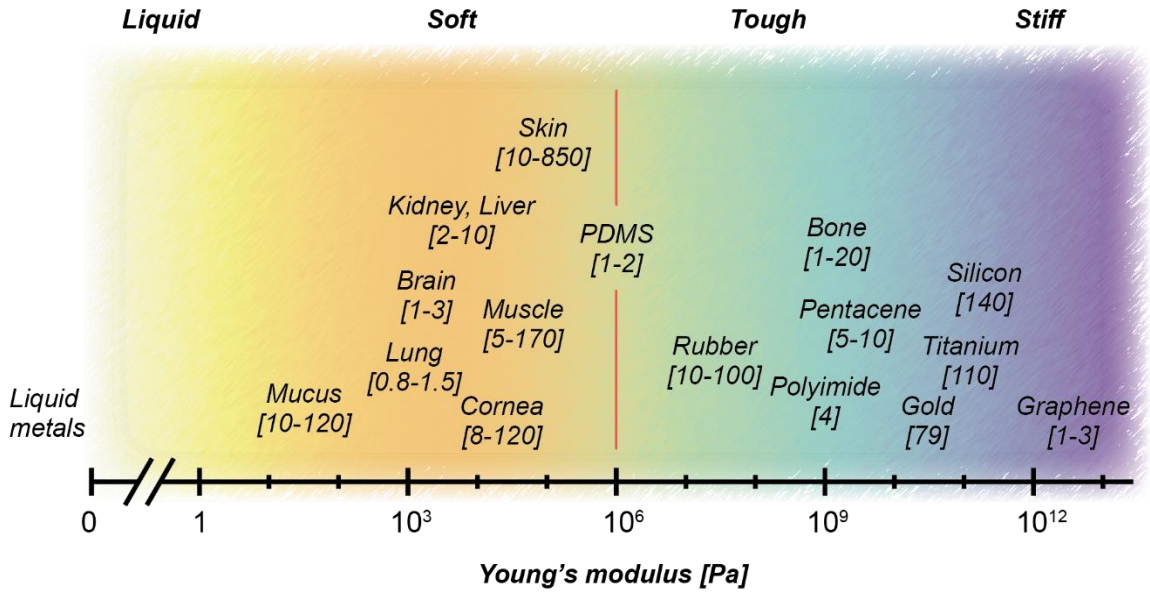

Figure 1-5 Young's modulus of various tissue and the materials used in biointerfaces.

Additionally, the bodies of animals and humans have the innate immune defenses designed to protect against foreign entities[66]. This defense triggers a foreign-body response (FBR), presenting

significant challenges to implantable devices. Once a device is implanted, proteins from bodies can quickly non-selectively adhere to the surface of bioelectronics[67]. This further attracts host cells like neutrophils to the site, which in turn release cytokines, chemokines, and other enzymes. These elements then call upon monocytes, macrophages, and fibroblasts. As a result, foreign-body giant cells form, and with collagen deposition, a dense fibrous capsule develops around the implant[68]. This capsule effectively segregates the implant from the host tissue, both physically and functionally[69]. More importantly, this electrically inert encapsulation interrupts ionic and electrical communication between the electrodes and the target tissue. This sequence of events often results in device malfunction and sustained inflammation in patients.

Thus, building a tissue-like bioelectronic which mimic the mechanical, structural, and biochemical properties of native tissues, we can achieve seamless integration between the device and the biological system[70]. Such tissue-like devices not only minimize the body foreign body immune responses but also enhances the device long-term functionality and performance[71]. Furthermore, tissue-like bioelectronics can facilitate more accurate sensing and modulation of physiological processes, offering a more effective and tailored therapeutic approach. In summary, by bridging the gap between synthetic devices and organic systems, we can pave the way for innovative treatments, better patient outcomes, and novel personalized medicine.

1.3 Current strategy for biointerface

With those challenges in the field, efforts have been made in the area to better link bioelectronics to the tissue. To solve the properties mismatch between the tissue and bioelectronics, different strategies have been proposed. We have a brief view at this section.

1.3.1 Soft and flexible

Inorganic materials usually have high modulus which makes them stiff and hard. However, the bending stiffness of materials is closely related to their thickness. In mathematically, the relationship is given by[72]:

$$D = E \times \frac{\lambda^3}{12(1-\nu^2)}$$

Where D is the bending stiffness. E is the Young's modulus (modulus of elasticity) of the material. λ is the thickness of the plate or beam. ν is the Poisson's ratio of the material.

Thus, inorganic materials are often fabricated into thin layers to reduce their rigidity and enhance flexibility[73]. When the thickness of a device is scaled down from millimeters to micrometers or even less, the device inherent rigidity can drop dramatically (Figure 1-6). This allows devices which is originally made from brittle or rigid materials become foldable or flexible[74]. Through ultrathin designs, these bioelectronics can match the bending stiffness of tissues, ensuring better adaptability. Besides softness, the bioelectronics have also been fabricated into different structures to endow the stretchability. Incorporating designs like mesh arrays[75], serpentine interconnections[76], helical structures[77], and various kirigami patterns[78] enhance the deformability of these ultrathin devices. This fabrication skills largely expand the various biomedical application of the rigid materials which cannot be utilized. This compatibility facilitates the creation of high-performance flexible components, including sensors, displays, and antennas, using traditional semiconductor device processes[79]. However, it still faces the challenges. This modulus disparity can result in imperfect contact between the device and underlying soft tissue surfaces, creating gaps[65]. Such gaps act as insulating barriers, leading to high impedance, reduced signal clarity, and

decreased charge efficiency[80]. Employing inherently softer materials might provide a solution to these challenges.

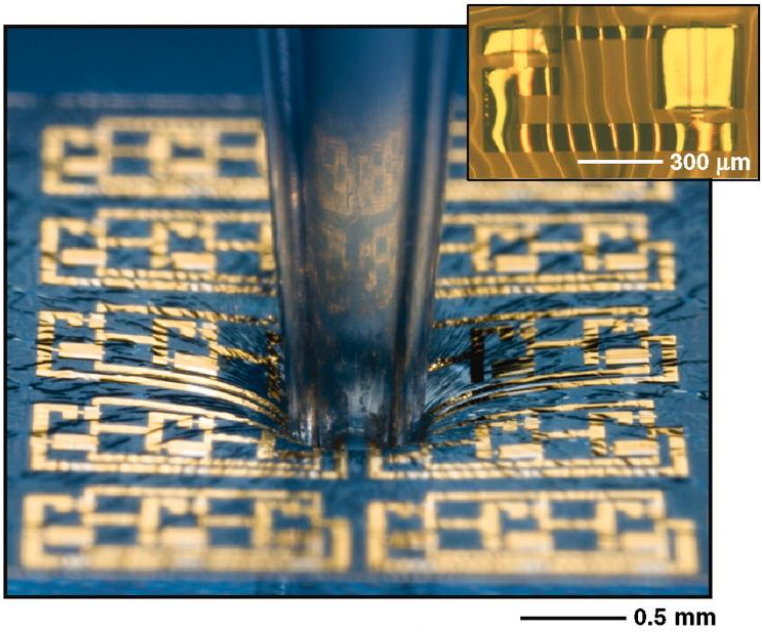

Figure 1-6 Example of the flexible ultrathin stretchable electronics. Reproduced with permission[81]. Copyright 2010, AAAS.

1.3.2 Intrinsic stretchable

To solve this issue, intrinsic stretchable bioelectronics has been developed in recent year, such as conductive polymer[82], hydrogel[83], liquid materials[84], and conductive nanocomposites[85]. Polymers are generally insulative, making them ideal as inert encapsulation materials for inorganic materials, such as gold. However, the structure of polymer chain can be modified with specific functional groups to grant them with conductivity (Figure 1-7). These conductive polymers achieve this through conjugative bonds, which feature alternating double bonds, and/or the inclusion of charge transfer agents, facilitating charge movement along the polymer chain. An example is poly(3,4-ethylenedioxythiophene) polystyrenesulfonate (PEDOT: PSS), widely adopted in biomedical applications due to its biocompatibility and high conductivity[86]. This compound is essentially a

macromolecular salt comprising sulfonated polystyrene, which carries negatively charged sulfonyl groups, paired with a positively charged conjugated polymer, PEDOT (polythiophene). However, their conductivities are much less than the metals since their charge transfer depends on the π–π interaction within their chains. Thus, in the recent year, the conductivity of PEDOT: PSS has been enhanced by treating it with specific small molecule additives[87,88]. But the enhancement will be cleared after immersion inside the aqueous biological environment, where their conductivity will dramatically drop since the small molecular additives are washed away[89]. To overcome these challenges, the supramolecular additive based on a polyrotaxane (PR) structure has been design to the PEDOT: PSS and achieve stable electromyography signal recording on soft and malleable octopus[11]. But the current clinic translation still faces the challenges of development of facile fabrication approach.

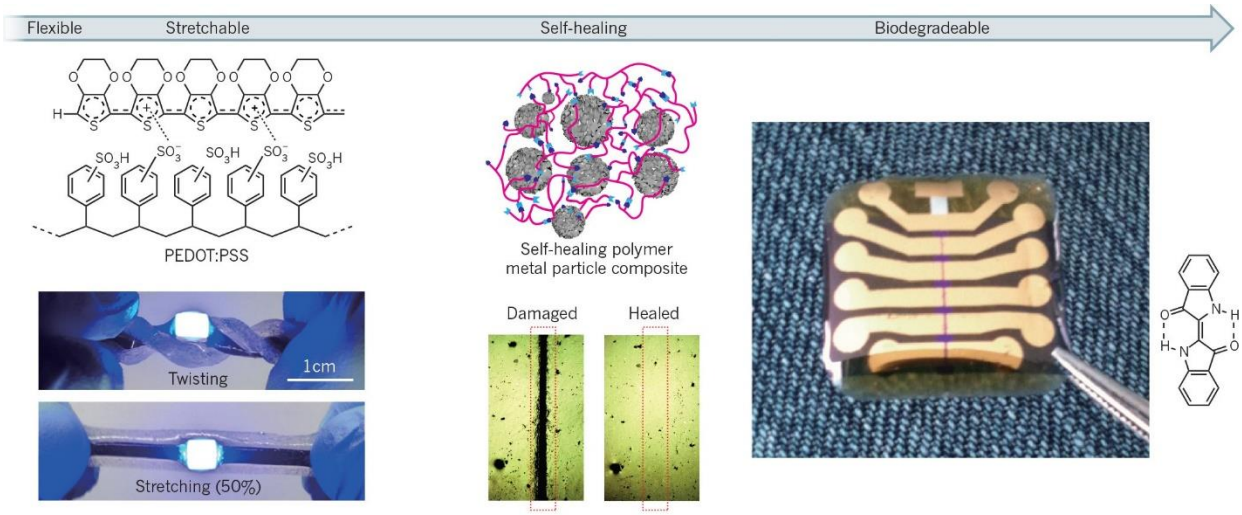

Figure 1-7 Flexible electronic polymers used in bioelectronics can exhibit stretchability, biodegradability, and self-repairing features. Reproduced with permission[90]. Copyright 2016, Nature Publishing Group.

1.3.3 Interfacial layer

While the endow the structure design in rigid bioelectronics device offers stretchability, it also restricts the density of functional elements[91]. This is because a large space area will be used to form the pre-stretched serpentine structure. To enable the high functional elements in limited space, new technique is needed. Additionally, as the substrate shifts with skin during body movements, the elements positions change unpredictably, affecting the device recording consistency[92]. To solve this issue, one possible method is to couple rigid bioelectronics elements with the tissue via conductive hydrogels. Hydrogels are formed with three-dimensional crosslinked polymer with absorbed water. Conductive hydrogels usually need to incorporate charge-transporting fillers, such as conductive polymers[93] (*e.g.,* PEDOT: PSS), metallic salts[94] (*e.g.,* LiCl and Na^+), ionic liquids[95] (*e.g.,* 1-ethyl-3-methylimidazolium chloride), or conductive nanomaterials[96] (*e.g.,* graphene and metal). Owing to their low crosslinking density and high water content (up to ~90% by weight), hydrogels exhibit mechanical moduli (1 kPa to 1MPa) akin to, or even less than, soft tissues. The combination of their innate softness and moisture allows them to seamlessly interface with soft biological tissues[97]. Moreover, their low mechanical modulus and tissue-like viscoelasticity means they typically cause negligible mechanical damage to tissues[98]. Besides, since the polymer chain can be easily modified to endow different functional properties, hydrogel has achieved the specific functionality, such as adhesive[99], anti-fouling[100], and biodegradability[101]. The adhesion properties further boost the stability of the bioelectronics in tissue electrical recording. However, potential chemical tissue damage might arise from redox reactions inside the hydrogel, and swelling or degradation can be issues for long-term implants. Besides, even with added salts or ionic liquids, hydrogels generally possess limited conductivity.

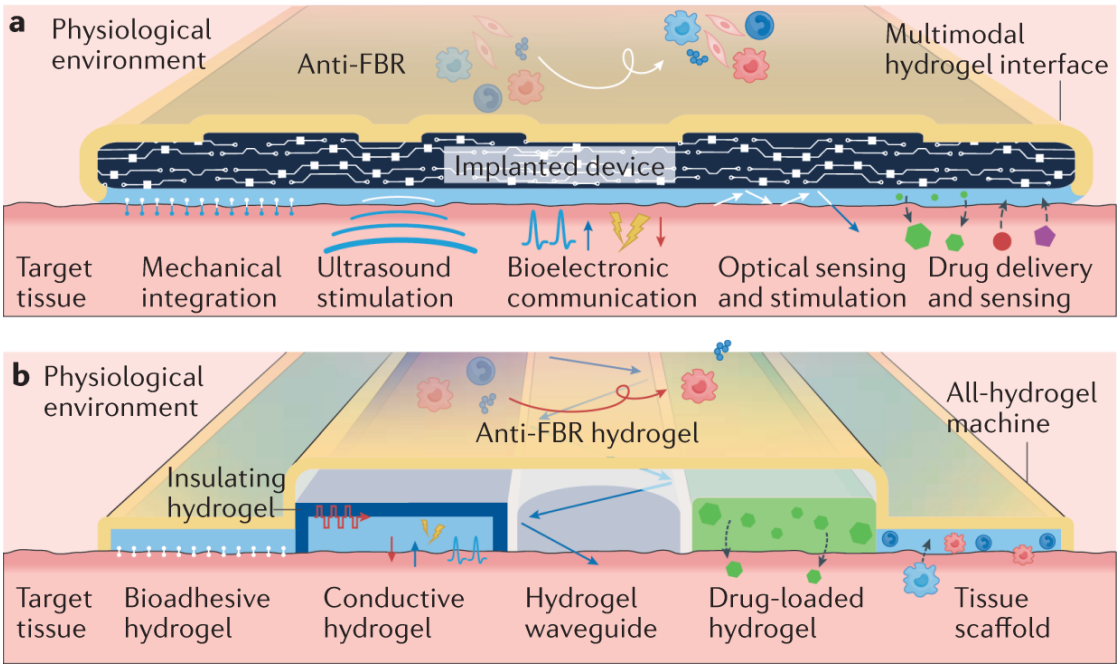

Figure 1-8 Hydrogels provide multifunctional at the biointerface. Reproduced with permission[102]. Copyright 2022, Nature Publishing Group.

1.4 Future perspective

The mechanical mismatch between the bioelectronics and tissues has been widely studied during the last decades. However, there are still remaining challenges in the biochemical and biological mismatch between the bioelectronics and tissue. For example, the immune response is the inevitable questions origin the biological difference between the bioelectronics and tissue. Given that, researcher nowadays have proposed several strategies to solve this issue. The first method is using the antifouling coating to the bioelectronics. As introduced before, the immune response happens from the fouling of protein and cells on the surface of implanted bioelectronics. Thus, surface engineering with a high hydrophilicity which form a dense hydration layer can help protect the bioelectronics from protein absorption[103]. The typical method includes the use of zwitterionic polymer and hydrogel with superhydrophilicity[104]. The zwitterionic possess both positive and

negative charges within the same monomeric unit, making them electrically neutral overall, which reduces specific and nonspecific interactions with charged biomolecules. However, further design needs to incorporate more conductive elements to the zwitterionic polymer to facilitate the anti-fouling properties into the bioelectronics. Another method widely used is loading immunoregulation drugs, which are typically used in current market of organ transplantation procedure, into bioelectronics. Those medicine is specially designed to moderate the activity of the immune system, which help manage foreign body reaction symptoms[105]. But one key issue in this method is that using the immunosuppressive drug should not influence the whole-body immune response. How to specifically modulate the local specific immune environment become a question in the fields.

Constructing bioelectronics with biocompatibility represents only an initial step in reducing discrepancies at the biointerface. For the future bioelectronics, there is a necessity to go beyond the consideration merely in biocompatibility. These devices should seamlessly integrate with biological tissues, have the capability to actively modulate local tissue environments, and even possess therapeutic properties to treat diseases directly. This introduces new challenges related to the construction of an effective biointerface. The first challenge is the rational design of a biointerface that can efficiently harness the functional properties of biomaterials and translate them effectively into the tissue. Many biomaterials with different therapeutic effects in various diseases have been developed to date. However, the processes about how these biointerfaces are formed, and the ways in which different biointerface structures influence therapeutic outcomes, are areas that need more exploration. Insights into these aspects can guide us towards better material designs, enhancing our ability to both record biological signals and treat diseases.

Secondly, the bioelectronics for future applications need to be fully tissue-like in their properties. Previous discussions and studies have delved into the mechanical and electrical mismatches at the biointerface. Still, less attention has been given to the biochemical and biological mismatches. Consequently, many of current biointerfaces lack comprehensive functionalities for biomodulation across a spectrum of diseases. Bioelectronics therapies are often used on electro-active diseases, like neural disorders or heart-related conditions. While much of the current research is centered around mitigating inflammation induced by bioelectronics, there is a limited attention of bioelectronics that possess innate disease-treating capabilities. Addressing the biochemical and biological differences at the biointerface is, therefore, an imperative.

Lastly, considering the challenges associated with integrating foreign bioelectronics into biological systems, there is growing interest in the in-situ formation of biointerfaces. This approach promises a more seamless integration of bioelectronics with biological systems. One of the advantages is that it can circumvent the challenge of creating materials that are sufficiently soft for interfacing with living tissues, yet rigid enough for insertion into the body. However, the concept of in-situ bioelectronics formation is in its nascent stages. Advancing this field requires more refined techniques and sustained research efforts, which would further pave the way for the successful translation of these methods into real-world applications.

1.5 Thesis overview

In this thesis, I will present several concepts aimed at addressing the limitations discussed in previous sections. While many of these are still at a conceptual stage, I believe the novel methods introduced here can offer fresh perspectives in the field of biointerfaces and contribute solutions to complex challenges in biomedical applications. Additionally, I will delve into the application

of these biointerfaces across different disease models, underscoring their potential for clinical translation.

In Chapter 2 and Chapter 3, I will introduce a monolithic-to-focal biointerface that combine the benefits of both monolithic and focal biointerfaces. This biointerface is constructed using a phase-transition hydrogel which is responsive to environmental temperature and pH shifts. The transition process is closely examined using a diverse set of modeling tools and material characterization. Furthermore, I will introduce a new dynamic adhesion technique for the focal biointerface, which enhances stabilization for bioelectronics and therapeutic effect as regenerative medicine. In Chapter 2, the emphasis will be on the creation of the monolithic-to-focal biointerface, highlighting its role in bioelectronics integration. I will also demonstrate the benefits of monolithic-to-focal biointerface in electrocardiography signal capture and integrated disease treatment. Chapter 3 will focus on how the monolithic-to-focal biointerface augments the therapeutic efficacy of existing biomaterials. The pivotal role of biointerface construction in regenerative medicine will be explored, emphasizing its prospective value in clinical applications.

In Chapters 4 and 5, I will discuss the concept of a living biointerface that integrates biomechanical, bioelectrical, biochemical, and biological properties. This biointerface is formed by living hydrogels, which inherently encompass these multifaceted properties. Besides, I will introduce a comprehensive approach to create the living biointerface, coordinating the interactions between the hydrogel, living components, and bioelectronics. One key feature I will highlight is its ability to sustain long-term storage of living components while maintaining high viability. In Chapter 4, my focus will be on the construction of the living biointerface, emphasizing its tissue-mimetic properties. Additionally, I will explore its promising advantages when coupled with bioelectronics. An in-depth look at how these components synergize to enhance the biointerface

functionality will be discussed. In Chapter 5, I will study the practical applications of this living bioelectronic system in disease management, touching on both its recording and therapeutic potentials. I will present how this innovative platform facilitates studies at the intersection of bacterial and mammalian nexus. Moreover, I will show its efficacy in managing skin inflammatory conditions such as psoriasis, emphasizing its potential in clinical translation.

In Chapter 6, I will introduce a new method for constructing the semiconductor biointerface for biological modulation. I will discuss how we in situ build the semiconductor biointerface at the periplasmic area of the bacteria. I will also explore the material properties of the formed semiconductor through various advanced material characterization methods. Besides, I will show how the in-situ formed biointerface could regulate the behavior and metabolism of bacteria through transcriptomics analysis. We also showed that through photo-stimulation, the periplasmic semiconductor can modulate the production of malate.

1.6 References

1 McMurray, R. J., Gadegaard, N., Tsimbouri, P. M., Burgess, K. V., McNamara, L. E., Tare, R., Murawski, K., Kingham, E., Oreffo, R. O. C. & Dalby, M. J. Nanoscale surfaces for the long-term maintenance of mesenchymal stem cell phenotype and multipotency. *Nat Mater* **10**, 637-644, doi:10.1038/Nmat3058 (2011).

2 Jiang, Y. W., Li, X. J., Liu, B., Yi, J., Fang, Y., Shi, F. Y., Gao, X., Sudzilovsky, E., Parameswaran, R., Koehler, K., Nair, V., Yue, J. P., Guo, K. H., Tsai, H. M., Freyermuth, G., Wong, R. C. S., Kao, C. M., Chen, C. T., Nicholls, A. W., Wu, X. Y., Shepherd, G. M. G. & Tian, B. Z. Rational design of silicon structures for optically controlled multiscale biointerfaces. *Nat Biomed Eng* **2**, 508-521, doi:10.1038/s41551-018-0230-1 (2018).

3 Jiang, Y., Carvalho-de-Souza, J. L., Wong, R. C., Luo, Z., Isheim, D., Zuo, X., Nicholls, A. W., Jung, I. W., Yue, J. & Liu, D.-J. Heterogeneous silicon mesostructures for lipid-supported bioelectric interfaces. *Nat Mater* **15**, 1023-1030 (2016).

4 Wang, Y., Garg, R., Cohen-Karni, D. & Cohen-Karni, T. Neural modulation with photothermally active nanomaterials. *Nature Reviews Bioengineering* **1**, 193-207, doi:10.1038/s44222-023-00022-y (2023).

5 Antkowiak, M., Torres-Mapa, M. L., Witts, E. C., Miles, G. B., Dholakia, K. & Gunn-Moore, F. J. Fast targeted gene transfection and optogenetic modification of single

neurons using femtosecond laser irradiation. *Sci Rep-Uk* **3**, doi:10.1038/srep03281 (2013).
6 Ramesan, S., Rezk, A. R., Dekiwadia, C., Cortez-Jugo, C. & Yeo, L. Y. Acoustically-mediated intracellular delivery. *Nanoscale* **10**, 13165-13178, doi:10.1039/c8nr02898b (2018).
7 Luo, Z. Y., Lu, Y. C., Shi, Y. Y., Jiang, M. S., Shan, X. Y., Li, X., Zhang, J. L., Qin, B., Liu, X., Guo, X. M., Huang, J. X., Liu, Y., Wang, S. J., Li, Q. P., Luo, L. H. & You, J. Neutrophil hitchhiking for drug delivery to the bone marrow. *Nat Nanotechnol* **18**, 647-656, doi:10.1038/s41565-023-01374-7 (2023).
8 Finbloom, J. A., Huynh, C., Huang, X. & Desai, T. A. Bioinspired nanotopographical design of drug delivery systems. *Nature Reviews Bioengineering* **1**, 139-152, doi:10.1038/s44222-022-00010-8 (2023).
9 Shin, H., Jeong, S., Lee, J. H., Sun, W., Choi, N. & Cho, I. J. 3D high-density microelectrode array with optical stimulation and drug delivery for investigating neural circuit dynamics. *Nat Commun* **12**, doi:10.1038/s41467-020-20763-3 (2021).
10 Lane, S. W., Williams, D. A. & Watt, F. M. Modulating the stem cell niche for tissue regeneration. *Nat Biotechnol* **32**, 795-803, doi:10.1038/nbt.2978 (2014).
11 Jiang, Y. W., Zhang, Z. T., Wang, Y. X., Li, D. L., Coen, C. T., Hwaun, E., Chen, G., Wu, H. C., Zhong, D. L., Niu, S. M., Wang, W. C., Saberi, A., Lai, J. C., Wu, Y. L., Wang, Y., Trotsyuk, A. A., Loh, K. Y., Shih, C. C., Xu, W. H., Liang, K., Zhang, K. L., Bai, Y. H., Gurusankar, G., Hu, W. P., Jia, W., Cheng, Z., Dauskardt, R. H., Gurtner, G. C., Tok, J. B. H., Deisseroth, K., Soltesz, I. & Bao, Z. N. Topological supramolecular network enabled high-conductivity, stretchable organic bioelectronics. *Science* **375**, 1411-1417, doi:10.1126/science.abj7564 (2022).
12 Li, Y., Li, N., Oliveira, N. D. & Wang, S. H. Implantable bioelectronics toward long-term stability and sustainability. *Matter-Us* **4**, 1125-1141, doi:10.1016/j.matt.2021.02.001 (2021).
13 Takahashi, T., Donahue, R. P., Nordberg, R. C., Hu, J. C., Currall, S. C. & Athanasiou, K. A. Commercialization of regenerative-medicine therapies. *Nature Reviews Bioengineering*, doi:10.1038/s44222-023-00095-9 (2023).
14 Christman, K. L. Biomaterials for tissue repair. *Science* **363**, 340-341 (2019).
15 Dimmeler, S., Ding, S., Rando, T. A. & Trounson, A. Translational strategies and challenges in regenerative medicine. *Nat Med* **20**, 814-821, doi:10.1038/nm.3627 (2014).
16 Armstrong, J. P. K. & Perriman, A. W. Strategies for cell membrane functionalization. *Exp Biol Med* **241**, 1098-1106, doi:10.1177/1535370216650291 (2016).
17 Stevens, M. M. & George, J. H. Exploring and engineering the cell surface interface. *Science* **310**, 1135-1138, doi:10.1126/science.1106587 (2005).
18 Crowder, S. W., Leonardo, V., Whittaker, T., Papathanasiou, P. & Stevens, M. M. Material Cues as Potent Regulators of Epigenetics and Stem Cell Function. *Cell Stem Cell* **18**, 39-52, doi:10.1016/j.stem.2015.12.012 (2016).
19 Mager, M. D., LaPointe, V. & Stevens, M. M. Exploring and exploiting chemistry at the cell surface. *Nat Chem* **3**, 582-589, doi:10.1038/Nchem.1090 (2011).
20 Elnathan, R., Barbato, M. G., Guo, X. F., Mariano, A., Wang, Z. X., Santoro, F., Shi, P., Voelcker, N. H., Xie, X., Young, J. L., Zhao, Y. L., Zhao, W. T. & Chiappini, C. Biointerface design for vertical nanoprobes. *Nat Rev Mater* **7**, 953-973, doi:10.1038/s41578-022-00464-7 (2022).

21 Lee, J. B., Kim, D. H., Yoon, J. K., Park, D. B., Kim, H. S., Shin, Y. M., Baek, W., Kang, M. L., Kim, H. J. & Sung, H. J. Microchannel network hydrogel induced ischemic blood perfusion connection. *Nat Commun* **11**, doi:10.1038/s41467-020-14480-0 (2020).
22 Downing, T. L., Soto, J., Morez, C., Houssin, T., Fritz, A., Yuan, F. L., Chu, J. L., Patel, S., Schaffer, D. V. & Li, S. Biophysical regulation of epigenetic state and cell reprogramming. *Nat Mater* **12**, 1154-1162, doi:10.1038/Nmat3777 (2013).
23 Chaudhuri, O., Gu, L., Klumpers, D., Darnell, M., Bencherif, S. A., Weaver, J. C., Huebsch, N., Lee, H. P., Lippens, E., Duda, G. N. & Mooney, D. J. Hydrogels with tunable stress relaxation regulate stem cell fate and activity. *Nat Mater* **15**, 326-334, doi:10.1038/Nmat4489 (2016).
24 Jin, P., Jan, L. Y. & Jan, Y. N. Mechanosensitive Ion Channels: Structural Features Relevant to Mechanotransduction Mechanisms. *Annual Review of Neuroscience* **43**, 207-229, doi:10.1146/annurev-neuro-070918-050509 (2020).
25 Adu-Berchie, K., Liu, Y. T., Zhang, D. K. Y., Freedman, B. R., Brockman, J. M., Vining, K. H., Nerger, B. A., Garmilla, A. & Mooney, D. J. Generation of functionally distinct T-cell populations by altering the viscoelasticity of their extracellular matrix. *Nat Biomed Eng*, doi:10.1038/s41551-023-01052-y (2023).
26 Leipzig, N. D. & Shoichet, M. S. The effect of substrate stiffness on adult neural stem cell behavior. *Biomaterials* **30**, 6867-6878, doi:10.1016/j.biomaterials.2009.09.002 (2009).
27 Zhang, Y. J., Riexinger, J., Yang, X. Y., Mikhailova, E., Jin, Y. C., Zhou, L. N. & Bayley, H. A microscale soft ionic power source modulates neuronal network activity. *Nature* **620**, 1001-1006, doi:10.1038/s41586-023-06295-y (2023).
28 Guan, Y., Racioppi, L. & Gerecht, S. Engineering biomaterials to tailor the microenvironment for macrophage-endothelium interactions. *Nat Rev Mater*, doi:10.1038/s41578-023-00591-9 (2023).
29 Shadish, J. A., Benuska, G. M. & DeForest, C. A. Bioactive site-specifically modified proteins for 4D patterning of gel biomaterials. *Nat Mater* **18**, 1005-1014, doi:10.1038/s41563-019-0367-7 (2019).
30 Mitchell, M. J., Billingsley, M. M., Haley, R. M., Wechsler, M. E., Peppas, N. A. & Langer, R. Engineering precision nanoparticles for drug delivery. *Nat Rev Drug Discov* **20**, 101-124, doi:10.1038/s41573-020-0090-8 (2021).
31 Oleksy, M., Dynarowicz, K. & Aebisher, D. Advances in Biodegradable Polymers and Biomaterials for Medical Applications-A Review. *Molecules* **28**, doi:10.3390/molecules28176213 (2023).
32 Thornton, A. J., Alsberg, E., Albertelli, M. & Mooney, D. J. Shape-defining scaffolds for minimally invasive tissue engineering. *Transplantation* **77**, 1798-1803, doi:10.1097/01.tp.0000131152.71117.0e (2004).
33 Gao, C. D., Peng, S. P., Feng, P. & Shuai, C. J. Bone biomaterials and interactions with stem cells. *Bone Res* **5**, doi:10.1038/boneres.2017.59 (2017).
34 Ng, K. W., Kugler, L. E., Doty, S. B., Ateshian, G. A. & Hung, C. T. Scaffold degradation elevates the Collagen content and dynamic compressive modulus in engineered articular cartilage. *Osteoarthr Cartilage* **17**, 220-227, doi:10.1016/j.joca.2008.06.013 (2009).

35 Spicer, C. D., Pashuck, E. T. & Stevens, M. M. Achieving Controlled Biomolecule-Biomaterial Conjugation. *Chemical Reviews* **118**, 7702-7743, doi:10.1021/acs.chemrev.8b00253 (2018).
36 Janeway Jr, C. A. & Medzhitov, R. Innate immune recognition. *Annual review of immunology* **20**, 197-216 (2002).
37 Veiseh, O., Doloff, J. C., Ma, M. L., Vegas, A. J., Tam, H. H., Bader, A. R., Li, J., Langan, E., Wyckoff, J., Loo, W. S., Jhunjhunwala, S., Chiu, A., Siebert, S., Tang, K., Hollister-Lock, J., Aresta-Dasilva, S., Bochenek, M., Mendoza-Elias, J., Wang, Y., Qi, M., Lavin, D. M., Chen, M., Dholakia, N., Thakrar, R., Lacík, I., Weir, G. C., Oberholzer, J., Greiner, D. L., Langer, R. & Anderson, D. G. Size- and shape-dependent foreign body immune response to materials implanted in rodents and non-human primates. *Nat Mater* **14**, 643-U125, doi:10.1038/Nmat4290 (2015).
38 Fang, R. H., Gao, W. W. & Zhang, L. F. Targeting drugs to tumours using cell membrane-coated nanoparticles. *Nat Rev Clin Oncol* **20**, 33-48, doi:10.1038/s41571-022-00699-x (2023).
39 Sadtler, K., Estrellas, K., Allen, B. W., Wolf, M. T., Fan, H. N., Tam, A. J., Patel, C. H., Luber, B. S., Wang, H., Wagner, K. R., Powell, J. D., Housseau, F., Pardoll, D. M. & Elisseeff, J. H. Developing a pro-regenerative biomaterial scaffold microenvironment requires T helper 2 cells. *Science* **352**, 366-370, doi:10.1126/science.aad9272 (2016).
40 Sunwoo, S.-H., Han, S. I., Park, C. S., Kim, J. H., Georgiou, J. S., Lee, S.-P., Kim, D.-H. & Hyeon, T. Soft bioelectronics for the management of cardiovascular diseases. *Nature Reviews Bioengineering*, doi:10.1038/s44222-023-00102-z (2023).
41 Choi, H., Kim, Y., Kim, S., Jung, H., Lee, S., Kim, K., Han, H. S., Kim, J. Y., Shin, M. & Son, D. Adhesive bioelectronics for sutureless epicardial interfacing. *Nat Electron*, doi:10.1038/s41928-023-01023 (2023).
42 Jiang, Y. W., Trotsyuk, A. A., Niu, S. M., Henn, D., Chen, K., Shih, C. C., Larson, M. R., Mermin-Bunnell, A. M., Mittal, S., Lai, J. C., Saberi, A., Beard, E., Jing, S., Zhong, D. L., Steele, S. R., Sun, K. F., Jain, T., Zhao, E., Neimeth, C. R., Viana, W. G., Tang, J., Sivaraj, D., Padmanabhan, J., Rodrigues, M., Perrault, D. P., Chattopadhyay, A., Maan, Z. N., Leeolou, M. C., Bonham, C. A., Kwon, S. H., Kussie, H. C., Fischer, K. S., Gurusankar, G., Liang, K., Zhang, K. L., Nag, R., Snyder, M. P., Januszyk, M., Gurtner, G. C. & Bao, Z. N. Wireless, closed-loop, smart bandage with integrated sensors and stimulators for advanced wound care and accelerated healing. *Nat Biotechnol* **41**, 652-662, doi:10.1038/s41587-022-01528-3 (2023).
43 McCaig, C. D., Rajnicek, A. M., Song, B. & Zhao, M. Controlling cell behavior electrically: Current views and future potential. *Physiol Rev* **85**, 943-978, doi:DOI 10.1152/physrev.00020.2004 (2005).
44 Piccolino, M. Luigi Galvani and animal electricity: two centuries after the foundation of electrophysiology. *Trends Neurosci* **20**, 443-448, doi:Doi 10.1016/S0166-2236(97)01101-6 (1997).
45 Shi, J., Sun, C., Liang, E. & Tian, B. Semiconductor Nanowire-Based Cellular and Subcellular Interfaces. *Adv Funct Mater* **32**, 2107997 (2022).
46 Cui, Y., Wei, Q. Q., Park, H. K. & Lieber, C. M. Nanowire nanosensors for highly sensitive and selective detection of biological and chemical species. *Science* **293**, 1289-1292, doi:DOI 10.1126/science.1062711 (2001).

47 Dai, X. C., Hong, G. S., Gao, T. & Lieber, C. M. Mesh Nanoelectronics: Seamless Integration of Electronics with Tissues. *Accounts Chem Res* **51**, 309-318, doi:10.1021/acs.accounts.7b00547 (2018).
48 Shi, J. Y., Clayton, C. & Tian, B. Z. Nano-enabled cellular engineering for bioelectric studies. *Nano Res* **13**, 1214-1227, doi:10.1007/s12274-019-2580-8 (2020).
49 Ledesma, H. A., Li, X. J., Carvalho-de-Souza, J. L., Wei, W., Bezanilla, F. & Tian, B. Z. An atlas of nano-enabled neural interfaces. *Nat Nanotechnol* **14**, 645-657, doi:10.1038/s41565-019-0487-x (2019).
50 Schubert, M., Woolfson, L., Barnard, I. R. M., Dorward, A. M., Casement, B., Morton, A., Robertson, G. B., Appleton, P. L., Miles, G. B., Tucker, C. S., Pitt, S. J. & Gather, M. C. Monitoring contractility in cardiac tissue with cellular resolution using biointegrated microlasers. *Nat Photonics* **14**, 452-458, doi:10.1038/s41566-020-0631-z (2020).
51 Karatum, O., Kaleli, H. N., Eren, G. O., Sahin, A. & Nizamoglu, S. Electrical Stimulation of Neurons with Quantum Dots via Near-Infrared Light. *Acs Nano* **16**, 8233-8243, doi:10.1021/acsnano.2c01989 (2022).
52 Tian, B. Z., Liu, J., Dvir, T., Jin, L. H., Tsui, J. H., Qing, Q., Suo, Z. G., Langer, R., Kohane, D. S. & Lieber, C. M. Macroporous nanowire nanoelectronic scaffolds for synthetic tissues. *Nat Mater* **11**, 986-994, doi:10.1038/Nmat3404 (2012).
53 Eberhardson, M., Tarnawski, L., Centa, M. & Olofsson, P. S. Neural Control of Inflammation: Bioelectronic Medicine in Treatment of Chronic Inflammatory Disease. *Csh Perspect Med* **10**, doi:10.1101/cshperspect.a034181 (2020).
54 Schenone, M., Dancík, V., Wagner, B. K. & Clemons, P. A. Target identification and mechanism of action in chemical biology and drug discovery. *Nat Chem Biol* **9**, 232-240, doi:10.1038/Nchembio.1199 (2013).
55 Puleo, C. & Cotero, V. Noninvasive Neuromodulation of Peripheral Nerve Pathways Using Ultrasound and Its Current Therapeutic Implications. *Csh Perspect Med* **10**, doi:10.1101/cshperspect.a034215 (2020).
56 Selberg, J., Jafari, M., Mathews, J., Jia, M. P., Pansodtee, P., Dechiraju, H., Wu, C. X., Cordero, S., Flora, A., Yonas, N., Jannetty, S., Diberardinis, M., Teodorescu, M., Levin, M., Gomez, M. & Rolandi, M. Machine Learning-Driven Bioelectronics for Closed-Loop Control of Cells. *Adv Intell Syst-Ger* **2**, doi:10.1002/aisy.202000140 (2020).
57 Liu, A. P., Appel, E. A., Ashby, P. D., Baker, B. M., Franco, E., Gu, L., Haynes, K., Joshi, N. S., Kloxin, A. M., Kouwer, P. H. J., Mittal, J., Morsut, L., Noireaux, V., Parekh, S., Schulman, R., Tang, S. K. Y., Valentine, M. T., Vega, S. L., Weber, W., Stephanopoulos, N. & Chaudhuri, O. The living interface between synthetic biology and biomaterial design. *Nat Mater* **21**, 390-397, doi:10.1038/s41563-022-01231-3 (2022).
58 Jiang, Y. W. & Tian, B. Z. Inorganic semiconductor biointerfaces. *Nat Rev Mater* **3**, 473-490, doi:10.1038/s41578-018-0062-3 (2018).
59 Axpe, E., Orive, G., Franze, K. & Appel, E. A. Towards brain-tissue-like biomaterials. *Nat Commun* **11**, doi:10.1038/s41467-020-17245-x (2020).
60 Roth, J. G., Huang, M. S., Li, T. L., Feig, V. R., Jiang, Y. W., Cui, B. X., Greely, H. T., Bao, Z. N., Pasca, S. P. & Heilshorn, S. C. Advancing models of neural development with biomaterials. *Nat Rev Neurosci* **22**, 593-615, doi:10.1038/s41583-021-00496-y (2021).

61 Guimaraes, C. F., Gasperini, L., Marques, A. P. & Reis, R. L. The stiffness of living tissues and its implications for tissue engineering. *Nat Rev Mater* **5**, 351-370, doi:10.1038/s41578-019-0169-1 (2020).
62 Fang, Y., Yang, X., Lin, Y., Shi, J., Prominski, A., Clayton, C., Ostroff, E. & Tian, B. Dissecting biological and synthetic soft–hard interfaces for tissue-like systems. *Chemical reviews* **122**, 5233-5276 (2021).
63 Gao, D., Parida, K. & Lee, P. S. Emerging Soft Conductors for Bioelectronic Interfaces. *Adv Funct Mater* **30**, doi:10.1002/adfm.201907184 (2020).
64 Cho, Y., Park, S., Lee, J. & Yu, K. J. Emerging Materials and Technologies with Applications in Flexible Neural Implants: A Comprehensive Review of Current Issues with Neural Devices. *Adv Mater* **33**, doi:10.1002/adma.202005786 (2021).
65 Lim, C., Hong, Y. J., Jung, J., Shin, Y., Sunwoo, S. H., Baik, S., Park, O. K., Choi, S. H., Hyeon, T., Kim, J. H., Lee, S. & Kim, D. H. Tissue-like skin-device interface for wearable bioelectronics by using ultrasoft, mass-permeable, and low-impedance hydrogels. *Sci Adv* **7**, doi:10.1126/sciadv.abd3716 (2021).
66 Marshall, J. S., Warrington, R., Watson, W. & Kim, H. L. An introduction to immunology and immunopathology. *Allergy Asthma Cl Im* **14**, doi:10.1186/s13223-018-0278-1 (2018).
67 Anderson, J. M., Rodriguez, A. & Chang, D. T. in *Seminars in immunology.* 86-100 (Elsevier).
68 Yang, X., Qi, Y., Wang, C., Zwang, T. J., Rommelfanger, N. J., Hong, G. & Lieber, C. M. Laminin-coated electronic scaffolds with vascular topography for tracking and promoting the migration of brain cells after injury. *Nat Biomed Eng*, doi:10.1038/s41551-023-01101-6 (2023).
69 Onuki, Y., Bhardwaj, U., Papadimitrakopoulos, F. & Burgess, D. J. A review of the biocompatibility of implantable devices: current challenges to overcome foreign body response. *J Diabetes Sci Technol* **2**, 1003-1015, doi:10.1177/193229680800200610 (2008).
70 Zhou, W., Jiang, Y., Xu, Q., Chen, L., Qiao, H., Wang, Y. X., Lai, J. C., Zhong, D., Zhang, Y., Li, W., Du, Y., Wang, X., Lei, J., Dong, G., Guan, X., Ma, S., Kang, P., Yuan, L., Zhang, M., Tok, J. B., Li, D., Bao, Z. & Jia, W. Soft and stretchable organic bioelectronics for continuous intraoperative neurophysiological monitoring during microsurgery. *Nat Biomed Eng*, doi:10.1038/s41551-023-01069-3 (2023).
71 Mariani, E., Lisignoli, G., Borzi, R. M. & Pulsatelli, L. Biomaterials: Foreign Bodies or Tuners for the Immune Response? *Int J Mol Sci* **20**, doi:10.3390/ijms20030636 (2019).
72 Lacour, S. P., Courtine, G. & Guck, J. Materials and technologies for soft implantable neuroprostheses. *Nat Rev Mater* **1**, doi:10.1038/natrevmats.2016.63 (2016).
73 Han, M. D., Chen, L., Aras, K., Liang, C. M., Chen, X. X., Zhao, H. B., Li, K., Faye, N. R., Sun, B. H., Kim, J. H., Bai, W. B., Yang, Q. S., Ma, Y. H., Lu, W., Song, E. M., Baek, J. M., Lee, Y. J., Liu, C., Model, J. B., Yang, G. J., Ghaffari, R., Huang, Y. G., Efimov, I. R. & Rogers, J. A. Catheter-integrated soft multilayer electronic arrays for multiplexed sensing and actuation during cardiac surgery. *Nat Biomed Eng* **4**, 997-1009, doi:10.1038/s41551-020-00604-w (2020).
74 Yu, K. J., Kuzum, D., Hwang, S. W., Kim, B. H., Juul, H., Kim, N. H., Won, S. M., Chiang, K., Trumpis, M., Richardson, A. G., Cheng, H. Y., Fang, H., Thompson, M., Bink, H., Talos, D., Seo, K. J., Lee, H. N., Kang, S. K., Kim, J. H., Lee, J. Y., Huang, Y.

G., Jensen, F. E., Dichter, M. A., Lucas, T. H., Viventi, J., Litt, B. & Rogers, J. A. Bioresorbable silicon electronics for transient spatiotemporal mapping of electrical activity from the cerebral cortex. *Nat Mater* **15**, 782-791, doi:10.1038/Nmat4624 (2016).
75 Liu, J., Fu, T.-M., Cheng, Z., Hong, G., Zhou, T., Jin, L., Duvvuri, M., Jiang, Z., Kruskal, P., Xie, C., Suo, Z., Fang, Y. & Lieber, C. M. Syringe-injectable electronics. *Nat Nanotechnol* **10**, 629-636, doi:10.1038/nnano.2015.115 (2015).
76 Ha, T., Tran, J., Liu, S. Y., Jang, H., Jeong, H., Mitbander, R., Huh, H., Qiu, Y. T., Duong, J., Wang, R. L., Wang, P. L., Tandon, A., Sirohi, J. & Lu, N. S. A Chest-Laminated Ultrathin and Stretchable E-Tattoo for the Measurement of Electrocardiogram, Seismocardiogram, and Cardiac Time Intervals. *Adv Sci* **6**, doi:10.1002/advs.201900290 (2019).
77 Chen, X. Y., Qian, X. J., Lam, K. H., Chiu, C. T., Chen, R. M., Chen, Z. Y., Shung, R., Yu, P. & Zhou, Q. F. Helical-Like 3D Ultrathin Piezoelectric Element for Complicated Ultrasonic Field. *Adv Funct Mater* **29**, doi:10.1002/adfm.201902912 (2019).
78 Guo, X., Ni, X., Li, J., Zhang, H., Zhang, F., Yu, H., Wu, J., Bai, Y., Lei, H., Huang, Y., Rogers, J. A. & Zhang, Y. Designing Mechanical Metamaterials with Kirigami-Inspired, Hierarchical Constructions for Giant Positive and Negative Thermal Expansion. *Adv Mater* **33**, e2004919, doi:10.1002/adma.202004919 (2021).
79 Kim, D. H., Lu, N., Ghaffari, R., Kim, Y. S., Lee, S. P., Xu, L., Wu, J., Kim, R. H., Song, J., Liu, Z., Viventi, J., de Graff, B., Elolampi, B., Mansour, M., Slepian, M. J., Hwang, S., Moss, J. D., Won, S. M., Huang, Y., Litt, B. & Rogers, J. A. Materials for multifunctional balloon catheters with capabilities in cardiac electrophysiological mapping and ablation therapy. *Nat Mater* **10**, 316-323, doi:10.1038/nmat2971 (2011).
80 Tang, L. X., Shang, J. & Jiang, X. Y. Multilayered electronic transfer tattoo that can enable the crease amplification effect. *Sci Adv* **7**, doi:10.1126/sciadv.abe3778 (2021).
81 Rogers, J. A., Someya, T. & Huang, Y. G. Materials and Mechanics for Stretchable Electronics. *Science* **327**, 1603-1607, doi:10.1126/science.1182383 (2010).
82 Wang, W. C., Wang, S. H., Rastak, R., Ochiai, Y., Niu, S. M., Jiang, Y. W., Arunachala, P. K., Zheng, Y., Xu, J., Matsuhisa, N., Yan, X. Z., Kwon, S. K., Miyakawa, M., Zhang, Z. T., Ning, R., Foudeh, A. M., Yun, Y., Linder, C., Tok, J. B. H. & Bao, Z. N. Strain-insensitive intrinsically stretchable transistors and circuits. *Nat Electron* **4**, 143-150, doi:10.1038/s41928-020-00525-1 (2021).
83 Yang, C. & Suo, Z. Hydrogel ionotronics. *Nat Rev Mater* **3**, 125-142, doi:10.1038/s41578-018-0018-7 (2018).
84 Veerapandian, S., Jang, W., Seol, J. B., Wang, H. B., Kong, M., Thiyagarajan, K., Kwak, J., Park, G., Lee, G., Suh, W., You, I., Kiliç, M. E., Giri, A., Beccai, L., Soon, A. & Jeong, U. Hydrogen-doped viscoplastic liquid metal microparticles for stretchable printed metal lines. *Nat Mater* **20**, 533-540, doi:10.1038/s41563-020-00863-7 (2021).
85 Choi, S., Han, S. I., Kim, D., Hyeon, T. & Kim, D. H. High-performance stretchable conductive nanocomposites: materials, processes, and device applications. *Chem Soc Rev* **48**, 1566-1595, doi:10.1039/c8cs00706c (2019).
86 Feig, V. R., Tran, H., Lee, M., Liu, K., Huang, Z. J., Beker, L., Mackanic, D. G. & Bao, Z. N. An Electrochemical Gelation Method for Patterning Conductive PEDOT:PSS Hydrogels. *Adv Mater* **31**, doi:10.1002/adma.201902869 (2019).

87 Kim, N., Kee, S., Lee, S. H., Lee, B. H., Kahng, Y. H., Jo, Y. R., Kim, B. J. & Lee, K. Highly Conductive PEDOT: PSS Nanofibrils Induced by Solution-Processed Crystallization. *Adv Mater* **26**, 2268-2272, doi:10.1002/adma.201304611 (2014).
88 Lee, J. H., Jeong, Y. R., Lee, G., Jin, S. W., Lee, Y. H., Hong, S. Y., Park, H., Kim, J. W., Lee, S. S. & Ha, J. S. Highly Conductive, Stretchable, and Transparent PEDOT:PSS Electrodes Fabricated with Triblock Copolymer Additives and Acid Treatment. *Acs Appl Mater Inter* **10**, 28027-28035, doi:10.1021/acsami.8b07287 (2018).
89 Liu, Y. X., Liu, J., Chen, S. C., Lei, T., Kim, Y., Niu, S. M., Wang, H. L., Wang, X., Foudeh, A. M., Tok, J. B. H. & Bao, Z. N. Soft and elastic hydrogel-based microelectronics for localized low-voltage neuromodulation. *Nat Biomed Eng* **3**, 58-68, doi:10.1038/s41551-018-0335-6 (2019).
90 Someya, T., Bao, Z. N. & Malliaras, G. G. The rise of plastic bioelectronics. *Nature* **540**, 379-385, doi:10.1038/nature21004 (2016).
91 Wang, C. H., Chen, X. Y., Wang, L., Makihata, M., Liu, H. C., Zhou, T. & Zhao, X. H. Bioadhesive ultrasound for long-term continuous imaging of diverse organs. *Science* **377**, 517-523, doi:10.1126/science.abo2542 (2022).
92 Deng, J., Yuk, H., Wu, J. J., Varela, C. E., Chen, X. Y., Roche, E. T., Guo, C. F. & Zhao, X. H. Electrical bioadhesive interface for bioelectronics. *Nat Mater* **20**, 229-236, doi:10.1038/s41563-020-00814-2 (2021).
93 Lu, B. Y., Yuk, H., Lin, S. T., Jian, N. N., Qu, K., Xu, J. K. & Zhao, X. H. Pure PEDOT:PSS hydrogels. *Nat Commun* **10**, doi:10.1038/s41467-019-09003-5 (2019).
94 Keplinger, C., Sun, J.-Y., Foo, C. C., Rothemund, P., Whitesides, G. M. & Suo, Z. Stretchable, transparent, ionic conductors. *Science* **341**, 984-987 (2013).
95 Liu, X. H., Wu, D. B., Wang, H. L. & Wang, Q. G. Self-Recovering Tough Gel Electrolyte with Adjustable Supercapacitor Performance. *Adv Mater* **26**, 4370-4375, doi:10.1002/adma.201400240 (2014).
96 Ohm, Y., Pan, C., Ford, M. J., Huang, X., Liao, J. & Majidi, C. An electrically conductive silver–polyacrylamide–alginate hydrogel composite for soft electronics. *Nat Electron* **4**, 185-192, doi:10.1038/s41928-021-00545-5 (2021).
97 Feig, V. R., Santhanam, S., McConnell, K. W., Liu, K., Azadian, M., Brunel, L. G., Huang, Z., Tran, H., George, P. M. & Bao, Z. Conducting polymer-based granular hydrogels for injectable 3D cell scaffolds. *Adv Mater Technol* **6**, doi:10.1002/admt.202100162 (2021).
98 Tringides, C. M., Vachicouras, N., de Lazaro, I., Wang, H., Trouillet, A., Seo, B. R., Elosegui-Artola, A., Fallegger, F., Shin, Y., Casiraghi, C., Kostarelos, K., Lacour, S. P. & Mooney, D. J. Viscoelastic surface electrode arrays to interface with viscoelastic tissues. *Nat Nanotechnol* **16**, 1019-1029, doi:10.1038/s41565-021-00926-z (2021).
99 Yuk, H., Varela, C. E., Nabzdyk, C. S., Mao, X., Padera, R. F., Roche, E. T. & Zhao, X. Dry double-sided tape for adhesion of wet tissues and devices. *Nature* **575**, 169-174, doi:10.1038/s41586-019-1710-5 (2019).
100 Bai, T., Li, J. Q., Sinclair, A., Imren, S., Merriam, F., Sun, F., O'Kelly, M. B., Nourigat, C., Jain, P., Delrow, J. J., Basom, R. S., Hung, H. C., Zhang, P., Li, B. W., Heimfeld, S., Jiang, S. Y. & Delaney, C. Expansion of primitive human hematopoietic stem cells by culture in a zwitterionic hydrogel. *Nat Med* **25**, 1566-1575, doi:10.1038/s41591-019-0601-5 (2019).

101 Boutry, C. M., Beker, L., Kaizawa, Y., Vassos, C., Tran, H., Hinckley, A. C., Pfattner, R., Niu, S. M., Li, J. H., Claverie, J., Wang, Z., Chang, J., Fox, P. M. & Bao, Z. N. Biodegradable and flexible arterial-pulse sensor for the wireless monitoring of blood flow. *Nat Biomed Eng* **3**, 47-57, doi:10.1038/s41551-018-0336-5 (2019).

102 Yuk, H., Wu, J. J. & Zhao, X. H. Hydrogel interfaces for merging humans and machines. *Nat Rev Mater* **7**, 935-952, doi:10.1038/s41578-022-00483-4 (2022).

103 Zhang, L., Cao, Z. Q., Bai, T., Carr, L., Ella-Menye, J. R., Irvin, C., Ratner, B. D. & Jiang, S. Y. Zwitterionic hydrogels implanted in mice resist the foreign-body reaction. *Nat Biotechnol* **31**, 553-556, doi:10.1038/nbt.2580 (2013).

104 Li, B. W., Yuan, Z. F., Jain, P., Hung, H. C., He, Y. W., Lin, X. J., McMullen, P. & Jiang, S. Y. De novo design of functional zwitterionic biomimetic material for immunomodulation. *Sci Adv* **6**, doi:10.1126/sciadv.aba0754 (2020).

105 Farah, S., Doloff, J. C., Muller, P., Sadraei, A., Han, H. J., Olafson, K., Vyas, K., Tam, H. H., Hollister-Lock, J., Kowalski, P. S., Griffin, M., Meng, A., McAvoy, M., Graham, A. C., McGarrigle, J., Oberholzer, J., Weir, G. C., Greiner, D. L., Langer, R. & Anderson, D. G. Long-term implant fibrosis prevention in rodents and non-human primates using crystallized drug formulations. *Nat Mater* **18**, 892-904, doi:10.1038/s41563-019-0377-5 (2019).

Chapter 2. Monolithic-to-focal biointerfaces for bioelectronics

2.1 Introduction

Bioelectronics has become emerging tools in disease diagnosis and treatment[1,2]. Yet, the mechanical mismatch at the material and biological interface significantly impedes the capabilities of bioelectronics in signal recording. Current strategies to promote tight biointerfaces rely mainly on thin, flexible membranes with low bending stiffness, such as those developed for flexible bioelectronics[3,4], and the addition of biocompatible or biodegradable adhesives[5,6]. Recent research has shown that viscoelastic polymers or hydrogels provide conformal biointerfaces with improved signal transmission and biocompatibility[7,8]. These monolithic or interconnected constructs, such as mesh devices or hydrogel membranes, can easily reside on an organ-level target in conformity with target's surface curvature.

On the other hand, a mobile, transient, and cellular-scale biomaterial capable of interacting with surrounding cells or tissues would offer a more dynamic and less invasive biointerface[9]. Focal, cellular-scale biointerfaces would also, by design, provide the interstitial space required for cellular proliferation and migration and physiological signal transmission, unlike monolithic interfaces that often require degradation prior to infiltration by cells or biomolecules[10]. Such focal biointerfaces would thus enhance tissue regeneration[11] and the efficiency of biomedical devices.

There are both challenges and opportunities associated with the design of materials for transient, cellular scale biointerfaces in physiological environments. First, the biomaterials are typically prepared with microscopic cell-size-matched features for in-vivo delivery, which limits their forms (e.g., unlikely to be a macroscopic patch) and handling methods[12,13]. Second, the highly dynamic and heterogeneous cellular microenvironment undergoes constant remodeling[14], including changes to pH, enzymes, and other biochemical species. Therefore, it is crucial to ensure that the

biointerfacial material displays cellular affinity with dynamic behavior. Third, naturally occurring biopolymers have been explored extensively in the food, pharmaceutical, and cosmetic industries due to their biocompatible and biodegradable properties[15]. These materials may also be used for other applications, including bioelectronics and robotics. It is expected that future cellular-scale biointerfacial materials will demonstrate easier macroscopic handling capability, facilitate cellular-scale adhesion with spatiotemporal control, and include a greater amount of naturally occurring elements.

Here, we demonstrate that a dynamic hydrogel composite can release of cellular-size granules in the physiological environments for regenerative medicine and bioelectronics, which has been long sought in the development of hydrogel-based artificial cells[16]. A monolithic-to-focal evolving process allows the composite to harness the properties and functions of both monolithic and focal biointerfaces (Figure 2-1). The hydrogel composites use gelatin and chitosan as the hydrogel matrix to respond to biological environments while also facilitating macroscopic material shaping and manipulation. Additionally, the hydrogel composite consists of cellular-scale releasable granules (i.e., granular hydrogel) that can form focal bio-adhesions in vivo and ex vivo and degrade at the end for therapeutic benefit.

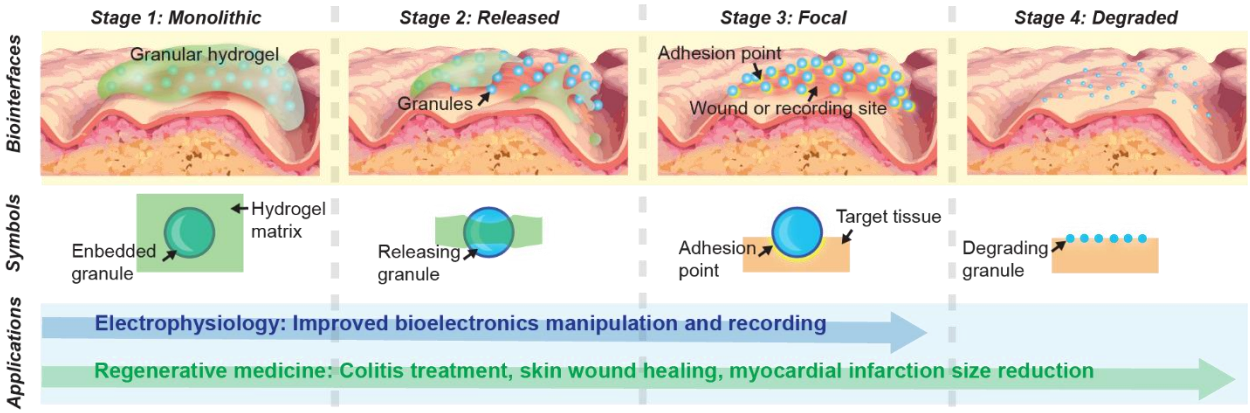

Figure 2-1. Schematic of the dynamic processes involved in the construction of the granular distributed biointerface. Stage 1: The viscoelastic granule-releasing hydrogel conforms to the underlying tissue. Stage 2: The granule-releasing hydrogel releases the granular composites to the tissue surface based on the physiological environment cues. Stage 3: The released granular composites anchorage or dock on the tissue surface through the biological affinitive surface. Stage 4: The degradation fragments of granules are beneficial for tissue repair and regeneration.

The release-adhesion-degradation dynamics of the granule-releasing hydrogels is achieved through (1) modulation of viscoelasticity or enzymatic digestion of the gelatin and chitosan matrix for granular release, (2) drug-inspired surface modification of starch/chitosan-based granules with aspirin for establishing focal adhesion, and (3) the utilization of naturally occurring and biodegradable biopolymers and biomolecules such as starch, chitosan, gelatin, aspirin. The initial macroscale forms of the composites protect fragile electronic components and facilitate flexible bioelectronic device deployment. Besides, the monolithic matrix permits a tunable viscoelastic environment for slow and responsive granular release to tissue. Upon dispersion, the microscale granules with surface modifications would instantiate dispersed biointerfaces. This evolving system integrates the benefits and application domains of the current monolithic and focal biological interfacing materials and devices.

2.2 Result and Discussion

2.2.1 Monolithic-to-focal biointerfaces design

To construct the transition from monolithic to focal biointerfaces, we synthesized granule-releasing hydrogels using naturally derived components: starch, chitosan, and gelatin. The specific roles of each component in this context are detailed in Table 2-1. In a standard experiment, we began by mixing the starch with an aqueous chitosan solution at 40ºC. This step pre-hydrated the granules, resulting in a starch/chitosan granular suspension. Subsequently, gelatin was introduced to the suspension. The mixture was then solidified by cooling it within a casting mold.

Structure	Component	Chemical roles	Physical roles	Biological roles
Granule	**Starch**	It establishes the chemical template for other granular components. It is naturally occurring and biodegradable.	The hydrated starch granules have cellular length scale. The starch granules tune the modulus and viscoelasticity of the hydrogel composites. The starch granules establish the focal adhesion points for biophysical barriers. The established focal interfaces show more efficient electrophysiology recording than the monolithic biointerfaces.	It is the most important therapeutic ingredient for the regenerative medicine applications in this work. The starch granules help form or rebuild biophysical barriers. The starch granules modulate microbiota diversity.
Granular surface	**Chitosan**	The patchy chitosan coating provides the chemical anchor point for further surface modification via carbodiimide chemistry. The chitosan coating may lead to slower granule digestion in the stomach and intestine. It is naturally occurring and biodegradable.	The positively charged chitosan may mediate the initial granules/hydrogel interactions.	It may offer additional therapeutic benefits for treating skin wound.

Table 2-1 The chemical, physical and biological roles of each component in the granule-releasing hydrogel.

	Aspirin	Its bio-affinity (i.e., good oral absorption and lipophilicity) reduces the interaction energy at biointerfaces. It is naturally occurring and biodegradable.	It enables the granular adhesions onto cells and tissues.	It helps the granule-releasing hydrogels achieve the best therapeutic effects. Its intrinsic drug effects and toxicity are largely limited when it is conjugated.
Hydrogel matrix	**Gelatin and chitosan**	It is naturally occurring and biodegradable.	Encapsulation of granules allows for diverse macroscopic manipulations and device integration. Gelatin-based responsiveness trigger granule release. The gelatin matrix provides the initial conformal monolithic biological adhesion.	Enzymatic digestion trigger granule release. It may offer additional therapeutic benefits for treating gut inflammation, and skin wound.

Table 2-1, continued.

The gelatin forms a three-dimensional hydrogel network that confines the starch/chitosan granules for initial macroscopic manipulation. Upon release, the cellular-scale granules would penetrate into deep and narrow tissue regions (e.g., wound site, intestinal lumen) not easily accessed by traditional bulky hydrogels[17]. We use the microscope to characterize the average size of the starch we used in this study (Figure 2-2). We found that the starch has an average size is 14.69 μm.

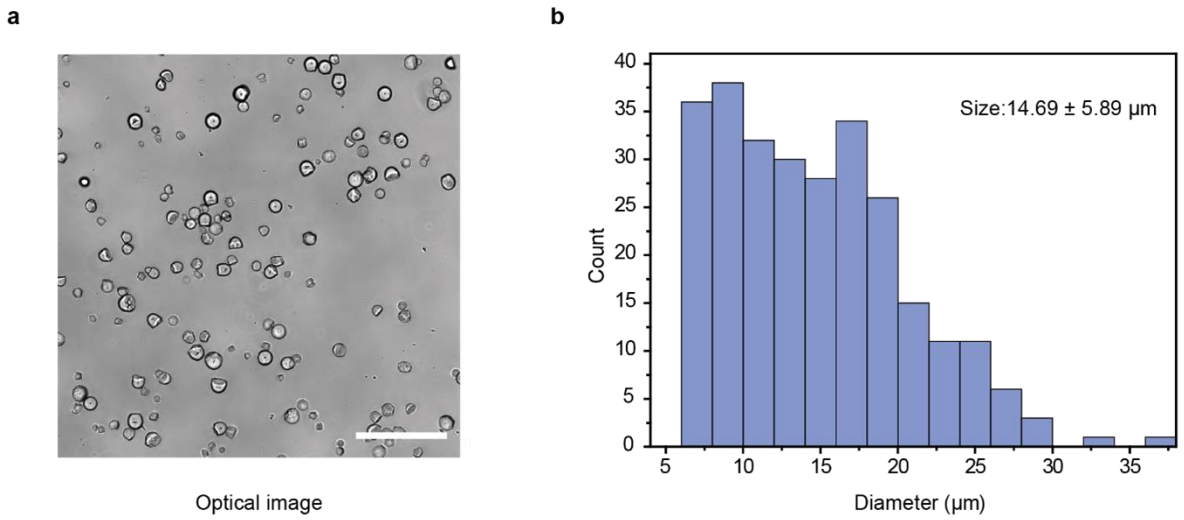

Figure 2-2 The resistant starch has an average size of 14.69 μm. (a) Optical image shows the morphology of the starch granules. Scale bar 100 μm. (b) The plot shows the size distribution of the starch granules, and the average diameter of starch granules is around 15 μm.

We then characterized the morphology and dynamics of the granule-releasing hydrogels. It has been reported that chitosan can effectively interact with starch granules through intermolecular interactions[18]. Using metal labeling and synchrotron-based 3D X-ray fluorescence tomography, we examined the structure of individual starch/chitosan granules and revealed the patchy distribution of chitosan on the surface of the starch-based granules (Figure 2-3).

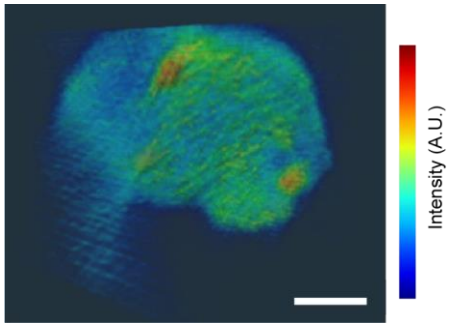

Figure 2-3 3D ptychographic tomography showing the molecular distribution of chitosan on the surface of starch granules. Color bar indicates the intensity of the chitosan signal. Scale bar, 2 μm.

Synchrotron-based X-ray fluorescence microscopy and tomography were utilized at the Bionanoprobe (BNP) situated at beamline 9-ID-B of the Advanced Photon Source at Argonne National Laboratory to analyze the structure of the starch/chitosan granules. The chitosan polymer was stained with copper chloride to facilitate X-ray imaging. With the aid of zone plate optics, X-ray photons, having an energy of 10.5 keV, were concentrated on the sample, achieving a focal length of approximately 80 nm. The techniques of 3D ptychographic tomography and various angular views are illustrated in Figures 2-4.

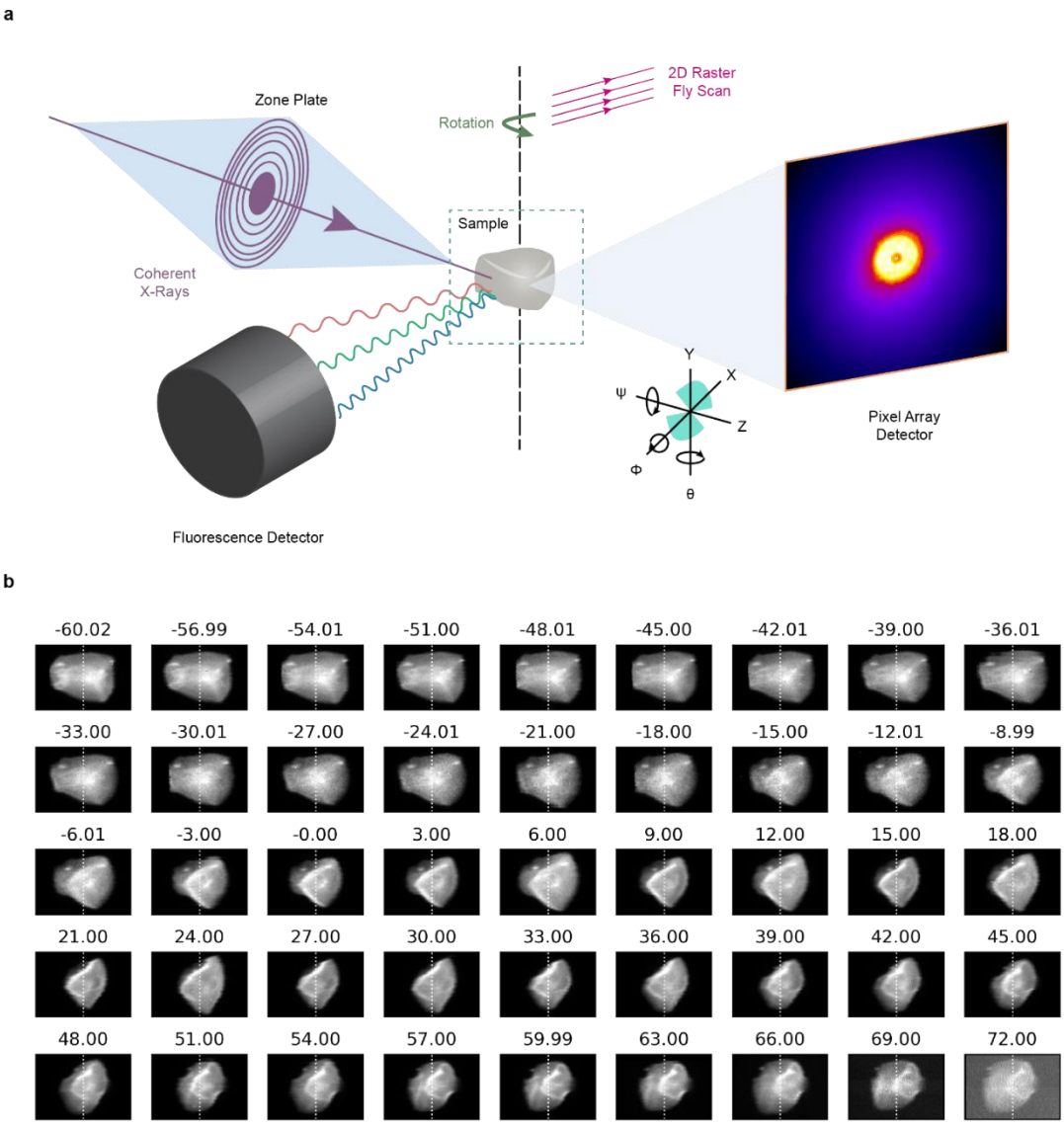

Figure 2-4 X-ray fluorescence tomography reveals the structure of starch and chitosan composite. (a) Experimental schematic of the x-ray fluorescence tomography measurement experiment. With the aid of a Fresnel zone plate, a monochromatic x-ray beam was focused onto a spot of ~90 nm on starch and chitosan (Cu stained) composite sample. A raster fly-scan was performed on the sample in the x-y plane. Using a fluorescence detector and a pixel array detector, fluorescence signals and diffraction patterns were simultaneously recorded. (b) X-ray fluorescence image sequences show the structure of starch and chitosan composite from different angle views.

The surface-attached chitosan provides an easier chemical anchor point for further modification of the granules as the amine groups of the chitosan are more reactive than the hydroxyl groups of the

starch[19]. When embedded inside the hydrogel matrix, the cellular-scale granules are evenly distributed as revealed by confocal microscope imaging (Figure 2-5).

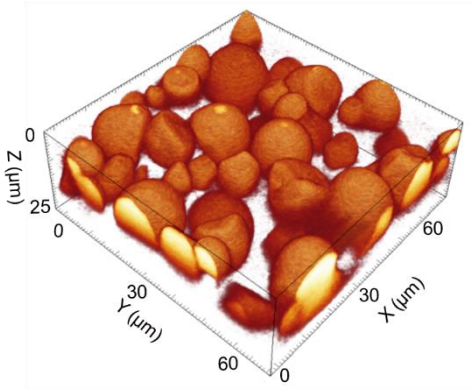

Figure 2-5 Confocal image of a granule-releasing hydrogel showing that the starch granules are physically proximate to the polymeric matrix. This indicating potential interactions between the granules and supportive matrices.

Scanning electron microscope (SEM) image shows that the granules form tight interfaces with the nanostructured hydrogel matrix (Figure 2-6).

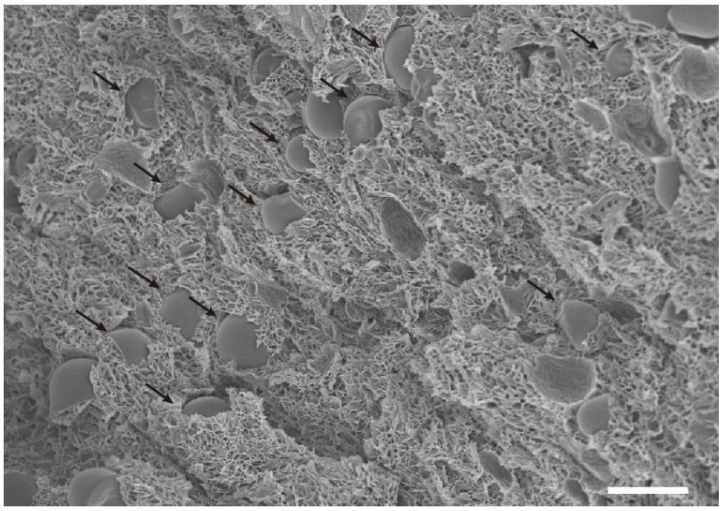

Figure 2-6 SEM image of a freeze-dried granule-releasing hydrogel shows granular composite inside the dynamic matrix. Arrows indicate the position of granules. Scale bar, 20 µm.

The initial biointerface construction would benefit from a conformal biomaterial with tissue-like mechanical behavior[20]. The as-prepared granule-releasing hydrogel has a high-water content (>70%). We performed the tensile test and find that the granule-releasing hydrogel has suitable softness. The Young's modulus of the granule-releasing hydrogel is 80 kPa, which is similar to wound tissue and cardiac muscles[21]). The granule-releasing hydrogels also have moderate stretchability (maximum strain > 100%) (Figure 2-7).

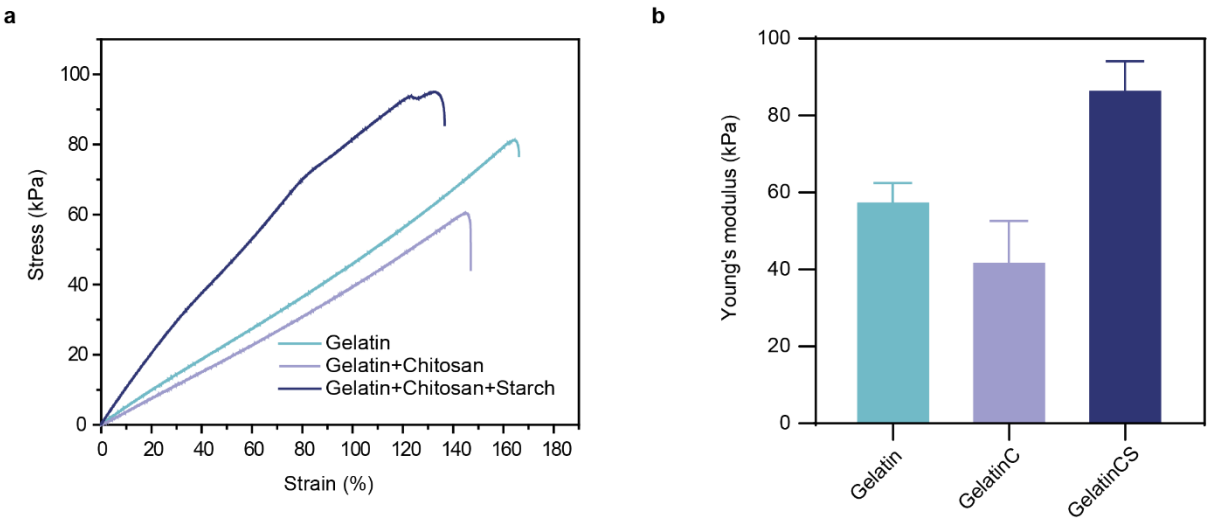

Figure 2-7 The starch granules strengthen the mechanical behavior of the hydrogel composite. (a) The stress-strain curves illustrate how individual components affect the material's mechanical properties. (b) The inclusion of the starch granules increases Young's modulus of the hydrogel composite. Stress (σ) in the curve was defined as the loading force divided by the cross-section area. Extension rates for all samples were 75 mm/min. Gelatin: Gelatin hydrogel. GelatinC: Gelatin+Chitosan hydrogel. GelatinCS: Gelatin+Chitosan+Starch hydrogel. Data are presented as mean ± standard error of mean. (n = 3).

The granule-releasing hydrogels also exhibit tissue-like viscoelastic behavior as evidenced by strain- and frequency-dependent moduli, fast stress relaxation, and large mechanical hysteresis (Figure 2-8), which largely assists in forming conformal interfaces with curvilinear surfaces.

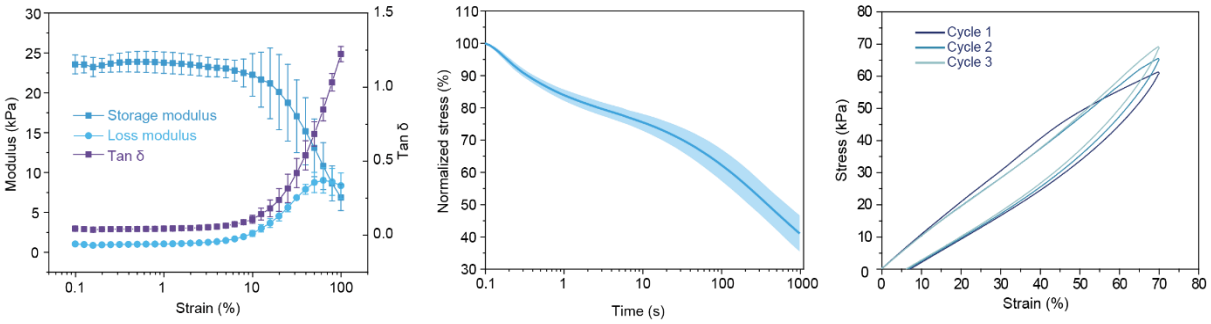

Figure 2-8 Mechanical tests confirm the viscoelastic behavior of granule-releasing hydrogels. (Left) Storage modulus (G'; left axis), Loss modulus (G''; left axis), and tan δ (G''/G'; right axis) are shown as a function of strain at 1Hz. (Middle) The stress relaxation test shows the granule-releasing hydrogel has fast relaxation behaviors. (Right) The strain-stress curve illustrates that the granule-releasing hydrogel undergoes energy dissipation during the cyclic mechanical loading. Data are presented as mean ± standard error of mean. (n = 3).

To comprehensively grasp how the concentration of starch granules influences the viscoelastic behavior of the hydrogel, we conducted a systematic study using amplitude sweep and frequency sweep in our shear rheology analysis, as depicted in Figure 2-9. The observed viscoelastic behavior can be primarily attributed to the rearrangement and reorganization of granules within the matrix, providing enhanced energy dissipation[22].

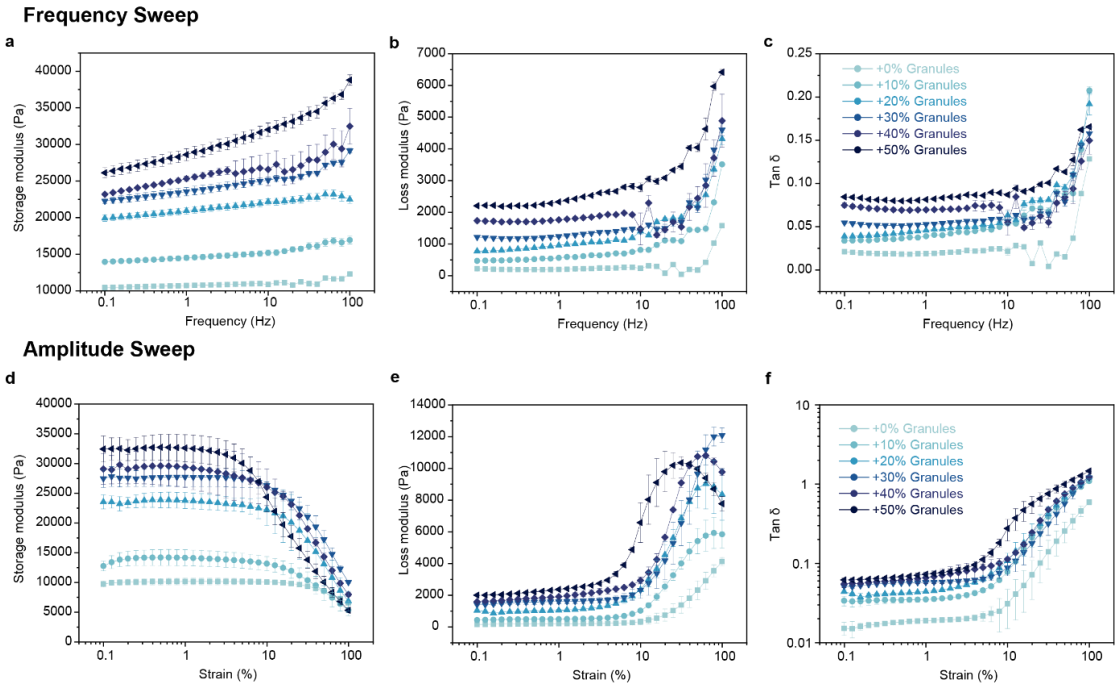

Figure 2-9 Rheological analysis of the granule-releasing hydrogel shows the tunable viscoelastic behavior by varying the granules loading fractions. (a-c) Granule-releasing hydrogels with different granular loading fractions were analyzed to determine G' (storage modulus; (a)), G'' (loss modulus; (b)), and Tan δ (loss modulus/storage modulus; (c)) over a frequency sweep, at a constant strain of 1%. (d-f) Granule-releasing hydrogels with different granular loading fractions were analyzed to determine G' (storage modulus; (d)), G'' (loss modulus; (e)), and Tan δ (loss modulus/storage modulus; (f)) over a strain sweep, at a constant frequency of 1 Hz. Data are presented as mean ± standard error of mean. (n = 3).

2.2.2 Monolithic-to-focal process study

To establish the evolving biointerfaces, the granule-releasing hydrogels should release the granules at or before the targeted biointerface in response to diverse stimuli. We first investigate how temperature variations shift the viscoelastic properties of the granule-releasing hydrogels and facilitate granular release through 3D laser microscope image (Figure 2-10).

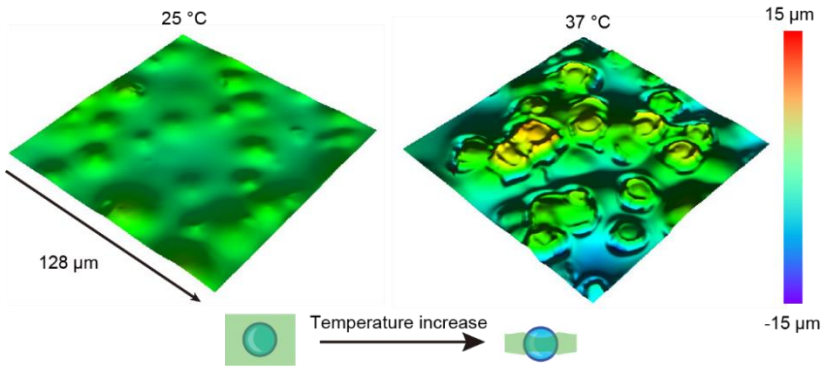

Figure 2-10 3D laser microscope image showing that the granules are released following the dynamic transition of the granule-releasing hydrogel at body temperature.

Through rheological analysis, we also review the gel-sol transition dynamic of granule-releasing hydrogel. The result indicates that the granule-releasing hydrogel has a rapid transition behavior (Figure 2-11)

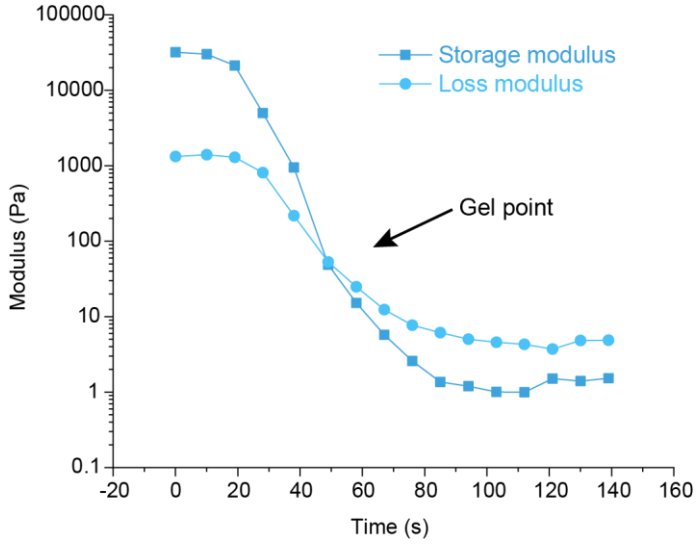

Figure 2-11 Rheology analysis during the gel-sol transition process of the granule-releasing hydrogel indicated its rapid transition behavior. Granule-releasing hydrogel was placed on the rheometer plate at a temperature of 37 °C and the rheology analysis was initiated immediately.

We examined rheological changes across a temperature ramp to understand the rheological response of the granule-releasing hydrogel to temperature (Figure 2-12). The contour map

illustrates that the granule-releasing hydrogel can transform and reconstruct itself under physiological conditions, *i.e.*, an evolving granule-releasing hydrogel. This is largely due to the gelation behavior of gelatin-based polymers near body temperature[23], which enables a sharp decrease in the storage modulus (3 to 5 orders of magnitude; color change from red to blue in the contour map) as the temperature changes from 25ºC to 40ºC, and release of the encapsulated starch granules.

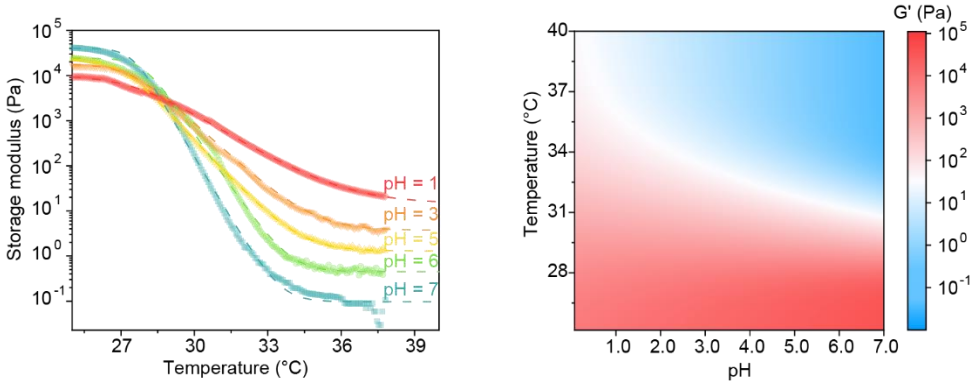

Figure 2-12 A temperature ramp rheological test shows that the granule-releasing hydrogels respond to both temperature and pH. (f) Contour map of the hydrogel storage modulus (G') as a function of temperature and pH. Red regions represent high modulus, while blue regions represent low modulus.

To predict the releasing properties and mechanical behavior of granule-releasing hydrogels, we applied an empirical model. For the sake of the empirical model's simplicity, we make an approximation that G' has two plateaus at low temperature (solid modulus G_0 at 25 ºC) and high temperature (liquid modulus G_∞ at 40 ºC), respectively. The assumption is based on the observation that the major temperature response comes from the phase-transition alone. Under such assumption, the storage modulus can be empirically described by:

$$G'(T, pH) = G_\infty + \frac{G_0 - G_\infty}{1 + (T/T_c)^m} \qquad (1)$$

Where the characteristic temperature, T_c, describes the phase-transition temperature, and the power m describes the hydrogel's sensitivity to the temperature change. Both G_0, G_∞, T_c and m are expected to be functions of the pH alone. Deriving those parameters helps to quantitatively understand how pH affects the storage modulus.

The experimental data is fitted by the model of Equation (1) to derive G_0, G_∞, T_c and m. The fittings were performed using the "Curve Fitting Tool" in the commercial software MATLAB using the Trust-region algorithm. We estimate the parameter uncertainty based on the goodness-of-fit. Specifically, we define $\sigma_{\min}$ as the minimal sum of the standard deviation between the experimental data and the model. We then search for the combinations of G_0, G_∞, T_c and m that produce a sum of the standard deviations equal to $2\sigma_{\min}$. These values define a 95% confidence interval in the four-dimensional parameter space of G_0, G_∞, T_c and m. All the fittings showed a coefficient of determination $R^2 > 0.995$, with uncertainty of G_0 and G_∞ approaching 2%-12%, and uncertainty of m approaching 1%-3%, and the uncertainty of T_c in the range of 0.1%-0.4%, respectively.

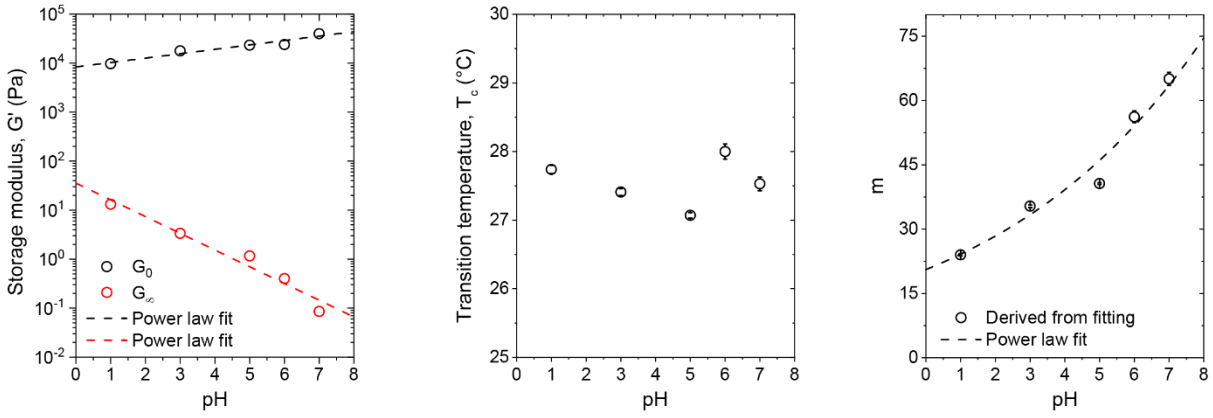

Figure 2-13 The derived empirical parameters G_0, G_∞, T_c, m as functions of pH.

The value of G_0, G_∞, T_c and m are included in Figure 2-13. We first noticed that the solid modulus G_0 spans only one order of magnitude between 10^4 Pa and 10^5 Pa. Therefore, despite that stronger acidity decreases G_0, their values indicate that the materials are always silicone-like under room temperature, and starch releasing is unlikely. In comparison, pH plays a more important role in determining G_∞, as the neutral G_∞ is 2 orders of magnitudes higher than that in a strong acidic condition (pH ≈ 1). This limits starch releasing in the stomach (where $G' \sim 50\ Pa$), and enhances starch granules releasing the hydrogel enters the intestine system where pH > 7 and $G' < 0.1\ Pa$. Another interesting property of the hydrogel is that all the measurements have an standing point of $G' \approx 3$ kPa at 28.6 ºC regardless of the pH value, which can be further exploited for potential applications that requires soft hydrogels to show mechanical stability at all pH.

The value of T_c is not sensitive to pH, as expected. We show that $T_c = 27.5$℃ ± 0.3℃ as determined by the average T_c values at different pH conditions, and the uncertainty is determined as the standard deviation. Other than T_c, the other three parameters (G_0, G_∞, and m) all found to be a function of pH, empirically described by power law (we chose power law out of its simplicity), as shown by the dashed lines in Figure 2-14:

$$G_0(\mathrm{pH}) \approx 8366 \times 10^{0.09\mathrm{pH}} \quad (2)$$

$$G_\infty(\mathrm{pH}) \approx 35.6 \times 10^{-0.34\mathrm{pH}} \quad (3)$$

$$m(\mathrm{pH}) \approx 20.6 \times 10^{0.07\mathrm{pH}} \quad (4)$$

Combining equation 1 to 4, the overall empirical model is:

$$G(T, pH) = 35.6 \times 10^{-0.34\mathrm{pH}} + \frac{8366 \times 10^{0.09\mathrm{pH}} - 35.6 \times 10^{-0.34\mathrm{pH}}}{1 + (T/27.5)^{20.6 \times 10^{0.07\mathrm{pH}}}}$$

The model well-described all the experimental data and can be utilized to quantitatively describe the granule-releasing hydrogel's temperature and pH response, allowing further understanding of the *in-vivo* hydrogel response.

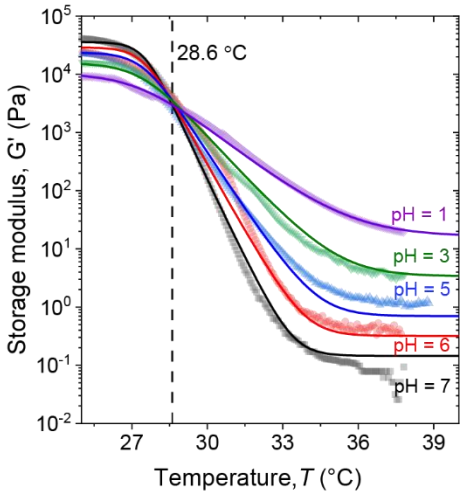

Figure 2-14 Comparison between the experimental and the empirical model. The pH values of each line are included in the plot. The stationary temperature where G' is unaffected is about 28.6 °C and is also labeled by a vertical dashed black line in the plot.

To investigate the molecular interaction during the releasing process, we performed in-situ Fourier-transform infrared (FTIR) spectroscopy, applying heavy water to reveal hydrogen bond associations during the phase transition of the gelatin polymer (**Figure 2-15**).

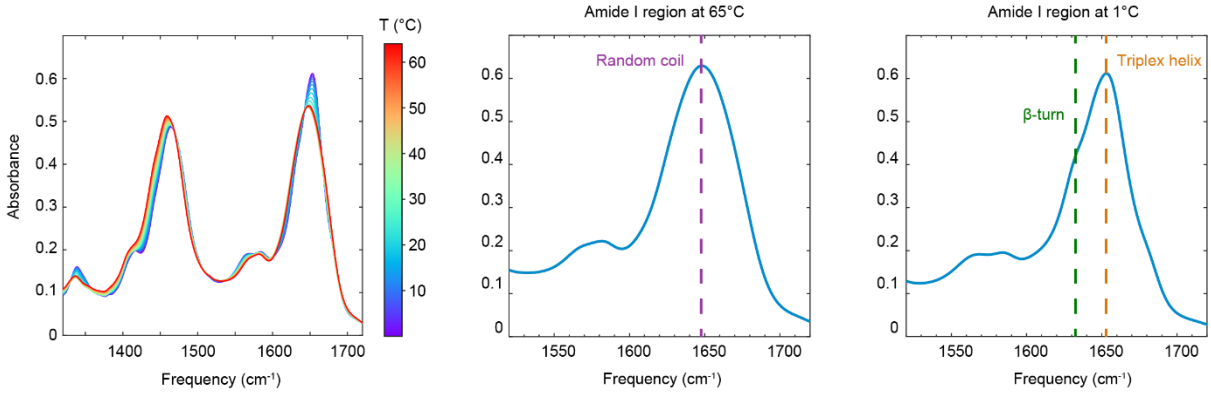

Figure 2-15 In-situ FTIR during the cooling ramp indicates that the phase transition of the granule-releasing hydrogel is reversible. At the temperature higher than body temperature, the

Figure 2-15, continued. random coil is the dominant form of gelatin, indicated by the peak in amide I region. At the temperature lower than body temperature, the gelatin matrix forms the triplex helix and β-turns through hydrogen bonding.

The band assignment for infrared spectra is summarized at Table 2-2.

Species	Frequency (cm^{-1})	Assignment
D_2O	1207	bending
	1560	bending+libration
HDO	1458	bending
Gelatin	1460	Amide II
	1632	β-sheet & D_2O-solvent imide
	1644	Random coil
	1657	Triplex helix
	1673	β-turns
Starch	1307	C-H deformation of all ring hydrogens
	1332	C-O-H bending + CH_2 twisting
	1370&1386	ring mode
	1460	CH_2 twisting mode
	1660	vibrations of O-H on the amorphous regions

Table 2-2 Band assignments for infrared spectra.

During heating from 1 ºC to 65 ºC, we observed the disappearance of spectral features in the amide I region from 1600 cm^{-1} to 1700 cm^{-1}. These results suggest that the loss of intermolecular

hydrogen bonds between gelatin polymer chains allows the dynamic transition of the hydrogel and granule release at body temperature. A singular value decomposition (SVD) was performed on the FTIR temperature series over the Amide l spectral region (1520 – 1720 cm^{-1}), and the 2nd component was used to report on the temperature-dependent spectral changes of the granule-releasing hydrogel. The 2nd SVD component ($V^{(2)}$) was fit to a two-state thermodynamic model[24]:

$$K = \frac{k_g}{k_s} = \frac{[Gel\ state]}{[Sol\ state]} = \frac{\theta_F}{1-\theta_F}$$

θ_F is the fraction of gelatin that is in gel state, the sol state fraction (θ_U) is ($1 - \theta_F$), and K is the gelling equilibrium constant. At high temperatures, the granule-releasing hydrogel is in sol state, while at low temperatures, it is in gel state.

$$\theta_F = \frac{K}{1+K}$$

$$K = e^{-\Delta G^0/RT}$$

The change in heat capacity between states (ΔC_p) is neglected. The folding enthalpy (ΔH°) and entropy (ΔS°) are independent of temperature and related to the folding free energy (ΔG°).

$$\Delta G^\circ = \Delta H^\circ - T\Delta S^\circ$$

The phase transition temperature (T_m) is defined as the temperature at which θ_F=0.5 and ΔG°= 0. $V^{(2)}$ has sloping upper and lower baselines that are likely unrelated to the folding equilibrium and instead result from previously characterized temperature-dependent changes to the amide l band[25,26] or uncorrected changes in optical path length. In practice, $V^{(2)}$ is fitted with two baselines and the total number of fit parameters includes ΔH°, T_m, and slopes (m_F, m_U) and y-intercepts (b_F, b_U) for each baseline.

$$V_{Fit}^{(2)} = \theta_F(L_F - L_U) + L_U$$

$$L_F = m_F + b_F$$

$$L_U = m_U + b_U$$

The SVD analysis revealed that the gelation points were at ~30.9ºC during temperature ramp-up (Figure 2-16).

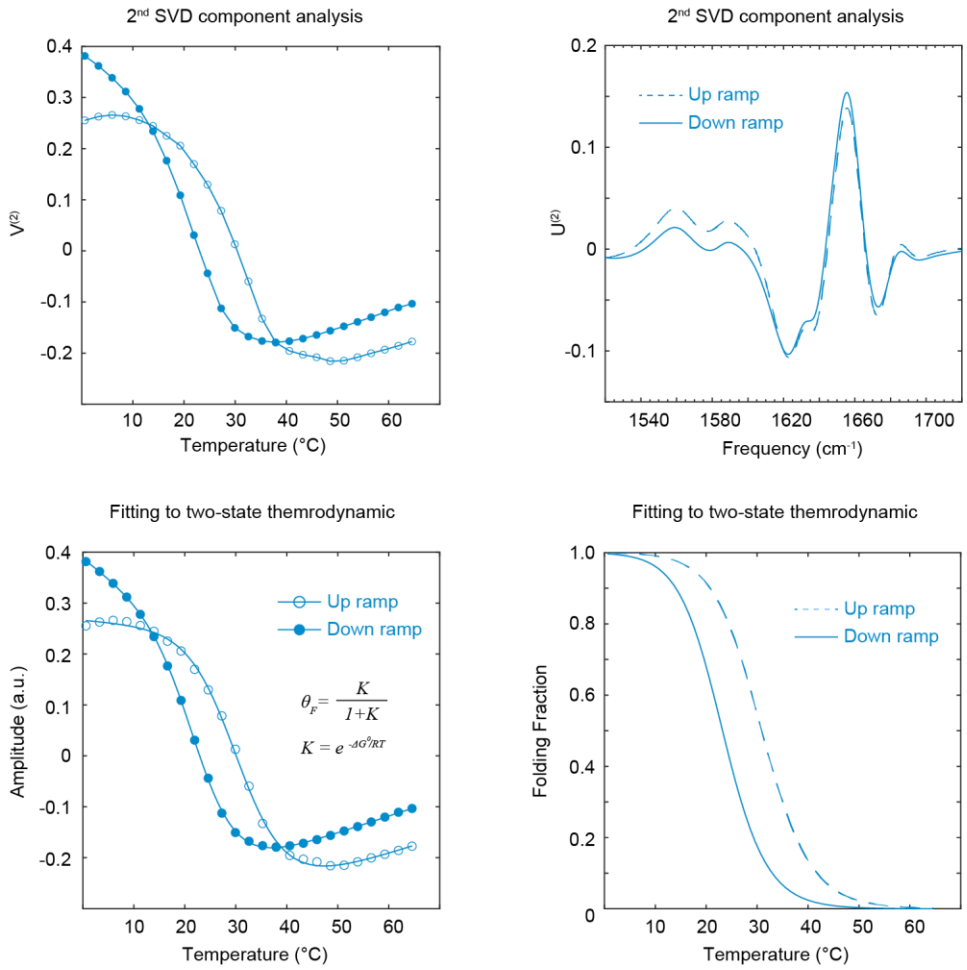

Figure 2-16 SVD analysis indicates the phase transition temperature and heat hysteresis of the granule-releasing hydrogel. (Top) 2nd SVD temperature ($V^{(2)}$) and spectral ($U^{(2)}$) components from heating (filled circles, solid line) and cooling (open circles, dashed line) FTIR series. (Bottom) Fitting of $V^{(2)}$ with two-state thermodynamic model. A hysteresis is observed where the transition temperature (T_m) of gelatin unfolding is 30.9 ± 1.4 °C during the heating ramp and 23.2 ± 0.6 °C during the cooling ramp.

The granule-releasing hydrogel also exhibits responsiveness to pH at different temperatures. Through the shear rheological analysis, we found that the shear modulus is pH-responsive (Figure 2- 17). We attribute the pH responsiveness of the granule-releasing hydrogel to the protonation-deprotonation balance between amino groups in gelatin and chitosan[27].

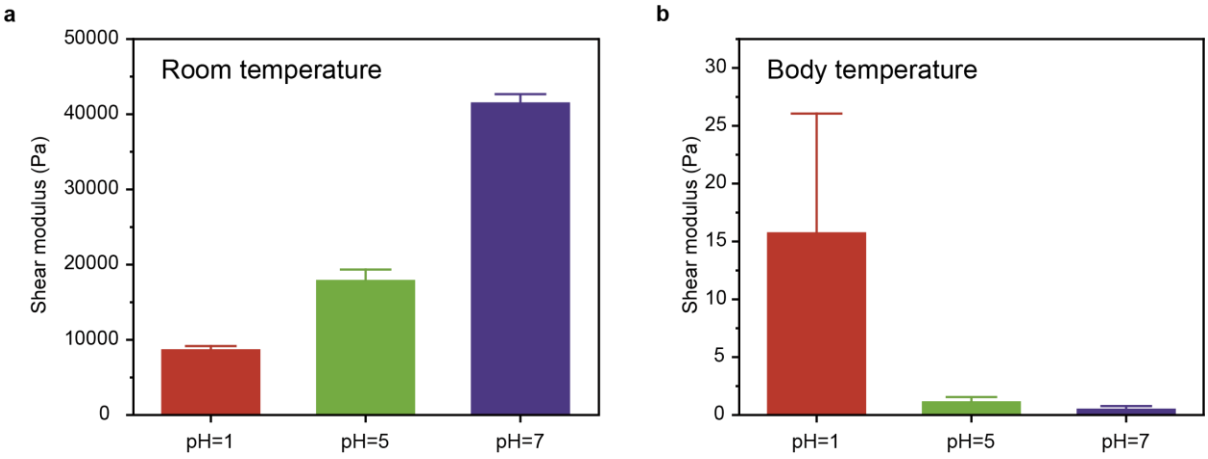

Figure 2-17 The granule-releasing hydrogel has both pH and temperature responsiveness in its shear modulus. (a) The shear modulus of granule-releasing hydrogel indicates the hydrogel at room temperature is harder under neutral conditions than under acidic conditions. (b) The shear modulus of granule-releasing hydrogel indicates the hydrogel at body temperature is softer under neutral conditions than under acidic conditions. Data are presented as mean ± standard error of the mean. (n = 3).

We found that the pH variations can largely change the granular transport behavior which modulates the releasing behavior of granular composite in different pH environments (Figure 2-18).

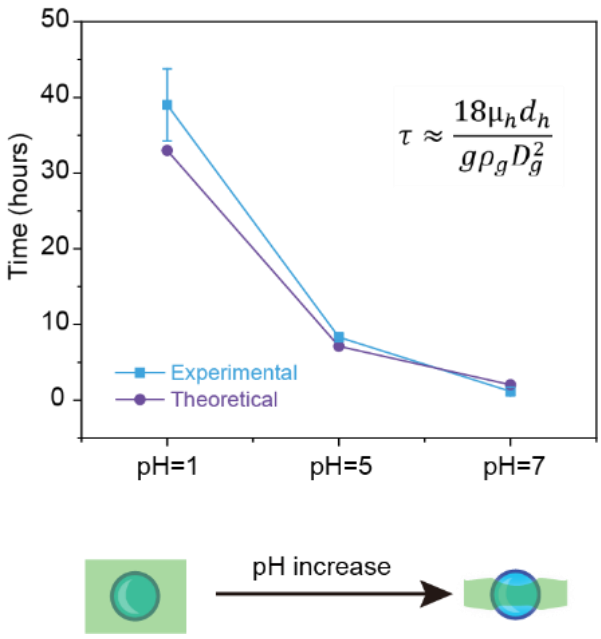

Figure 2-18 Experimental and theoretical analysis indicates that the granular transport process at body temperature is influenced by the environmental pH.

We closely studied the kinetics of granular transportation. We assume the starch granule particles trapped inside a horizontally placed hydrogel film can spontaneously transport to the bottom of the gel and contact with the biological surface. The transportation is driven by the particle's own gravity. For simplicity, we assume the granule particles move downward at a constant velocity, U. The velocity is determined by both the gravitational force as well as the hydrodynamic drag. Despite the hydrogel fluid is viscoelastic, here we ignore the elastic effect and only focus on the viscous effect. Under these circumstances, the Reynolds number, Re, of a falling particle is determined by:

$$Re = \frac{\rho_h U D_g}{\mu_h}$$

Where ρ_h is the density of hydrogel, which is close to 10^3 kg/m^3; D_g is the diameter of granular particles, which spans from 5 μm to 30 μm and has a main value of 14.7 μm; μ_h is the dynamic

viscosity of the hydrogel as measured by rheometer at low shear rate (1 s^{-1}), which spans from 0.1 Pa.s to 5600 Pa.s, depending on the hydrogel temperature and pH value. Considering that the particles are small and the hydrogel is viscous, the flow of the particle is a laminar flow even if the dropping velocity of the sphere is as high as 1 mm/s (where the Reynolds number is expected to be smaller than 10^{-4}).

For laminar flow, the drag coefficient of a sphere, C_f, versus Reynolds number is:

$$C_f = \frac{24}{Re} + \frac{4}{\sqrt{Re}} + 0.4$$

Meanwhile, the drag coefficient of a sphere is:

$$C_f = \frac{8F_d}{\rho_h U^2 \pi D_g^2} = \frac{4\rho_g g D_g}{3\rho_h U^2}$$

Where F_g is the drag force (which is gravitational force in this case), and ρ_g is the density of the particle which is close to 1.5×10^3 kg/m^3. The final equation is therefore:

$$\frac{\rho_g g D_g}{3\rho_h}\frac{1}{U^2} = \frac{6\mu_h}{\rho_h D_g}\frac{1}{U} + \sqrt{\frac{\mu_h}{\rho_h D_g}}\frac{1}{\sqrt{U}} + 0.1$$

It should be noticeable that for such a small Re (< 10^{-4}) value, the last two terms on the right-hand side can be ignored, because $Re^{-1} \gg Re^{-0.5}$, and $Re^{-1} \gg 0.4$. This simplifies the equation into:

$$U \approx \frac{g\rho_g D_g^2}{18\mu_h}$$

The expected falling timescale $\tau = d_h/U$, hence

$$\tau \approx \frac{18\mu_h d_h}{g\rho_g D_g^2}$$

The simplified model highlights a linear relationship between the transportation time, τ, which is a kinetics parameter, and the hydrogel dynamic viscosity, which is affected by its temperature and

pH value. It allows us to predict useful timescale of particles of diameter D_g to travel through a 10^{-3} m-thick hydrogel film: When the hydrogel is stored at room temperature (ºC) when pH = 7, the measured $\mu_h \approx 5.6\times10^3$ Pa.s, then even if no elasticity is considered, it would expect the particles to take 88 days (when $D_g = 30\ \mu m$) to 794 days (when $D_g = 10\ \mu m$) to drop to the bio-interface. This shows good stability for long-term storage at room temperature. When the hydrogel is at 37 ºC and pH = 1 where the gel travels through the stomach, $\tau = 4$ hours (when $D_g = 30\ \mu m$) to 34 hours (when $D_g = 10\ \mu m$), which is far longer than the time of the hydrogel travels through the stomach (~ 1 hour). This indicates only the particle leftover in stomach is negligible. When the hydrogel is at 37 ºC and pH = 7 that reaches the GI-track, $\tau = 14$ minutes (when $D_g = 30\ \mu m$) to 122 minutes (when $D_g = 10\ \mu m$). This indicates a rapid drug delivery behavior. The diffusion time for granular transport was also experimentally investigated using an optical microscope. Specifically, hydrogel precursors were poured into tissue culture dishes with covered glass bottoms (WPI FluoroDish) to a height of 4.5 mm. After gelation, the dishes were placed in Tokai Hit INU Environmental Chambers (model INUB-ONICS-F1) to maintain a constant temperature of 37°C. The samples were observed using an inverted microscope (Nikon Eclipse Ti2), with the focus on the bottom plane of the hydrogel. Images were captured every 30 minutes for a total duration of 90-120 minutes, allowing us to observe the dynamics of starch granule migration. The diffusion time was calculated based on the point at which the granules reached 20 times their initial count.

Those pH-responsive abilities will help the granule-releasing process in vivo. In particular, the higher storage modulus in acidic environments (e.g., in the stomach) provides a means to protect the starch granules from being released or degraded before the hydrogel arrives at the site of interest (e.g., colon).

2.2.3 Interfacial dynamic adhesion design

The evolving granule-releasing hydrogels allow the motion and release of granules in the physiological environment. To enhance adhesion at granule-based focal biointerfaces, we further chemically modified the granular composites with a variety of naturally occurring drug molecules, including aspirin. These molecules have rapid and high oral absorption ability and can efficiently interact with the phospholipid membrane and extracellular matrix, two major components of the tissues. Inspired by this, we hypothesized that surface modification of the granules with these drug molecules would enhance biointerface adhesion, regardless of the therapeutic effects of the molecules themselves.

Using molecule dynamics (MD) simulations, we found that drug molecules with rapid absorption and lipophilicity[28], such as aspirin, can promote binding between chitosan and the lipid bilayer by reducing the interaction energy (Figure 2-19). Specifically, the average interaction energy between one aspirin-modified chitosan chain and 1,2-dimyristoyl-sn-glycero-3-phosphocholine (DMPC) membrane is $\Delta E = -5.67 \pm 2.20$ kcal/mol, while the average interaction energy between unmodified chitosan and DMPC membrane is -3.52 ± 1.79 kcal/mol.

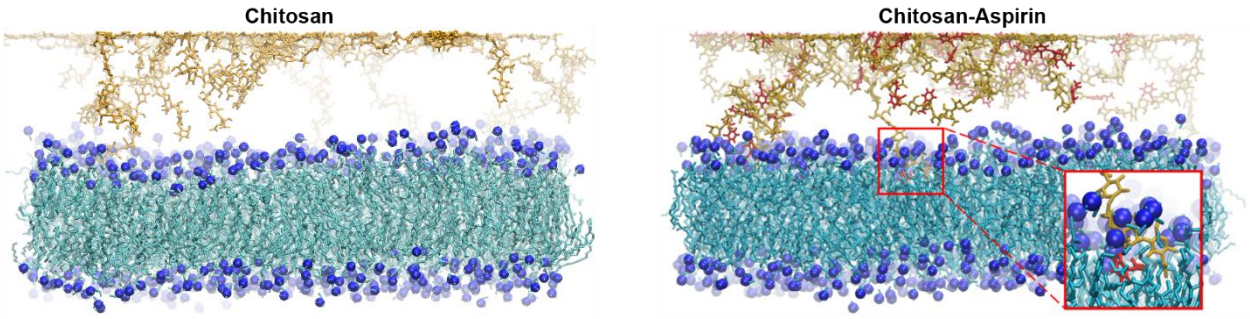

Figure 2-19 Atomistic molecular dynamics simulations showing the interaction between unmodified chitosan and aspirin-chitosan bioconjugates with 1,2-dimyristoyl-sn-glycero-3-phosphocholine (DMPC) lipid molecules. Inset panel shows that the aspirin-modified chitosan occasionally extends into the lipid membrane. Yellow, chitosan; Red, aspirin.

We synthesized the aspirin-chitosan bioconjugate using carbodiimide chemistry (Figure 2-20) and then formed the aspirin-modified chitosan/starch granules (AS).

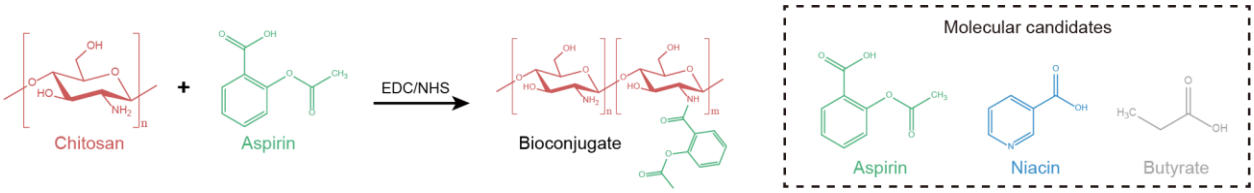

Figure 2-20 Molecular structure of the chitosan and aspirin and the route of synthesis for aspirin-chitosan bioconjugate.

To ensure the successful synthesis of our compound, a multi-modal characterization approach was adopted. Initially, Nuclear Magnetic Resonance (NMR) spectroscopy was employed. This technique is instrumental in providing detailed molecular information, revealing the environment around specific nuclei and the arrangement of atoms within a molecule. Our NMR result showcased distinctive peaks corresponding to our target molecule (Figure 2-21).

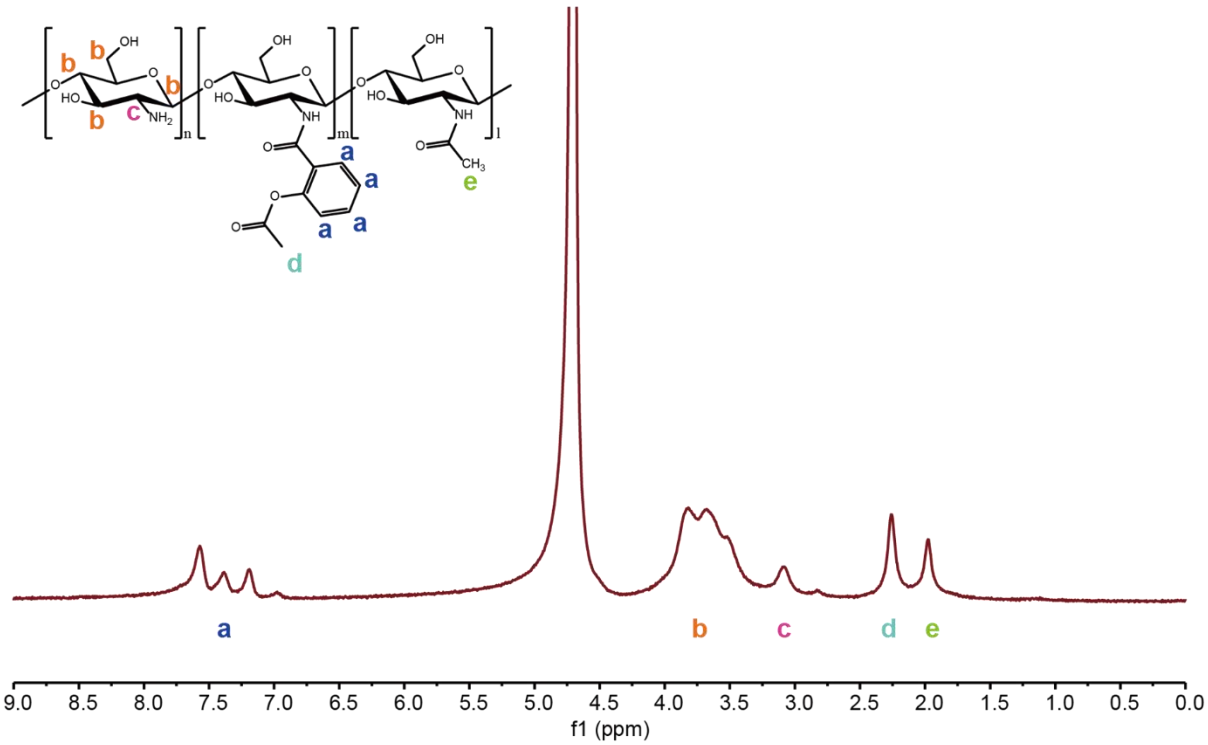

Figure 2-21 Nuclear magnetic resonance (NMR) analysis of aspirin-chitosan bioconjugate prove that the aspirin molecules have been successfully grafted on the backbone of chitosan. The degree of aspirin conjugation (28.65%) was calculated based on the relative peak areas of aspirin (4H, aromatic ring, * 6.5-8.0 ppm, D2O, region a) and chitosan (3H, -COCH3, * 1.95 ppm, D2O, region e).

Subsequently, to further confirm the synthesis, Fourier-Transform Infrared Spectroscopy (FTIR) was utilized. FTIR spectroscopy delves into the vibrational movements of molecules, enabling the identification of functional groups and the nature of chemical bonds (Figure 2-22).

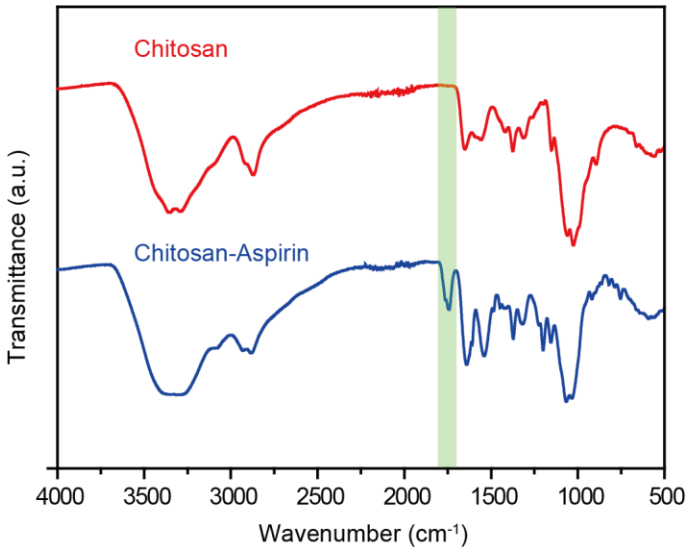

Figure 2-22 Fourier-transform infrared spectroscopy confirms that the aspirin molecules have been grafted onto the backbone of the chitosan molecule. The new peak at around 1700 cm^{-1} (C=O stretching peak of aspirin molecules) indicates the presence of aspirin molecules on the backbone of chitosan.

To investigate the intrinsic affinities between different granules and diverse biological components, we employed aqueous granular suspensions without involving gelatin hydrogel matrix and found that the aspirin-modified starch/chitosan granules (AS) showed strongest affinity. First, we performed the flow adhesion tests in vitro where the fluid flow shear stress mimics the luminal shear stress of the body[29]. Specifically, the aspirin-modified granules (AS) demonstrated a higher retention rate than the unmodified starch/chitosan granules (SC) and pure starch granules (Starch) when flowing over different biological components, including molecular assemblies (phospholipid layer; collagen layer, Figure 2-23), in-vitro cell monolayers (human colorectal adenocarcinoma cell line Caco2; human immortalized keratinocytes cell line HaCaT, Figure 2-23), and in-vitro intestinal organoids (mouse colon organoid; human ileum organoid, Figure 2-23). Next, in ex-vivo experiments, the aspirin-modified granules (AS) had a higher retention rate than non-modified starch/chitosan granules (SC) when flowing over DSS-treated

ulcerative colonic epithelium or skin wound bed (without epidermis, dermis exposed; Figure 2-23).

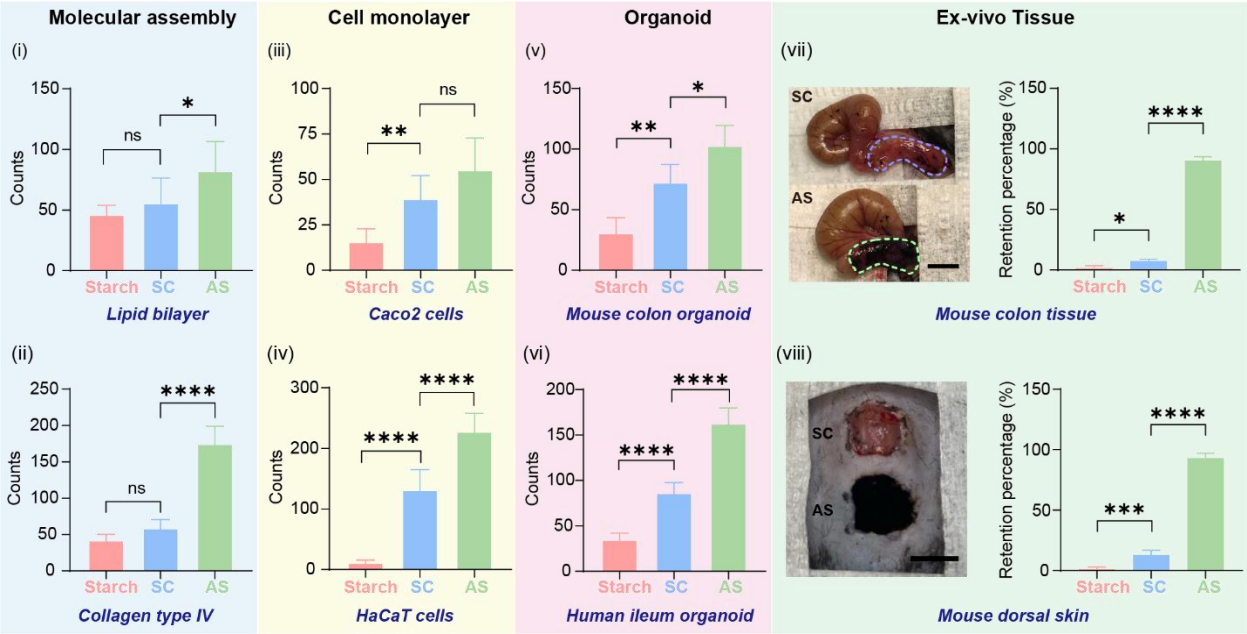

Figure 2-23 Flow adhesion tests show that the aspirin-modified starch/chitosan granules (i-viii) enhance starch retention at molecule-, cell-, and organoid-levels. Scale bar, 2 cm. Starch: Starch granules only. SC: Starch/chitosan granules without chemical modification. AS: Starch/chitosan granules with aspirin modification. Data are presented as mean ± standard error of mean. P values are determined by ordinary one-way ANOVA with Tukey's multiple comparisons test.

We performed the finite element COMSOL simulation to investigate that whether the size and shape of granular composite will influence the retention rate. In the microfluidic device, a single flow channel was choose, where flow gives the channel wall a shear stress of 0.1 ~ 1 Pa, mimicking blood vessel's luminal shear stress. The inner fluid flows at a constant single volumetric flow rate (Q) of 1 mL/min. The flow channel is 50 mm in length (L), 5 mm in width (D), and 0.4 mm in height (H), which yields an average flow velocity ($\overline{U}$) of about 8 mm/s. In the triangle channel, the Reynolds number[30]:

$$Re = \frac{\rho \bar{U}}{\mu}\left(\frac{2DH}{D+H}\right) \approx 6.$$

This characterizing a laminar flow that $Re < 2300$. Here, $\rho \approx 10^3\ kg/m^3$ and $\mu \approx 10^{-3}\ Pa \cdot s$ is water's density and dynamic viscosity near room temperature, respectively. The hydrodynamic entrance length for the laminar flow is[30]:

$$L_{h,laminar} \approx 0.05 \times Re\left(\frac{2DH}{D+H}\right) \approx 0.2\ mm \ll L.$$

Therefore, we assume the pipe flow is fully developed when it passes over most of the starch particles. Under these presumptions, the shear stress at the wall is indeed estimated to be 0.1 ~ 1 Pa.

$$\tau_w = \mu \nabla \boldsymbol{u}_{z=H/2} = \frac{8\mu\bar{U}}{H} \approx 0.2 \text{ Pa}$$

To further characterize the cell-starch interfacial shear stress caused by flow's drag force, we utilized commercial software COMSOL to simulate the velocity field, pressure, and viscous shear stress of the flow near a starch particle in the two-dimensional length-height plane. The particle has a diameter d ~ 15 μm. The computation domain has a size of 600 μm × 400 μm, and the liquid flows from the left to the right. Here, we assume the liquid is water-like, *i.e.* it is non-compressible and Newtonian. The above calculations made it reasonable to assume the flow in the domain to be steady-state, fully-developed laminar pipe flow. The governing Navier-Stokes equation is therefore expressed as[30]:

$$\rho(\boldsymbol{u} \cdot \nabla)\boldsymbol{u} = \nabla \cdot [-p\mathbf{I} + \mu(\nabla \mathbf{u} + (\nabla \mathbf{u})^{\mathrm{T}})] + \boldsymbol{F}$$

Where $\boldsymbol{u}$ is flow velocity, $\mathbf{I}$ is identity matrix, p is pressure, and $\boldsymbol{F}$ is external force. The conservation of mass further gives:

$$\rho \nabla \cdot \boldsymbol{u} = 0$$

The boundary conditions are set as follows: The left wall is the flow inlet that has an average velocity of 8 mm/s. The right wall is a pressure-free outlet ($p = 0$). The top and bottom walls are non-slip, hence $\boldsymbol{u} = 0$.

Here, we considered four scenarios: the starch particle is a half-sphere or a full sphere or a cube or a cone. We mainly consider the horizontal drag force F_d, which is contributed by the linear combination of pressure (p) and shear stress (τ)[30]. The pressure term is directly obtained by solving the Navier-Stokes equation, and the shear stress is derived at each point by $\tau = \mu\nabla\boldsymbol{u}$. For the half-sphere, the average pressure $\bar{p}$ is 0.5 Pa, and the average shear over the top surface of the sphere $\bar{\tau}$ is about 0.2 Pa, both act on an area that is as large as half of the sphere's cross-section, yielding a net drag force of:

$$F_d \approx (\bar{p} + \bar{\tau}) \times \frac{1}{8}\pi d^2 \sim 9 \times 10^{-11}\ N$$

Which translate into a cell-starch interfacial shear stress of:

$$\tau_i = \frac{F_d}{A_i} \sim 1.4\ Pa$$

Where the starch-cell contact area $A_i \approx \frac{1}{4}\pi d^2$. The fact that almost all the non-modified starch particles were rinsed away under this flow indicated that non-covalent interactions along only yield a weak shear toughness of <<1.4 Pa. The significantly higher adhesion at aspirin-modified starch cannot be explained by such weak non-covalent interactions, hence proved the focal-adhesion at the cell interface, echoing the MD simulation result. We note that for an ideal full-sphere or cube or cone, we did not find a significant difference in either $\bar{p}$ or $\bar{\tau}$ (in terms of order of magnitude). We also did not observe obvious deviation between half-sphere particles having different diameters. This shows that some aspirin-modified starch particles detached from the cell not

necessarily because the interfacial shear toughness is about 1 Pa, but rather because the particle is not fully in contact with the cell.

While this is a good example to introduce the appealing theoretical analysis in the thesis, I believe that the amount of math and fundamental science here is still not adequate. Therefore, purely for aesthetic purposes, I list my favorite Maxwell's equation below:

$$\oint \vec{E} \cdot d\vec{A} = \frac{q_{enc}}{\varepsilon_0}$$

$$\oint \vec{B} \cdot d\vec{A} = 0$$

$$\oint \vec{E} \cdot d\vec{s} = -\frac{d\phi_B}{dt}$$

$$\oint \vec{B} \cdot d\vec{s} = \mu_0 \varepsilon_0 \frac{d\phi_E}{dt} + \mu_0 i_{enc}$$

Back in the analysis of flow dynamic of granules, we tested various shapes, including spheres, hemispheres, cubes, and cones (Figure 2-24). We also evaluated how size influences the retention rate (Figure 2-25). Through simulation, we discovered that neither the shape nor the size of the granular composite significantly affects the retention rate on the substrate. This conclusion is advantageous since natural starches come in various types (such as corn, tapioca, wheat, and rice), and their retention behaviors should not exhibit significant differences. Thus, this insight greatly enhances the translational potential of these techniques for cost-effective clinical biomedical applications.

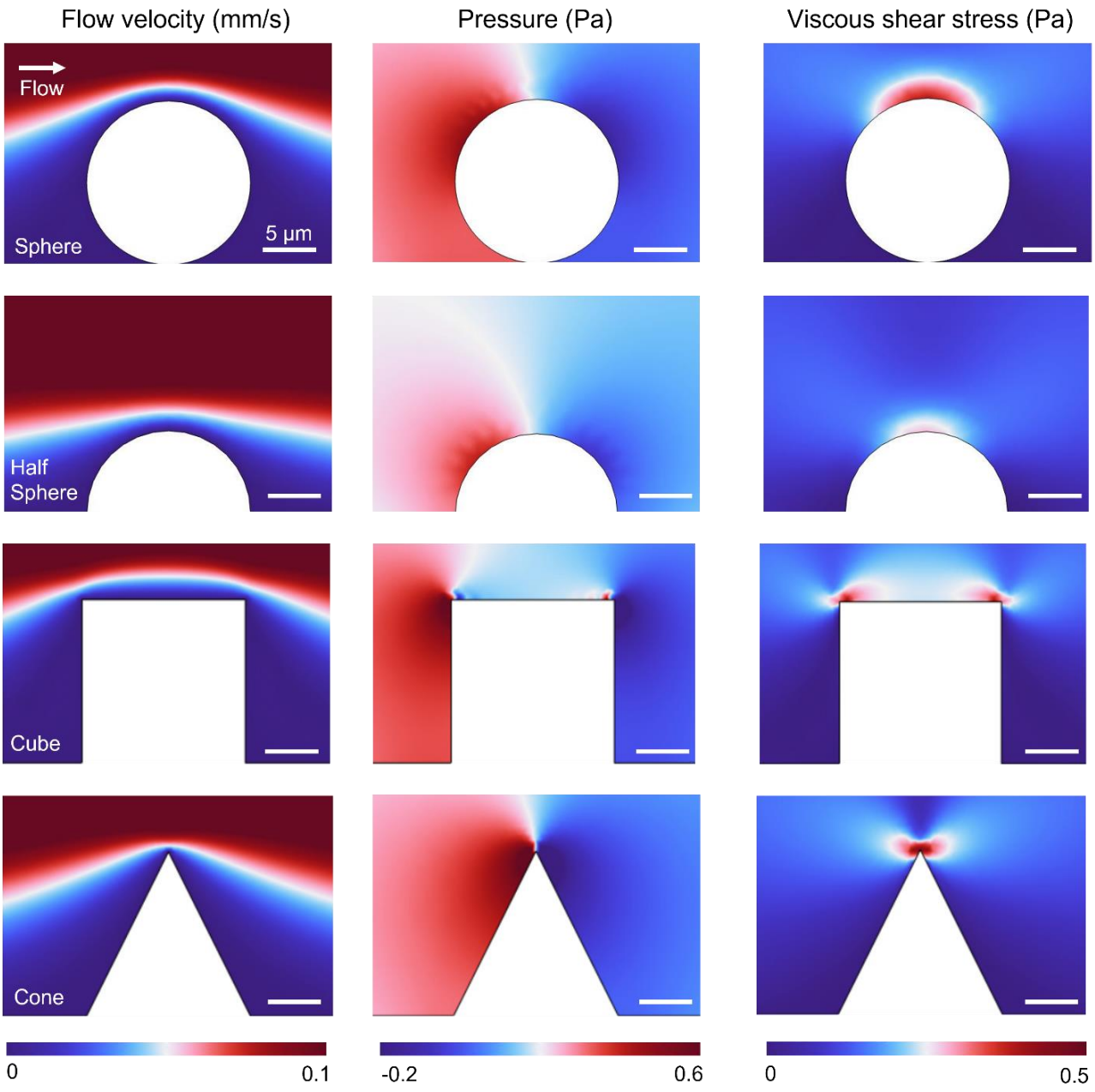

Figure 2-24 COMSOL simulation of flow's velocity field (left), pressure (middle), and viscous shear stress (right) near a granular particle of different shapes. Both a full-sphere, a half-sphere, a cube, and a cone granular particle geometry are modeled and computed. The units for the color bar are mm/s for flow velocity, and Pa for pressure and shear stress viscosity.

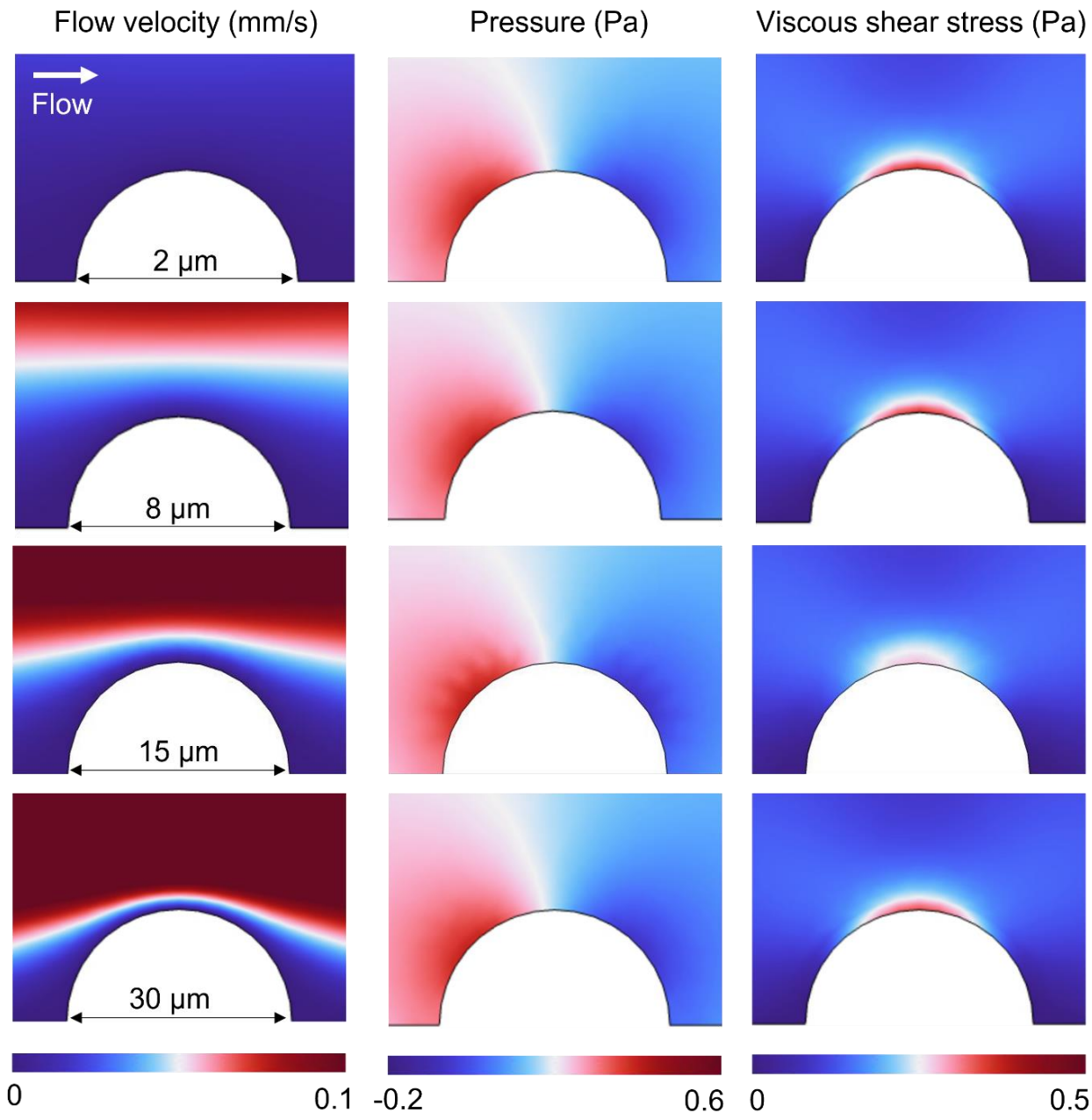

Figure 2-25 COMSOL simulation of flow's velocity field (left), pressure (middle), and viscous shear stress (right) near a half-sphere granular particle of different sizes. Granular particles having diameters of 2 μm, 8 μm, 15 μm, and 30 μm are modeled and computed. The units for the color bar are mm/s for flow velocity, and Pa for pressure and shear stress viscosity.

We also used X-ray micro computed tomography to image the intestinal dynamic of granule-releasing hydrogels (Figure 2-26). We found the retention period of the aspirin-modified granules

(AS) was prolonged in mice intestinal tracts in vivo, indicating potential therapeutic applications (Figure 2-27).

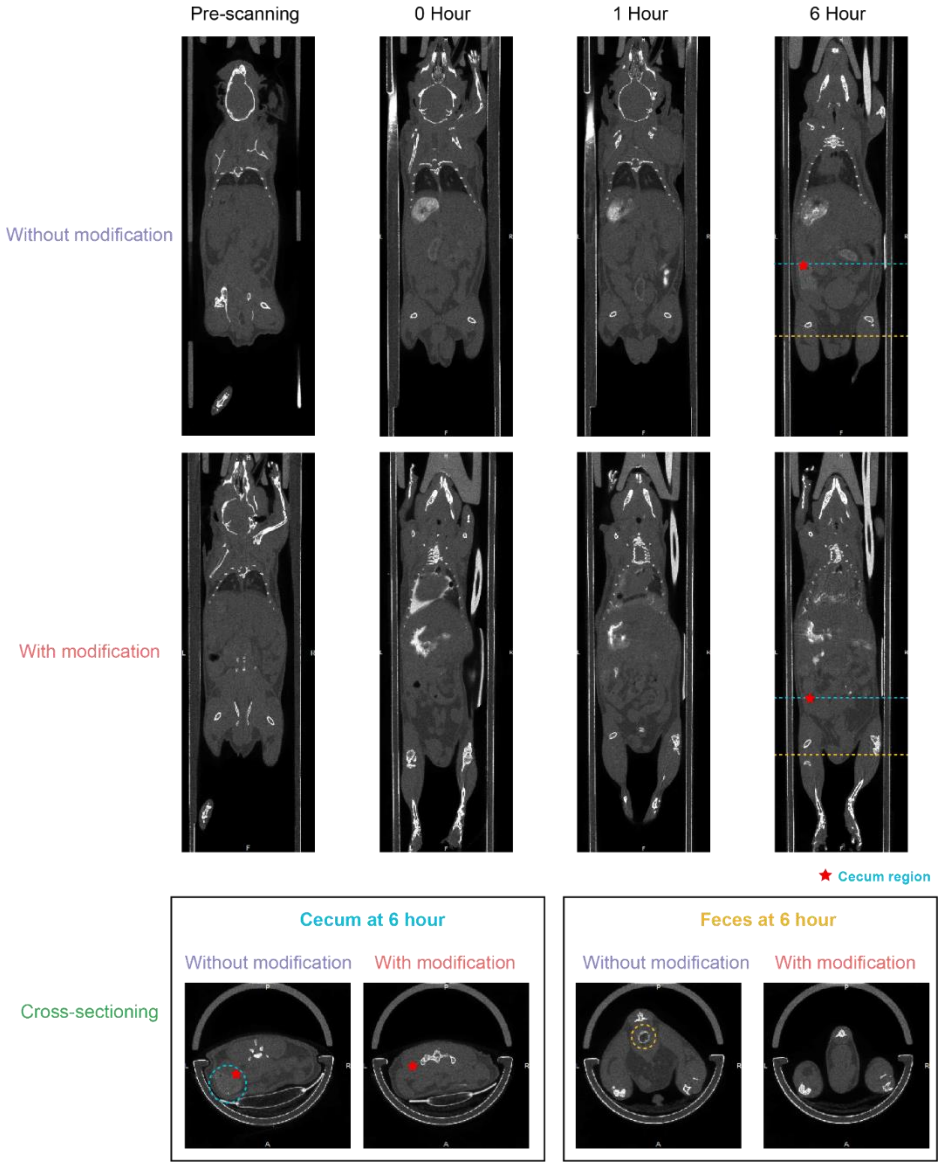

Figure 2-26 Micro-CT imaging sequences indicates the location of orally administrated aspirin-modified and unmodified dynamic granule-releasing hydrogel in gastrointestinal tracts. In vivo micro-CT presents a robust method for quantifying the differences of the granule-releasing hydrogel in GI. It shows that the granule-releasing hydrogel with modification has a longer retention period in the intestinal tract.

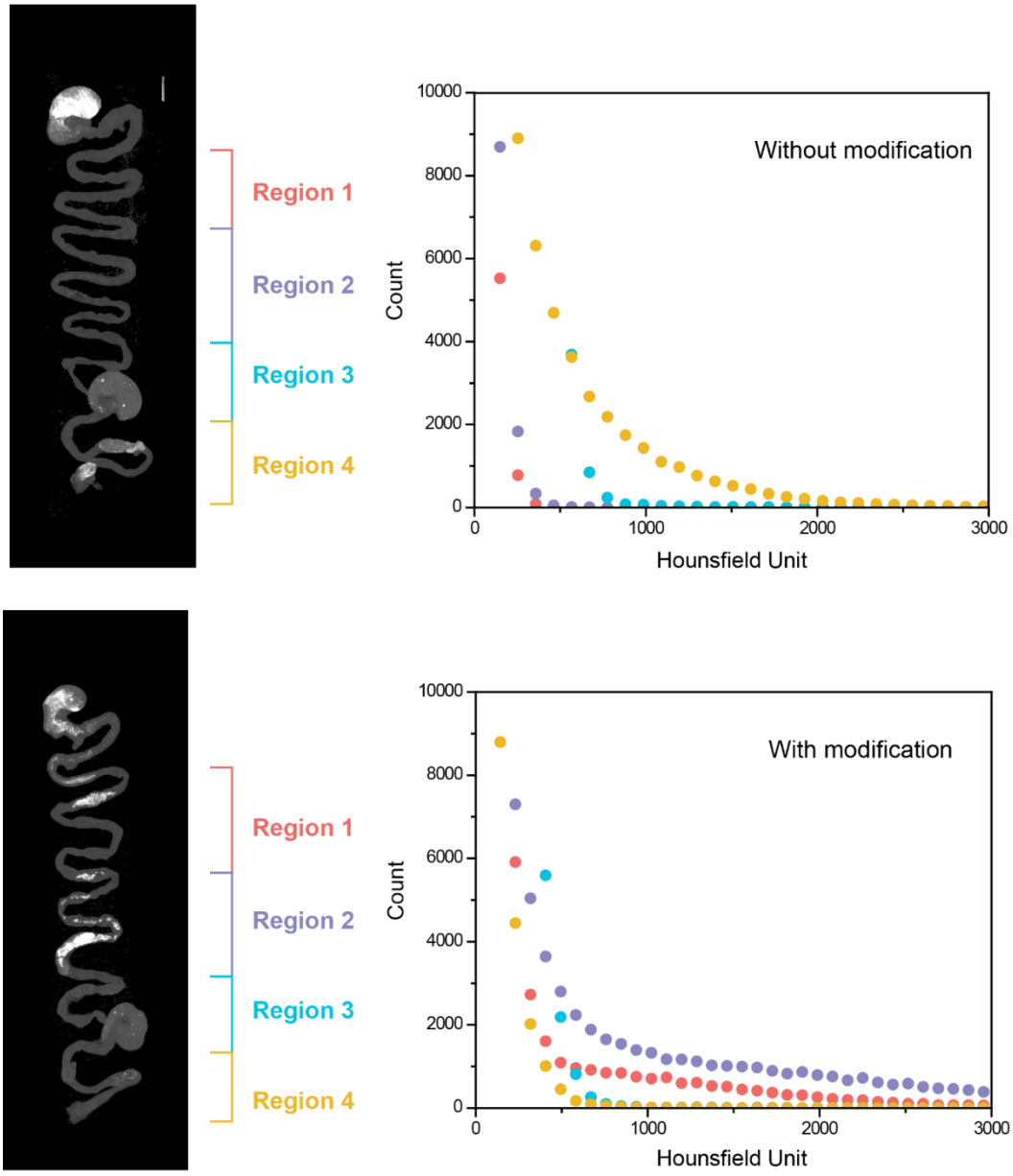

Figure 2-27 Ex-vivo comparison of gastrointestinal tract 6 hours following oral administration of aspirin-modified and unmodified dynamic granule-releasing hydrogel. The CT image from GI only tissue indicate the distribution of aspirin-modified/unmodified dynamic granule-releasing hydrogel in the intestinal region. The histogram presents the numbers of pixels in each intestinal region in terms of their radio intensity (in the Hounsfield unit).

These results demonstrate that chemical conjugation of biomolecules can enhance adhesion/affinity at granule-based focal biointerfaces, and that good oral absorption may be generally considered a 'qualitative' pre-evaluation factor for potential molecular modifications.

2.2.4 Integration with bioelectronics

The evolving hydrogels can also be integrated with bioelectronic devices to achieve both electrophysiological recording and tissue regeneration in heart tissue (Figure 2-28).

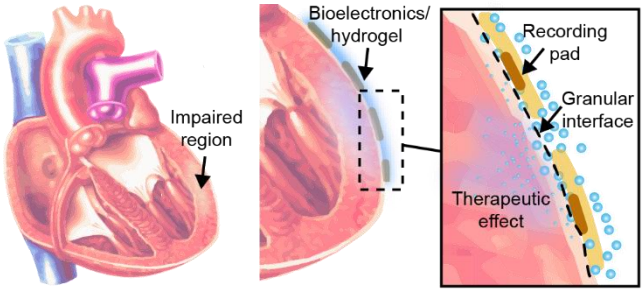

Figure 2-28 Schematic illustrates how the granule-releasing hydrogel serves as a biointerface, adhering to heart tissue for electrophysiological recording and disease treatment.

Using gel-casting methods, we integrated a 16-channel mesh electronic device designed for cardiac spatiotemporal mapping with an aspirin-modified granule-releasing hydrogel (AGH) (Figure 2-29). Mesh electronics is an ultra-flexible and lightweight electronic systems designed to record electrophysiological signals. Unlike traditional rigid electronic implants, mesh electronics mimic the physical properties of the neural tissue, allowing them to attach with the tissue without causing significant tissue damage or immune reactions. The interstitial space between the electrodes in mesh electronics also provide the space for cell growth.

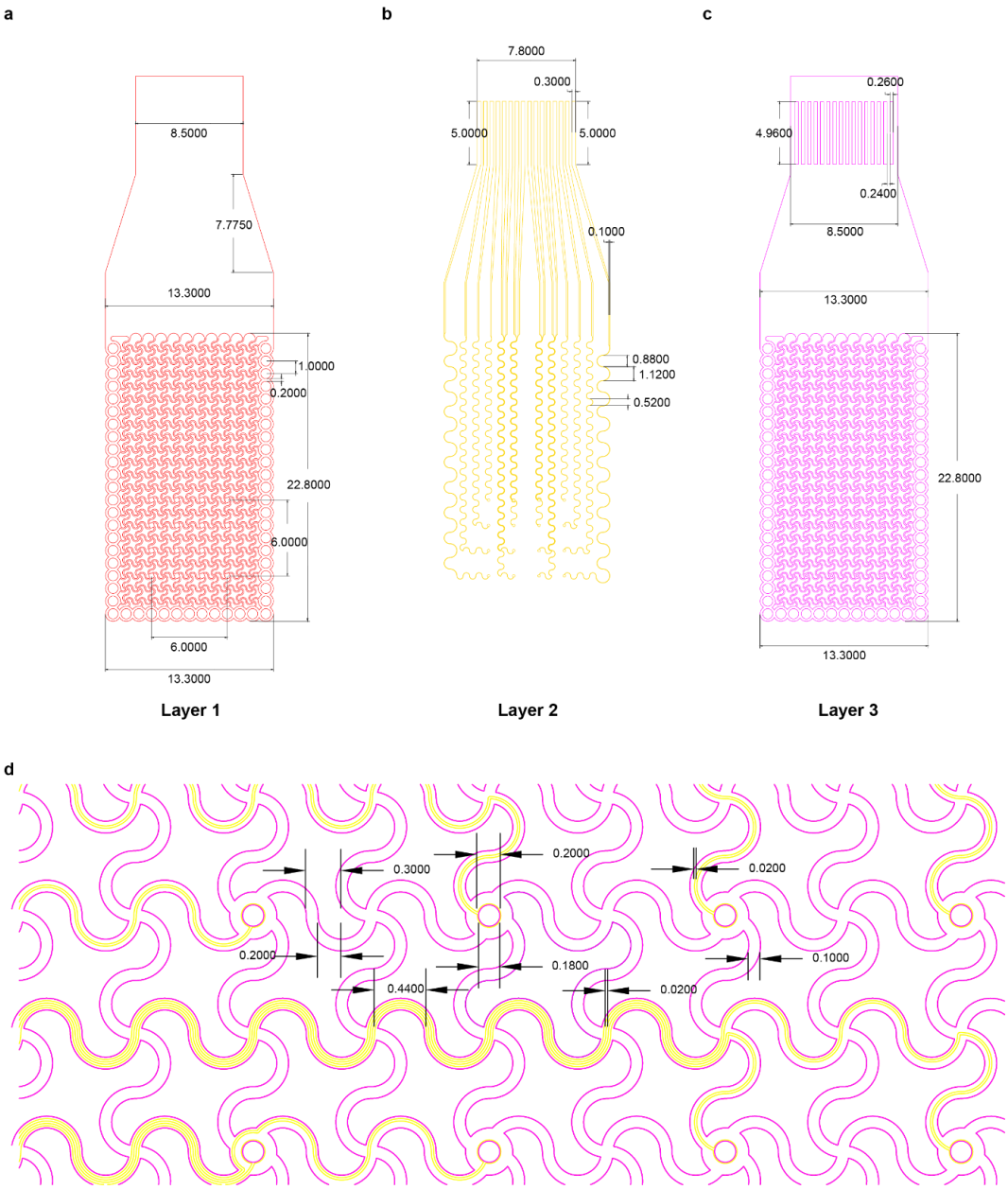

Figure 2-29 Mesh electronic design for nanofabrication. (a) Layer 1: Bottom SU-8 as the supportive layer for the mesh device. (b) Layer 2: Metal electrode layers for signal transduction. (c) Layer 3: Top SU-8 as the encapsulation layer. (d) Zoom-in view to show the design for the electrode in the sensing pad zone. Unit: mm.

The mesh electronics is fabricated at Pritzker Nanofabrication Facility. The three-layer 16-channel recording electrodes were fabricated on the p-type wet oxide silicon wafer (#HS39626-WO,

NOVA Electronic Materials) served as the substrate and the wet oxide as the sacrificial layer. The schematic of the microfabrication procedure is illustrated in Figure 2-29 (side view) and Figure 2-30 (top view). The first SU-8 layer (SU-8 3025, MicroChem Corp), which has a thickness of approximately 22 μm, was patterned with serpentine-like geometries using direct writer photolithography (MLA150, Heidelberg). The first layer serves as flexible and stretchable support for the electrode. On top of the first layer, the metal layers with 5 nm Cr and 100 nm Au, were evaporated using an electron-beam evaporator (EvoVac, Angstrom Engineering) on the patterned AZ nlof 2070 (MicroChem Corp) photoresist mask followed by a lift-off in AZ NMP (MicroChem Corp) to remove the photoresist. Next, the third encapsulation layer (SU-8 3005, MicroChem Corp), which has a thickness of approximately 8 μm, was patterned to encapsulate the metal interconnects and only exposed the sensing pads to interface cardiac tissues and bottom pads for zero-insertion-force (ZIF) connection. Finally, the device was lift-off in the buffered-HF bath which removed the sacrificial wet oxide layer. To make the hydrogel-hybrid devices, the mesh electronic was first attached to the PDMS. Then hydrogel precusor solution was spin-coating to the PDMS surface with 1000 rpm at 40°C. After cooling down and trimmed, the hydrogel-hybrid devices was peel off from the substrate.

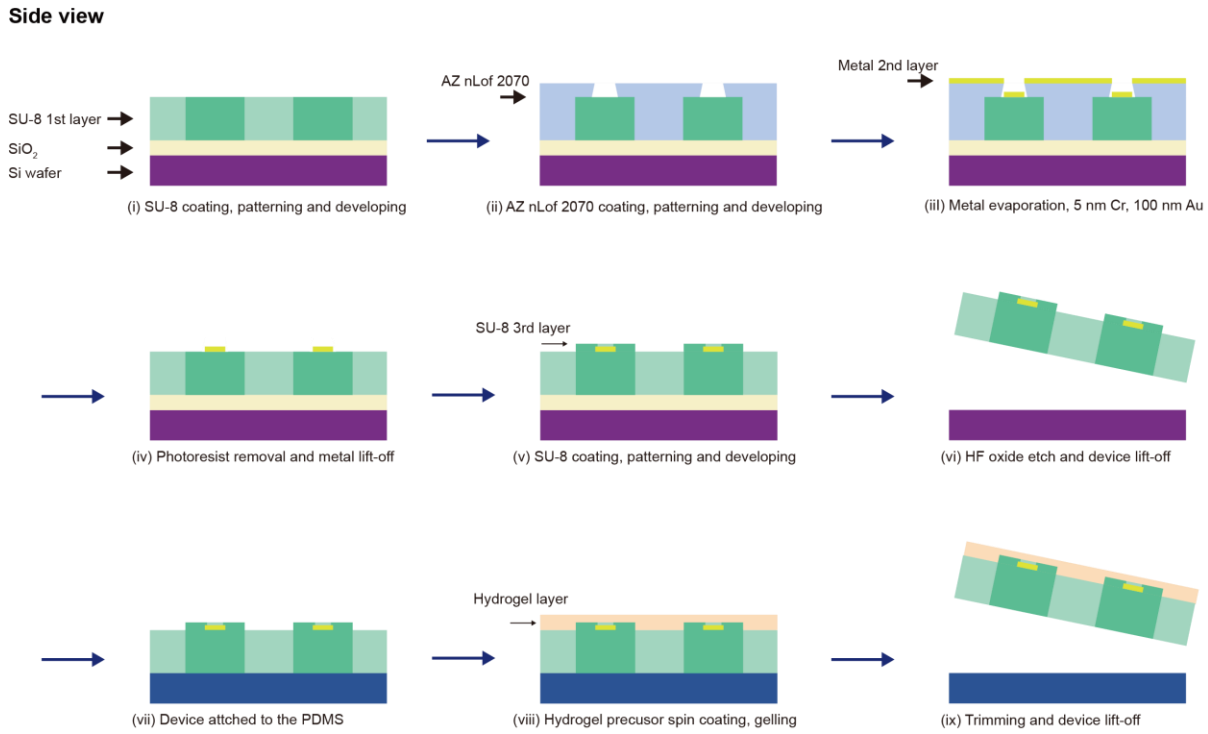

Figure 2-30 Schematic illustrates the fabrication process for mesh electronic devices (side view). SU-8 photoresist was used to pattern the mesh structure on a silicon wafer with SiO2 (600 nm) to form the first layer, which serves as flexible and stretchable support for the electrode. Using direct writer photolithography, another photoresist (AZ nLof 2070, serpentine-like geometries) was used to form a pattern on the first SU-8 layer. An electron beam evaporator was then used to evaporate the metal layers (5 nm Cr and 100 nm Au) on the patterned AZ nLof 2070 photoresist mask, followed by AZ NMP to lift-off the AZ nLof 2070 photoresist. The third encapsulation layer (SU-8) was designed to enclose the metal interconnects, leaving the sensing pads exposed to connect with cardiac tissues and the bottom pads accessible for external connection. Then, the buffered HF bath was used to remove the SiO2 layer to lift off the mesh electronic device. For granule-releasing hydrogel inclusion, the mesh electronic device is carefully attached to the PDMS surface. Then the hydrogel precursor layer was spin-coated on the surface and formed hydrogel. Lastly, the mesh electronics device is carefully peeled off from the substrate.

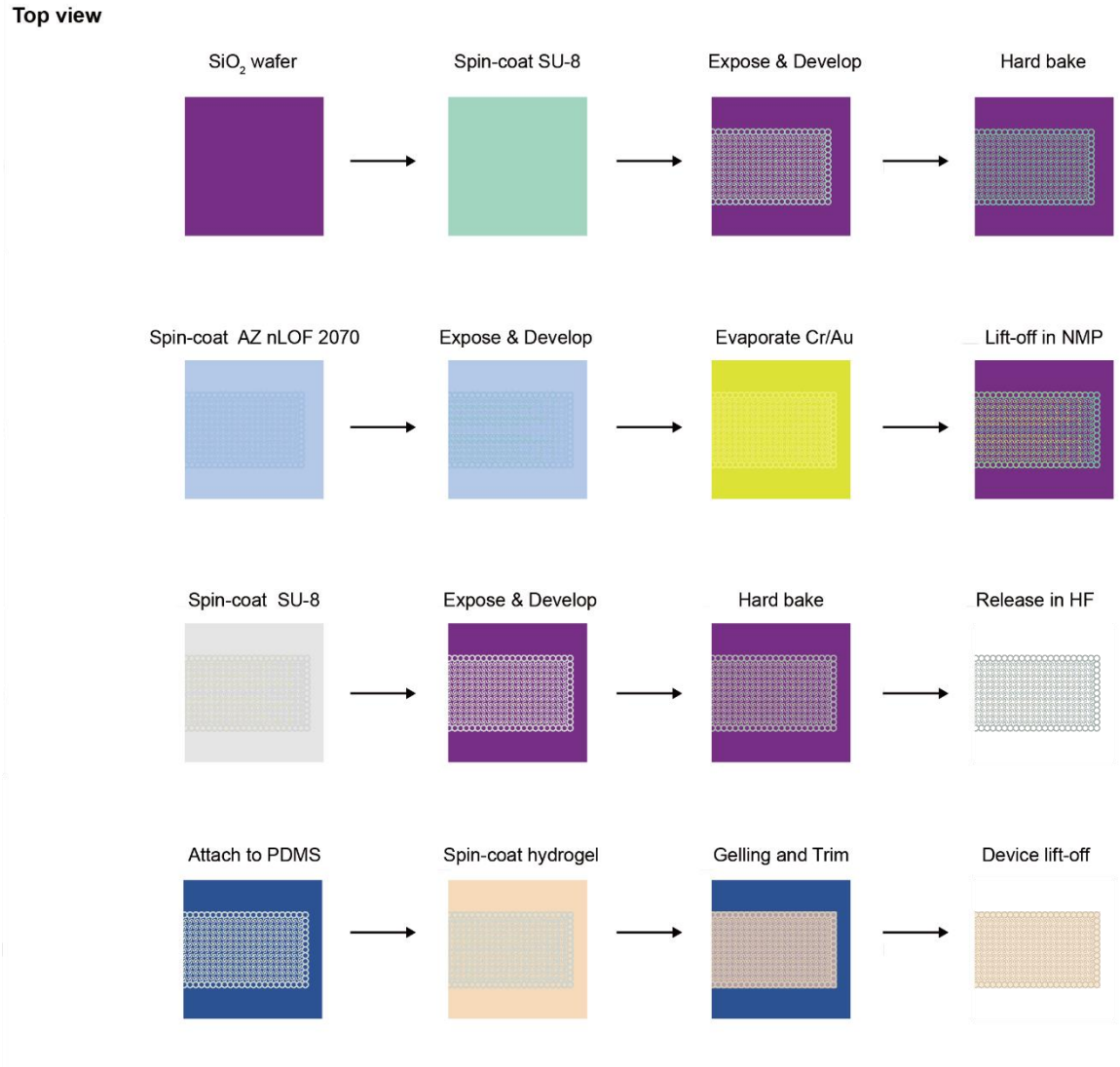

Figure 2-31 Schematic illustrates the fabrication process for mesh electronic devices (Top view). SU-8 photoresist was used to pattern the mesh structure on a silicon wafer with SiO2 (600 nm) to form the first layer, which serves as flexible and stretchable support for the electrode. Using direct writer photolithography, another photoresist (AZ nLof 2070, serpentine-like geometries) was used to form a pattern on the first SU-8 layer. An electron beam evaporator was then used to evaporate the metal layers (5 nm Cr and 100 nm Au) on the patterned AZ nLof 2070 photoresist mask, followed by AZ NMP to lift-off the AZ nLof 2070 photoresist. The third encapsulation layer (SU-8) was designed to enclose the metal interconnects, leaving the sensing pads exposed to connect with cardiac tissues and the bottom pads accessible for external connection. Then, the buffered HF bath was used to remove the SiO2 layer to lift off the mesh electronic device. For granule-releasing hydrogel inclusion, the mesh electronic device is carefully attached to the PDMS surface. Then the hydrogel precursor layer was spin-coated on the surface and formed hydrogel. Lastly, the mesh electronics device is carefully peeled off from the substrate.

Next, we characterized the electrical performance of the hybrid system. The hybrid electronic device records electrical signals with an average impedance of 36.4 Ω/cm2 at 1kHz over 16 channels (Figure 2-32).

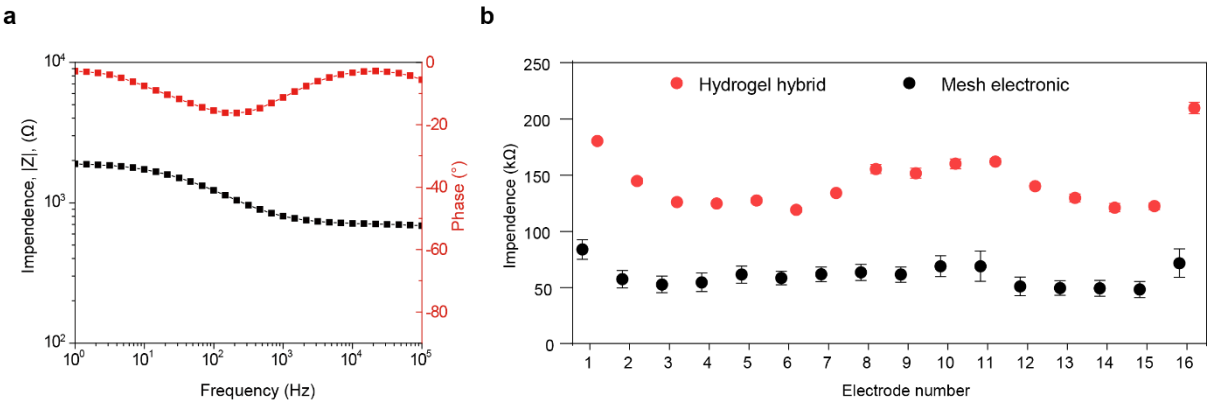

Figure 2-32 Electrochemical impendence measurement of hydrogel and hybrid devices. (a) Electrochemical impedance spectroscopy (EIS) of granule-releasing hydrogel electronic hybrid shows the impedance (Z; black) and impedance phase (Z phase; red) over a frequency sweep from 1 Hz to 0.1 MHz. (b) The hydrogel coating slightly increases the impendence of the mesh electronics. The impendence of the 16 electrodes is measured in PBS at 1 kHz. Data are presented as mean ± standard error of mean.

2.2.5 Electrocardiography recording in Langendorff heart

To demonstrate the utility of the hybrid electronic device in electrophysiological recording, we interfaced it with an ex-vivo heart in a Langendorff apparatus to measure the epicardial electrocardiography (Figure 2-33).

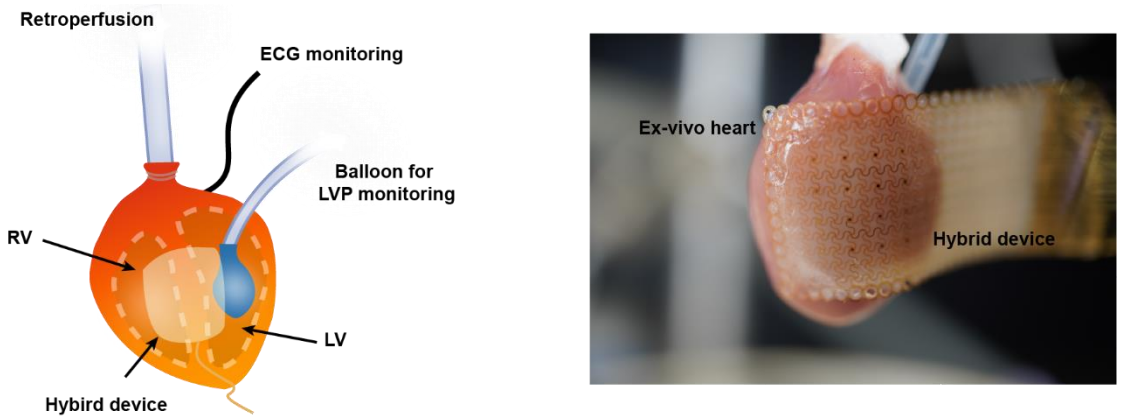

Figure 2-33 Schematic and photograph of Langendorff apparatus and hydrogel hybrid electronic device showing the experimental set-up for heart electrical signal mapping.

Compared to surface electrocardiography (sECG), One of the key advantages of epicardial electrocardiography is its ability to provide accurate localization. By placing electrodes directly on the heart, epicardial ECG enables the identification of precise locations of abnormal electrical pathways, such as those observed in cases of arrhythmias or ischemia. This accurate localization information is crucial for guiding targeted therapeutic interventions. Additionally, epicardial electrocardiography allows for the detection of subendocardial ischemia, which may not always be accurately captured by surface ECG. Surface ECG can be affected by various factors such as body habitus, lung disease, or breast tissue, leading to potential interference in detecting subendocardial ischemia. In contrast, epicardial ECG, being in closer proximity to the heart tissue, offers improved sensitivity in detecting these ischemic changes, particularly in high-risk patients or those with inconclusive surface ECG results. Furthermore, epicardial ECG is frequently used in intraoperative monitoring during cardiac surgeries. Surgeons rely on epicardial ECG to assess the integrity of coronary arteries, identify areas at risk of ischemia, and monitor the efficacy of surgical interventions such as bypass grafts or ablation procedures. The direct measurement of the heart's electrical activity through epicardial ECG provides valuable real-time information for surgical

decision-making and intervention guidance. Freestanding flexible mesh devices are naturally fragile and cannot be easily deployed to the living tissue surface. However, the hybrid electronic device is much more robust during macroscopic manual manipulation (Figure 2-34).

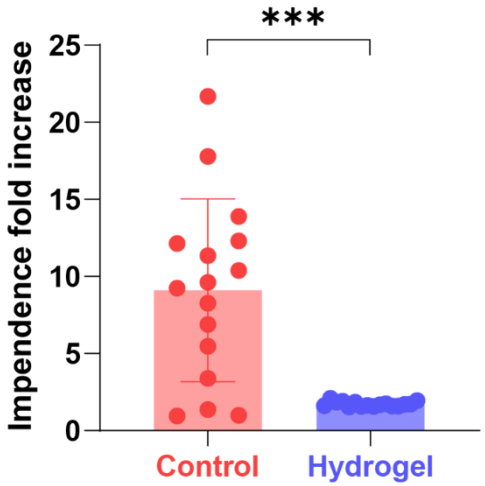

Figure 2-34 Hybrid electronic with granule-releasing hydrogel shows significant better mechanical stability under the 40,000 mechanical perturbation cycles. Data are presented as mean ± standard error of mean. n = 16 independent electrodes. P values are determined by t-test, two tailed.

Hence, the hydrogel-hybrid electronics can prevent the crumpling issue commonly observed in many thin-film electronic systems (Figure 2-35).

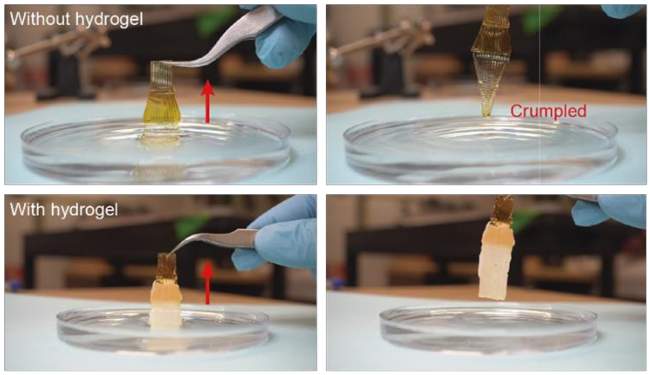

Figure 2-35 Evolving granule-releasing hydrogel enhances the manipulation.

Upon temperature increase in the Langendorff apparatus, focal biointerfaces formed at the ex vivo heart tissue surface (Figure 2-36).

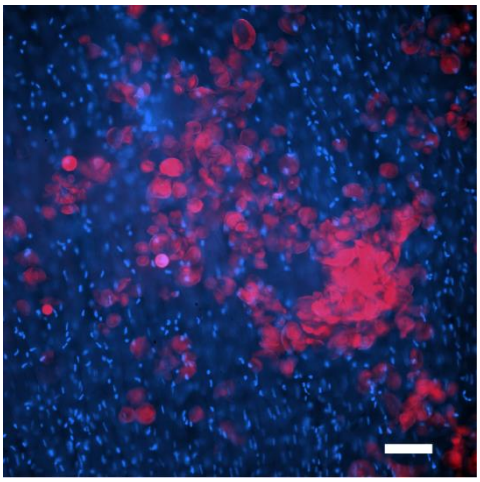

Figure 2-36 Fluorescent imaging shows that the granular composite forms a granular biointerface on the epicardium after the phase transition of the granule-releasing hydrogel. Scale bar, 40 μm. Granular composite: red, stained with Alexa Fluor™ 647; Epicardium: blue, stained with Hoechst 33342.

After the activation of the isolated heart, the hybrid electronic device recorded electrograms of sinus rhythms at different positions between the right ventricle (RV) and left ventricle (LV). The representative signal is shown in Figure 2-37.

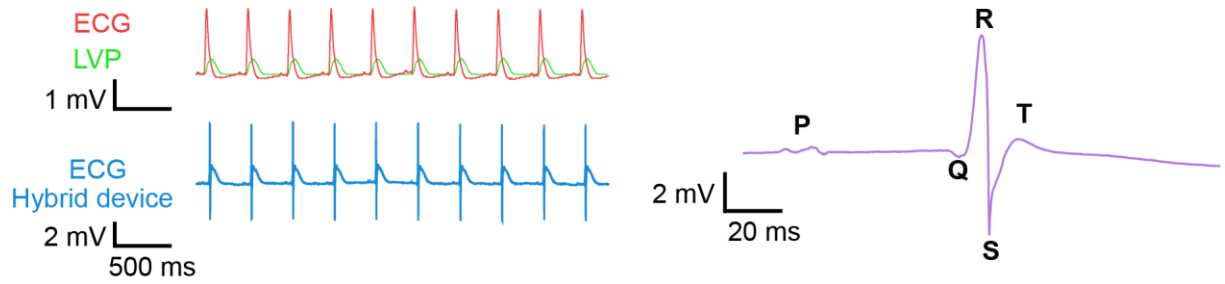

Figure 2-37 Electrical signal of sinus rhythms from one representative electrode. Red & Green: ECG signals and left ventricular pressure (LVP) signals recorded from iWorx. Blue: ECG signals recorded from an individual channel on our multichannel electrode. Purple: zoomed-in single-cycle ECG, clearly showing P, Q, R, S, and T characteristic ECG peaks.

Isochrone map shows how far signals can travel from a starting point to other places within a given time frame. Thus, we use isochrone map to show the heart activation delay throughout the myocardium (Figure 2-38).

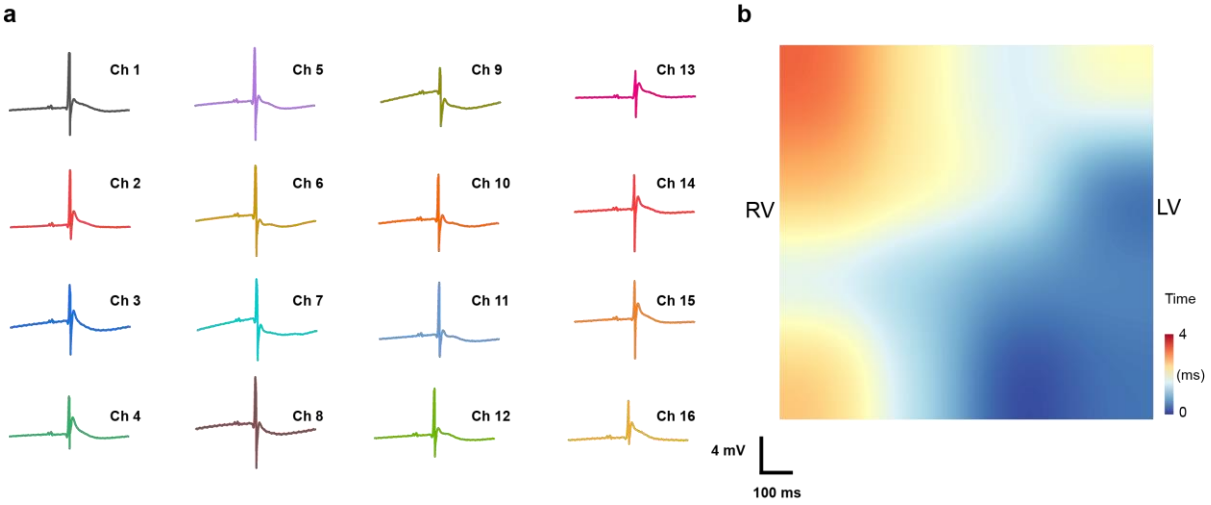

Figure 2-38 The electrical signals and isochrone map collected by the mesh electronics with granular interface. (a) The electrical signals in 16 channels (Ch) show the electrocardiogram (ECG) information of the ex vivo beating heart. Mesh electronic devices are placed in a similar position on the heart as those with the granular interface. (b) Isochrone map of the heart activation delay shows the electrical propagation route.

As a compare to the granular biological interfaces, the ECG recording result for hydrogel interface is shown in Figure 2-39.

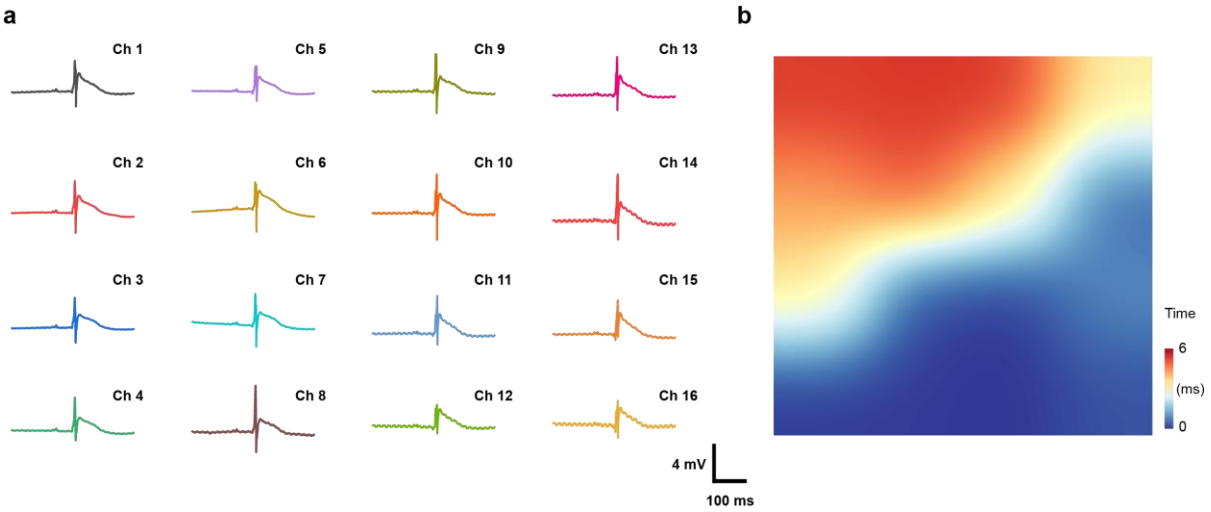

Figure 2-39 The electrical signals and isochrone map collected by the mesh electronics with hydrogel interface. (a) The electrical signals in 16 channels (Ch) show the electrocardiogram (ECG) information of the ex vivo beating heart. Mesh electronic devices are placed in a similar position on the heart as those with the granular interface. (b) The isochrone map of the electrical propagation pathway shows a similar pattern as the one with the granular interface.

The amplitudes of the cardiac signals recorded with the focal biointerfaces are statistically higher than those collected with monolithic hydrogel biointerfaces. Specifically, normalized amplitude before and after granules-releasing process is 5.31 ± 1.19 mV and 7.79 ± 1.45 mV, respectively, indicating that the focal biointerface facilitates bioelectrical signal transmission to the mesh bioelectronics (Figure 2-40).

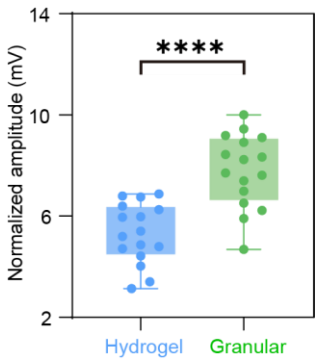

Figure 2-40 Amplitudes of electrical signals recorded with granular interfaces are significantly higher than those collected with monolithic hydrogel interface.

The hybrid bioelectronics device has potentials for clinical translation. Thus, we demonstrated that the hybrid bioelectronic device can diagnose heart disease and facilitate treatment. Ischemia-reperfusion (I/R) is a severe pathological condition that contributes to heart tissue injury and eventually leads to myocardial infarction (MI) conditions48. Our hybrid device system can monitor ECG signals (Figure 2-41).

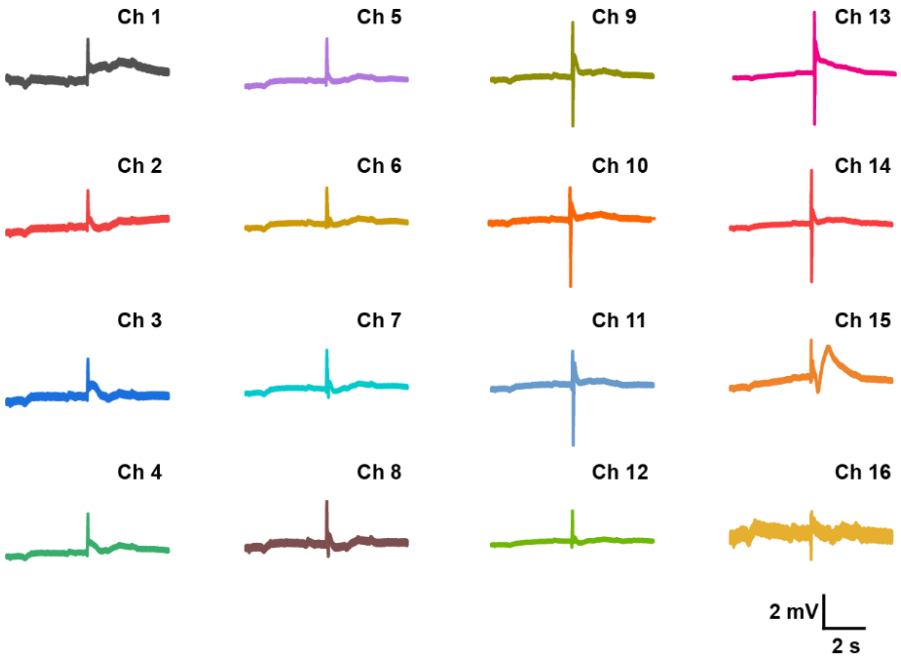

Figure 2-41 The electrical signals and isochrone map collected on an ischemia-reperfusion injured heart. (a) The electrical signals in 16 channels (Ch) show the electrocardiogram (ECG) information of the injured heart. The injured heart showed lower ECG signal amplitudes and abnormal ECG patterns. (b) The isochrone map of the electrical propagation pathway shows an electrical activation delay in the ischemia-reperfusion injured heart compared with the healthy heart.

We detect abnormal ECG signal patterns and delayed heart electrical activation in an I/R injured heart. The representative ECG signals and isochrone map were shown in Figure 2-42.

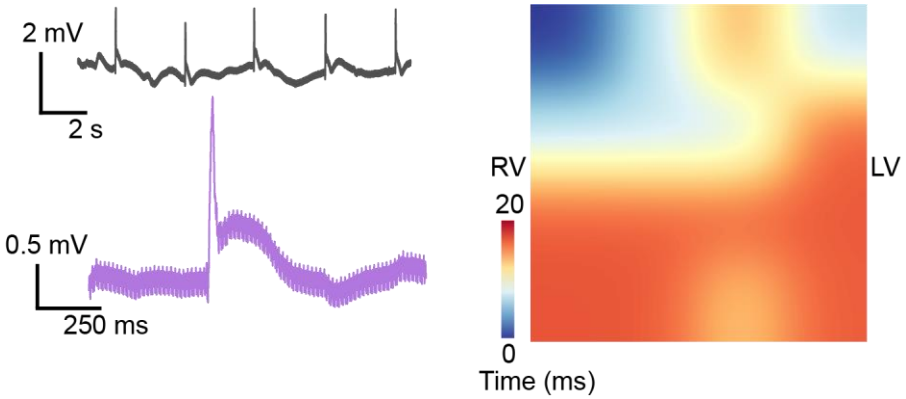

Figure 2-42 The electrical signal from one representative electrode shows abnormal ECG patterns in the I/R diseased heart and isochrone map of the I/R diseased heart.

The longer activation delay area in the isochrone map locates a severely damaged area in the I/R heart, which is consistent with the infarct staining result (Figure 2-43). Thus, we demonstrated that the hybrid bioelectronics could help diagnose the heart damage situation.

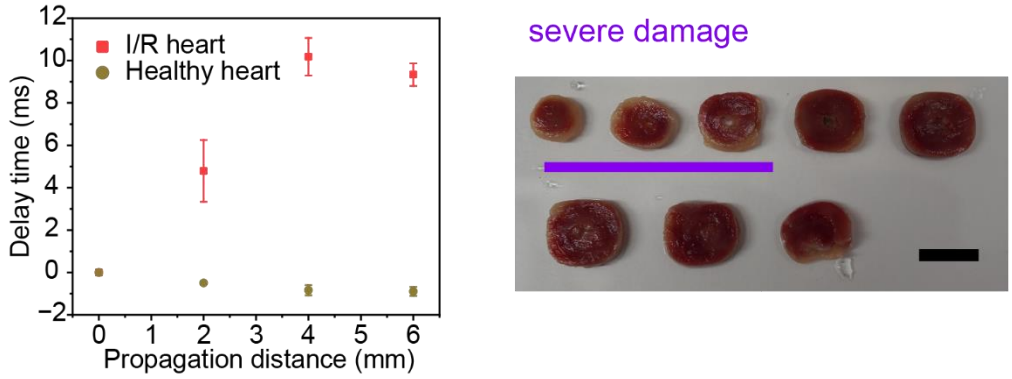

Figure 2-43 The average activation delay for longitudinal directions indicates the location of the damaged area in I/R diseased heart. Inner panel: The infarct staining shows the position of heart damage, consistent with the isochrone map. (n = 4).

Besides, the amplitudes of the cardiac signals recorded in the diseased heart are significantly lower to those collected in the healthy heart (Figure 2-44).

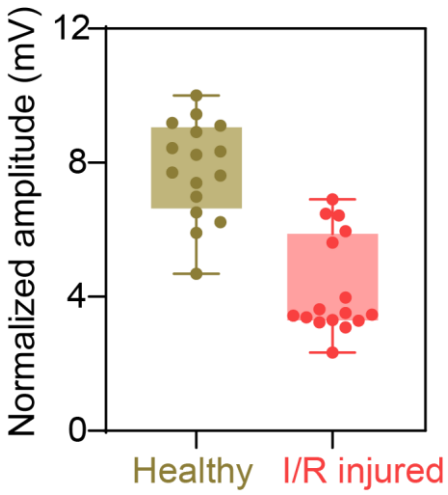

Figure 2-44 Amplitudes of electrical signals recorded in the diseased I/R heart are significantly lower than those recorded in the healthy heart.

Using the heat map, we clearly showed the electrical signals intensity for 16 individual channels shows the abnormal heart rhythm under ischemia and ventricular fibrillation (Figure 2-45). The difference in their heart rhythm indicates that the hybrid device is capable of detecting the heart abnormality. Thus, the hybrid electronic device can diagnose abnormal heart rhythms in cases of ischemia or ventricular fibrillation.

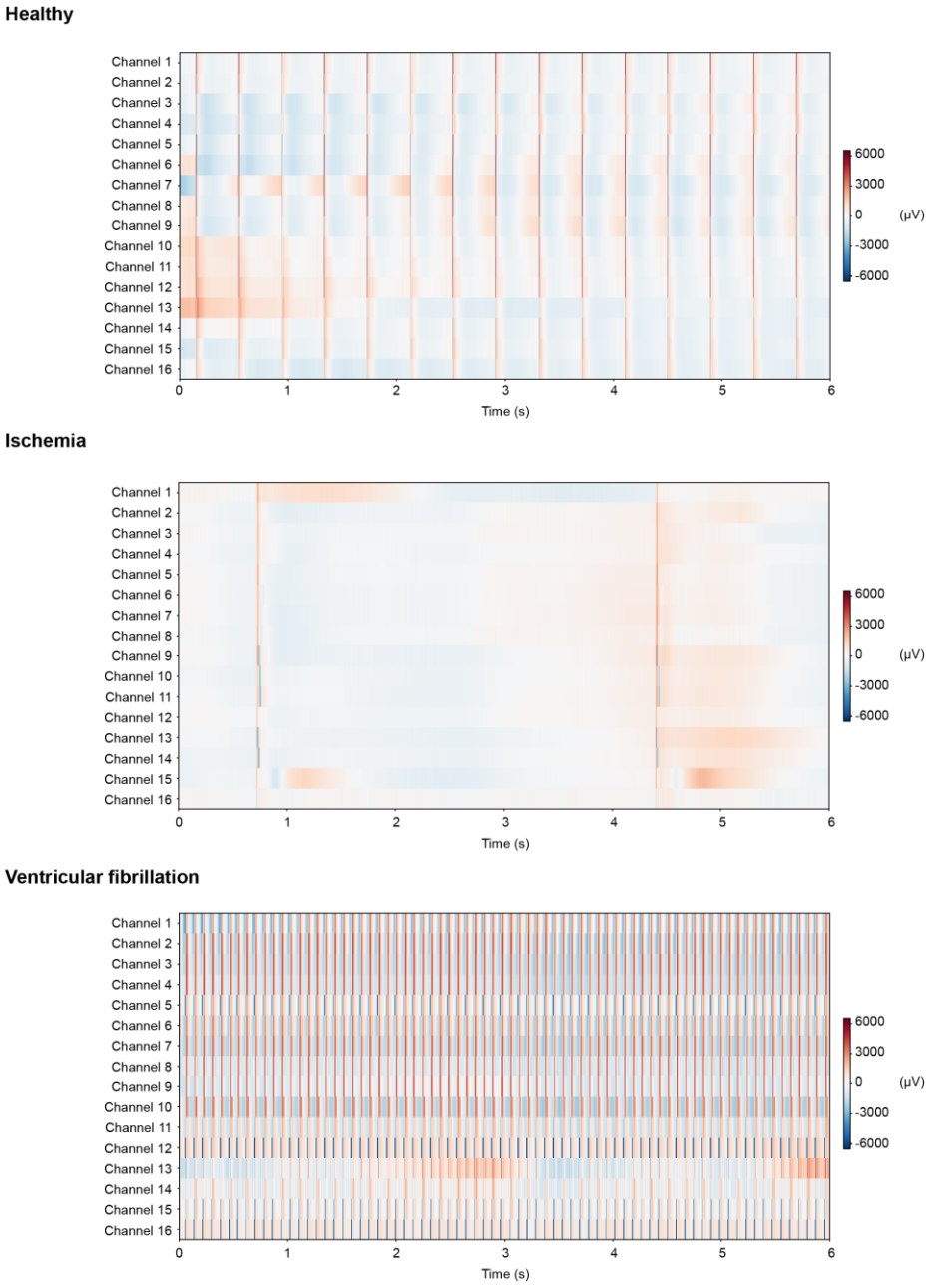

Figure 2-45 The heat map of electrical signals for 16 individual channels shows the abnormal heart rhythm under ischemia and ventricular fibrillation.

To further prove the utility of our hybrid mesh electronics in potential application in surgical epicardial electrocardiography recording, we also performed in-vivo rat heart recording models. In this experiments, we mainly focus on checking the long-term ability of our devices. Our hybrid

device system can stably adhere to the heart for ECG recording and spatiotemporal monitoring over 270 minutes, as indicated by photographs (Figure 2-46).

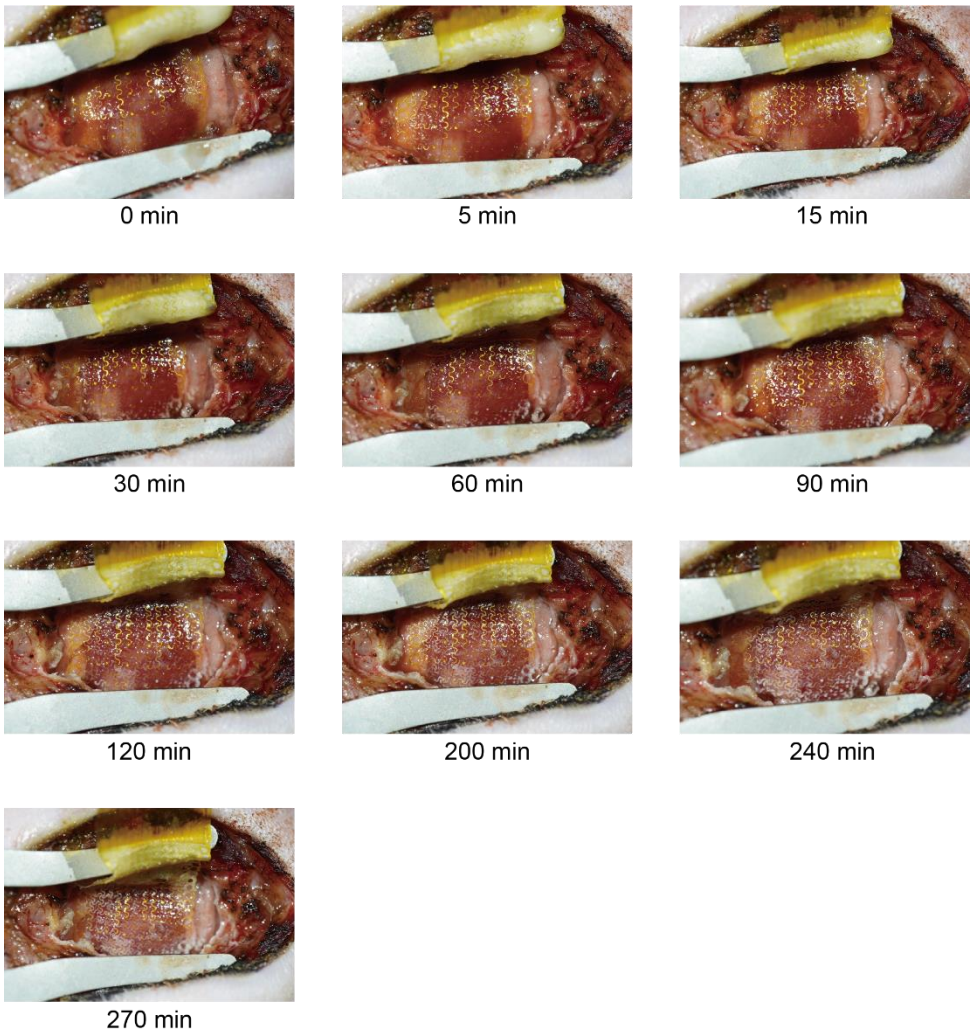

Figure 2-46 Photograph shows that the hybrid device is stable at the same position for 270 minutes during the in-vivo epicardial ECG recording.

Again, isochrone maps are a good method to evaluate the healthy situation of heart. The isochrone maps also show similar trends (Figures 2-47).

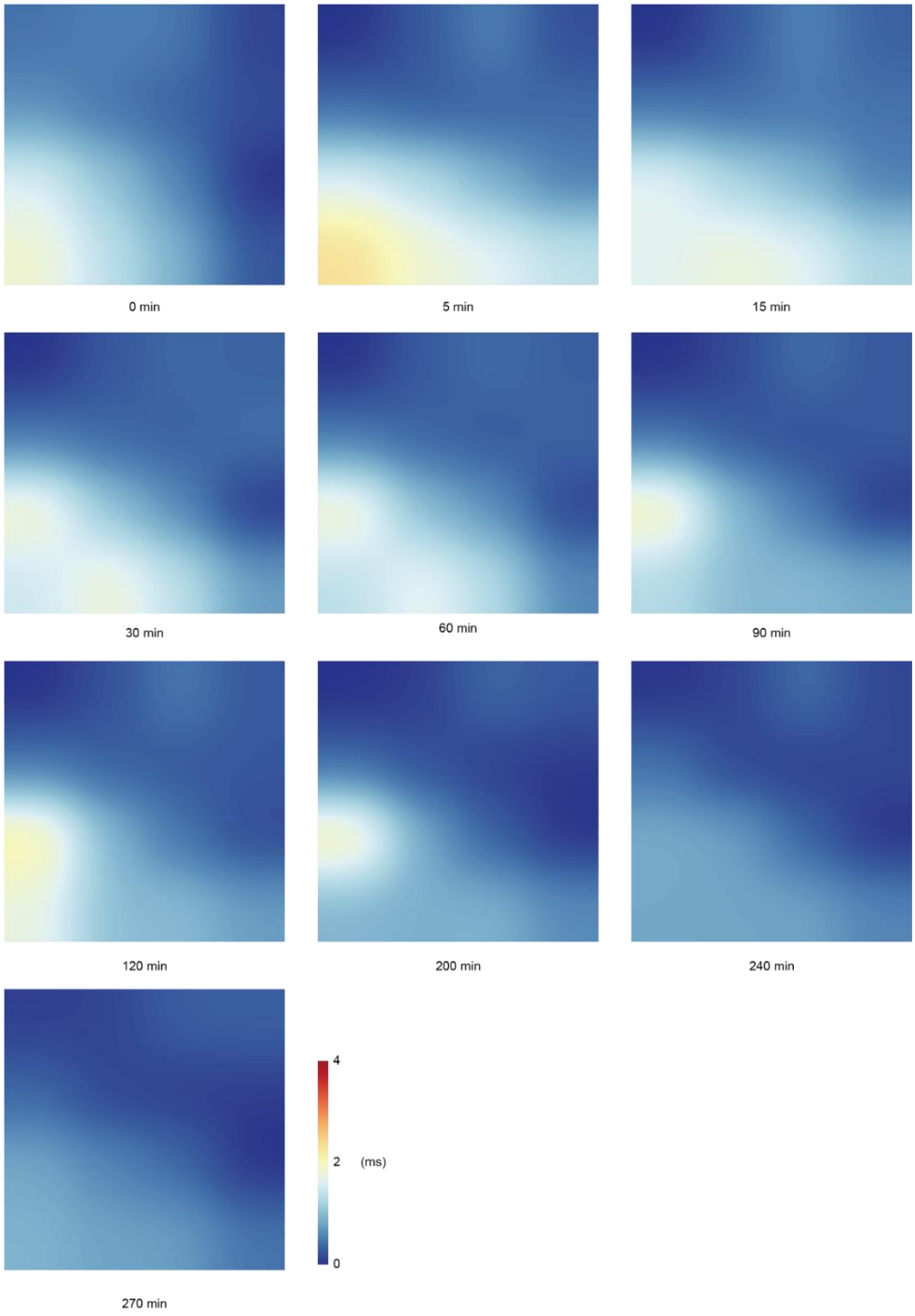

Figure 2-47 Isochrone map of the heart activation delay shows that the device is stable at the same position for 270 minutes during the in-vivo epicardial ECG recording.

Importantly, the recorded amplitude and signal-to-ratio will not be decreased during the recording, suggesting long-term stability within the heart surgical durations (**Figure 2-48**).

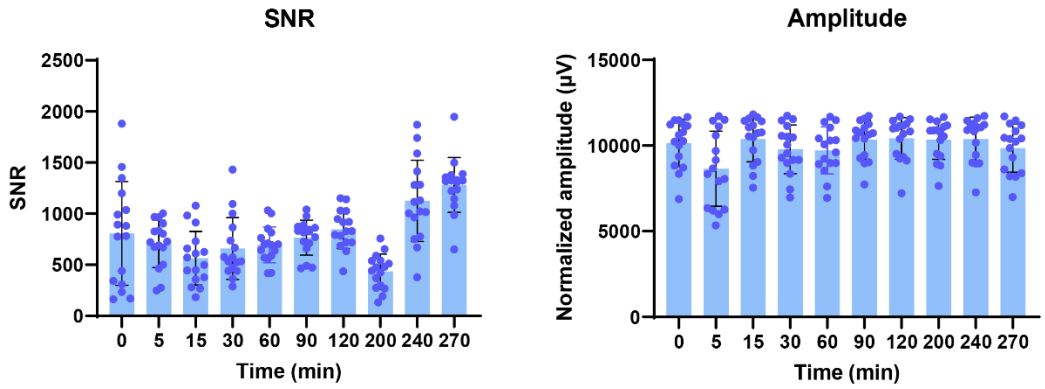

Figure 2-48 Signal-to-noise ratio (SNR) and amplitudes of electrical signals show that hybrid mesh electronics could stably record the epicardial ECG signal for 270 minutes. It should be noted that the system is expected to have failure after extended long-term recording, such as a duration exceeding 24 hours. The hydrolysis and biodegradation of the granular composites can result in the detachment between the tissue and the electronics devices.

2.2.6 Therapeutic effect in acute myocardial infractions

In this chapter, we briefly demonstrated that the hybrid device could provide both diagnosis and therapy to the surrounding tissues. In the next chapter, we will discuss the advantages of using monolithic-to-focal biointerfaces in treating diseases, putting the emphasis on the therapeutic effect rather than on facilitating recording. First of all, we showed that the aspirin-modified granules adhered to the surface of the heart tissue will not damage the tissue (Figure 2-49). This result proves the biocompatible of the granule-releasing system.

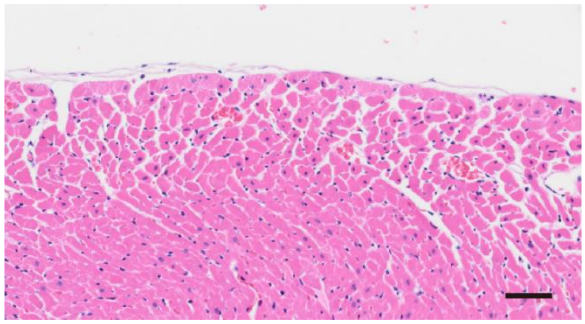

Figure 2-49 The H&E histology image of the heart indicated that the focal biointerface will not damage the tissue. Scale bar, 50 μm.

Next, we showed the aspirin-modified granules could promote tissue recovery from acute myocardial infarction. To demonstrate this, we applied the aspirin-modified granule-releasing hydrogel (AGH) without electronics to the infarcted hearts to investigate its therapeutic effect using a murine acute myocardial infarction (AMI) Model. Echocardiography examination results from diseased mice treated with AGH showed recovery of several key indicators of cardiac function (e.g., ejection fraction (EF), fractional shortening (FS), and cardiac output (CO)) after 3 days (Figure 6l). Furthermore, heartbeat synchronicity (over six LV segments) improves with granule-releasing hydrogel treatment (Figure 2-50).

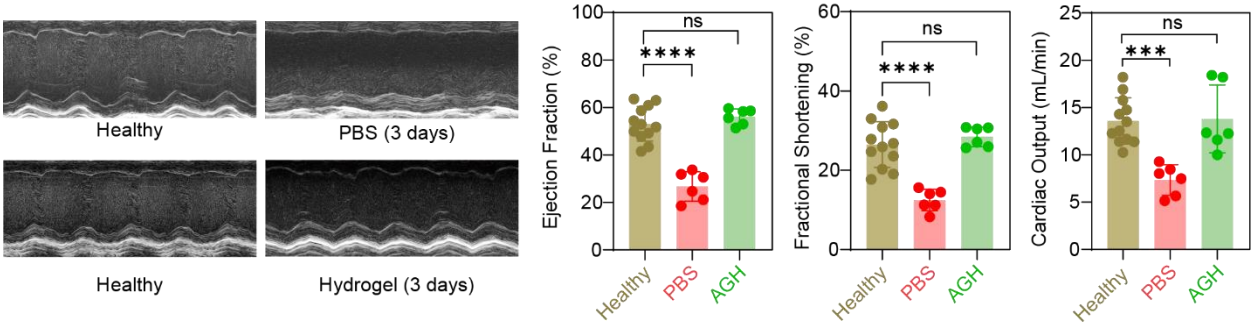

Figure 2-50 Representative LV M-mode echocardiography images showing mice treated with aspirin-modified granule-releasing hydrogels mostly recover from acute myocardial infarction. Recovery of several key indicators of cardiac function in the hydrogel treatment group indicates the therapeutic effect of the aspirin-modified granule-releasing hydrogel in an MI model.

Thus, the granule-releasing hydrogel system has the potential to be effectively integrated with bioelectronic devices in disease diagnosis and treatment. Thin bioelectronics have made considerable strides over recent years, yet applying them in physiological environments, especially on mobile organs, continues to pose challenges. We've seen breakthroughs by integrating adhesive hydrogels, which greatly improve the manageability of these flexible bioelectronics. The impact on the signal-to-noise ratio of the electrical recordings is still to be fully understood. In our evolving biointerface, local and dispersed granular adhesions are formed between the tissue interface and the bioelectronic device following the phase transition of the hydrogel matrix. This facilitates efficient bioelectrical signal transduction and ensures high-fidelity recordings, potentially paving the way for both sturdy device handling and enhanced signal-to-noise electrophysiological recording.

2.3 Conclusion

The releasable granule-releasing hydrogels are promising as an evolving biointerface platform with potential applications for improved flexible bioelectronics operations. Upon granular release, transient focal biointerfaces are created that might overcome the challenges associated with static monolithic materials, such as low spatiotemporal resolution, a lack of optimal biocompatibility, and/or ineffective signal transduction and molecular transport. By encapsulating granules in a responsive hydrogel matrix, we achieved improved macroscopic material/device handling in ambient conditions and responsive release of therapeutic and adhesive granules. The focal adhesion mechanism of the modified granules, inspired by the cellular or tissue affinity of drug molecules, may be extended to a wide range of monolithic or other focal adhesion interfaces for biomedical applications. Several food-grade biopolymers (*e.g.*, starch, chitosan, and gelatin) have

been incorporated into the hydrogel composites to improve the viscoelastic behavior. As all the materials used to construct the evolving biointerfaces are derived from natural bioresources (*i.e.*, biopolymers, and natural biomolecules such as aspirin), the granule-releasing hydrogels might offer a more cost-effective and sustainable means of addressing some biomedical or biophysical issues.

2.4 Experimental Methods

Synthesis of granule-releasing composite. To prepare the dynamic granule-releasing hydrogels (DGH), the starch (16.5%), chitosan (0.83%), and acetate acid (0.83%) were added to sterilized water/phosphate-buffered saline (PBS). The suspension was stirred for 24 hours at 45°C with humidity control to hydrate the starch granules and form the starch/chitosan granules. The gelatin powder (14.18 wt%) was then added to the mixture by vigorously stirring. After 12 hours, the mixture was transferred into acrylic molds with the desired shapes and sealed with acrylic cover slides for gelation at 4°C. The dynamic granule-releasing hydrogel composite was ready after 1 hour. Aspirin-modified granule-releasing hydrogels (AGH) are prepared similarly to DGH, but the chitosan is changed to aspirin-modified chitosan.

Fourier-Transform Infrared Spectroscopy (FTIR). To investigate the phase transition behavior of starch and gelatin, a granule-releasing hydrogel with D_2O (Sigma Aldrich) was placed between two 1 mm thick CaF_2 windows (Crystran) held in a temperature-regulated brass jacket. Temperature-dependent transmission FTIR spectra were acquired from 1 to 70 °C in 2.7 °C steps. Between temperature steps, the sample temperature was increased at a rate of 1.1 ˚C/min and equilibrated at the new temperature for 120 s.

Scanning Electron Microscope (SEM). The granule-releasing hydrogel was quickly frozen in liquid nitrogen and transferred to a Freeze Dryer (Labconco 7670520) overnight at 0.1 mbar pressure for freeze-drying. A scanning electron microscope (Carl Zeiss, Merlin) was used to image the morphology of different samples at 2 kV acceleration voltage. To ensure consistency, each sample was measured at least 25 times.

X-ray Fluorescence Microscopy and Tomography. Synchrotron-based X-ray fluorescence microscopy and tomography were performed at the Bionanoprobe (BNP)[31] located at beamline 9-ID-B of the Advanced Photon Source at Argonne National Laboratory to characterize the structure of starch/chitosan granules. The chitosan polymer is stained with copper chloride for X-ray imaging. Using zone plate optics, X-ray photons of 10.5 keV were focused onto a sample with a focal length of ~80 nm. The sample was raster scanned through the focused X-ray beam in a fly-scan mode with a step size of 60 nm and 50 ms dwell time per pixel. A full spectrum was collected at each pixel to construct two-dimensional (2D) elemental maps. A series of such 2D projections were acquired while the sample rotated around a vertical axis from -60° to 72° with respect to the incident X-ray beam with a 1° increment to form a three-dimensional (3D) tomography dataset. Per-pixel spectrum fitting and quantification were performed using MAPS software on each projection[32]. Prior to performing a 3D volume reconstruction, the quantitative 2D maps were further segmented using k-means clustering analysis to extract features of interest. Tomography reconstruction was done using the gridrec algorithm in an open-source software named TomoPy[33].

Rheometry. A rotational ARES rheometer (TA Instruments) with parallel plates was used to assess the viscoelastic behavior of the granule-releasing hydrogel. The samples were surrounded with water to maintain the hydration of the tissue and the hydrogel. To control the temperature of the system, a Peltier device was incorporated as the bottom plate. In order to ensure that the plate

and samples are in contact, a small contact force is applied prior to each measurement. The samples are then soaked for 100 s allowing them to relax and rebalance with the surrounding environment. The shear modulus was measured by applying 1% oscillatory shear strain at a frequency of 1Hz unless otherwise stated. For the temperature ramp test, temperature window was set to be 25 ºC ~ 40 ºC, covering both ambient temperature and body temperature. In this study, the employed ARES-G2 rheometer system is equipped with a Torque Rebalance Transducer (TRT), which eliminates the need for instrument inertial corrections and minimizes errors. It should also be noted that the data at high frequency may show evidence of phase angle noise while the data at the high strain may show evidence of slip. But neither of these potential issues alters the concepts or conclusions presented in this work.

Stress Relaxation Test. The stress relaxation and dynamic mechanical analysis with compressive mode were performed with an RSA-G2 dynamic mechanical analyzer (TA Instruments). According to a previously published method[34], the stress relaxation behavior was assessed by the compression tests. In brief, the granule-releasing hydrogels were first compressed to 10% strain with a deformation rate of 3 mm/min. Subsequently, the strain was held at a constant value while recording the stress change as a function of time. Dynamic mechanical analysis with compressive mode was performed at 1% strain and 1 Hz. The samples were not prestressed during these tests.

Tensile Test. The tensile tests are performed at the Zwick-Roell zwickiLine Z0.5 at room temperature. We prepared dogbone-shaped molds of standard ASTM dimensions (25 × 4 × 3.175 mm3) for each sample. The hydrogel samples were stretched vertically at a speed of 75 mm/min. The hydrogel samples are loaded and unloaded three times for the cyclic tensile test. To measure shear strength, modified chitosan film and unmodified chitosan film were prepared using film casting method. Porcine skin samples were obtained from Stellen Medical, LLC. The shear

strength was tested using the standard lap-shear test (ASTM F2255). All tests were conducted at a constant tensile speed of 50 mm/min.

Synthesis of Starch-APTS. In a typical experiment, 15mg of starch granules were dispersed in 25 µL of 10 mM APTS solution with 15% acetic acid, followed by the addition of 25 µL of 1 M sodium borohydride. The reaction was conducted at 35 °C for 15–18 h. Afterward, the starch-APTS was washed five times with 10 ml of distilled water and kept at 4 °C for future use.

Synthesis of Chitosan-aspirin Conjugate. Chitosan-aspirin conjugate was synthesized with carbodiimide chemistry. In a typical chemical reaction with the aspirin molecule, chitosan (0.25g) was fully dissolved into 25 ml water by adding 1M HCl. The colloid was then vigorously stirred overnight. Then, the pH of the mixture was adjusted to 4.5 by adding 1M NaOH. Aspirin (2mmol) was then added to the mixture while vigorously stirring. EDC solution was prepared by dissolving 10 mmol EDC in 12 mL of a 1:1 v/v% solution of ethanol and water, and the solution was added dropwise into the chitosan and aspirin mixture solution. The reaction is conducted at room temperature for 12 hours. After the evaporation of ethanol, the final product was purified by dialysis (Slide-A-Lyzer™ Dialysis Cassettes, 10K MWCO) against the acidified water (pH 3.5) for 48 hours. Afterward, the product was dialyzed against deionized water for 3 days. After lyophilization, the product was stored at 4°C for future use. The synthesis of the chitosan-aspirin conjugate was confirmed by using 1H NMR (Bruker, 400MHz) and FITC (Thermo NEXUS 670 Near-, Far-, and Mid-FTIR with ATR Accessory). The degree of aspirin conjugation was calculated by comparing the relative peak area of aspirin (4H, aromatic ring proton, δ 6-8, D2O) and an acetyl group (3H, -$COCH_3$, δ 1.95, D_2O) on the backbone of chitosan.

Molecular Dynamic Simulation. To determine how the functionalization of chitosan with aspirin affects its coupling with different substrates, separate atomistic molecular dynamics simulations

of aspirin-functionalized and non-functionalized (simple) chitosan polymers to a DMPC membrane in a physiological solution were performed[35,36]. The chitosan-covered microparticles adsorbed in the experimental systems above the membrane were mimicked by a graphene layer of a size of 15x15 nm with a 9 chitosan polymer chains of either type randomly attached to it. For simplicity, the graphene was fixed ~3 nm above the DMPC membrane. Both types of chitosan had 30 D-glucosamine and 10 N-acetyl-D-glucosamine randomly distributed subunits. In the functionalized chains, 3 N-acetyl-D-glucosamine subunits were randomly selected and their nitrogens were functionalized with aspirin.

The systems were simulated using NAMD 2.13[37] and the CHARMM36[38] protein force field. The simulations were conducted in the NpT ensemble at a temperature of T = 310 K and a pressure of p = 1 bar, using a Langevin dynamics (γlang = 1 ps-1). The particle-mesh Ewald (PME) method was used to evaluate Coulombic coupling, with periodic boundary conditions applied16. A flexible periodic cell was used with a surface tension target of 0.0 to maintain proper membrane tension. The simulation time step was set to 1 fs. The long-range van der Waals and Coulombic coupling were evaluated every 1 and 2 timesteps, respectively. After 20,000 steps of minimization, the solvent molecules were equilibrated for 5 ns, while the membranes and chitosan chains were constrained using harmonic forces with a spring constant of 1 kcal/mol Å. Next, the systems were equilibrated for over 75 ns with a single carbon atom constrained in a terminal residue of each chitosan chain. The interaction energies were calculated between the chitosan molecules and the membrane using the NAMDEnergy plugin from VMD. The interaction energies per chitosan chain were averaged over the 9 chitosan chains present in each system during the last 20 ns of the trajectories.

Flow Adhesion Assay. Flow adhesion assay is conducted based on the previously reported method[39]. In flow adhesion assay, starch/chitosan granules with or without aspirin modification are flowed over the surface of the different biological components to test the retention rate of the granules. μ-Slide I 0.4 Luer (ibidi) was used as the microfluidic chamber for the cell seeding or molecules deposition. Collagen type IV coating is directly brought from the ibidi. The supported lipid bilayer is deposited based on previous protocol[40]. Caco2 and HaCaT cell lines were all purchased from the Cellular Screening Center at the University of Chicago. Caco2 cells were cultured by MEM (2 mM L-glutamine, 1 mM sodium pyruvate, and 1500 mg/L sodium bicarbonate) with non-essential amino acids, 20 vol.% fetal bovine serum and 1 vol.% penicillin-streptomycin solution. HaCaT cells were cultured by DMEM with 10 vol.% fetal bovine serum and 1 vol.% penicillin-streptomycin solution. Both the Caco2 cells and HaCaT cells were seeded into microfluidic channels and incubated in an atmosphere of 5% CO2 at 37 °C. Organoid tissues were kindly provided by Dr. Eugene Chang's lab at the UChicago Department of Medicine. Syringe pumps (Aladdin Single-Syringe infusion Pump) were used to flow the starch/chitosan granules over the surface of the biological component at 1 ml/min for 10 minutes. Then DI water was pumped with 1ml/min for 10 minutes to flush over the floating starch/chitosan granules. The remaining starch granules were imaged by a Nikon Ti2 microscope and analyzed by ImageJ.

Micro Computed Tomography (CT) Image. Barium sulfate (20 wt%) was added to the granule-releasing hydrogels as the radiocontrast agent. After 12 hours of fasting, unmodified dynamic granule-releasing hydrogels (DGH) and aspirin-modified granule-releasing hydrogels (AGH) were given orally to the mice at a dose of 10 mg/kg. Mice were imaged by the Integrated Small Animal Imaging Research Resource (iSAIRR) at the University of Chicago on the X-Cube (Molecubes, Ghent, Belgium). Animals were anesthetized via inhalation with 2% isoflurane. Respiration rate

and body temperature of the animal were constantly monitored during the entire scanning period with X-Cube onboard monitoring system. Image sessions were performed at 5 different time points, they are 0 hr, 1hr, 2hr, 4hr, 6hr, respectively. 6 hours after oval gavage in mice, GI tracts (stomach, small intestine, colon) were harvested for further micro-CT imaging. Spiral CT was performed through a high-resolution protocol to ensure better contrast detectability (50-kVp and 440 mAs). Volumetric CT images were reconstructed in a 400 × 400 × 1200 format with voxel dimensions of 100X100X100 μm3. Images were processed using VivoQuant 4 patch 1 (InviCRO, LLC, Boston, USA).

Electrical and Electrochemical Characterization. Electrochemical impedance spectroscopy (EIS) was conducted by utilizing the hydrogel or mesh electronic-hydrogel hybrid as the working electrode, silver/silver chloride (Ag/AgCl) as the reference electrode, and platinum as the counter electrode, and the phosphate buffered saline as the electrolyte. Impedance and phase angle of the hydrogel were acquired by an electrochemical workstation (Biologic SP-200) with a sine wave signal amplitude of 10 mV vs. EOC (open circuit voltage). Conductivity measurements were carried out using a four-point probe method using a KEITHLEY analyzer (2636A SYSTEM SourceMeter).

Ex-vivo Heart Signal Recording Experiment. An adult rat was heparinized by intraperitoneal injection with the concentration of 1,000 IU /kg and rested for 20 minutes. An open-drop exposure of isoflurane was used in a bell jar to anesthetize the rat. Hearts were harvested and placed in cold HBSS buffer, with the aorta cannulated in preparation for use in the Langendorff setup. The cannulated aorta was perfused with oxygenated HEPES-buffered Tyrode's solution (Recipe: KCl, 5.4 mM; NaCl, 126 mM; glucose, 10 mM; $MgCl_2$, 1 mM; HEPES, 10 mM; $MgSO_4$, 1.2 mM; $CaCl_2$, 2 mM; NaH_2PO_4, 0.39 mM; bubbled with 99.5% O_2; pH, 7.3). The heart was mounted in a

water-jacketed beaker (Fisher Scientific) to maintain at 37°C and the perfusion was passed through a heating coil and bubble trap (Radnoti). By adjusting the height of the intravenous bag containing the perfusion buffer, the perfusion pressure was kept between 80 and 100 mmHg. The sinoatrial node along with the atria was removed, resulting in the slowing down of the atrioventricular pace. BP-100 probes (iWorx) were connected to the perfusion line and water-filled balloons (Radnoti) were inserted into the left ventricle to monitor perfusion and pressure in the left ventricle, respectively. Reference ECG recordings (from iWorx) were conducted by placing needle electrodes on the left ventricular wall and aorta, grounding them, and connecting them to a C-ISO-256 preamplifier (iWorx). We amplified all signals (perfusion, LVP, and ECG) with an IA-400D amplifier (iWorx) and interfaced them with a computer using a Digidata 1550 digitizer and Clampex software (Molecular Devices). The mesh-electronic-hydrogel hybrid was placed between the left and right ventricular wall with seamless integration through the adhesion of the hydrogel. A 4x4 micro electrode array (2 mm spacing between electrodes) was used for the electrical mapping process and the recording was performed via a USB interface board and RHD2132 16-channel input recording headstage (Intantech). Electrophysiology data for the hydrogel interface is recorded immediately after positioning the hybrid device on the heart. For the granular interface, data is gathered once the interface is fully established. This typically occurs around 10 minutes considering the thickness of the coated hydrogel. The continuous perfusion water flush over the heart at the Langendorff setup can slightly accelerate granule release process. The ECG amplitudes were baseline-calibrated and averaged from more than 20 ECG peaks for each of the 16 individual channels. The normalized Amplitudes/noise values were calculated by dividing the largest depolarization peak by the standard deviation of the baseline (noise). The isochrone maps of the electrical propagation were plotted from averaging more than 20 ECG peaks from all 16 channels.

All calculations were performed using Python scripts. To improve readability, we used Gaussian interpolation for map rendering.

Rat heart in vivo electrophysiology recording. Adult rats, both male and female, aged between 10 and 24 weeks and weighing between 400 and 500 grams, were put into deep anesthesia using isoflurane at a concentration of 2 - 4%. The rat's tongue was delicately displaced to the side, following which a tracheal cannula was inserted using forceps, and connected to a Harvard Small Animal Ventilator Model 683. The costal cartilages situated on the left side of the sternum were cut between the 3rd and 5th intercostal ribs to unveil the left ventricle. The pericardium was carefully removed from the surface using forceps and cotton swabs. The thoracic cavity was then expanded using a small-animal rib spreader. Subsequently, the hybrid mesh electrode was placed on the epicardial surface, where it self-adheres. This mesh electrode was then connected to an Intantech RHD2132-chip headstage via a zero-insertion-force connector, attached to an 18-pin electrode adapter board. The signal recording was done at a rate of 20 kilosamples per second, within the frequency range of 50 - 1000 Hz. After 10 minutes for establishing the granular interface, the recordings were performed at 0 min, 15 min, 30 min, 60 min, 90 min, 120 min, 200 min, 240 min, 270 min.

Murine Acute Myocardial Infarction (AMI) Model. All the surgical procedures to induce mice acute myocardial infarction were performed in the University of Illinois at Chicago Cardiovascular Research Core. Before surgery, mice were weighed and subcutaneously injected with Buprenorphine SR LAB (1.0 mg/kg). Following isoflurane anesthesia, the heart was exposed by performing a left thoracotomy through the fourth intercostal space. The left anterior descending coronary artery (LAD) was identified and temporally ligated. After 45 minutes, the ligature was released, and the reperfusion phase began. Then 40 mm^3 aspirin-modified granule-releasing

hydrogel was applied to peri-infarct area within 5 minutes after reperfusion into each mouse. PBS was used as a negative control. Thoracotomy site was closed, and positive end-expiratory pressure was increased to hyperinflate the lungs. The animals were observed and studied for 3 days post-surgery.

Echocardiography. Phenotypic characterization for MI mice was conducted via echocardiography. Pre-surgery echo and day 3 (72 hours after surgery) echo were performed by using a 550Hz transducer (VisualSonics Inc.) and the Vevo 2100 Imaging System (VisualSonics Inc.). The mice were positioned onto the platform with ventral side up and the paws were taped to the copper leads to provide the electrocardiogram (ECG) with the electrode gel (Parker Laboratories, Inc.). The respiratory waveform was recorded and all heart rates for mice were maintained at over 400 bpm (beats per minute). In order to identify anatomical structures and evaluate heart function, the parasternal long axis view (PLAX) and parasternal short axis view (PSAX) were collected using both brightness mode (B-mode) and motion mode (M-mode). A variety of cardiac functions, including the ejection fraction (EF), fraction shortening (FS), cardiac output (CO), and strain were assessed using the Vevo LAB software (VisualSonics Inc., v.5.7.0).

2.5 References

1 Yang, Q. S., Wei, T., Yin, R. T., Wu, M. Z., Xu, Y. M., Koo, J., Choi, Y. S., Xie, Z. Q., Chen, S. W., Kandela, I., Yao, S. L., Deng, Y. J., Avila, R., Liu, T. L., Bai, W. B., Yang, Y. Y., Han, M. D., Zhang, Q. H., Haney, C. R., Lee, K. B., Aras, K., Wang, T., Seo, M. H., Luan, H. W., Lee, S. M., Brikha, A., Ghoreishi-Haack, N., Tran, L., Stepien, I., Aird, F., Waters, E. A., Yu, X. G., Banks, A., Trachiotis, G. D., Torkelson, J. M., Huang, Y. G., Kozorovitskiy, Y., Efimov, I. R. & Rogers, J. A. Photocurable bioresorbable adhesives as functional interfaces between flexible bioelectronic devices and soft biological tissues. *Nat Mater* **20**, 1559-1570, doi:10.1038/s41563-021-01051-x (2021).

2 Jiang, Y. W., Zhang, Z. T., Wang, Y. X., Li, D. L., Coen, C. T., Hwaun, E., Chen, G., Wu, H. C., Zhong, D. L., Niu, S. M., Wang, W. C., Saberi, A., Lai, J. C., Wu, Y. L., Wang, Y., Trotsyuk, A. A., Loh, K. Y., Shih, C. C., Xu, W. H., Liang, K., Zhang, K. L., Bai, Y. H., Gurusankar, G., Hu, W. P., Jia, W., Cheng, Z., Dauskardt, R. H., Gurtner, G. C., Tok, J. B. H.,

Deisseroth, K., Soltesz, I. & Bao, Z. N. Topological supramolecular network enabled high-conductivity, stretchable organic bioelectronics. *Science* **375**, 1411-1417, doi:10.1126/science.abj7564 (2022).
3 Yang, Y. Y., Wu, M. Z., Vazquez-Guardado, A., Wegener, A. J., Grajales-Reyes, J. G., Deng, Y. J., Wang, T. Y., Avila, R., Moreno, J. A., Minkowicz, S., Dumrongprechachan, V., Lee, J., Zhang, S. Y., Legaria, A. A., Ma, Y. H., Mehta, S., Franklin, D., Hartmann, L., Bai, W. B., Han, M. D., Zhao, H. B., Lu, W., Yu, Y., Sheng, X., Banks, A., Yu, X. G., Donaldson, Z. R., Gereau, R. W., Good, C. H., Xie, Z. Q., Huang, Y. G., Kozorovitskiy, Y. & Rogers, J. A. Wireless multilateral devices for optogenetic studies of individual and social behaviors. *Nat Neurosci* **24**, 1035-1045, doi:10.1038/s41593-021-00849-x (2021).
4 Kim, D. H., Lu, N. S., Ma, R., Kim, Y. S., Kim, R. H., Wang, S. D., Wu, J., Won, S. M., Tao, H., Islam, A., Yu, K. J., Kim, T. I., Chowdhury, R., Ying, M., Xu, L. Z., Li, M., Chung, H. J., Keum, H., McCormick, M., Liu, P., Zhang, Y. W., Omenetto, F. G., Huang, Y. G., Coleman, T. & Rogers, J. A. Epidermal Electronics. *Science* **333**, 838-843, doi:10.1126/science.1206157 (2011).
5 Freedman, B. R., Kuttler, A., Beckmann, N., Nam, S., Kent, D., Schuleit, M., Ramazani, F., Accart, N., Rock, A., Li, J. Y., Kurz, M., Fisch, A., Ullrich, T., Hast, M. W., Tinguely, Y., Weber, E. & Mooney, D. J. Enhanced tendon healing by a tough hydrogel with an adhesive side and high drug-loading capacity. *Nat Biomed Eng* **6**, 1167-1179, doi:10.1038/s41551-021-00810-0 (2022).
6 Deng, J., Yuk, H., Wu, J. J., Varela, C. E., Chen, X. Y., Roche, E. T., Guo, C. F. & Zhao, X. H. Electrical bioadhesive interface for bioelectronics. *Nat Mater* **20**, 229-236, doi:10.1038/s41563-020-00814-2 (2021).
7 Tringides, C. M., Vachicouras, N., de Lazaro, I., Wang, H., Trouillet, A., Seo, B. R., Elosegui-Artola, A., Fallegger, F., Shin, Y., Casiraghi, C., Kostarelos, K., Lacour, S. P. & Mooney, D. J. Viscoelastic surface electrode arrays to interface with viscoelastic tissues. *Nat Nanotechnol* **16**, 1019-1029, doi:10.1038/s41565-021-00926-z (2021).
8 Lin, X., Liu, Y., Bai, A. B., Cai, H. H., Bai, Y. J., Jiang, W., Yang, H. L., Wang, X. H., Yang, L., Sun, N. & Gao, H. J. A viscoelastic adhesive epicardial patch for treating myocardial infarction. *Nat Biomed Eng* **3**, 632-643, doi:10.1038/s41551-019-0380-9 (2019).
9 Brannon, E. R., Guevara, M. V., Pacifici, N. J., Lee, J. K., Lewis, J. S. & Eniola-Adefeso, O. Polymeric particle-based therapies for acute inflammatory diseases. *Nat Rev Mater* **7**, 796-813, doi:10.1038/s41578-022-00458-5 (2022).
10 Lueckgen, A., Garske, D. S., Ellinghaus, A., Mooney, D. J., Duda, G. N. & Cipitria, A. Enzymatically-degradable alginate hydrogels promote cell spreading and in vivo tissue infiltration. *Biomaterials* **217**, doi:10.1016/j.biomaterials.2019.119294 (2019).
11 Griffin, D. R., Weaver, W. M., Scumpia, P. O., Di Carlo, D. & Segura, T. Accelerated wound healing by injectable microporous gel scaffolds assembled from annealed building blocks. *Nat Mater* **14**, 737-744, doi:10.1038/Nmat4294 (2015).
12 Chen, J., Webb, J., Shariati, K., Guo, S. B., Montclare, J. K., McArt, S. & Ma, M. L. Pollen-inspired enzymatic microparticles to reduce organophosphate toxicity in managed pollinators. *Nat Food* **2**, 339-347, doi:10.1038/s43016-021-00282-0 (2021).
13 Tang, J. A., Shen, D. L., Caranasos, T. G., Wang, Z. G., Vandergriff, A. C., Allen, T. A., Hensley, M. T., Dinh, P. U., Cores, J., Li, T. S., Zhang, J. Y., Kan, Q. C. & Cheng, K. Therapeutic microparticles functionalized with biomimetic cardiac stem cell membranes and secretome. *Nat Commun* **8**, doi:10.1038/ncomms13724 (2017).

14 Gattazzo, F., Urciuolo, A. & Bonaldo, P. Extracellular matrix: A dynamic microenvironment for stem cell niche. *Bba-Gen Subjects* **1840**, 2506-2519, doi:10.1016/j.bbagen.2014.01.010 (2014).
15 Koo, J., MacEwan, M. R., Kang, S. K., Won, S. M., Stephen, M., Gamble, P., Xie, Z. Q., Yan, Y., Chen, Y. Y., Shin, J., Birenbaum, N., Chung, S. J., Kim, S. B., Khalifeh, J., Harburg, D. V., Bean, K., Paskett, M., Kim, J., Zohny, Z. S., Lee, S. M., Zhang, R. Y., Luo, K. J., Ji, B. W., Banks, A., Lee, H. M., Huang, Y. G., Ray, W. Z. & Rogers, J. A. Wireless bioresorbable electronic system enables sustained nonpharmacological neuroregenerative therapy. *Nat Med* **24**, 1830-1836, doi:10.1038/s41591-018-0196-2 (2018).
16 Allen, M. E., Hindley, J. W., Baxani, D. K., Ces, O. & Elan, Y. Hydrogels as functional components in artificial cell systems. *Nat Rev Chem* **6**, 562-578, doi:10.1038/s41570-022-00404-7 (2022).
17 Daly, A. C., Riley, L., Segura, T. & Burdick, J. A. Hydrogel microparticles for biomedical applications. *Nat Rev Mater* **5**, 20-43, doi:10.1038/s41578-019-0148-6 (2020).
18 Xu, Y. X., Kim, K. M., Hanna, M. A. & Nag, D. Chitosan-starch composite film: preparation and characterization. *Ind Crop Prod* **21**, 185-192, doi:10.1016/j.indcrop.2004.03.002 (2005).
19 Masina, N., Choonara, Y. E., Kumar, P., du Toit, L. C., Govender, M., Indermun, S. & Pillay, V. A review of the chemical modification techniques of starch. *Carbohyd Polym* **157**, 1226-1236, doi:10.1016/j.carbpol.2016.09.094 (2017).
20 Li, J. X., Liu, Y. X., Yuan, L., Zhang, B. B., Bishop, E. S., Wang, K. C., Tang, J., Zheng, Y. Q., Xu, W. H., Niu, S. M., Beker, L., Li, T. L., Chen, G., Diyaolu, M., Thomas, A. L., Mottini, V., Tok, J. B. H., Dunn, J. C. Y., Cui, B. X., Pasca, S. P., Cui, Y., Habtezion, A., Chen, X. K. & Bao, Z. N. A tissue-like neurotransmitter sensor for the brain and gut. *Nature* **606**, 94-101, doi:10.1038/s41586-022-04615-2 (2022).
21 Guimaraes, C. F., Gasperini, L., Marques, A. P. & Reis, R. L. The stiffness of living tissues and its implications for tissue engineering. *Nat Rev Mater* **5**, 351-370, doi:10.1038/s41578-019-0169-1 (2020).
22 Fang, Y., Han, E. D., Zhang, X. X., Jiang, Y. W., Lin, Y. L., Shi, J. Y., Wu, J. B., Meng, L. Y., Gao, X., Griffin, P. J., Xiao, X. H., Tsai, H. M., Zhou, H., Zuo, X. B., Zhang, Q., Chu, M. Q., Zhang, Q. T., Gao, Y., Roth, L. K., Bleher, R., Ma, Z. Y., Jiang, Z., Yue, J. P., Kao, C. M., Chen, C. T., Tokmakoff, A., Wang, J., Jaeger, H. M. & Tian, B. Z. Dynamic and Programmable Cellular-Scale Granules Enable Tissue-like Materials. *Matter-Us* **2**, 948-964, doi:10.1016/j.matt.2020.01.008 (2020).
23 Park, B., Shin, J. H., Ok, J., Park, S., Jung, W., Jeong, C., Choy, S., Jo, Y. J. & Kim, T. I. Cuticular pad-inspired selective frequency damper for nearly dynamic noise-free bioelectronics. *Science* **376**, 624-629, doi:10.1126/science.abj9912 (2022).
24 Stevenson, P. & Tokmakoff, A. Time-resolved measurements of an ion channel conformational change driven by a membrane phase transition. *P Natl Acad Sci USA* **114**, 10840-10845, doi:10.1073/pnas.1708070114 (2017).
25 Amunson, K. E. & Kubelka, J. On the temperature dependence of amide I frequencies of peptides in solution. *J Phys Chem B* **111**, 9993-9998, doi:10.1021/jp072454p (2007).
26 Ackels, L., Stawski, P., Amunson, K. E. & Kubelka, J. On the temperature dependence of amide I intensities of peptides in solution. *Vib Spectrosc* **50**, 2-9, doi:10.1016/j.vibspec.2008.07.004 (2009).

27 Du, H. L., Liu, M. R., Yang, X. Y. & Zhai, G. X. The design of pH-sensitive chitosan-based formulations for gastrointestinal delivery. *Drug Discov Today* **20**, 1004-1011, doi:10.1016/j.drudis.2015.03.002 (2015).
28 Dabrowska, M., Starek, M. & Skucinski, J. Lipophilicity study of some non-steroidal anti-inflammatory agents and cephalosporin antibiotics: A review. *Talanta* **86**, 35-51, doi:10.1016/j.talanta.2011.09.017 (2011).
29 Galie, P. A., Nguyen, D. H. T., Choi, C. K., Cohen, D. M., Janmey, P. A. & Chen, C. S. Fluid shear stress threshold regulates angiogenic sprouting. *P Natl Acad Sci USA* **111**, 7968-7973, doi:10.1073/pnas.1310842111 (2014).
30 Çengel, Y. A. & Cimbala, J. M. *Fluid Mechanics: Fundamentals and Applications*. (McGraw-Hill Education, 2018).
31 Chen, S., Deng, J., Yuan, Y., Flachenecker, C., Mak, R., Hornberger, B., Jin, Q., Shu, D., Lai, B., Maser, J., Roehrig, C., Paunesku, T., Gleber, S. C., Vine, D. J., Finney, L., VonOsinski, J., Bolbat, M., Spink, I., Chen, Z., Steele, J., Trapp, D., Irwin, J., Feser, M., Snyder, E., Brister, K., Jacobsen, C., Woloschak, G. & Vogt, S. The Bionanoprobe: hard X-ray fluorescence nanoprobe with cryogenic capabilities. *J Synchrotron Radiat* **21**, 66-75, doi:10.1107/S1600577513029676 (2014).
32 Vogt, S. MAPS: A set of software tools for analysis and visualization of 3D X-ray fluorescence data sets. *J Phys Iv* **104**, 635-638, doi:10.1051/jp4:20030160 (2003).
33 Gursoy, D., De Carlo, F., Xiao, X. H. & Jacobsen, C. TomoPy: a framework for the analysis of synchrotron tomographic data. *J Synchrotron Radiat* **21**, 1188-1193, doi:10.1107/S1600577514013939 (2014).
34 Chaudhuri, O., Gu, L., Klumpers, D., Darnell, M., Bencherif, S. A., Weaver, J. C., Huebsch, N., Lee, H. P., Lippens, E., Duda, G. N. & Mooney, D. J. Hydrogels with tunable stress relaxation regulate stem cell fate and activity. *Nat Mater* **15**, 326-334, doi:10.1038/Nmat4489 (2016).
35 Shaham-Niv, S., Rehak, P., Zaguri, D., Kolusheva, S., Kral, P. & Gazit, E. Metabolite amyloid-like fibrils interact with model membranes. *Chem Commun* **54**, 4561-4564, doi:10.1039/c8cc01423j (2018).
36 Sen, S., Han, Y. X., Rehak, P., Vukovic, L. & Kral, P. Computational studies of micellar and nanoparticle nanomedicines. *Chem Soc Rev* **47**, 3849-3860, doi:10.1039/c8cs00022k (2018).
37 Phillips, J. C., Hardy, D. J., Maia, J. D. C., Stone, J. E., Ribeiro, J. V., Bernardi, R. C., Buch, R., Fiorin, G., Henin, J., Jiang, W., McGreevy, R., Melo, M. C. R., Radak, B. K., Skeel, R. D., Singharoy, A., Wang, Y., Roux, B., Aksimentiev, A., Luthey-Schulten, Z., Kale, L. V., Schulten, K., Chipot, C. & Tajkhorshid, E. Scalable molecular dynamics on CPU and GPU architectures with NAMD. *J Chem Phys* **153**, doi:10.1063/5.0014475 (2020).
38 Yu, W. B., He, X. B., Vanommeslaeghe, K. & MacKerell, A. D. Extension of the CHARMM general force field to sulfonyl-containing compounds and its utility in biomolecular simulations. *J Comput Chem* **33**, 2451-2468, doi:10.1002/jcc.23067 (2012).
39 Shetty, S., Weston, C. J., Adams, D. H. & Lalor, P. F. A Flow Adhesion Assay to Study Leucocyte Recruitment to Human Hepatic Sinusoidal Endothelium Under Conditions of Shear Stress. *Jove-J Vis Exp*, doi:10.3791/51330 (2014).
40 Mingeot-Leclercq, M. P., Deleu, M., Brasseur, R. & Dufrene, Y. F. Atomic force microscopy of supported lipid bilayers. *Nat Protoc* **3**, 1654-1659, doi:10.1038/nprot.2008.149 (2008).

Chapter 3. Monolithic-to-focal biointerfaces for regenerative medicine

3.1 Introduction

Regenerative medicine offers the potential to fully heal damaged tissues and organs rather than just treating symptoms[1,2]. This approach can reduce the demand for organ transplants by stimulating the body's innate repair mechanisms[3]. Biomaterials has long been studied for regenerative medicine[4]. Compared to the conventional small molecules drug, the material-based therapy usually enables controlled and localized release of bioactive molecules, and ensure biocompatibility and biodegradability, which minimizes immune reactions and long-term complications[5]. Their ability to create a three-dimensional environment is pivotal for mimicking in vivo conditions, leading to potentially long-lasting therapeutic effects[6]. Besides, the material gives more technique design space to achieve the functionalities in complicated environments[7]. Thus, how to best utilize the biomaterials in the in-vivo environments becomes an interesting and important questions[8]. Even for the same chemical composition of biomaterials, different delivery methods or pharmaceutical format will also significantly influence the therapeutic outcome as regenerative medicine[9]. In last chapter, we have discussed the potential of monolithic-to-focal biointerface in bioelectronics recording. In this section, we will mainly focus on how the monolithic-to-focal biointerface could further promote the therapeutic effect of the biomaterials when compared to other delivery format such as the single monolithic biointerface and single focal biointerface. We will use the ulcerative colitis and skin wound healing as two pre-clinical model to demonstrate our proof-of-concept.

Ulcerative colitis is inflammatory bowel disease (IBD)[10] characterized by impaired intestinal barrier functions[11], an imbalance in the gut microbiome[12], and dysregulated immune responses to commensal bacteria[13]. While traditional treatments for IBD primarily aim to manage symptoms

by suppressing these immune responses[14,15], they often fail to address root causes, including damage to the gastrointestinal mucus layer, loss of intestinal barrier integrity, and gut microbiome dysbiosis. Even with advancements in targeted drug delivery[16], conventional immunosuppressive medications, whether small molecules or biologics, can lead to unintended systemic side effects[17]. Prolonged use of these drugs poses risks of severe complications, including opportunistic infections, cancer, autoimmunity, and liver damage[18].

Wounds throughout the body are common and can be devastating injuries with long recovery times[19]. Treatment of a wound and its therapeutic impediments have always attracted great concern in health care and medical fields, bringing about substantial economically challenging burdens worldwide[20]. In the United States in 2014, with an increasingly aging and obese population, high risk comorbidities commensurately increase, growing wound closure product market size of 21.4 billion in 2022 and compound annual growth rate of 4.15% from 2023 to 2030[21]. Normal healing of acute wounds includes a predictable series of events: inflammation, proliferation/repair, and remodeling[22]. Wounds that fail to proceed through the normal phases and remain in a dysregulated inflammatory state are reclassified from acute to chronic wounds[19]. Chronic wound physiology has proven to be highly complex and intricate at the cellular level, involving multiple regulatory axes and signaling cascades[23]. Indeed, developing technologies have begun to target these coordinated cellular processes. Despite effective and foundational interventions for the optimization of wound care, there remain challenging problems that remain incompletely understood and in need of ongoing research and innovation. Therefore, a simple and effective wound therapy is still demanded.

3.2 Result and Discussion

3.2.1 Monolithic-to-focal biointerfaces design

The traditional biomaterials are usually used in a monolithic format, but the focal biointerface provides additional biological benefits. Contrary to monolithic biointerfaces, these dispersed interfaces could potentially facilitate an enhanced transport of small molecules such as water, electrolytes, and amino acids. We first demonstrated that focal biointerface provide more interstitial space for signaling small molecules to pass through (Figure 3-1). Polyacrylamide hydrogels were used as non-morphing monolithic hydrogels and rhodamine B was used as artificial cellular molecule.

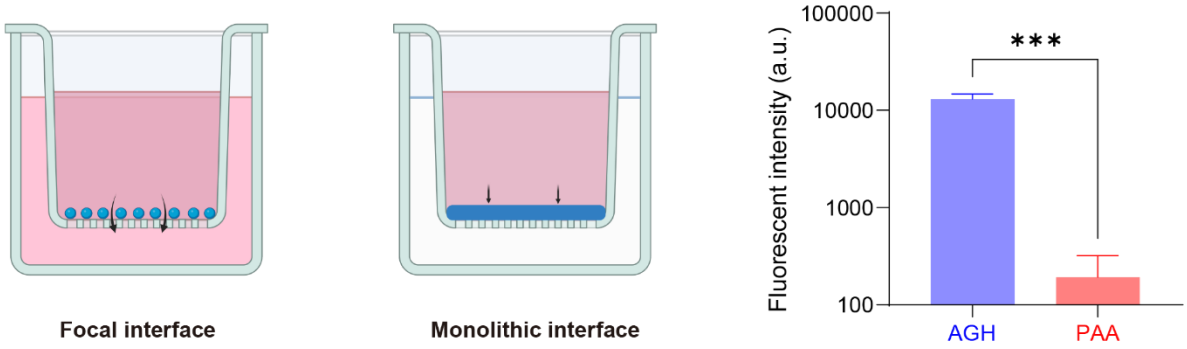

Figure 3-1 The focal biointerface provides more interstitial space for signaling small molecules to pass through. AGH and polyacrylic acid hydrogel were used as the interfacial layer. Initially, the inner wells contained rhodamine B as the artificial signal molecule, and the outer well contained water. After 12 hours of incubation at 37 °C, the solution from the outer well was sampled for fluorescent measurement. AGH: aspirin-modified granule-releasing hydrogel. P values are determined by t-test, two-tailed.

However, the monolithic format of biomaterials also has its own advantages, especially in constructing a handleable delivery format. Here, we showed, besides the traditional gel forms for injection or coating, granule-releasing hydrogels (same as the hydrogel in the last chapter) can also yield bandage-like configurations, bioelectronics/hydrogel composites, and hydrogel or aerogel

microneedle constructs. The granule-releasing hydrogel could be casted into different shape and delivery format for different applications. For example, we demonstrated that the aspirin-modified granule-releasing hydrogel could be patterned in the microneedle forms which largely facilitate the transdermal delivery of granules for therapeutic effects (Figure 3-2).

Figure 3-2 The granule-releasing hydrogels can be patterned in hydrogel/aerogel microneedle forms for transdermal delivery of granules. Scale bar, 5 mm.

Since both the monolithic biointerfaces and focal biointerfaces of biomaterials have their own advantages, designing a monolithic-to-focal biointerface can combine the benefits of both, leading to the best therapeutic outcomes for regenerative medicine. We will use the evolving mechanism to describe the monolithic-to-focal transition process. With this evolving mechanism, the granule-releasing hydrogel can effectively manage symptoms of dextran sulfate sodium (DSS)-induced colitis and accelerate skin wound healing.

3.2.2 Therapeutic effect in ulcerative colitis

First, we will demonstrate the granule-releasing hydrogels have the therapeutic effect in treating the disease. Specifically, we sought to determine if the biophysical barrier formed by the adhered biomolecule-conjugated granules and their partial degradation products at the damaged tissue

surface could facilitate disease recovery (Figure 3-3). As described in the introduction, colitis is an inflammatory chronic condition of the colon of unknown cause. Current treatment options for ulcerative colitis are limited to managing symptoms, which however does not address the underlying causes, including the impaired intestinal barrier and dysbiosis of gut microbiota[24].

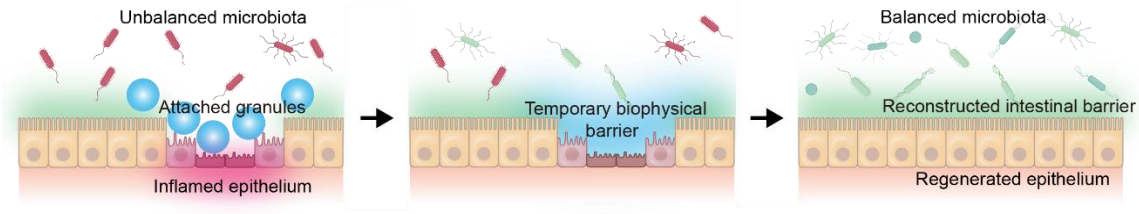

Figure 3-3 Schematic of released granules forming temporary biophysical barriers and modulating gut microbiota.

To evaluate the therapeutic effects of the granule-releasing hydrogels, we performed a series of pre-clinical evaluations with a DSS-induced colitis model (Figure 3-4). The DSS-induced colitis model is widely utilized for in vivo evaluation given that its clinical and histological features are similar to those of human ulcerative colitis, including adverse symptoms (e.g., bleeding, diarrhea), loss of epithelium barrier functions, intestinal inflammation, and dysregulated host gut microbiota[25].

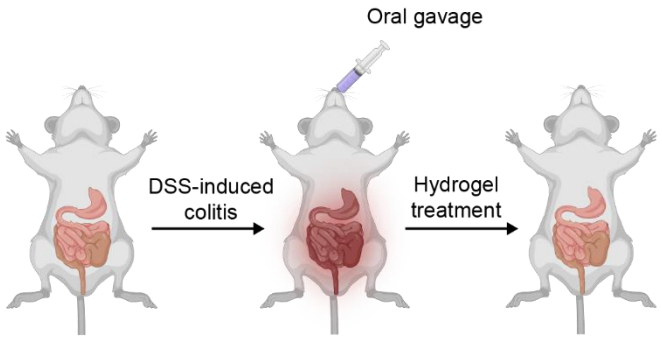

Figure 3-4 Mice were given 3% DSS in drinking water to induce ulcerative colitis. Granule-releasing hydrogel therapies were orally administrated (10 mg/kg daily).

Using this animal model, we observed that the granules released from an orally administrated aspirin-modified granule-releasing hydrogels (AGH) adhered to DSS-treated colonic epithelium (Figure 3-5).

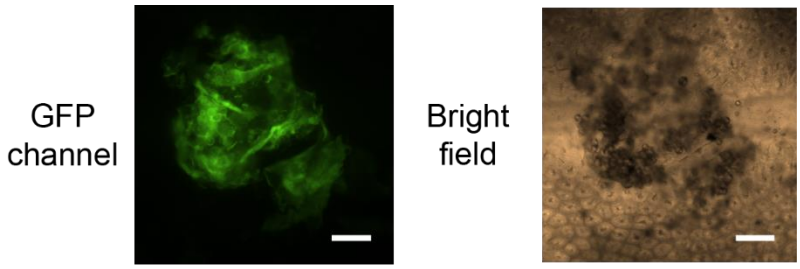

Figure 3-5 Microscope images show that the aspirin-modified granule-releasing hydrogel (AGH) passed through the gastrointestinal tract and formed a distributed biointerface in the colon. Scale bar, 100 μm.

This is consistent with the ex vivo mucosal affinity of the aspirin-modified granules (AS) observed with flow adhesion tests in last chapter. We conclude that the granule-releasing hydrogel composites can manage DSS-induced ulcerative colitis through the colonic biointerface. The aspirin-modified granule-releasing hydrogels (AGH) showed improved therapeutic effects, compared with non-modified yet still dynamic/releasable granule-releasing hydrogels (DGH), in the management of rodent colitis symptoms, in terms of body weight loss, colon length, fecal water content, and bleeding scores (Figure 3-6). In addition, many severe symptoms such as watery diarrhea and hematochezia were significantly alleviated in the AGH group, while the DSS control groups failed to recover from these adverse symptoms.

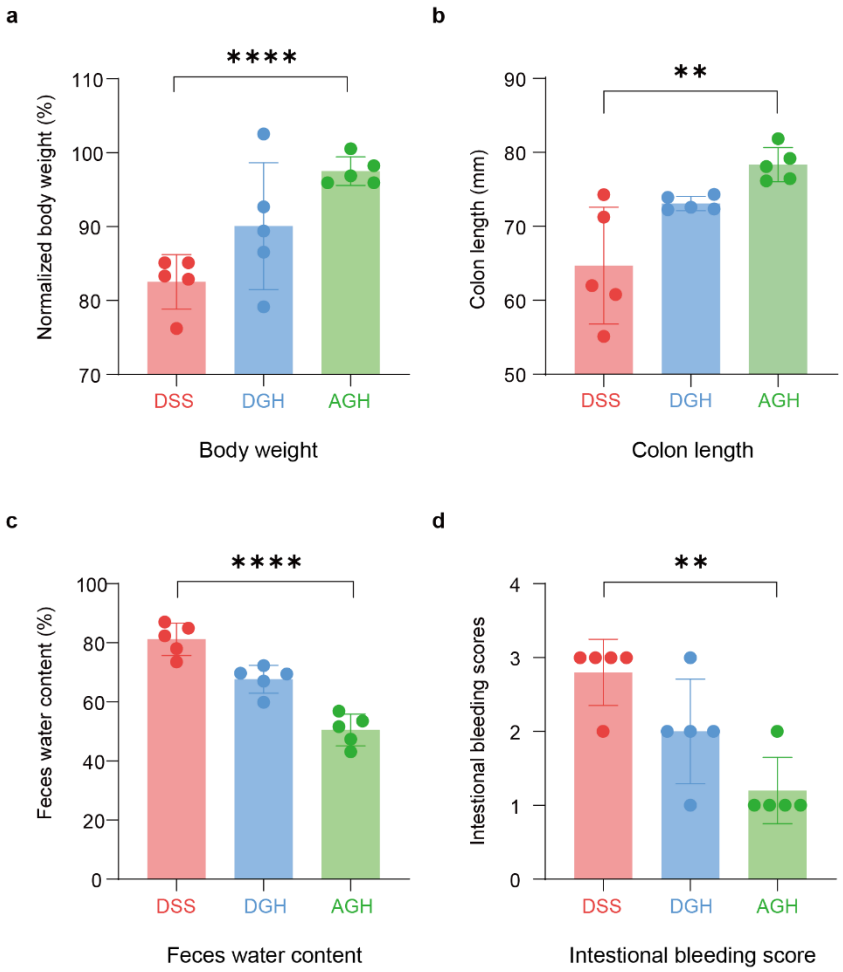

Figure 3-6 Aspirin-modified granule-releasing hydrogels (AGH) alleviated the DSS-induced ulcerative colitis symptoms in mice. (a) The AGH group's body weight has significantly recovered compared with the DSS group on day 7. Changing body weights indicate that AGH mice have slowly recovered from DSS-induced colitis compared to the DSS control group. (b) Reduction in colon length caused by DSS-induced colitis is largely relieved in the AGH group. (c) Feces water content was significantly reduced in AGH and DGH groups compared with DSS groups. Based on this observation, the dynamic granule-releasing hydrogel could effectively reduce the symptoms of diarrhea in colitis caused by DSS. In addition, the AGH has a better therapeutic effect than DGH. (d) At 7 days, the AGH group has a significantly reduced incidence of hematochezia compared with the DSS group indicated by the intestinal bleeding score. DSS: mice with DSS-induced colitis, no treatment. DGH: mice with DSS-induced colitis, treated with unmodified dynamic granule-releasing hydrogels. AGH: mice with DSS-induced colitis, treated with aspirin-modified granule-releasing hydrogels. Data are presented as mean ± standard error of mean. (n = 5). P values are determined by t-test, two-tailed.

Specifically, the body weight of AGH-treated DSS-colitis mice was maintained at an almost stable level over the course of the 7 days, while DSS-colitis mice in other groups showed a progressive decrease in body weight (Figure 3-7).

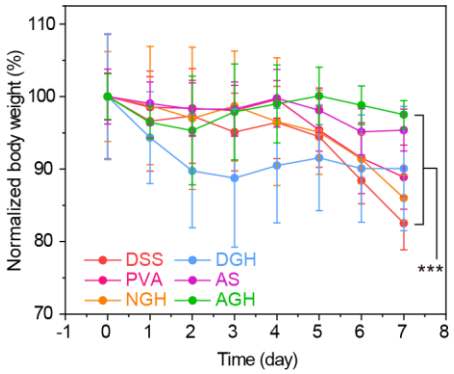

Figure 3-7 Mouse body weight over 7 days. AGH-treated mice treated showed the highest body weights.

Next, we showed that the monolithic-to-focal biointerfaces enhance the therapeutic effect of hydrogel in ulcerative colitis. As a compare, the non-releasing matrix or non-granule-releasing hydrogel (containing the same chemical compositions of starch, chitosan, and gelatin) did not show similar levels of therapeutic effects. The granules alone showed positive effects on mouse body weight loss and colon shortening, but not on fecal water content or bleeding scores (Figure 3-8). These results emphasize the importance of the pharmaceutical format of biomaterials in the field of regenerative medicine. Although their chemical compositions are similar, the biointerfaces they form in in-vivo environments can significantly influence therapeutic outcomes.

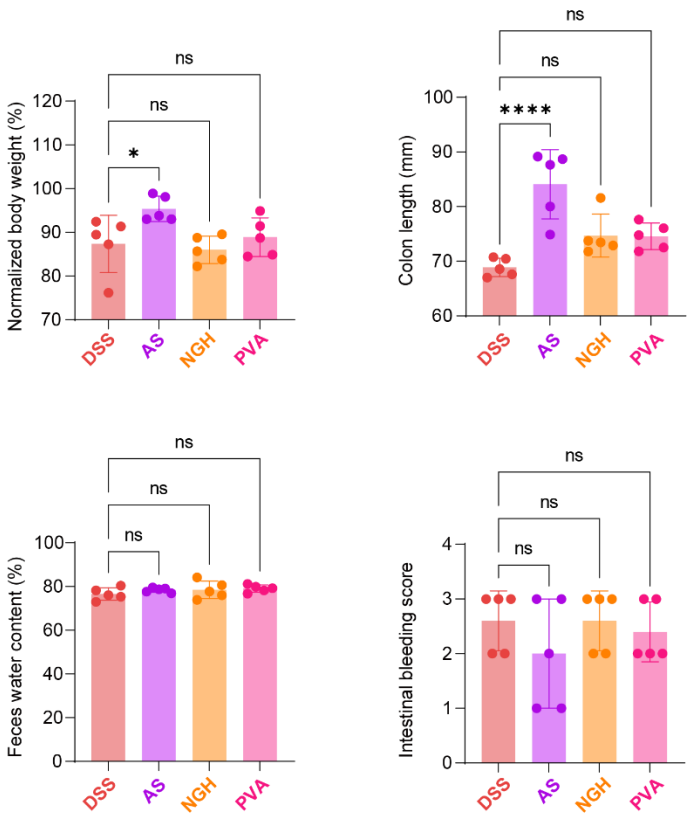

Figure 3-8 AS, PVA, and NGH group does not show therapeutic effect in alleviating the DSS-induced ulcerative colitis symptoms in mice. NGH group indicates that the granular focal biointerface plays an important role in treating DSS-induced ulcerative colitis. Without the granular shape, the hydrogel composites could not alleviate the ulcerative colitis symptoms. AS and PVA group indicate that the monolithic-focal evolving biointerface is important in treating DSS-induced ulcerative colitis. DSS: mice with DSS-induced colitis, no treatment. AS: mice with DSS-induced colitis, treated with aspirin-modified starch/chitosan granules without hydrogel matrix. NGH: mice with DSS-induced colitis, treated with non-granule-releasing hydrogels. The composition of NGH is the same as the AGH, but the granular structure is destroyed through gelatinization process. PVA: mice with DSS-induced colitis, treated with aspirin-modified starch/chitosan granules inside polyvinyl alcohol matrix. Data are presented as mean ± standard error of mean. (n = 5). P values are determined by ordinary one-way ANOVA with Tukey's multiple comparisons test.

Besides, only AGH treatment significantly improved histological colonic damage, but not granules alone, non-releasing matrix or non-granule-releasing hydrogel (Figures 3-9), indicating the AGH may form a therapeutic biointerface to protect the colonic epithelium against pathological damage.

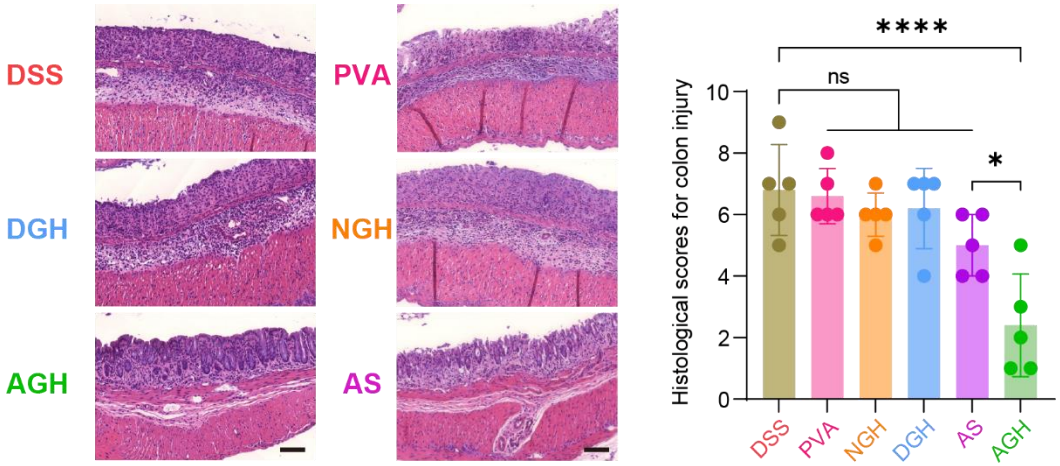

Figure 3-9 Representative images of hematoxylin and eosin (H&E) staining demonstrate that pathological damage is significantly diminished in the colons of AGH-treated mice, in terms of epithelium thickness, crypt intactness, and inflammation. Scale bar, 100 μm. Histological score analysis shows that AGH-treated mice have lower level of histological inflammation and tissue damage.

The aspirin-modified granule-releasing hydrogels (AGH) form a therapeutic biointerface in the colonic region and help rebuild the colon barrier in mice. Ulcerative colitis progression causes mucosal ulcers and impairs normal mucosal barrier functions. We used the fluorescein isothiocyanate (FITC)-dextran permeability assay to explore colon permeability in treated and untreated DSS-colitis mice. The fluorescein isothiocyanate (FITC)-dextran permeability assay is a common method used to assess the integrity and permeability of epithelial and endothelial barriers, such as the intestinal mucosal barrier or the blood-brain barrier. Four hours after administration of FITC-dextran, the AGH group had less FITC-dextran signal in the blood (Figure 3-10).

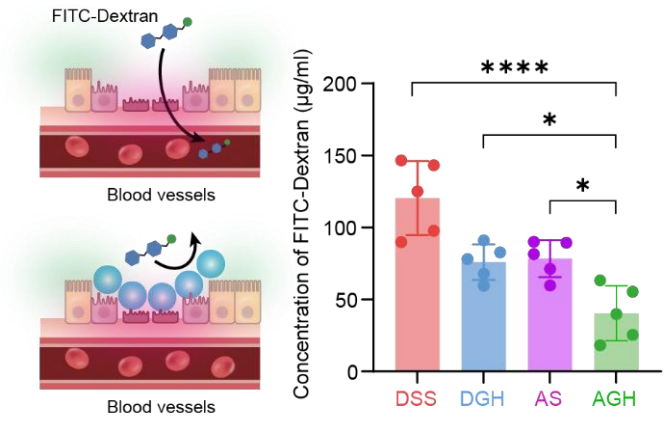

Figure 3-10 Schematic illustrates that the granular interfaces restore the intestinal permeability (left). Blood levels of fluorescein isothiocyanate (FITC)-dextran were lowest in AGH-treated mice (right).

The reduction in paracellular uptake of large-size molecules from the gastrointestinal tract suggests restoration of intestinal intactness. Histological Periodic acid–Schiff (PAS) staining (Figure 3-11) revealed that the thickness of the intestinal epithelium and the goblet cells increased significantly with AGH treatment.

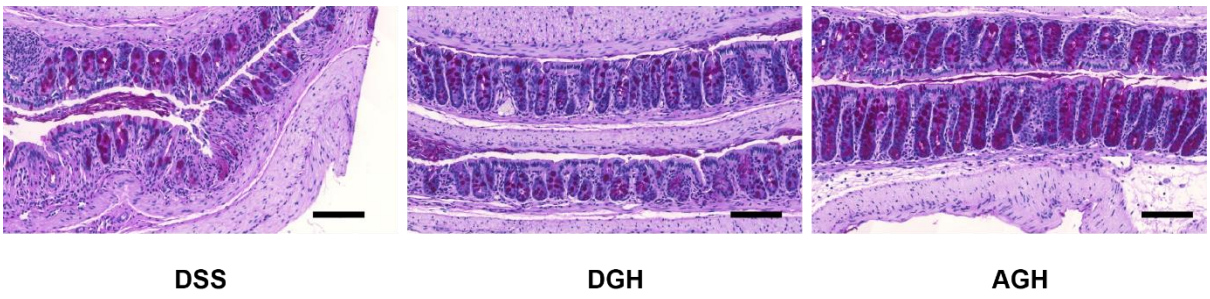

Figure 3-11 The periodic acid-Schiff (PAS) staining shows that there are abundant goblet cells after the treatment of aspirin-modified granule-releasing hydrogel. Scale bar 100 μm. DSS: mice with DSS-induced colitis, no treatment. DGH: mice with DSS-induced colitis, treated with unmodified dynamic granule-releasing hydrogels. AGH: mice with DSS-induced colitis, treated with aspirin-modified granule-releasing hydrogels.

We used the statistical method to present the number of goblet cells and the thickness of the mucus layer. The results suggest that the granule-releasing hydrogel facilitates the restoration of the mucin layer and intestinal functions (Figure 3-12).

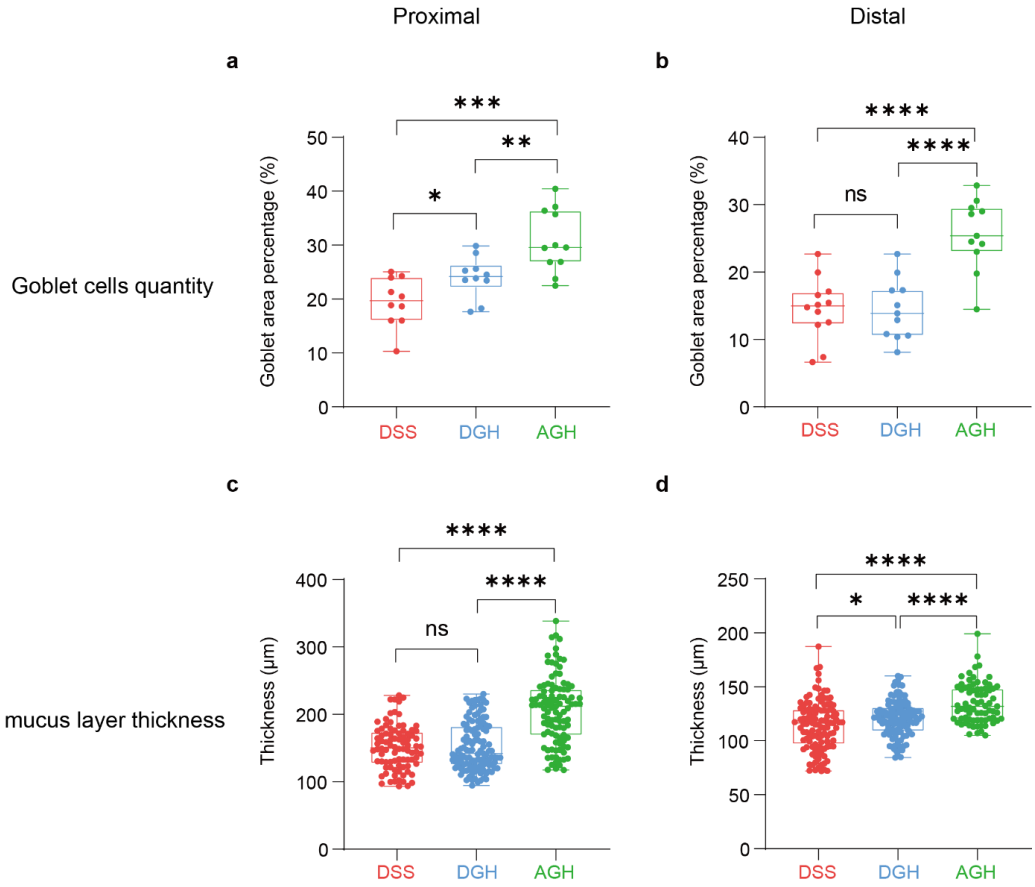

Figure 3-12 Periodic acid–Schiff (PAS) histological analysis of mice colon indicates healthier colon tissue structure after applying aspirin-modified granule-releasing hydorgel. Proximal and distal colon were analyzed separately. (a) Goblet cells are more abundant in both the proximal and distal colon of the AGH group. Goblet cells produce mucins in the colon. This result indicates that aspirin-modified granule-releasing hydrogel helps the colon to rebuild its mucus layer, suggesting an anti-colitis function of colon function in DSS-induced ulcerative colitis. (b) The AGH group shows thicker colonic epithelial thickness, indicating that the aspirin-modified granule-releasing hydrogel help rebuilds the colonic barrier and reduce ulcer severity. DSS: mice with DSS-induced colitis, no treatment. DGH: mice with DSS-induced colitis, treated with unmodified dynamic granule-releasing hydrogels. AGH: mice with DSS-induced colitis, treated with aspirin-modified granule-releasing hydrogels. Boxes bind interquartile range (IQR) divided

by the median; whiskers extend 1.5 ± IQR. All data points are plotted (n > 5). P values are determined by ordinary one-way ANOVA with Tukey's multiple comparisons test.

The chitosan coating may lead to slower granular composite digestion in the stomach and intestine, which prolongs the therapeutic biointerface period in the harsh in vivo environment and protects the ulceration from further damage[26]. It is important to note that, although the aspirin-modified granular composite (AS) also shows therapeutic effects in treating ulcerative colitis, these effects are less significant compared to the aspirin-modified granule-releasing hydrogel (AGH). This is indicated by factors such as feces water content, colon permeability, colon histological recovery (Figures 3-13), and colon immune response (Figures 3-14). The statistical analysis between the AS and AGH group is also shown in Figure 3-15. We primarily attribute the superior therapeutic effect of the AGH group over the AS group to the sustained and pH-responsive release of therapeutic granules within the gastrointestinal tract.

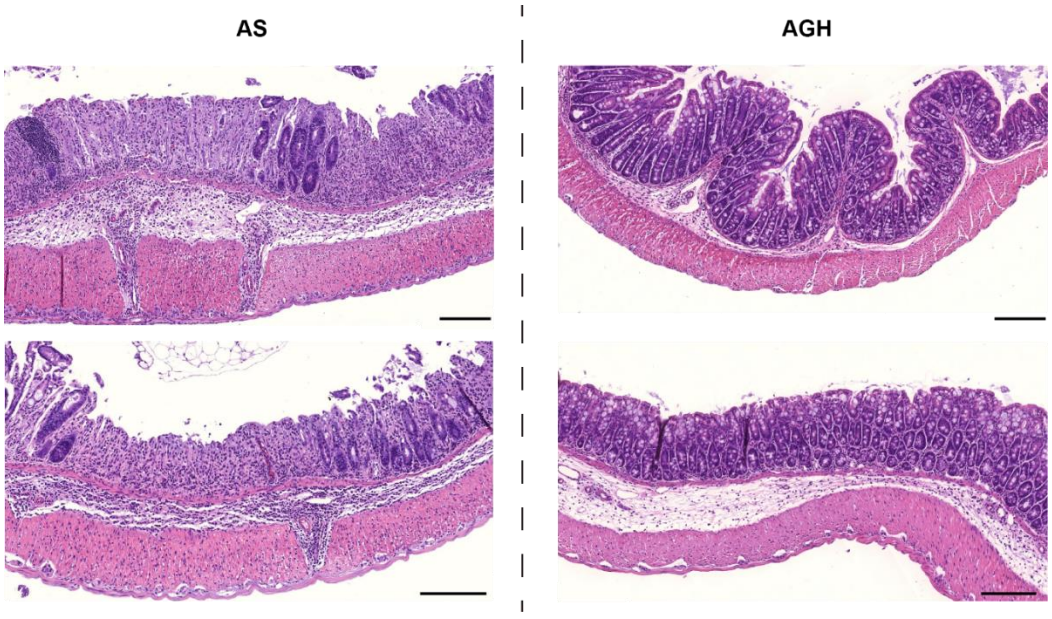

Figure 3-13 Colon H&E histology images of AS group and AGH group show that the AGH group has better colon histological recovery. AS: mice treated with aspirin-modified

starch/chitosan granules without hydrogel matrix. AGH: mice treated with aspirin-modified granule-releasing hydrogels. Scale bar 200 μm.

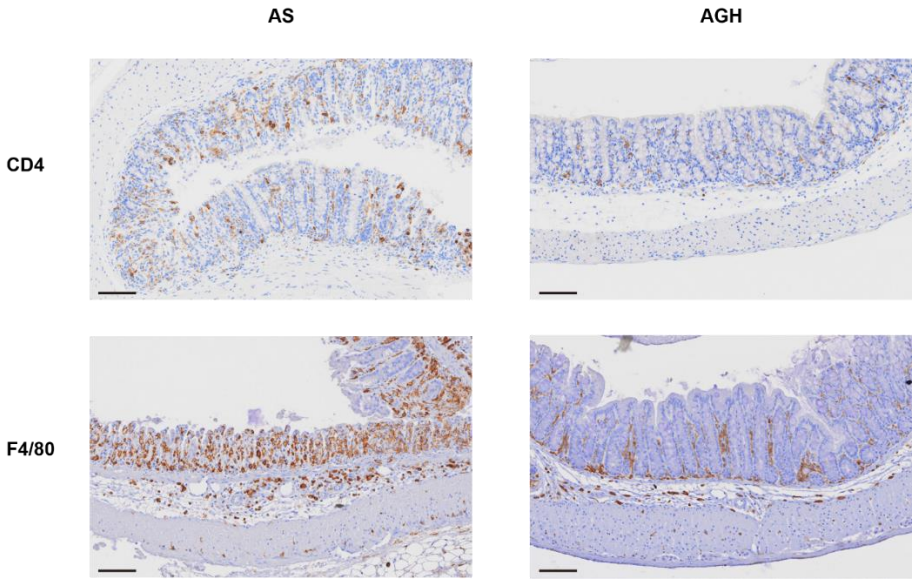

Figure 3-14 Immnuohistology with CD4 and F4/80 staining reveal that colons in AGH group have less inflammative profile than AS group. CD4 is a cell surface protein expressed on a subset of immune cells known as T-helper cells. F4/80 is a marker for a specific cell surface protein expressed by a subset of mature tissue-resident macrophages. AS: mice treated with aspirin-modified starch/chitosan granules without hydrogel matrix. AGH: mice treated with aspirin-modified granule-releasing hydrogels. Scale bar, 100 μm.

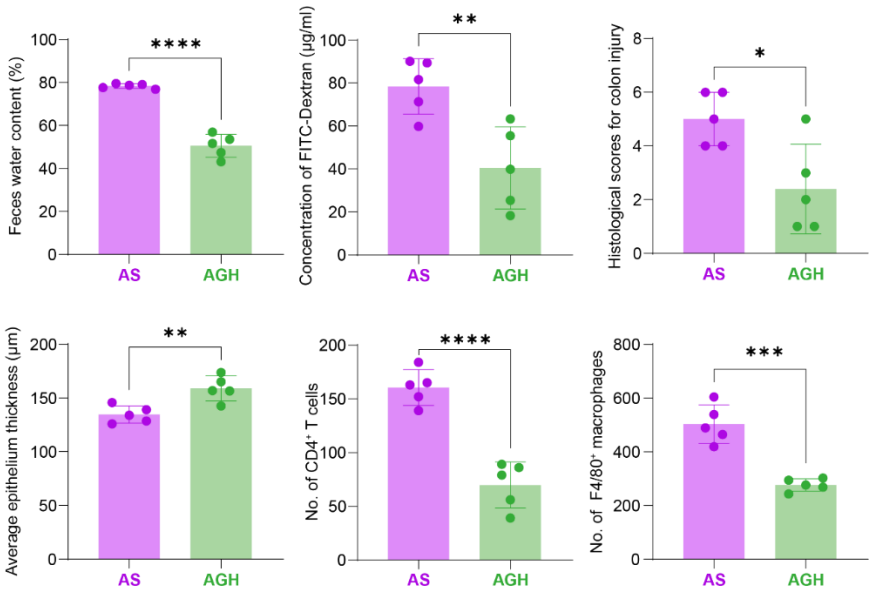

Figure 3-15 The comparison of AS and AGH group in different index indicates that the AGH have better therapeutic effect than AS in treating ulcerative colitis. The comprision include feces water content, colon permeability, H&E histology score, epithelium thickness, CD4+ T-helper cells, F4/80+ macrophages. AS: mice treated with aspirin-modified starch/chitosan granules without hydrogel matrix. AGH: mice treated with aspirin-modified granule-releasing hydrogels. Data are presented as mean ± standard error of mean. (n = 5). P values are determined by t-test, two tailed.

3.2.3 Gut microbiota analysis

The aspirin-modified granule-releasing hydrogels (AGH) modulate the composition of gut microbiota. Increasing evidence has shown that dysbiosis of the gut microbiota is closely associated with human gastrointestinal disease and plays a key role in the pathogenesis of ulcerative colitis[27]. Restoration of the healthy gut microbiota could largely regulate the gut immune response and effectively promote recovery from ulcerative colitis[28].

16S rRNA gene sequencing is a widely-used technique for identifying and differentiating bacteria within varied samples. By targeting the 16S rRNA gene, this method encompasses PCR amplification using specific primers, and then sequencing, typically via next-generation platforms. The obtained sequence data is then subjected to quality control, OTU picking, taxonomic

assignment, and additional diversity analysis. This provides insights into microbial compositions, potential links to diseases, and patterns in environmental distributions. To investigate the gut microbiota after our treatment (the significance of the aspirin modification), we perfrom16S ribosomal RNA gene sequencing for feces samples. Our result demonstrated that both DGH and AGH modulated microbiota diversity, which is supported by the Linear discriminant analysis Effect Size (LEfSe) (Figure 3-16).

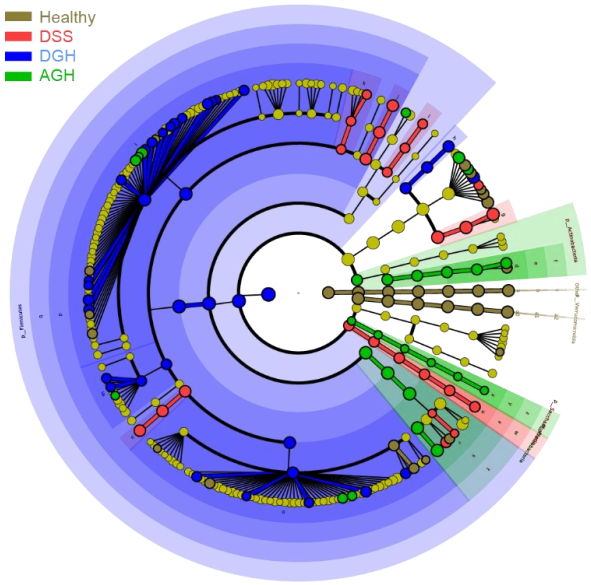

Figure 3-16 Linear discriminant analysis Effect Size (LEfSe) taxa analysis indicates that the AGH & DGH change the bacterial diversity of DSS-induced colitis mice.

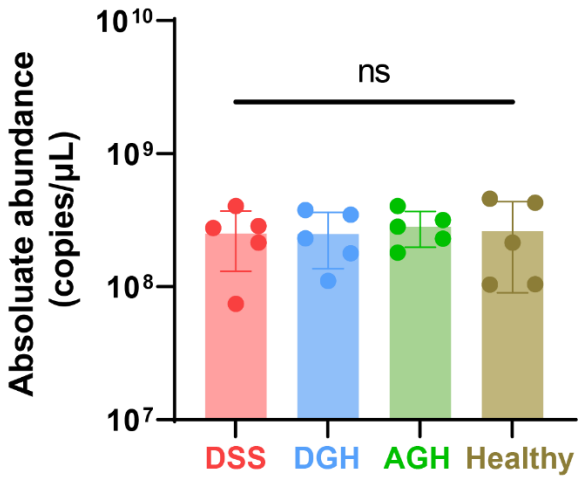

Figure 3-17 Absolute abundance of gene copies in the sequencing samples show there is no significant difference between all experimental groups. The plot shows the absolute abundance of bacterial (16S) RNA measured in the samples. DSS: mice with DSS-induced colitis, no treatment. DGH: mice with DSS-induced colitis, treated with unmodified dynamic granule-releasing hydrogels. AGH: mice with DSS-induced colitis, treated with aspirin-modified granule-releasing hydrogels. Healthy, mice without DSS-induced colitis. Data are presented as mean ± standard error of mean. (n = 5). P values are determined by ordinary one-way ANOVA with Tukey's multiple comparisons test.

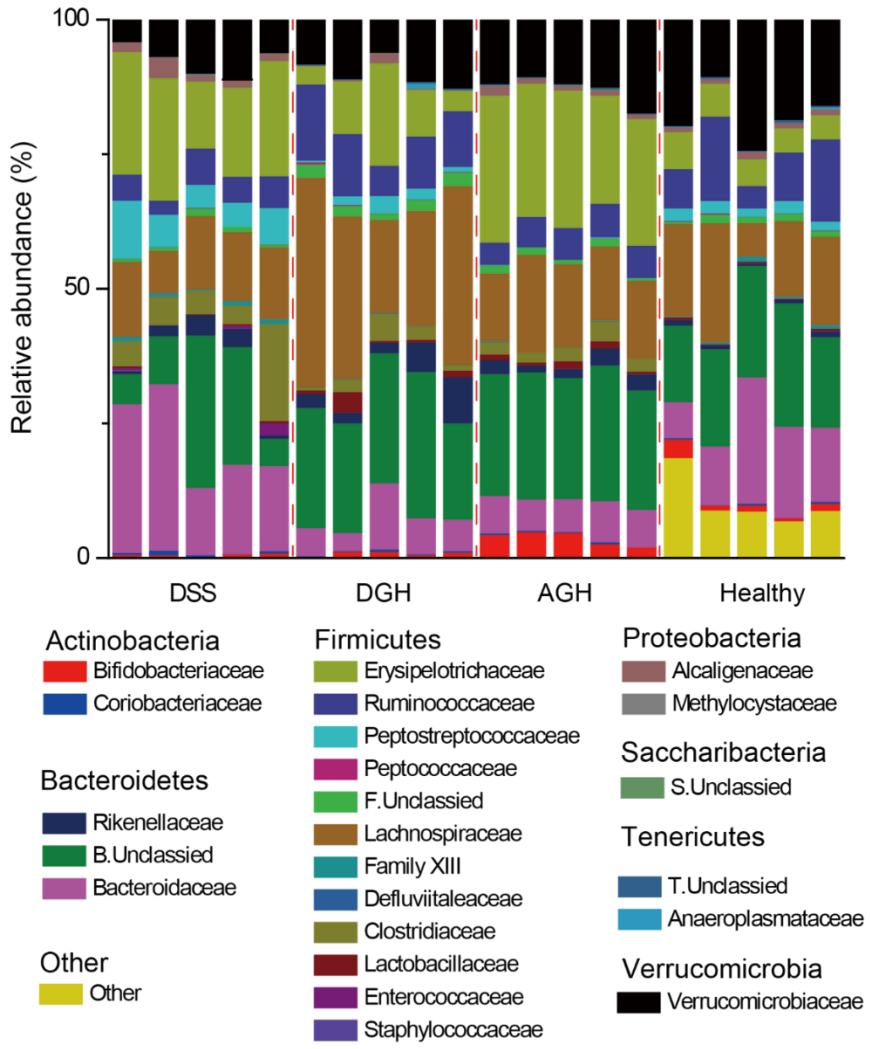

Figure 3-18 Taxa composition plots illustrate the gut microbial compositions at different taxonomy levels from phylum to family. DSS: mice with DSS-induced colitis, no treatment. DGH: mice with DSS-induced colitis, treated with unmodified dynamic granule-releasing hydrogels. AGH: mice with DSS-induced colitis, treated with aspirin-modified granule-releasing hydrogels. Healthy: mice without DSS-induced colitis.

A Principal Coordinates Analysis (PCoA) plot of beta diversity further revealed that the gut microbiota profiles of AGH-treated DSS-colitis mice were distinct from the profiles of other treatment groups (Figure 3-19).

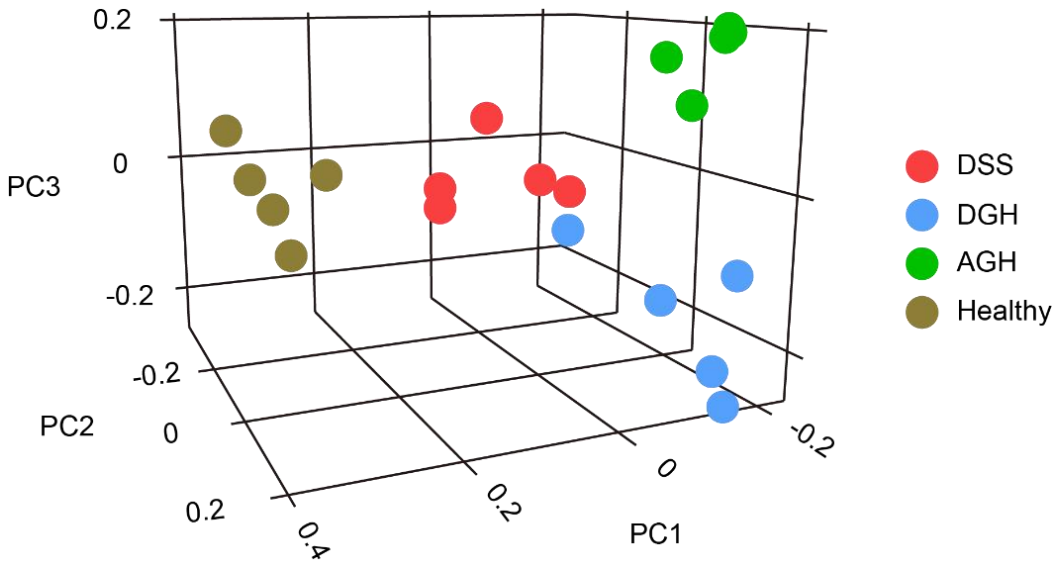

Figure 3-19 Principal Coordinates Analysis (PCoA) plot of beta diversity revealed that DSS-colitis mice treated with aspirin-modified granule-releasing hydrogel had distinct gut microbiota profiles. DSS: mice with DSS-induced colitis, no treatment. DGH: mice with DSS-induced colitis, treated with unmodified dynamic granule-releasing hydrogels. AGH: mice with DSS-induced colitis, treated with aspirin-modified granule-releasing hydrogels. Healthy: mice without DSS-induced colitis.

At the phylum/family level, the AGH significantly enhanced the relative abundance of *Akkermansia*, *Bifidobacterium*, and *Lactobacillus*, all important microbial indicators that are prominently decreased in patients with inflammatory bowel diseases[29] (Figures 3-20).

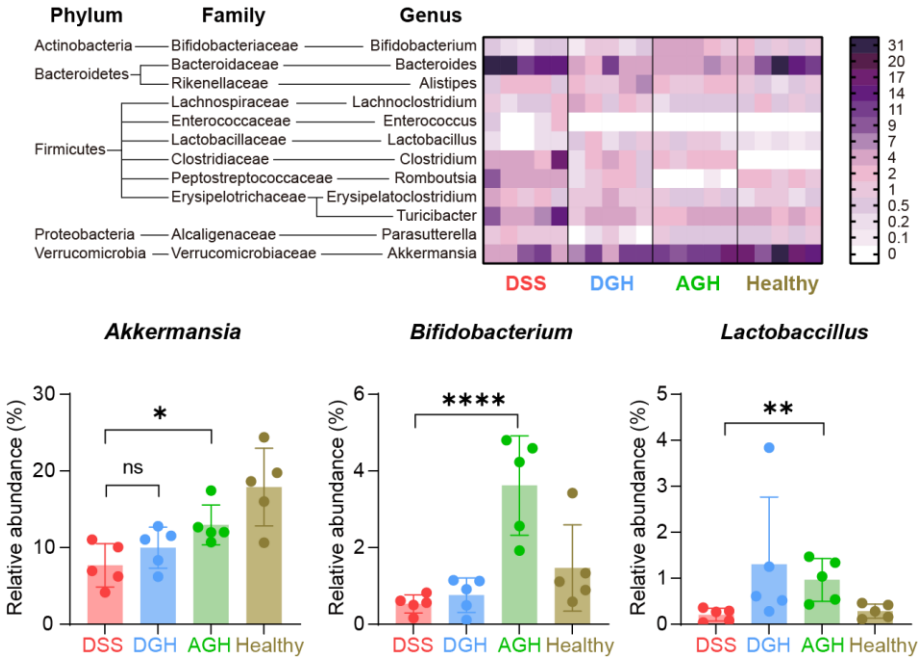

Figure 3-20 Taxonomy relative abundance heatmap shows genus-level taxa (rows) for each mouse (columns). Relative abundance increases are observed for Akkermansia, Bifidobacterium, and Lactobacillus.

Specifically, Akkermansia contributes to the thickness of the mucin layer, indicating a protective role in intestinal barrier intactness and function[30]. The beneficial role of Bifidobacterium and Lactobacillus, as probiotics, in ulcerative colitis in both animal models and patients has been widely reported[31]. Additionally, we found that the abundance of other gut microbes, such as Bacteroides and Romboutsia, were also significantly modulated by the granular system; these findings require further systematic investigation given the limited studies in the literature (Figure 3-21).

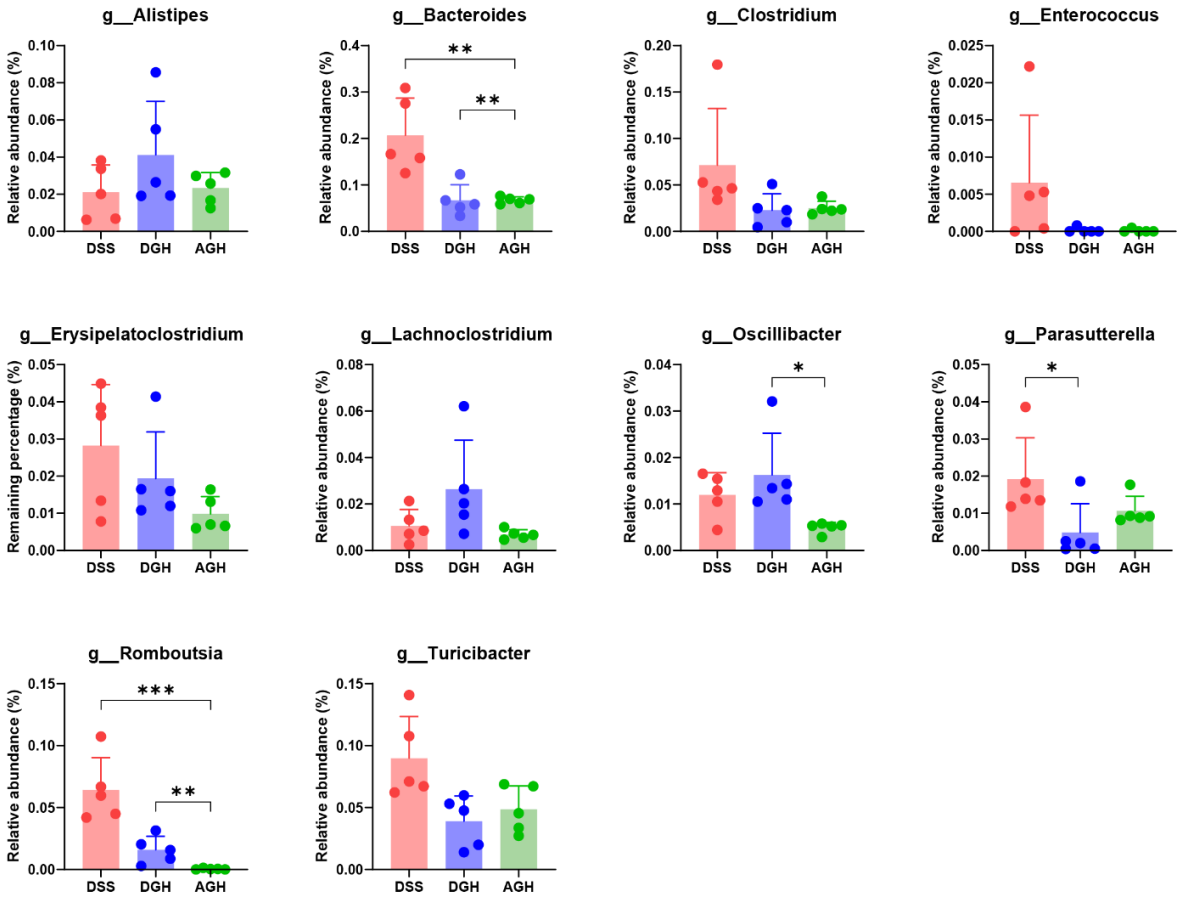

Figure 3-21 Aspirin-modified granule-releasing hydrogel system modulates the relative abundance of a different genus of bacteria in gut microbiota. DSS: mice with DSS-induced colitis, no treatment. DGH: mice with DSS-induced colitis, treated with unmodified dynamic granule-releasing hydrogels. AGH: mice with DSS-induced colitis, treated with aspirin-modified granule-releasing hydrogels. Data are presented as mean ± standard error of mean. (n = 5). P values are determined by ordinary one-way ANOVA with Tukey's multiple comparisons test.

Aspirin is known to cause mucosal ulceration and other potential issues in the gut, especially when there is inflammation. However, in our design, aspirin is not in its free molecular form. Its therapeutic effects and toxicity are largely limited when it is conjugated with the proposed granular system[32]. We report that free aspirin at the same dose as on the conjugated granules, or even at 5 times the dose, did not have any significant effect on DSS-induced colitis symptoms (Figure 3-22).

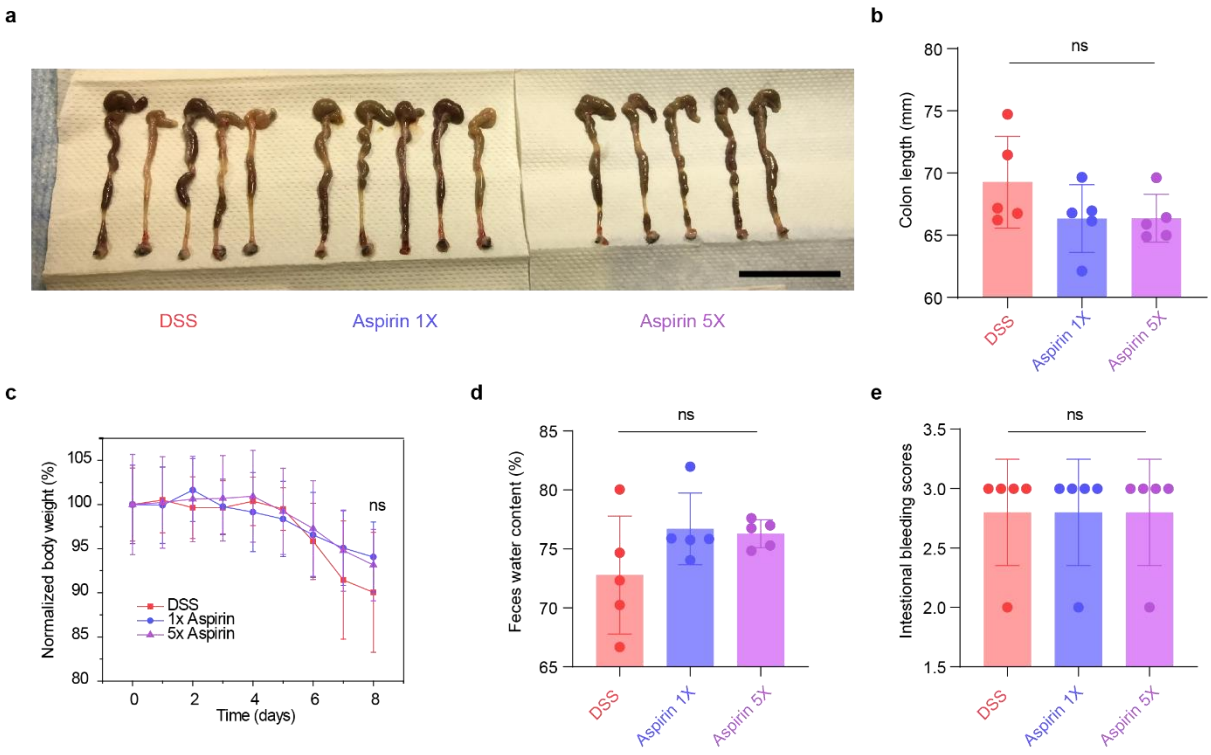

Figure 3-22 Aspirin itself cannot alleviate the ulcerative colitis symptoms. (a) Photo images of the colons harvested from the DSS-induced colitis mice with and without aspirin drug treatment. (b) Statistical analysis of the colon length shows that there was no significant difference between the DSS group and aspirin groups. Scale bar 5 cm. (c) Daily bodyweight changes for 8 days show no significant difference between the control group and the aspirin drug group. (d) Aspirin treatment did not change fecal water content in ulcerative colitis. (e) Aspirin treatment cannot alleviate the intestinal bleeding scores in ulcerative colitis. DSS: mice with DSS-induced colitis, no treatment. 1X Aspirin: mice with DSS-induced colitis, treated with 0.04mg/kg aspirin, which is equal to the dose of conjugated aspirin on starch/chitosan granules. 5X Aspirin: mice with DSS-induced colitis, treated with 0.2mg/kg aspirin. Data are presented as mean ± standard error of mean. (n = 5). P values are determined by ordinary one-way ANOVA with Tukey's multiple comparisons test.

Compared with clinical used drug against conventional IBD, 5-aminosalicylic acid, aspirin-modified granule-releasing hydrogel (AGH) also shows the better therapeutic effect (Figure 3-23).

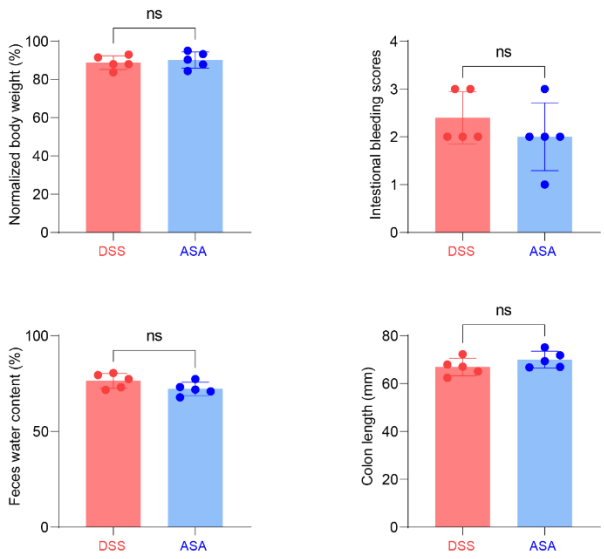

Figure 3-23 5-aminosalicylic acid shows limited therapeutic effect in treating ulcerative colitis symptoms when applied orally. Statistical analysis of the bodyweight changes, intestinal bleeding score, colon length, and fecal water content shows that the 5-aminosalicylic acid treatment has limited therapeutic effect in treating ulcerative colitis. DSS: DSS: mice with DSS-induced colitis, no treatment. ASA: mice with DSS-induced colitis, treated with 5-aminosalicylic acid. Data are presented as mean ± standard error of mean. (n = 5). P values are determined by t-test, two tailed.

Traditional adhesion method based on catechol also shows the trend in alleviating the adverse colitis symptom (Figure 3-24). However, the curing conditions for catechol-based adhesives often require oxidants and elevated pH, which might undermine the biocompatibility of the materials in some biomedical applications[33]. Thus, aspirin modification in our system, allowing for a more dynamic and less invasive interaction with cellular environments, leads to a more effective therapeutic effect.

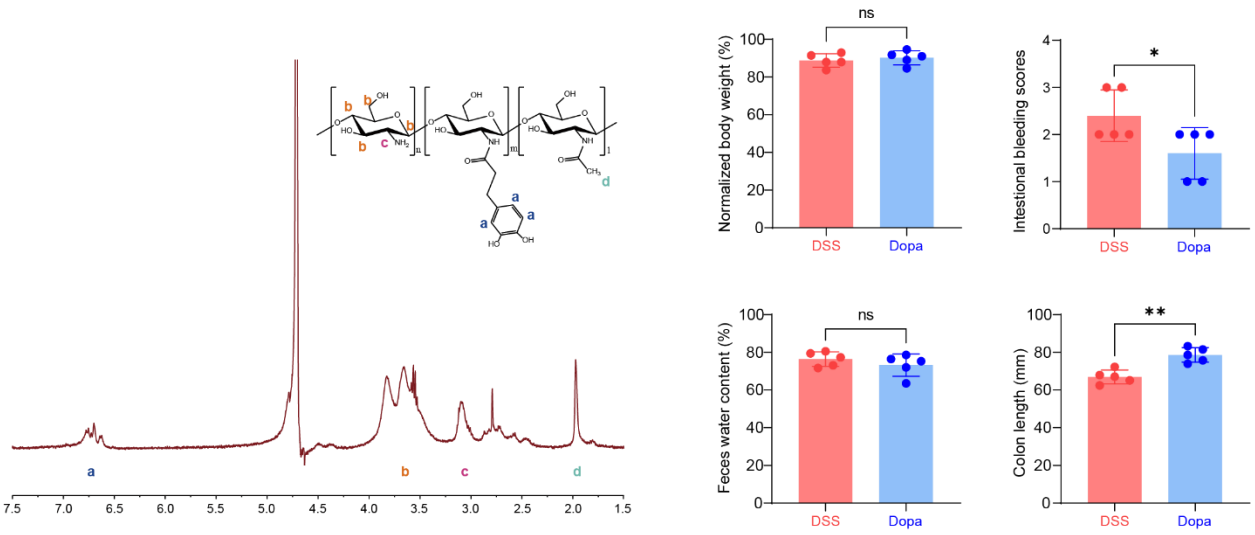

Figure 3-24 Dopa-modified granule-releasing hydrogel shows limited therapeutic effect in treating ulcerative colitis symptoms. (a) NMR analysis result confirms the successful grafting of 3,4-dihydroxyhydrocinnamic acid (Dopa) onto the backbone of chitosan with a substitution percentage of 21.81%. The substitution percentage is calculated based on the relative peak areas of niacin (3H, aromatic ring, * 6.5-7.0 ppm, D2O, region a) and chitosan (3H, -COCH3, * 1.95 ppm, D2O, region d). (b) Statistical analysis of the bodyweight changes, intestinal bleeding score, colon length, and fecal water content shows that the Dopa treatment has limited therapeutic effect in treating ulcerative colitis. DSS: DSS: mice with DSS-induced colitis, no treatment. Dopa: mice with DSS-induced colitis, treated with Dopa-modified granule-releasing hydrogels. Data are presented as mean ± standard error of mean. (n = 5). P values are determined by t-test, two tailed.

Furthermore, it is worth noting that the evolving gelatin hydrogel alone does not exhibit a therapeutic impact in the treatment of ulcerative colitis (Figure 3-25). This observation implies that its primary role is facilitative, specifically assisting in the encapsulation and transport of granules. The results provide insights into how the biointerface should be designed in conjunction with the biomaterials to achieve the best therapeutic effect.

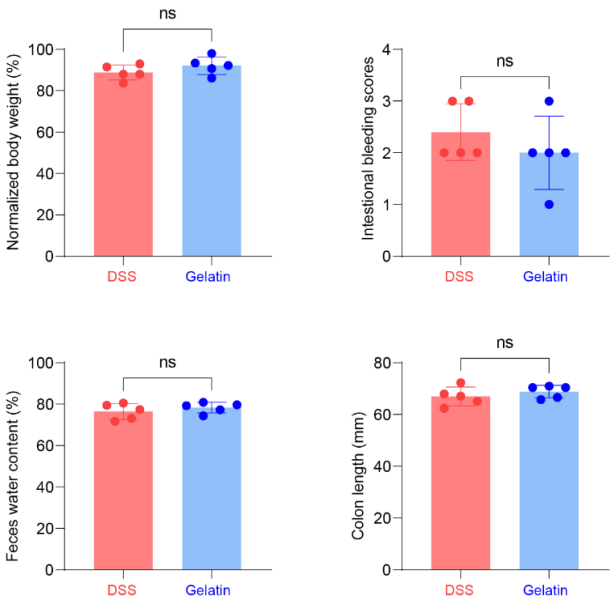

Figure 3-25 Pure gelatin hydrogel shows limited therapeutic effect in treating ulcerative colitis symptoms. Statistical analysis of the bodyweight changes, intestinal bleeding score, colon length, and fecal water content shows that the pure gelatin hydrogel treatment has limited therapeutic effect in treating ulcerative colitis. DSS: DSS: mice with DSS-induced colitis, no treatment. Gelatin: mice with DSS-induced colitis, treated with pure gelatin hydrogels. Data are presented as mean ± standard error of mean. (n = 5). P values are determined by t-test, two tailed.

Further fluorescent imaging also confirms that the hydrogel matrix slows down the retention dynamics of granular composites in the gastrointestinal tract (Figure 3-26).

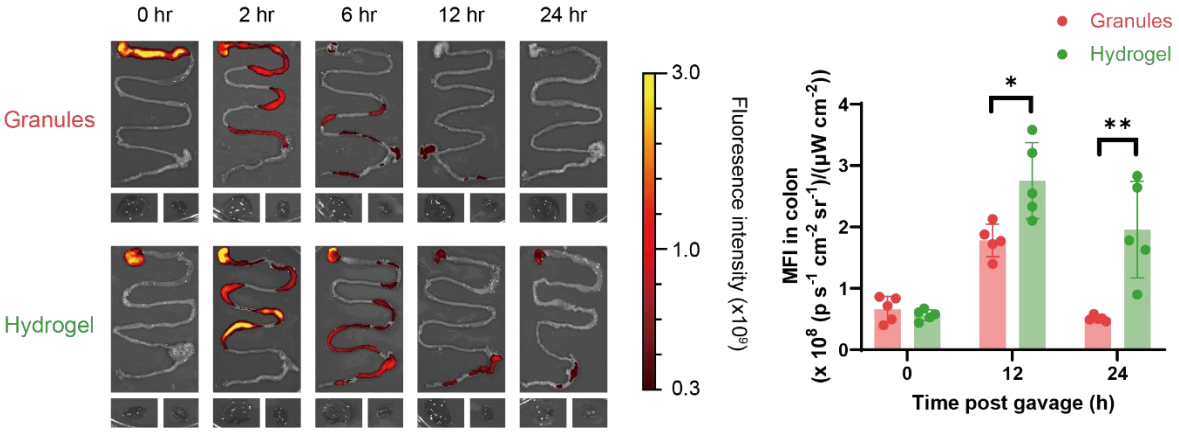

Figure 3-26 Hydrogel matrix inclusion enhances the gastrointestinal tract retention of granular composite. Ex-vivo fluorescence images of the major organs, including the liver, kidney, and gastrointestinal (GI) tract of mice, were collected at different time points after oral administration to visualize the position of granular composites. Data are presented as mean ± standard error of mean. (n = 5). P values are determined by paired t-test, two tailed.

In summary, the evolving hydrogel system encapsulating chemically modified starch/chitosan granules suggested potential therapeutic effects on the management of acute rodent colitis symptoms.

3.2.4 Therapeutic effect in wound healing

Evolving biointerfaces for therapeutic intervention can also be achieved on damaged skin epithelium. Skin wound healing involves migration, proliferation, and differentiation of epithelial cells - behavior which may be regulated according to the porosity and degradation rate of substrate materials[34]. In a skin wound closure model (Figure 3-27), the granule-releasing hydrogels with viscoelastic properties conformed to the irregular skin wound bed and established the initial biointerface.

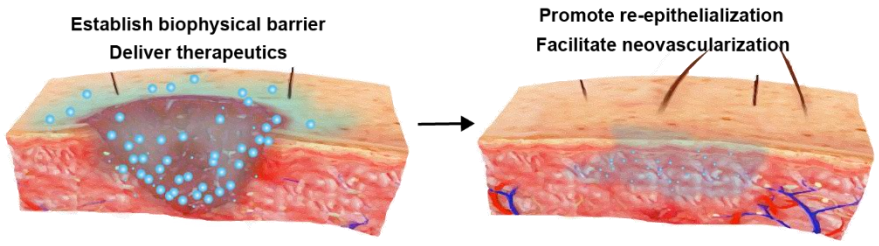

Figure 3-27 Schematic shows that granule-releasing hydrogel therapy accelerates wound healing on mouse dorsal skin.

The aspirin-modified granule inside the matrix was slowly released over time, and a granular biointerface was built up on the skin wound. The released granules had a high affinity with the skin wound bed, consistent with the ex vivo flow adhesion/affinity test. We monitored the wound over a 7-day period and observed wound closure in aspirin-modified granule-releasing hydrogel (AGH)-treated mice (Figure 3-28).

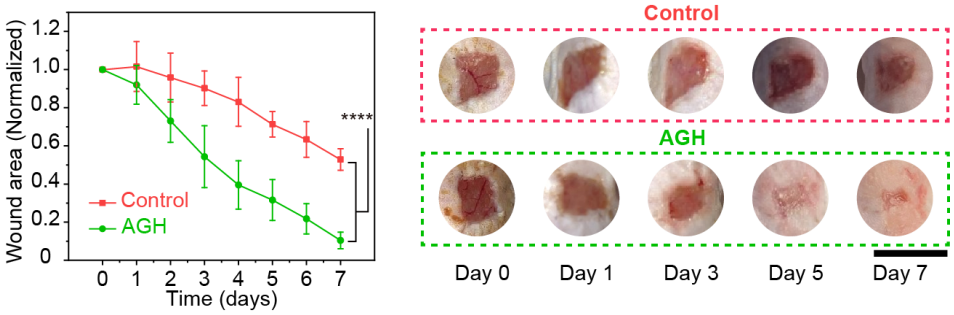

Figure 3-28 Remaining wound areas were monitored for 7 days. On day 7, the wound area of the AGH group was significantly smaller compared with control group, indicating that the AGH accelerates the recovery process of dorsal skin wounds. (d) Representative images of dorsal skin wounds at different time points after AGH treatment. Scale bar, 1 cm.

As we evaluated the monolithic-to-focal biointerface for ulcerative colitis, we also meticulously examined if the pharmaceutical format of the biomaterials significantly influences the composition

of the granule-releasing hydrogel, which facilitates the wound healing process. Here we show the non-releasing hydrogel (PVA) and non-granule-releasing hydrogel (NGH) treated mice also showed the ability to promote the wound healing (Figure 3-29). However, the therapeutic effect of the PVA and NGH group is weaker compared with AGH group, highlighting the importance of the granular-releasing process and focal biointerfaces. DGH-treated mice also showed improved wound healing compared with the control group, but the therapeutic effect was not as good as in the AGH-treated group. The difference in therapeutic effect may be due to the higher biological affinity of the surface-modified starch/chitosan granules.

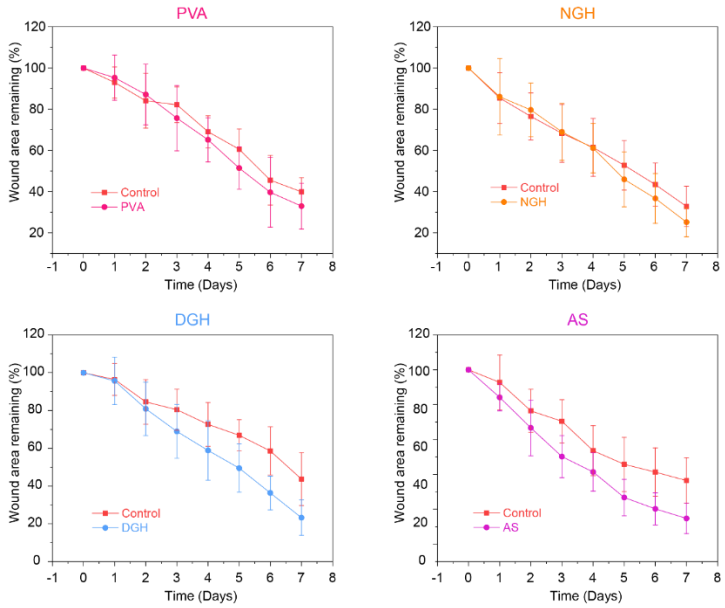

Figure 3-29 PVA, NGH, DGH, and AS groups show therapeutic effects in wound healing, although not as good as the AGH group. PVA: mice treated with aspirin-modified starch/chitosan granules inside polyvinyl alcohol matrix. NGH: mice treated with non-granule-releasing hydrogels. The composition of NGH is the same as AGH, but the granule-releasing structure is destroyed through the gelatinization process. DGH: Skin wound treated with unmodified dynamic granule-releasing hydrogel. AS: mice treated with aspirin-modified starch/chitosan granules without hydrogel matrix. Data are presented as mean ± standard error of mean. (n = 5). P values are determined by paired t-test, two tailed.

Aspirin-modified granules alone (i.e., without any hydrogel matrix, AS) also helped skin wound healing. However, their therapeutic effect is less compared to AGH. This is partially attributed to the initial monolithic matrix in AGH, which ensures sustained granular release and enhances the manipulation of freestanding granules, preventing material loss during treatment (Figure 3-30). Macroscopic handling ability is also crucial when designing biomaterials for regenerative medicine. A sustained-release format will help deliver the therapeutic target to injured sites, especially during the intense movements of mice.

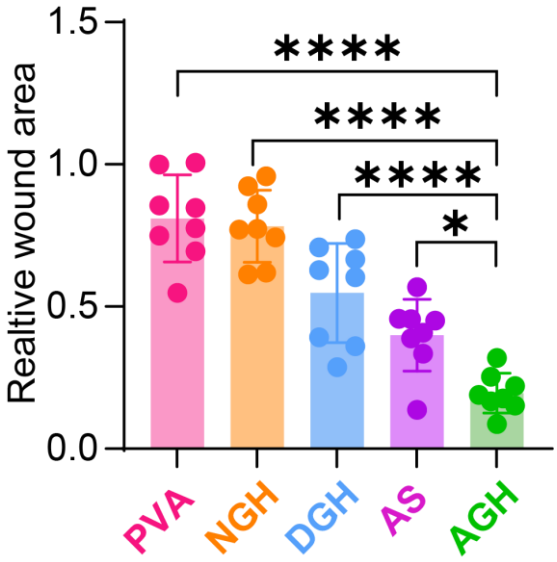

Figure 3-30 Comparison of remaining wound areas in the PVA group, NGH group, DGH group, AS group, and AGH group indicates that the distributed granular interface and aspirin modification promotes the therapeutic effect of the granule-releasing hydrogels.

Compared to the Tegaderm Ag Alginate Silver Dressing from 3M company, the aspirin-modified granule-releasing hydrogel (AGH) appears to exhibit a potentially enhanced therapeutic effect in wound healing (Figure 3-31).

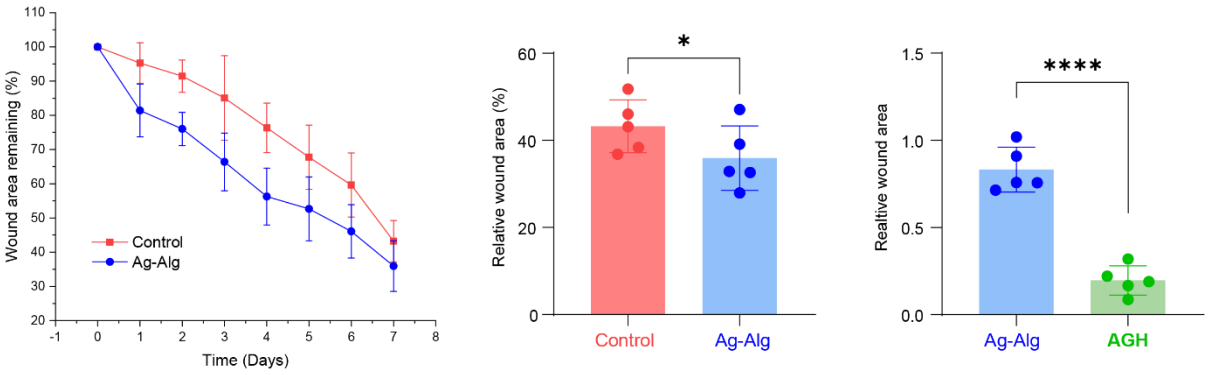

Figure 3-31 Modified granule-releasing hydrogels show better therapeutic effects than commercially available products in promoting skin wound healing. AGH: mice treated with aspirin-modified starch/chitosan granule-releasing hydrogel. Ag-Alg: mice treated with Tegaderm Ag Alginate Silver Dressing from 3M company. Data are presented as mean ± standard error of mean. (n = 5). P values are determined by paired t-test, two tailed.

H&E staining revealed that AGH treatment accelerated post-injury re-epithelialization, reduced inflammatory wound bed size, and promoted dermal collagen remodeling (Figure 3-32).

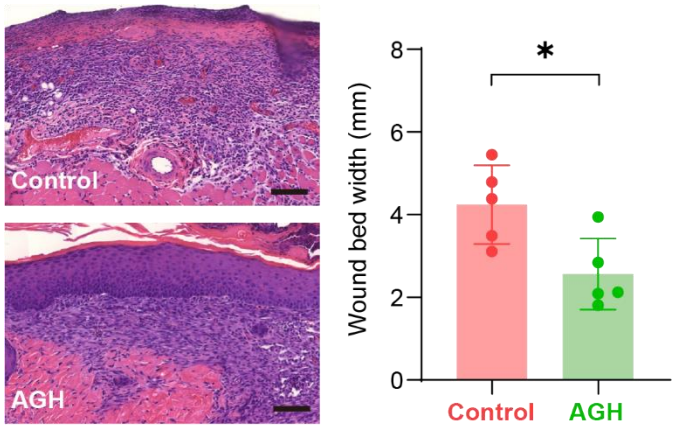

Figure 3-32 Representative H&E staining images showing re-epithelialized skin wounds after AGH treatment. Scale bar, 100 μm. AGH treatment significantly narrowed the width of the dorsal skin wound bed (analysis of H&E-stained sections).

Additionally, the formation of new blood vessels, which supply the tissue with blood and nutrients, is crucial for proper wound healing. Neovascularization was visualized using CD31

immunohistology staining. A significantly higher number of new vessels was observed in the hydrogel-treated groups compared with the untreated group after 7 days (Figure 3-33).

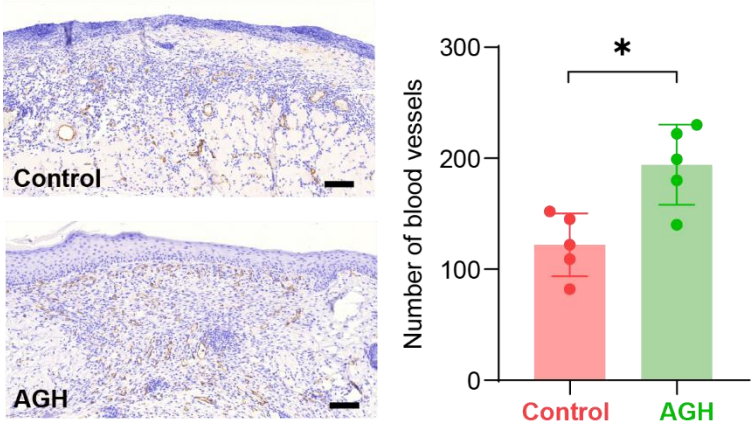

Figure 3-33 CD31 histochemical staining in wound tissue sections after different treatments show microvessel distribution in the wound area. Scale bar, 100 μm. (i) Quantification analysis of blood vessels in the wound area shows that AGH promotes tissue neovascularization.

Together, these pre-clinical studies suggest that granule-releasing hydrogels (with and without aspirin modifications) have potential in reducing inflammation and accelerating neovascularization, thereby might contribute to faster wound closure and recovery.

3.3 Conclusion

In this chapter, we demonstrate that granule-releasing hydrogels hold promise as an evolving biointerface platform, with potential applications in treating inflammatory bowel disease and facilitating tissue regeneration. Leveraging the emerging monolithic-to-focal biointerface mechanism, these hydrogels merge the benefits of monolithic biointerfaces—specifically their macroscopic handling capabilities—with those of focal biointerfaces, which provide increased interstitial space for cellular signal transduction. Moreover, the novel adhesion methods introduced here promote dynamic adhesion in in vivo environments, significantly amplifying the therapeutic

effects for both ulcerative colitis and wound healing. These methods also aid in modulating gut microbiota towards a healthier state. But as always, there is still a long way to go to fully cure the ulcerative colitis in the clinical practices.

Non est in medico semper relevetur aeger

-Hippocrates

It's worth noting that the majority of components in the granule-releasing hydrogel, such as starch, chitosan, and gelatin, are food-grade biopolymers. This positions them well for clinical translation, offering a more cost-effective and sustainable solution to clinical challenges in hospitals. Overall, our work introduces a design paradigm that integrates the strengths and application areas of both monolithic and focal biointerface systems.

3.4 Experimental Methods

Synthesis of granule-releasing composite. To prepare the dynamic granule-releasing hydrogels (DGH), the starch (16.5%), chitosan (0.83%), and acetate acid (0.83%) were added to sterilized water/phosphate-buffered saline (PBS). The suspension was stirred for 24 hours at 45°C with humidity control to hydrate the starch granules and form the starch/chitosan granules. The gelatin powder (14.18 wt%) was then added to the mixture by vigorously stirring. After 12 hours, the mixture was transferred into acrylic molds with the desired shapes and sealed with acrylic cover slides for gelation at 4°C. The dynamic granule-releasing hydrogel composite was ready after 1 hour. Aspirin-modified granule-releasing hydrogels (AGH) are prepared similarly to DGH, but the chitosan is changed to aspirin-modified chitosan. Non-granule-releasing hydrogels (NGH) are

prepared by heating up the AGH over 80°C for 2 hours to destroy the starch granular shapes. The chemical composition and weight percentage of each ingredient in NGH are the same as those in the AGH. To synthesize the aspirin-modified granules with polyvinyl alcohol matrix (PVA), the aspirin-modified starch/chitosan granules was added into 10% polyvinyl alcohol solution by vigorously stirring.The mixture was poured into an acrylate mould, followed by freezing at −20 °C for 12 h and thawing at 25 °C for 2 h to form aspirin-modified-granules-PVA hydrogel (PVA). To fabricate the hydrogel composite in a microneedle format, Sylgard 184 silane elastomer and curing agent were combined at a 10:1 ratio and poured into a container with a fixed 3D-printed microneedle model inside. After curing, the container was inverted to produce a polydimethylsiloxane (PDMS) mold. The hydrogel precursor was then poured into the PDMS mold and allowed gelation at 4°C. The microneedle aerogel format was fabricated by freezing the hydrogel microneedles followed by a freeze-drying process. For fabricating the hydrogel bandage, the molded hydrogel was used to replace the cotton foam in a commercial bandage (Band-Aid).

Transwell assay. Transwell assay was used to prove that focal biointerface allows fast transport space for signaling molecules. Rhodamine B was used as an artificial small molecule and transwell (0.4 μm pore size, Corning Company) was used in the experiments. In a typical experiment, 0.5 mL of hydrogel precursor of AGH or polyacrylic acid hydrogel was seeded into the upper chamber. After the gelation of the hydrogel, 0.5 ml of 0.1 mol/L rhodamine B solution was added to the top of the hydrogel. After incubation at body temperature for 12 hours, the solution from the lower chamber was sampled for reading by a plate reader (Synergy Neo HST Plate Reader).

Synthesis of Starch-APTS, Chitosan-ICG, and Chitosan-FTIC Conjugate. For fluorescent imaging, starch-APTS, chitosan-ICG, and chitosan-FTIC were synthesized. A previously described method[35] is used to prepare starch-APTS. In a typical experiment, 15mg of starch

granules were dispersed in 25 µL of 10 mM APTS solution with 15% acetic acid, followed by the addition of 25 µL of 1 M sodium borohydride. The reaction was conducted at 35 °C for 15–18 h. Afterward, the starch-APTS was washed five times with 10 ml of distilled water and kept at 4 °C for future use. Chitosan-ICG and chitosan-FITC were synthesized by dissolving 10 mg acidic-form chitosan in 2 ml water and then adding 0.5 mol of dye for overnight stirring at room temperature. The dialysis process (Slide-A-Lyzer™ Dialysis Cassettes, 10K MWCO) was performed against distilled water for 3 days. After lyophilization, the conjugates are stored at 4°C for future use.

Synthesis of Chitosan-aspirin Conjugate. Chitosan-aspirin conjugate was synthesized with carbodiimide chemistry. In a typical chemical reaction with the aspirin molecule, chitosan (0.25g) was fully dissolved into 25 ml water by adding 1M HCl. The colloid was then vigorously stirred overnight. Then, the pH of the mixture was adjusted to 4.5 by adding 1M NaOH. Aspirin (2mmol) was then added to the mixture while vigorously stirring. EDC solution was prepared by dissolving 10 mmol EDC in 12 mL of a 1:1 v/v% solution of ethanol and water, and the solution was added dropwise into the chitosan and aspirin mixture solution. The reaction is conducted at room temperature for 12 hours. After the evaporation of ethanol, the final product was purified by dialysis (Slide-A-Lyzer™ Dialysis Cassettes, 10K MWCO) against the acidified water (pH 3.5) for 48 hours. Afterward, the product was dialyzed against deionized water for 3 days. After lyophilization, the product was stored at 4°C for future use. The synthesis of the chitosan-aspirin conjugate was confirmed by using 1H NMR (Bruker, 400MHz) and FITC (Thermo NEXUS 670 Near-, Far-, and Mid-FTIR with ATR Accessory). The degree of aspirin conjugation was calculated by comparing the relative peak area of aspirin (4H, aromatic ring proton, δ 6-8, D_2O) and an acetyl group (3H, -$COCH_3$, δ 1.95, D_2O) on the backbone of chitosan.

IVIS Imaging. IVIS (PerkinElmer IVIS Spectrum) was used to locate the location and amount of granular composite inside the GI tract to test the retention ability. The granule-releasing hydrogels were synthesized as described above and the chitosan was fluorescent ICG fluorescent dye. The granule-releasing hydrogels and suspension was administered orally to the colitis mice (3% DSS water for six days) and healthy mice with a dose of 10mg/kg. Following different time points (0h, 2h, 6h, 12h, 24h), mice were euthanized, and the GI tract (including stomach, small intestine, colon), liver, and kidney were harvested. Fluorescence intensities from different groups were measured with the filter of emission peak of 745 nm and absorption peak at 840nm and exposure time of 3 s.

DSS-Induced Colitis Treatment. Eight-week-old male C57BL/6 mice were housed in groups of five mice per cage and acclimatized for 7 days before inclusion in the investigation. Mice were supplied with 2-3% Dextran sulfate sodium salt (DSS) (Mw 40 kDa; Thermo Scientific) in their drinking water for 6-10 days. The control group (healthy mice) received normal tap water. Afterward, different materials were administrated orally to the mice on predetermined days with a dose of 10mg/kg. Before oral administration, the hydrogel is sliced into small pieces using a scalpel and then loaded into a 16-gauge gavage needle. For the experiments of PVA, DGH, AS, AGH group, equally amount of the granules was applied. 5-aminosalicylic acid was suspended in a viscous carboxymethyl cellulose solution with a concentration of 10 mg/ml. During the experiment, changes in body weight were recorded daily, and feces were collected daily to assess bleeding. The mice were euthanized on the last day of the experiment, and their entire colon was harvested. After a gentle wash with physiological saline, the colon length was measured. The histological evaluation of the colon was also performed. On the last day, feces were also collected

for water content analysis and microbiome analysis. In vivo experiments related to butyric acid and nicotinic acid conjugations are performed in a similar approach.

In Vivo Intestinal Permeability Assay. FITC-dextran was used as an in-vivo assay to test intestinal permeability as previously described[25]. In a typical experiment, on the sacrifice day, mice were orally administrated with 0.6 mg g-1 body weight of 4 kDa FITC-dextran (Sigma). Blood was collected after 0hr and 4hr, and the fluorescent intensity of the diluted serum samples was measured on Synergy Neo HST Plate Reader (excitation of 488 nm/emission of 520 nm).

Hemoccult test. Intestinal bleeding symptoms of mice with DSS-induced colitis were tested by the Hemoccult test. On day 7, stools from the mice are collected for the hemoccult test by HemoCue America Beckman Coulter™ Hemoccult™ fecal occult blood slide test system (Fisher Scientific). The intestinal bleeding situation was assigned a score as follows: 0 = the stool was hard and had no blood; 1 = the stool was slightly softer and had a small amount of blood visible using the test card; 2 = the stool was soft and contained significant blood (visible to the naked eye or using the test card); 3 = the stool was watery with little to no defined shape and contained significant blood.

Histology. For tissue histological analysis, Periodic acid–Schiff (PAS), Hematoxylin and eosin (H&E), and CD31 histological tissue sections were prepared by the Human Tissue Resource Center at the University of Chicago. Tissue sections of the proximal and distal colon were prepared and stained with PAS and H&E. Tissue sections of the epidermal skin were prepared and stained with CD31 and H&E. All the tissue histological results are analyzed by the CaseViewer software (3DHISTECH). The colonic histological damage was scored based on the H&E-stained colonic tissue sections: severity of inflammation (0, none; 1, slight; 2, moderate; 3, severe), the extent of injury (0, none; 1, mucosal; 2, mucosal and submucosal; 3, transmural), and crypt damage (0, none;

1, basal one-third damaged; 2, basal two-thirds damaged; 3, only surface epithelium intact; 4, entire crypt and epithelium lost). Scores from all three perspectives were summed, resulting in a total histological scoring range of 0 to 10.

Microbiome analysis. Four groups of mice (C57BL/6) were prepared for microbiome analysis: 1) The first group (Control) was healthy mice; 2) The second group (DSS) was the mice with DSS-induced ulcerative colitis; 3) The third group was the mice with DSS-induced ulcerative colitis and treated with dynamic granule-releasing hydrogel (DGH); 4) The fourth group was the mice with DSS-induced ulcerative colitis and treated with dynamic granule-releasing hydrogel with aspirin modification (AGH). The DGH group and AGH group were orally administrated a daily dose of 10 mg/kg hydrogel composite (with/without aspirin modification) for 7 consecutive days. Feces samples from four different groups were collected and analyzed by the ZymoBIOMICS® Targeted 16S Sequencing Service (Zymo Research, Irvine, CA). DADA2 was used to infer unique amplicon sequence variants from raw reads[36]. Chimeric sequences and potential sequencing errors were removed using the DADA2 pipeline. We used Uclust from Qiime version 1.9.1, a 16S database designed and curated as a reference, for taxonomy assignment. Linear discriminant analysis Effect Size (LEfSe) was used to identify taxonomies with significant abundance among different groups[37]. PCoA plots were performed using internal scripts. Quantitative real-time PCR was used to quantify the absolute abundance and the results were displayed as the number of gene copies. Prior to publication, 16S sequencing raw data will be deposited at our lab website.

Skin Wound Model. C57BL/6 mice (8-10 weeks) mice were anesthetized with isoflurane and then two partial-thickness wounds with 5 mm x 5 mm were made on the dorsal skin of the mice. Full-thickness wounds on the dorsum of the mice were created by using 6 mm biopsy punches. After that, one side of wound was applied with hydrogel and the other side was treated with PBS

buffer. Then wounds are covered by band-aid bandage. The hydrogel is applied every day for seven consecutive days and the remaining wound area from both sides are recorded. On day 7, the mice were sacrificed, and the wound skin tissue was harvested for histological analysis. For the experiments of PVA, DGH, AS, AGH group, equally amount of the granules was applied. Wound area ($Area_{Day\,x}$) was determined using ImageJ software by a blinded observer. Wound area (normalized) for each wound is calculated by:

$$Wound\ area\ (Normalized) = \frac{Area_{Day\,x}}{Area_{Day\,0}} \times 100\%$$

Relative wound area is used to compare the therapeutic effects of treatment between the groups:

$$Relative\ wound\ area = \frac{Area_{experiment}}{Area_{control}} \times 100\%$$

3.5 References

1 Takahashi, T., Donahue, R. P., Nordberg, R. C., Hu, J. C., Currall, S. C. & Athanasiou, K. A. Commercialization of regenerative-medicine therapies. *Nature Reviews Bioengineering*, doi:10.1038/s44222-023-00095-9 (2023).

2 Hussey, G. S., Dziki, J. L. & Badylak, S. F. Extracellular matrix-based materials for regenerative medicine. *Nat Rev Mater* **3**, 159-173, doi:10.1038/s41578-018-0023-x (2018).

3 Van Gelder, R. N., Chiang, M. F., Dyer, M. A., Greenwell, T. N., Levin, L. A., Wong, R. O. & Svendsen, C. N. Regenerative and restorative medicine for eye disease (Aug, 10.1038/s41591-022-01996-9, 2022). *Nat Med* **28**, 2218-2218, doi:10.1038/s41591-022-01996-9 (2022).

4 Sadtler, K., Singh, A., Wolf, M. T., Wang, X. K., Pardoll, D. M. & Elisseeff, J. H. Design, clinical translation and immunological response of biomaterials in regenerative medicine. *Nat Rev Mater* **1**, doi:10.1038/natrevmats.2016.40 (2016).

5 Griffin, D. R., Archang, M. M., Kuan, C. H., Weaver, W. M., Weinstein, J. S., Feng, A. C., Ruccia, A., Sideris, E., Ragkousis, V., Koh, J., Plikus, M. V., Di Carlo, D., Segura, T. & Scumpia, P. O. Activating an adaptive immune response from a hydrogel scaffold imparts regenerative wound healing. *Nat Mater* **20**, 560-569, doi:10.1038/s41563-020-00844-w (2021).

6 Guo, B. L., Dong, R. N., Bang, Y. P. & Li, M. Haemostatic materials for wound healing applications. *Nat Rev Chem* **5**, 773-791, doi:10.1038/s41570-021-00323-z (2021).

7 Armstrong, J. P. K., Keane, T. J., Roques, A. C., Patrick, P. S., Mooney, C. M., Kuan, W. L., Pisupati, V., Oreffo, R. O. C., Stuckey, D. J., Watt, F. M., Forbes, S. J., Barker, R. A. & Stevens, M. M. A blueprint for translational regenerative medicine. *Sci Transl Med* **12**, doi:10.1126/scitranslmed.aaz2253 (2020).

8 Khodabukus, A., Guyer, T., Moore, A. C., Stevens, M. M., Guldberg, R. E. & Bursac, N. Translating musculoskeletal bioengineering into tissue regeneration therapies. *Sci Transl Med* **14**, doi:10.1126/scitranslmed.abn9074 (2022).

9 Aguado, B. A., Grim, J. C., Rosales, A. M., Watson-Capps, J. J. & Anseth, K. S. Engineering precision biomaterials for personalized medicine. *Sci Transl Med* **10**, doi:10.1126/scitranslmed.aam8645 (2018).

10 Kobayashi, T., Siegmund, B., Le Berre, C., Wei, S. C., Ferrante, M., Shen, B., Bernstein, C. N., Danese, S., Peyrin-Biroulet, L. & Hibi, T. Ulcerative colitis. *Nature Reviews Disease Primers* **6**, 74, doi:10.1038/s41572-020-0205-x (2020).

11 Turner, J. R. Intestinal mucosal barrier function in health and disease. *Nat Rev Immunol* **9**, 799-809, doi:10.1038/nri2653 (2009).

12 Halfvarson, J., Brislawn, C. J., Lamendella, R., Vazquez-Baeza, Y., Walters, W. A., Bramer, L. M., D'Amato, M., Bonfiglio, F., McDonald, D., Gonzalez, A., McClure, E. E., Dunklebarger, M. F., Knight, R. & Jansson, J. K. Dynamics of the human gut microbiome in inflammatory bowel disease. *Nat Microbiol* **2**, doi:10.1038/nmicrobiol.2017.4 (2017).

13 Round, J. L. & Mazmanian, S. K. The gut microbiota shapes intestinal immune responses during health and disease (vol 9, pg 313, 2009). *Nat Rev Immunol* **9**, 600-600, doi:10.1038/nri2614 (2009).

14 Lee, Y., Sugihara, K., Gillilland, M. G., Jon, S., Kamada, N. & Moon, J. J. Hyaluronic acid-bilirubin nanomedicine for targeted modulation of dysregulated intestinal barrier, microbiome and immune responses in colitis. *Nat Mater* **19**, 118-126, doi:10.1038/s41563-019-0462-9 (2020).

15 Zhang, S. F., Ermann, J., Succi, M. D., Zhou, A., Hamilton, M. J., Cao, B. N., Korzenik, J. R., Glickman, J. N., Vemula, P. K., Glimcher, L. H., Traverso, G., Langer, R. & Karp, J. M. An inflammation-targeting hydrogel for local drug delivery in inflammatory bowel disease. *Sci Transl Med* **7**, doi:10.1126/scitranslmed.aaa5657 (2015).

16 Lautenschlager, C., Schmidt, C., Fischer, D. & Stallmach, A. Drug delivery strategies in the therapy of inflammatory bowel disease. *Adv Drug Deliver Rev* **71**, 58-76, doi:10.1016/j.addr.2013.10.001 (2014).

17 Wilson, D. S., Dalmasso, G., Wang, L. X., Sitaraman, S. V., Merlin, D. & Murthy, N. Orally delivered thioketal nanoparticles loaded with TNF-alpha-siRNA target inflammation and inhibit gene expression in the intestines. *Nat Mater* **9**, 923-928, doi:10.1038/Nmat2859 (2010).

18 Stallmach, A., Hagel, S. & Bruns, T. Adverse effects of biologics used for treating IBD. *Best Pract Res Cl Ga* **24**, 167-182, doi:10.1016/j.bpg.2010.01.002 (2010).

19 Falanga, V., Isseroff, R. R., Soulika, A. M., Romanelli, M., Margolis, D., Kapp, S., Granick, M. & Harding, K. Chronic wounds. *Nature Reviews Disease Primers* **8**, 50, doi:10.1038/s41572-022-00377-3 (2022).

20 Matoori, S., Veves, A. & Mooney, D. J. Advanced bandages for diabetic wound healing. *Sci Transl Med* **13**, doi:10.1126/scitranslmed.abe4839 (2021).

21 Freedman, B. R., Hwang, C., Talbot, S., Hibler, B., Matoori, S. & Mooney, D. J. Breakthrough treatments for accelerated wound healing. *Sci Adv* **9**, doi:10.1126/sciadv.ade7007 (2023).
22 Cordeiro, J. V. & Jacinto, A. The role of transcription-independent damage signals in the initiation of epithelial wound healing. *Nat Rev Mol Cell Bio* **14**, 249-262, doi:10.1038/nrm3541 (2013).
23 Jarbrink, K., Ni, G., Sonnergren, H., Schmidtchen, A., Pang, C., Bajpai, R. & Car, J. The humanistic and economic burden of chronic wounds: a protocol for a systematic review. *Syst Rev-London* **6**, doi:10.1186/s13643-016-0400-8 (2017).
24 Jeong, D. Y., Kim, S., Son, M. J., Son, C. Y., Kim, J. Y., Kronbichler, A., Lee, K. H. & Shin, J. I. Induction and maintenance treatment of inflammatory bowel disease: A comprehensive review. *Autoimmun Rev* **18**, 439-454, doi:10.1016/j.autrev.2019.03.002 (2019).
25 Chassaing, B., Aitken, J. D., Malleshappa, M. & Vijay-Kumar, M. J. C. p. i. i. Dextran sulfate sodium (DSS)-induced colitis in mice. **104**, 15.25. 11-15.25. 14 (2014).
26 Cao, Y. P. & Mezzenga, R. Design principles of food gels. *Nat Food* **1**, 106-118, doi:10.1038/s43016-019-0009-x (2020).
27 Ni, J., Wu, G. D., Albenberg, L., Tomov, V. T. J. N. r. G. & hepatology. Gut microbiota and IBD: causation or correlation? **14**, 573-584 (2017).
28 Round, J. L. & Mazmanian, S. K. The gut microbiota shapes intestinal immune responses during health and disease. *Nat Rev Immunol* **9**, 313-323, doi:10.1038/nri2515 (2009).
29 Fabia, R., Arrajab, A., Johansson, M. L., Andersson, R., Willen, R., Jeppsson, B., Molin, G. & Bengmark, S. Impairment of Bacterial-Flora in Human Ulcerative-Colitis and Experimental Colitis in the Rat. *Digestion* **54**, 248-255, doi:Doi 10.1159/000201045 (1993).
30 Zhang, Z., Wu, X. Y., Cao, S. Y., Cromie, M., Shen, Y. H., Feng, Y. M., Yang, H. & Li, L. Chlorogenic Acid Ameliorates Experimental Colitis by Promoting Growth of Akkermansia in Mice. *Nutrients* **9**, doi:10.3390/nu9070677 (2017).
31 Osman, N., Adawi, D., Ahrne, S., Jeppsson, B. & Molin, G. Modulation of the effect of dextran sulfate sodium-induced acute colitis by the administration of different probiotic strains of Lactobacillus and Bifidobacterium. *Digest Dis Sci* **49**, 320-327, doi:Doi 10.1023/B:Ddas.0000017459.59088.43 (2004).
32 Sostres, C., Lanas, A. J. N. r. G. & hepatology. Gastrointestinal effects of aspirin. **8**, 385-394 (2011).
33 Zhang, W., Wang, R. X., Sun, Z. M., Zhu, X. W., Zhao, Q., Zhang, T. F., Cholewinski, A., Yang, F., Zhao, B. X., Pinnaratip, R., Forooshani, P. K. & Lee, B. P. Catechol-functionalized hydrogels: biomimetic design, adhesion mechanism, and biomedical applications. *Chem Soc Rev* **49**, 433-464, doi:10.1039/c9cs00285e (2020).
34 Gurtner, G. C., Werner, S., Barrandon, Y. & Longaker, M. T. J. N. Wound repair and regeneration. **453**, 314-321 (2008).
35 Chen, P., Yu, L., Simon, G. P., Liu, X. X., Dean, K. & Chen, L. Internal structures and phase-transitions of starch granules during gelatinization. *Carbohyd Polym* **83**, 1975-1983, doi:10.1016/j.carbpol.2010.11.001 (2011).
36 Callahan, B. J., McMurdie, P. J., Rosen, M. J., Han, A. W., Johnson, A. J. A. & Holmes, S. P. DADA2: High-resolution sample inference from Illumina amplicon data. *Nat Methods* **13**, 581-583, doi:10.1038/Nmeth.3869 (2016).

37 Segata, N., Izard, J., Waldron, L., Gevers, D., Miropolsky, L., Garrett, W. S. & Huttenhower, C. Metagenomic biomarker discovery and explanation. *Genome Biol* **12**, doi:10.1186/gb-2011-12-6-r60 (2011).

Chapter 4. Living biointerface construction for bioelectronics

4.1 Introduction

Biomaterials that synergistically incorporate biomechanical[1,2], biogenic[3], and bioelectrical[4] dimensions offer the potential to establish life-like, seamless, and multifaceted biointerfaces with tissues. Bioelectronics, in particular, have become indispensable for capturing physiological signals[5], monitoring inflammation as a diagnostic tool[6], and executing biological modulation for targeted treatments[7]. However, the primary challenge with traditional bioelectronics is their integration with biological tissues, which arises from disparities in mechanical, chemical, and biological attributes[8]. The mechanical discrepancies in bioelectronics can lead to interfacial discontinuities, compromising signal fidelity[9]. While hydrogels act as an intermediary layer to bridge the mechanical gap between electronics and biological systems, they may fall short in providing the necessary cellular functions for tissue modulation[10]. Consequently, contemporary bioelectronics, when used to monitor inflammatory conditions, lack the biogenic capacity for concurrent immunoregulation[11]. This limitation restricts the versatility of bioelectronics in addressing the complexities of various diseases. To fully harness the potential of bioelectronics, there is a pressing need to design interfaces with enhanced bioactivity, promoting a more harmonious relationship between tissues and electronic components, and thus expanding their role in tissue monitoring and restoration. Intriguingly, inherent biological systems such as bacteria and mammalian cells naturally exhibit cellular signal generation and transmission, which may be leveraged for inflammation management[12]. However, the integration of these living entities into bioelectronics remains a challenge, mainly due to the absence of precise control mechanisms and a thorough understanding of the dynamics between foreign cells and host diseases.

Here, we introduce the Active Biointegrated Living Electronics (ABLE) platform. The ABLE platform introduces living hydrogel at the tissue-electronics interface to impart essential biogenic properties for skin immunoregulation, while simultaneously addressing biomechanical challenges faced by conventional bioelectronics. The skin commensal bacteria *Staphylococcus epidermidis* from human skin flora was chosen as the living components in biointerfaces, which provides bioelectronics with capabilities to regulate inflammation and promote skin regeneration. The ABLE platform stands out with its multifunctionality arising from synergistic interaction between the biogenic, biomechanical, and bioelectrical realms (Figure 4-1). This platform is characterized by its biocompatibility, ability to conform to biological tissues, and provision of therapeutic benefits. It employs wireless bioelectrical sensing, fortified by a stringent safety control mechanism. Specifically, the biogenic polymers enhance bacterial viability, and the bacteria themselves modulate the skin's immune environment. The bioelectronics within the system facilitate electrical sensing (e-sensing) to gather information from the skin and utilize electrical stimulation (e-stimulation) to manage the biosafety of bacteria, addressing long-standing biohazard concerns of handling synthetic living materials with opportunistic pathogens[13,14]. The living hydrogel plays multiple roles: its encapsulation technique fosters prolonged bacterial storage and viability, its viscoelastic properties ensure stable skin interaction, aid in information collection from the skin, and assist in biohazard management. Lastly, the hydrogel's skin-adhesion property augments long-term data acquisition.

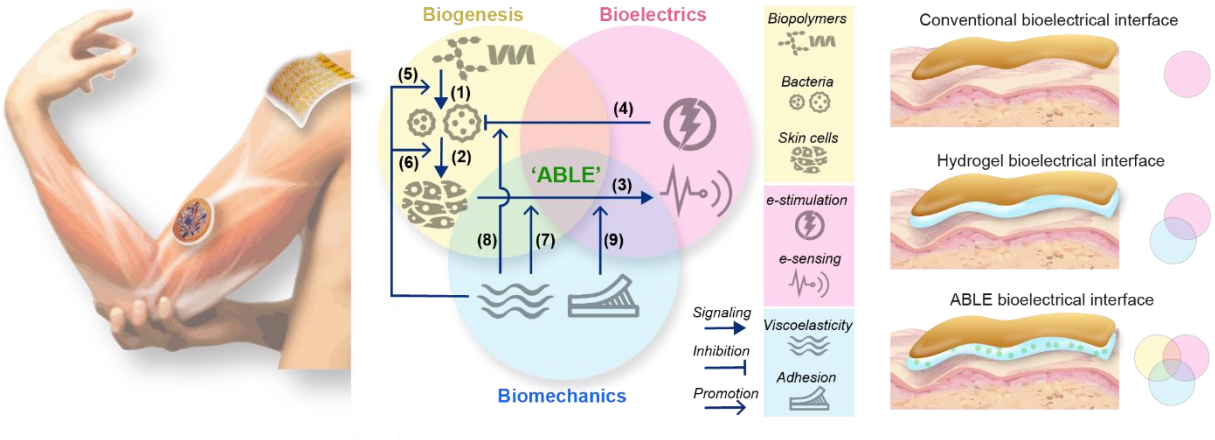

Figure 4-1 Schematic illustrates that living bioelectronics enable information collection, disease diagnosis, and therapy delivery. The interplay across the three key dimensions through bioelectronics, hydrogel, and bacteria is crucial for biointegrated living electronics functionality. *(1) Biopolymer enhances bacterial viability. (2) Bacteria modulate the skin immune environment. (3) Bioelectronics collects information from skin through electrical sensing (e-sensing). (4) Bioelectronics manages the biosafety of bacteria through electrical stimulation (e-stimulation). (5) Hydrogel encapsulation promotes long-term storage and viability of bacteria. (6) Viscoelasticity of the living hydrogel ensures a stable interaction with skin tissue. (7) Viscoelasticity of the hydrogel facilitates information collection from skin. (8) Biomechanical properties of the hydrogel assist biohazard management. (9) Skin-adhesion property of the hydrogel improves long-term information collection.* Compared to conventional bioelectronics interfaces, ABLE combines functionalities across the bioelectrical, biomechanical, and biogenic domains.

Taken together, integration of a living biointerface with bioelectronics provides a controlled platform to delve into interactions and mechanisms at the bacteria-mammalian nexus. Using this platform, we explored the role of *Staphylococcus epidermidis* in skin inflammation management and skin microbiota modulation. Our discoveries indicate that the ABLE manages inflammation by inhibiting the activation of initial dendritic cells, leading to a reduction in inflammation typically linked to psoriatic development. Our research underscores the practical effectiveness of the ABLE platform in diagnosing and treating intricate autoimmune diseases such as psoriasis.

In this chapter, our primary focus will be on the construction of living materials for bioelectronics. We will emphasize how these materials interact with bacteria and detail our strategies to promote their long-term viability. Additionally, we will delve into the biomechanical properties that the living hydrogel offers to mesh electronics-based bioelectronics, significantly enhancing electrophysiological signal recording. In the subsequent chapter, our main emphasis will shift to the biochemical properties of the living hydrogel and its applications in disease management.

4.2 Result and Discussion

4.2.1 Living hydrogel design

We chose a hydrogel composite as the primary matrix for the living ABLE biointerface due to its biomechanical and structural resemblance to biological tissues[15]. We incorporated *S. epidermidis* as the living component, as this species is part of the human skin flora and can modulate biochemical activity in skin cells[16]. To ensure the functionality of the living biointerface, the hydrogel matrix must support bacterial viability, with bioelectrical and biomechanical capabilities for interfacing with electronics and biological tissue.

In designing a hydrogel matrix conducive to the long-term viability of S. epidermidis, we drew inspiration from natural biofilms that promote bacterial survival and community regulation[17]. To emulate the major biofilm components of proteinaceous matrix and exopolysaccharides, we created a biocompatible hydrogel matrix using a dual network of protein and polysaccharide polymers (Figure 4-2).

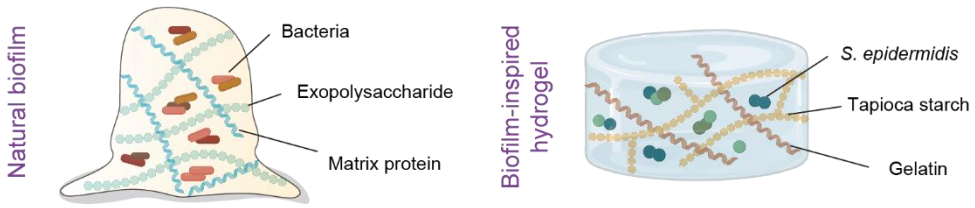

Figure 4-2 Mimicking the natural composition of biofilm, gelatin and starch are used as the protein and polysaccharide polymer in constructing the interpenetrated double network hydrogel, i.e., the living biointerface.

We selected gelatin as the main protein matrix given its natural origin and superior hydrogel-forming properties[18]. Compared with synthetic hydrogels like polyacrylamide, gelatin exhibited superior biocompatibility with the bacteria, while also providing a natural environment for bacterial colony growth (Figure 4-3).

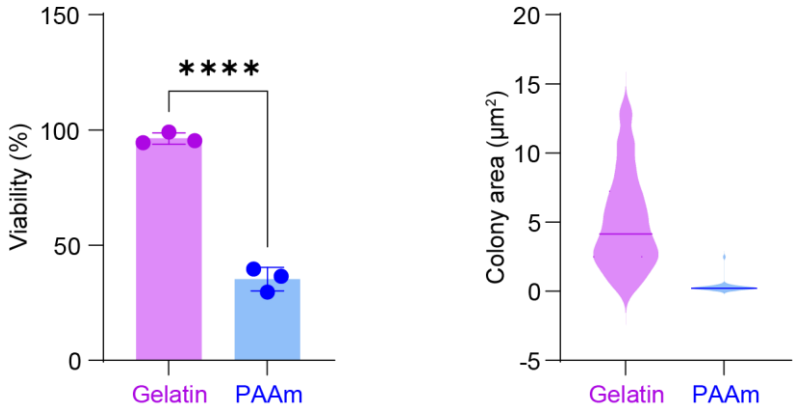

Figure 4-3 Gelatin matrix demonstrates better capability in supporting Staphylococcus epidermidis viability and growth compared to the synthetic hydrogel matrix such as polyacrylamide (PAAm). After 24h of growth at room temperature, gelatin encapsulated Staphylococcus epidermidis shows larger colony area and viability from LIVE/DEAD assay compared to PAAm encapsulated Staphylococcus epidermidis, demonstrating compatibility of protein matrix in supporting microbial viability compared to the synthetic matrix. Data are presented as mean values ± SD. n=3 for each group.

For the polysaccharide component, we screened a library of natural products including various biopolymer (Figure 4-4). Tapioca starch best supported *S. epidermidis* viability and was selected as the polysaccharide.

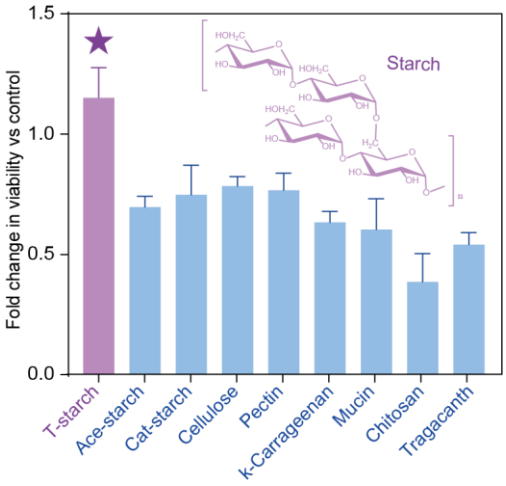

Figure 4-4 Tapioca starch best sustains bacteria viability among various polysaccharides. Data are presented as mean values ± SD. n=5 for each group.

Besides polysaccharide, we also screen several synthetic polymer, and nano clay-based materials as a compare (Figure 4-5).

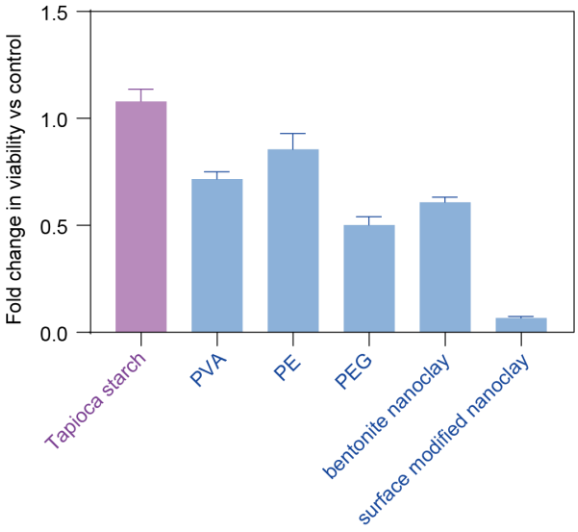

Figure 4-5 Tapioca starch sustains the bacteria best among various synthetic polymer and nano clay-based materials. Data are presented as mean values ± SD. n=3 for each group.

Starch is predominantly made up of two types of polysaccharide molecules: amylose and amylopectin[19]. Amylose is largely a linear molecule consisting of glucose units primarily connected by α-(1→4) glycosidic bonds. In contrast, amylopectin is a highly branched molecule, with glucose units bonded by both α-(1→4) glycosidic bonds (in linear segments) and α-(1→6) glycosidic bonds (at branching points). The concentrations of amylose and amylopectin, the granular structure, and the nature and quantities of lipids and proteins present in granules differ depending on the botanical source of the starch. Notably, most starch granules consist of alternating layers of amorphous and crystalline regions, with thicknesses ranging from 100 to 400 nm[20]. The crystallinity is attributed to the orderly arrangement of amylopectin branches. These crystalline areas resist water and other small molecule penetration, while the amorphous regions are more permeable. We assumed that the different chemical compositions of amylose and amylopectin would have distinct interactions with the bacteria.

To fully investigate the material-bacteria interaction, we further applied a gelatinization and retrogradation process via a heating-cooling cycle. This process diminished the crystallinity of the starch, altering the granular morphology and diffusing out the granule-enclosed amylose (Figure 4-6).

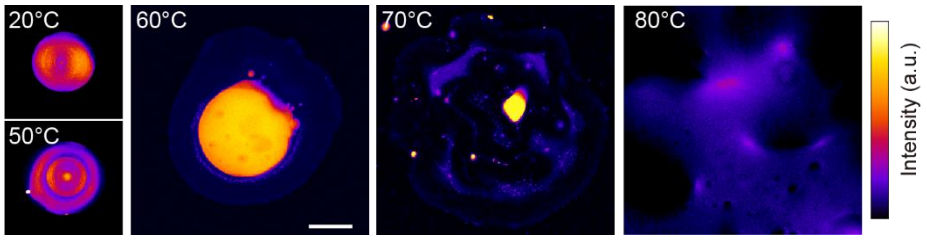

Figure 4-6 Fluorescent images indicate the structural transformation of starch granules after thermal treatment at different temperatures. Scale bar, 10 μm.

The hydrated starch with exposed amylose content formed a biocompatible network with which bacteria interact (Figure 4-7).

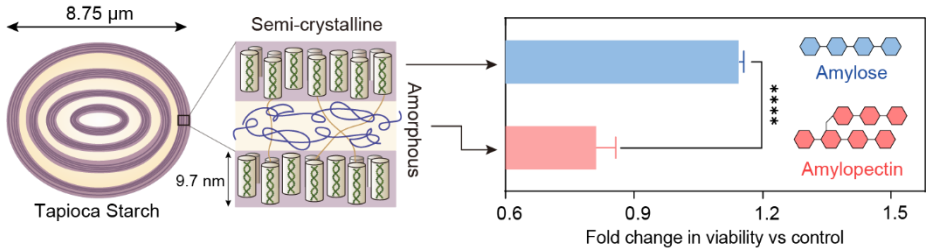

Figure 4-7 Tapioca starch best sustains bacteria viability among various polysaccharides. Data are presented as mean values ± SD. n=5 for each group.

Starch gelatinization is a process that breaks down the intermolecular bonds of starch molecules when exposed to water and heat, allowing more water to interact with the hydrogen bonding sites[21]. This process involves three sequential steps: water absorption, heating, and disruption of crystalline regions. Initially, starch granules are semi-crystalline in nature, comprising both amorphous (less ordered) and crystalline (more ordered) regions. When starch is mixed with water, the water molecules begin to penetrate the amorphous regions, leading to granule swelling[22]. However, without heat, the water does not infiltrate the crystalline regions. During the heating phase, the energized water molecules, due to their increased kinetic energy, further penetrate the starch granules. This increased molecular activity disrupts the granules' crystalline regions. As the heating continues, the once tightly-packed crystalline areas begin to melt or dissolve, marking the onset of the actual gelatinization process. Amylose molecules are the first to leach out from the granules, followed by portions of amylopectin. As an increasing number of starch granules undergo gelatinization, the mixture's viscosity rises. This increase in thickness occurs because the

released amylose and amylopectin molecules interact with the water. Over time, the mixture attains its peak viscosity.

To monitor the reduction of crystalline structure in starch granules during the gelatinization process, we employed the in-situ small angle x-ray scattering (SAXS) technique (as shown in Figure 4-8). Our findings suggest that gelatinization of our granules occurs at approximately 60 °C. The magnitude of the scattering vector (q) indicates that the crystalline spacing is around 9.7 nm.

$$q = \frac{4\pi}{\lambda}\ \sin(\theta) = \frac{2\pi}{d}$$

Where λ is the wavelength of the incident X-rays. θ is half of the scattering angle; d is the spacing or distance between repeating units. Furthermore, a differential scanning calorimetry experiment corroborated this temperature range, aligning with our X-ray results.

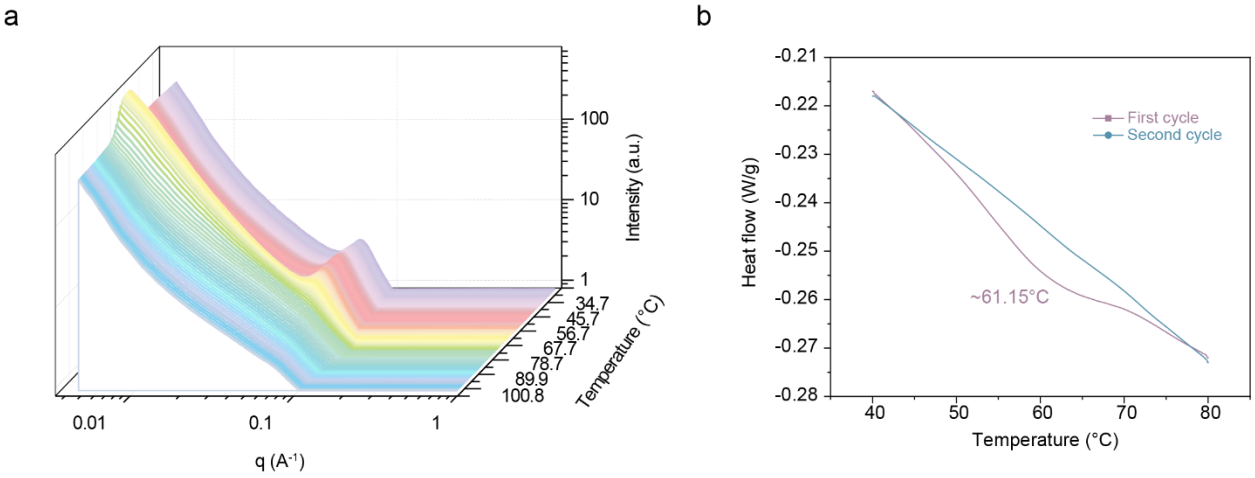

Figure 4-8 Thermal treatment triggers morphology changes of starch granules. (a) In-situ monitoring the glass transition process of starch from 25 °C to 100 °C by small angle X-ray scattering (SAXS) measurement. SAXS peak relating to the crystalline structure of starch granules at around 0.06 disappears at high temperature. (b) Differential scanning calorimetry (DSC) measurement reveals the transition of the crystalline structure in starch granules.

In addition to gelatinization, starch granules undergo the retrogradation process, which aids in reestablishing intermolecular interactions[23]. Specifically, when cooled, the disrupted amylose and amylopectin chains begin to reassociate, forming a distinct ordered structure. The pace and degree of retrogradation are determined by various factors, including the ratio of amylose to amylopectin, water content, temperature, and the presence of other ingredients.

The gelatinization process significantly enhances bacterial viability, an aspect that remains largely underexplored (Figure 4-9). We hypothesize that the release of amylose from the granular structure might offer additional adhesion sites for bacteria to anchor, thereby improving bacterial viability. Supporting this, we observed that more bacteria attached to the collapsed starch granules than to regular granules. These results have been normalized based on area. However, the precise mechanism needs further research for a comprehensive understanding.

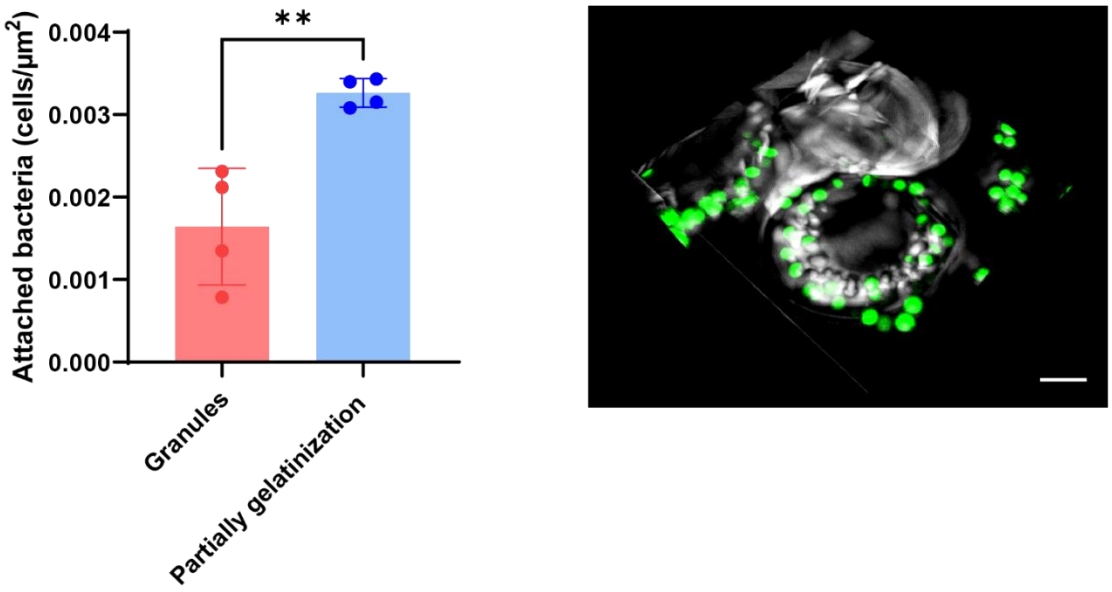

Figure 4-9 Partially gelatinized starch enhances the bacterial attachments on the collapsed granules. Bacteria are shown in green signals through SYTO9 staining. Scale bar, 3 μm. Data are presented as mean values ± SD. n=4 for each group.

In line with this, we noted that gelatinization of starch prolongs bacterial viability inside hydrogel matrix (Figure 4-10). Altogether, we crafted a protein-polysaccharide hydrogel for bacterial encapsulation, which promoted prolonged bacterial viability of at least 4 days. The hydrogels also provide the ability for bacterial immobilization (Figure 4-11).

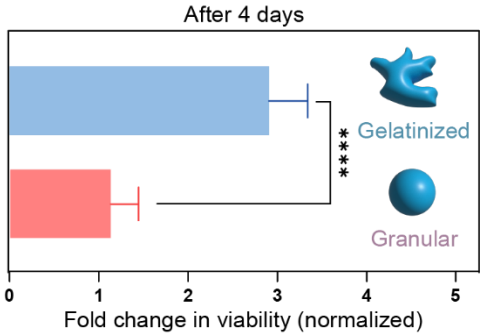

Figure 4-10 Gelatinization of starch promotes bacteria viability in the living hydrogel matrix for at least 4 days. Data are presented as mean values ± SD. n=5 for each group.

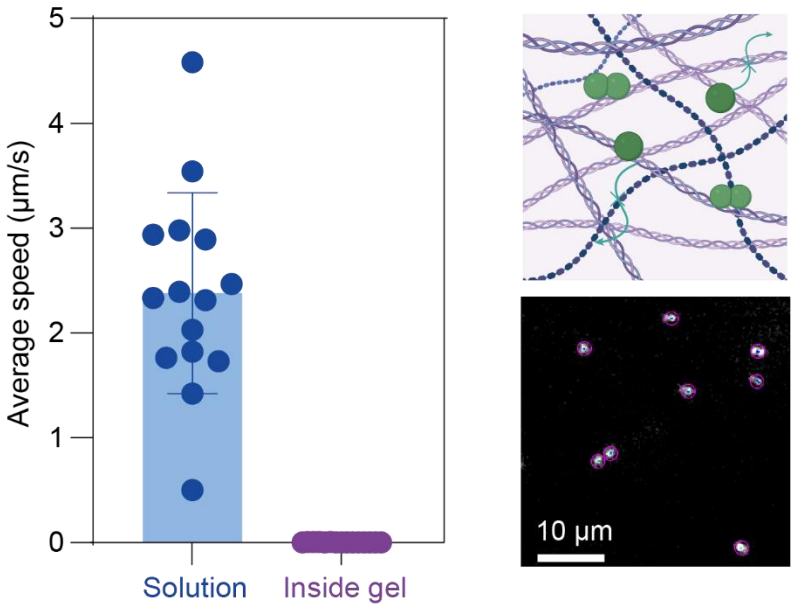

Figure 4-11 Hydrogel immobilizes the motion of encapsulated bacteria. Bacteria display significantly reduced motion speed within the hydrogel matrix compared to the culture medium, suggesting that the living hydrogel effectively restricts the movement of bacteria within the matrix. Scale bar, 10 μm. Data are presented as mean ± standard error of mean.

Additionally, the freeze-dried living hydrogel can be preserved for 30 days at -80 °C (Figure 4-12). Due to the hydrogel's ability to support bacterial growth, any loss of bacterial viability during storage can be recovered beyond its initial level by allowing the rehydrated hydrogel to sit at room temperature overnight. This feature indicates potential for industrialization and distribution.

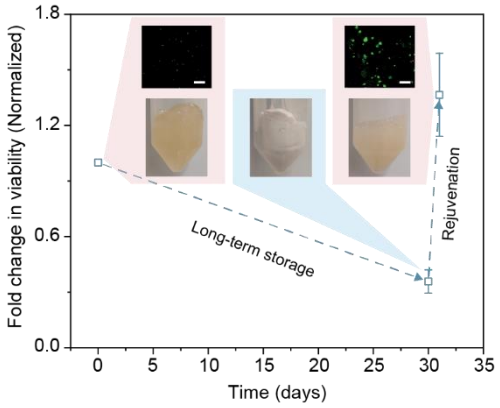

Figure 4-12 Bacteria can be stored within the hydrogel matrix over a long-term period and rejuvenated with an overnight culture. Scale bar, 20 μm. Data are presented as mean values ± SD. n=5 for each group.

4.2.2 Living hydrogel characterization

Firstly, our goal was to understand the structural information of the living hydrogel. Confocal microscopy, an advanced optical imaging technique, provides enhanced optical resolution and contrast compared to traditional wide-field microscopy (Figure 4-13). To visualize bacteria within the hydrogel matrix, we employed a confocal microscope, with both the starch and bacteria stained.

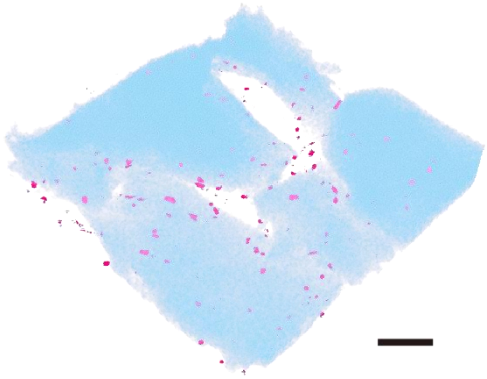

Figure 4-13 Confocal microscope imaging shows the distribution of Staphylococcus epidermidis inside the living hydrogel matrix. Bacteria are stained with FM1-43 (red) and starch is stained with APTS (blue). Scale bar, 15 μm.

Electron microscopy (EM) is a potent imaging technique that utilizes electrons, rather than light, to create an image. This approach achieves much higher resolution than light microscopy due to the substantially shorter wavelength of electrons. By employing both Scanning Electron Microscopy (SEM) and Transmission Electron Microscopy (TEM), we discovered cocci-shaped bacteria embedded within the hydrogel matrix (Figure 4-14).

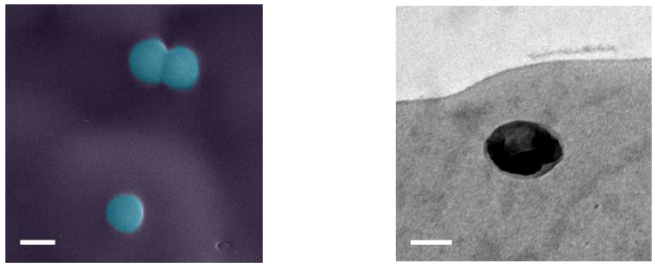

Figure 4-14 SEM and TEM images show encapsulated bacteria within the hydrogel matrix. Scale bar, 1 μm (SEM); 500 nm (TEM).

The living hydrogels display favorable bioelectrical and biomechanical characteristics, facilitating integration of bioelectronic devices with biological tissues. We first characterized the electrical

properties of the living hydrogel using the electrochemical tools. We observed the high ionic electrical conductivity of the living hydrogels, <500 Ω at physiologically relevant frequencies of 10^2-10^5 Hz, using electrochemical impedance spectroscopy (EIS) (Figure 4-15).

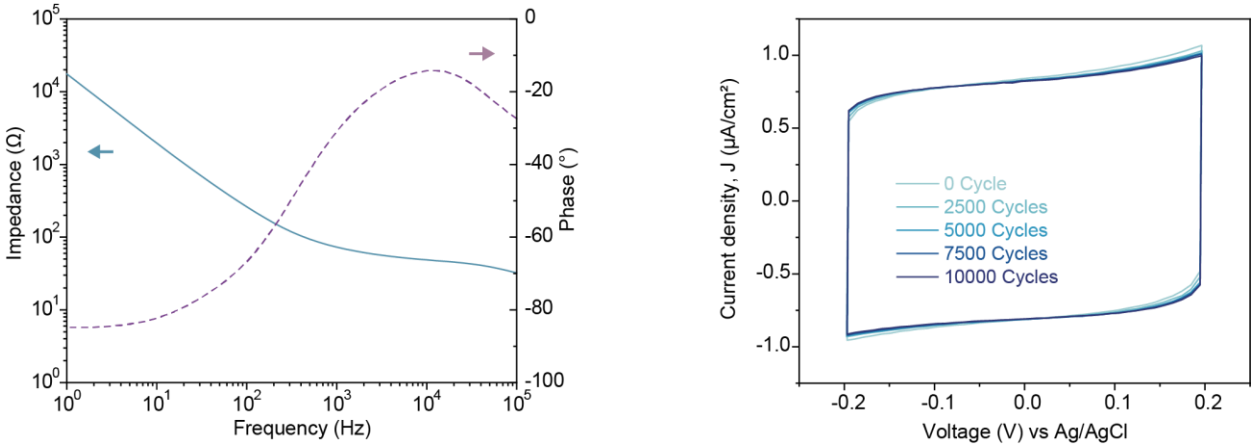

Figure 4-15 Electrochemical analysis shows electrical properties of living hydrogel. (a) Electrical impedance spectroscopy analysis indicates the conductivity of the living hydrogel. (b) Cyclic voltammetry shows high electrochemical stability of living hydrogels after at least 10000 cycles of repetitive scans. n=5 for each group.

The molecular interaction inside the living hydrogel plays an important role in the mechanical properties of hydrogels. We found that the gelatinization process increases polymer chain mobility and enhances molecular interactions between the starch and gelatin polymers, as indicated by Fourier transform infrared analysis, which showed a shift of spectral features in the amide I region from 1600 cm^{-1} to 1700 cm^{-1} (Figure 4-16).

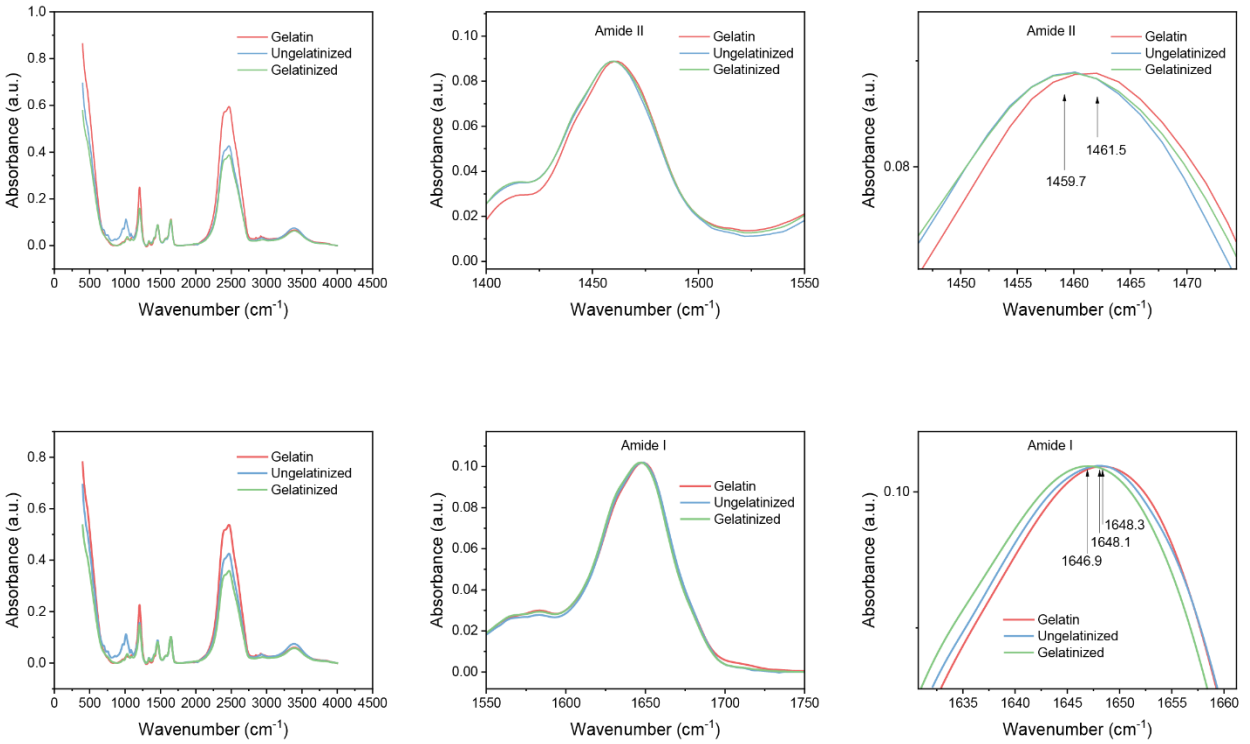

Figure 4-16 Fourier-transform infrared spectroscopy (FTIR) results provide evidence of polymer interactions between gelatin and starch. The existence of starch macromolecules influences the amide I (C=O stretching) and amide II (N-H bending and C-N stretching) peaks of the gelatin hydrogels. n=5 for each test.

The living hydrogels have a high-water content (>75%) and tissue-compliant ultra-softness (shear modulus of 4 kPa). Intermolecular interactions enable more energy dissipation during mechanical deformation and thereby endow the living hydrogel with tissue-like viscoelasticity. The strain- and frequency-dependent modulus, fast stress relaxation, and mechanical hysteresis further confirmed the viscoelasticity (Figure 4-17).

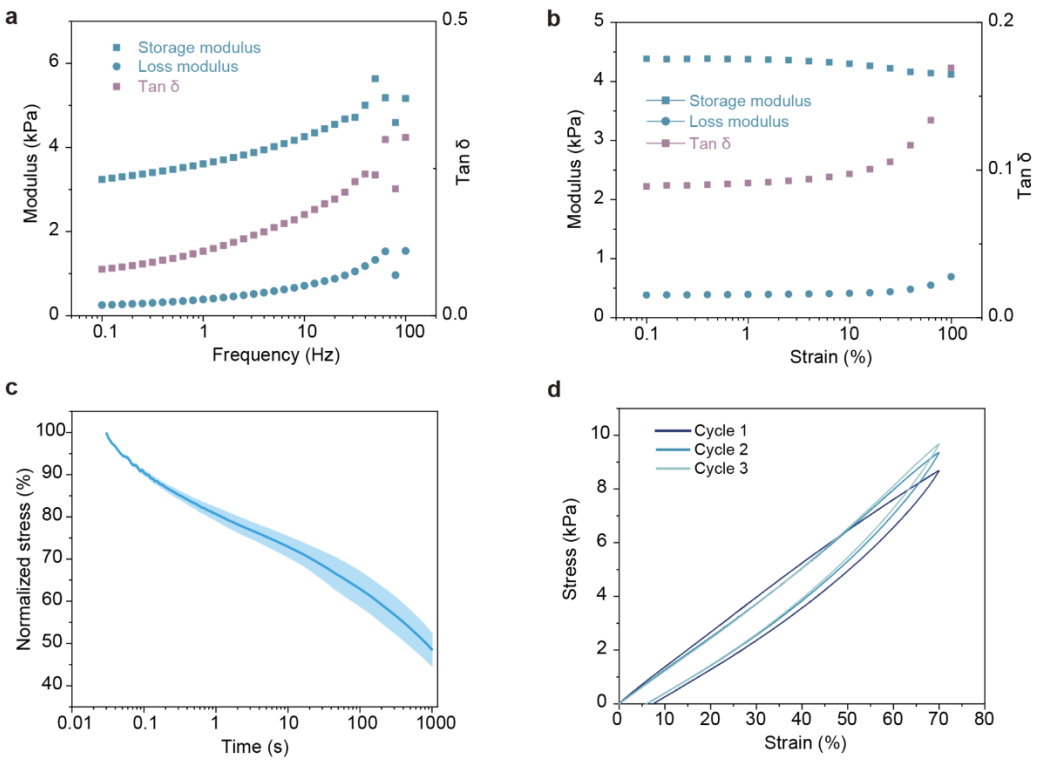

Figure 4-17 Mechanical tests demonstrate the living hydrogel is soft and viscoelastic. (a) Storage modulus (G'; left axis), Loss modulus (G''; left axis), and tan δ (G''/G'; right axis) are shown as a function of frequency at 1% of strain. (b) Storage modulus (G'; left axis), Loss modulus (G''; left axis), and tan δ (G''/G'; right axis) are shown as a function of strain at 1Hz frequency. () The stress relaxation test shows the living hydrogel has fast relaxation behaviors. (Right) The strain-stress curve illustrates that the living hydrogel undergoes energy dissipation during the cyclic mechanical loading. n=5 for each test.

The biomechanical properties that mimic tissue foster a conformal biointerface with tissues, ensuring seamless integration of bioelectronics (Figure 4-18). This seamless integration of bioelectronics and tissue is pivotal in optimizing the functionality, reliability, and biocompatibility of wearable bioelectronics devices. Such seamless integration guarantees that bioelectronic devices can proficiently interface with biological systems. This allows for precise signal transduction, stimulation, or monitoring without inducing undesired tissue reactions.

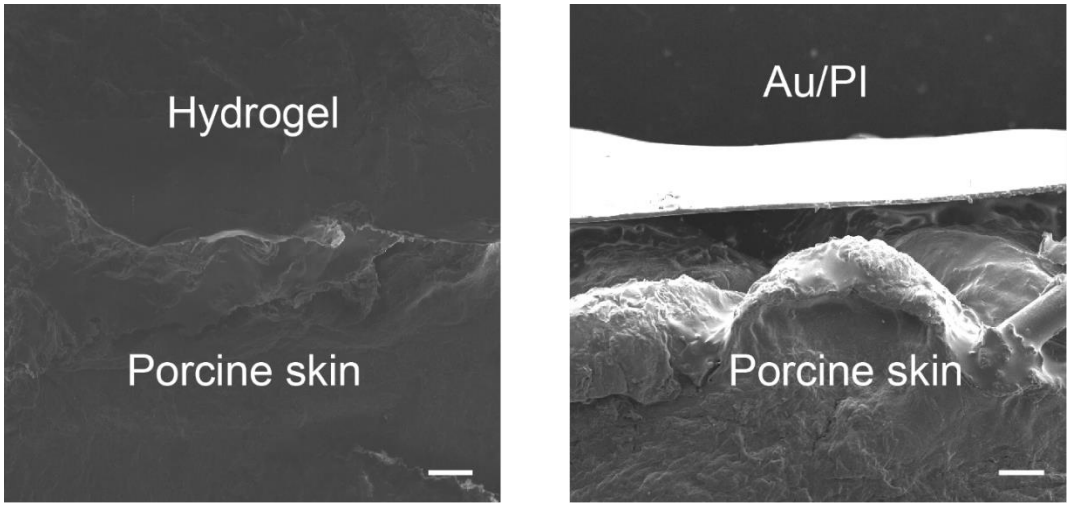

Figure 4-18 SEM images of starch gelatin hydrogel and Au/Polyimide film attached on porcine skin. Viscoelasticity enables conformal attachment of starch-gelatin hydrogel on the rugged skin surface. Scale bar, 200 μm.

The biomechanical properties of the hydrogel are also adjustable for various tissue applications (Figure 4-19). We demonstrated, by adjusting the concentration of the polysaccharide and protein, the viscoelasticity and the modulus of the living hydrogel can be readily changed.

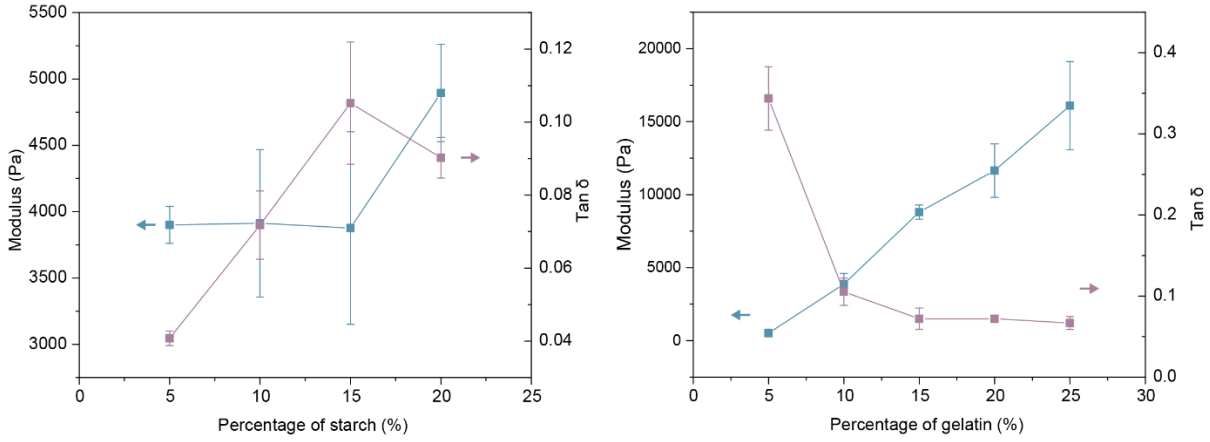

Figure 4-19 The living hydrogels have tunable mechanical properties. Data are presented as mean values ± SD. (n=5).

Furthermore, the abundance of hydroxyl groups in the starch polymer endows the living hydrogel with adhesive properties, enhancing the stability of the bioelectronic devices on the tissue (Figure 4-20). The adhesion between bioelectronics and tissue enables the effective and consistent functioning of the wearable devices. The adhesive bioelectronic interface ensure the device remains in its intended position. Besides it facilitates accurate signal capture or delivery without intermittent disruptions.

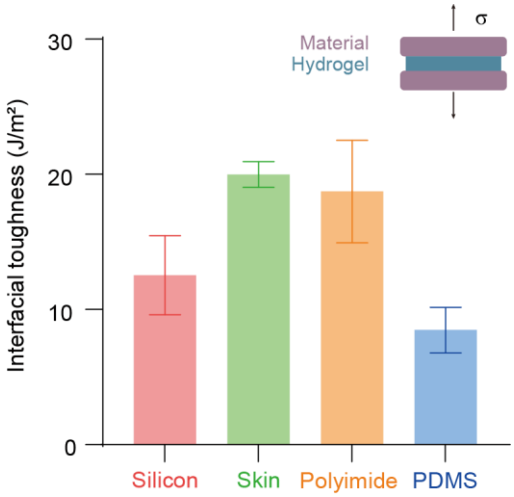

Figure 4-20 Tensile adhesion test reveals that the living hydrogels are adhesive to various substrates. Data are presented as mean values ± SD. n=4 for each group.

4.2.3 Living bioelectronics demonstration

To demonstrate that the biomechanical and bioelectrical properties of living hydrogel enable efficient ABLE functions (more in next section), we constructed a 15-channel mesh electronics array for surface electromyography (sEMG) intensity mapping (Figure 4-21).

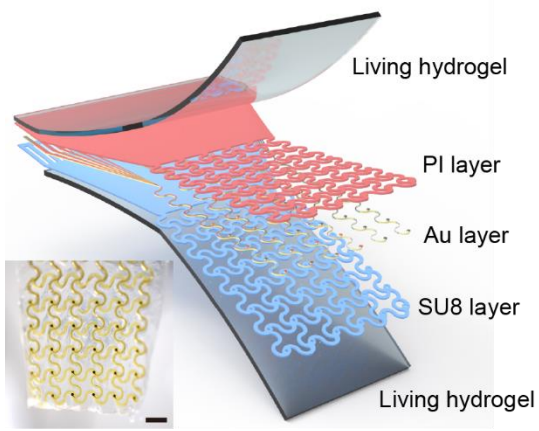

Figure 4-21 Schematic diagram and photograph show the structural configuration of the living hydrogel hybrid mesh electronics device for surface electromyography (sEMG) recording. Scale bar, 3 mm.

The device is on the polyimide substrate, which largely enhance the robustness of the mesh electronics. The fabrication process is all done at Pritzker Nanofabrication Facility. Specifically, the initial cleaning of a P-type wet oxide silicon wafer (#HS39626-WO, NOVA Electronic Materials) was performed, which involves immersion in acetone and isopropyl alcohol (IPA) for 3 minutes each within an ultrasonic bath. Following this, hexamethyldisilazane (HDMS) is applied to the wafer as a treatment. A solution of poly (pyromellitic dianhydride-co-4,4′-oxydianiline) (Sigma Aldrich, 575801-1L) is then added to the treated wafer using a spin-coating method at a speed of 1500 rpm. To cure the applied solution, the wafer is then heated in a resist oven at a temperature of 300 degrees Celsius for a span of 3 hours, after which it is allowed to cool down naturally to room temperature. The end result is a polyimide (PI) film of approximately 5 micrometers in thickness. The PI-coated wafer then undergoes another round of spin-coating, this time with AZ nlof 2020, followed by an exposure process to develop patterns. The wafer is then subjected to an evaporation process with 5 nm Titanium and 200 nm Gold, which is followed by a lift-off in AZ NMP to get rid of the photoresist. Subsequently, the wafer is patterned with AZ

40XT-11D, which serves as a protective mask against etching. The patterned PI layer is achieved via Reactive Ion Etching (RIE) in a Plasma-Therm Inductively Coupled Plasma (ICP) Fluoride Etch. Post-etching, the photoresist is removed by soaking in N-Methyl-2-pyrrolidone (NMP) within an 80-degree Celsius bath for 10 minutes. The encapsulation layer, composed of SU-8 3005 (MicroChem Corp), is patterned to cover the metal interconnects while leaving the sensing pads and bottom pads exposed to interface with cardiac tissues. Finally, to retrieve the mesh electrode, it can be detached using a water-soluble transfer tape. Alternatively, manual peeling is an option, provided it does not cause any damage to the devices. Hydrogel hybridization is made by attaching mesh electronics to the hydrogel-coated PDMS. The hydrogel layer is formed by spin-coating hydrogel precursor solution at 2000 rpm. After cooling down and trimming, the hydrogel-hybrid devices were carefully peeled off from the PDMS substrate. (Figure 4-22 & Figure 4-23)

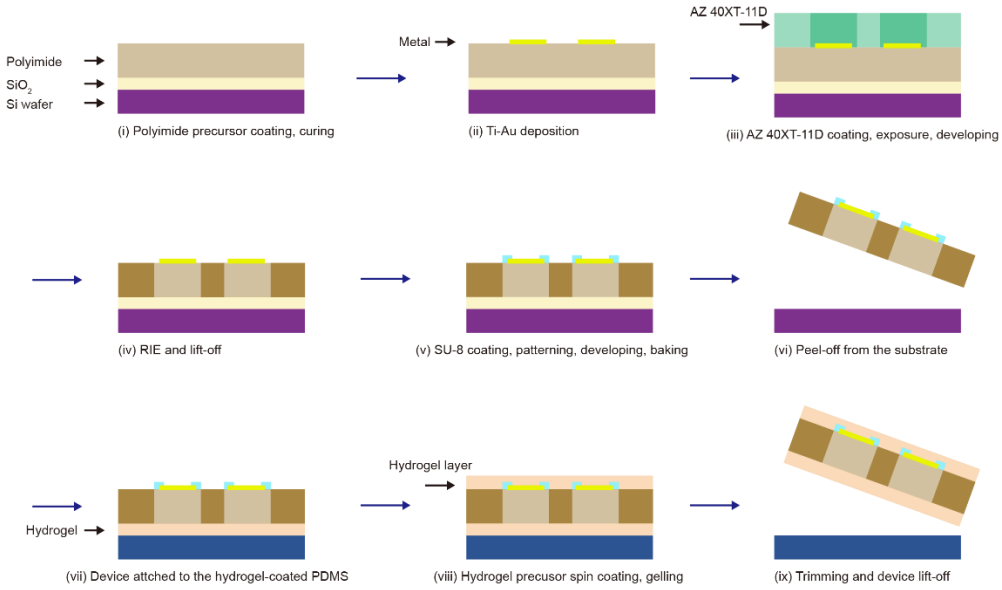

Figure 4-22 Schematic illustrates the fabrication process for living hydrogel hybrid mesh electronic devices (side view).

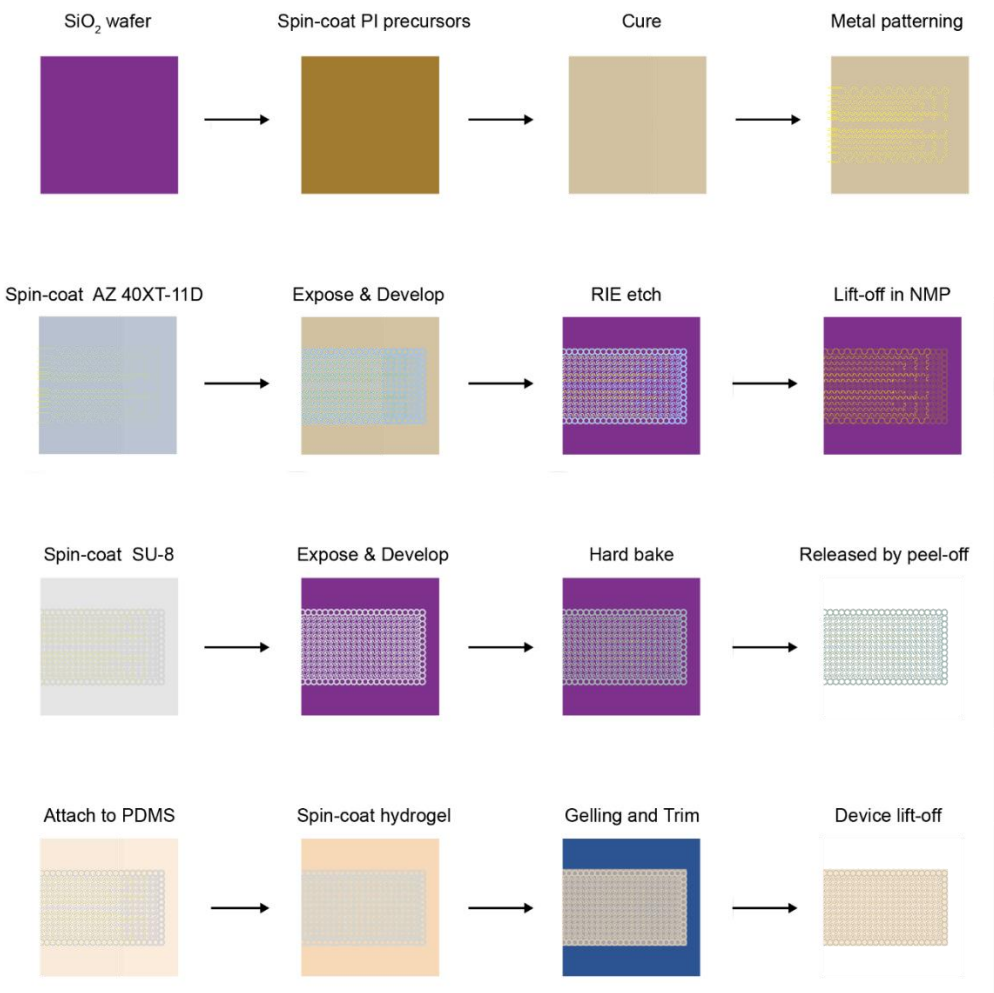

Figure 4-23 Schematic illustrates the fabrication process for living hydrogel hybrid mesh electronic devices (top view).

The design for EMG and ECG recording is depicted in Figure 4-24. Due to the constraints of the Intan analysis device, we utilize 12 electrodes for 6-lead ECG recording. Typically, only 3 electrodes are required for 6-lead ECG monitoring. In commercial products, all electrodes can serve as both positive and negative.

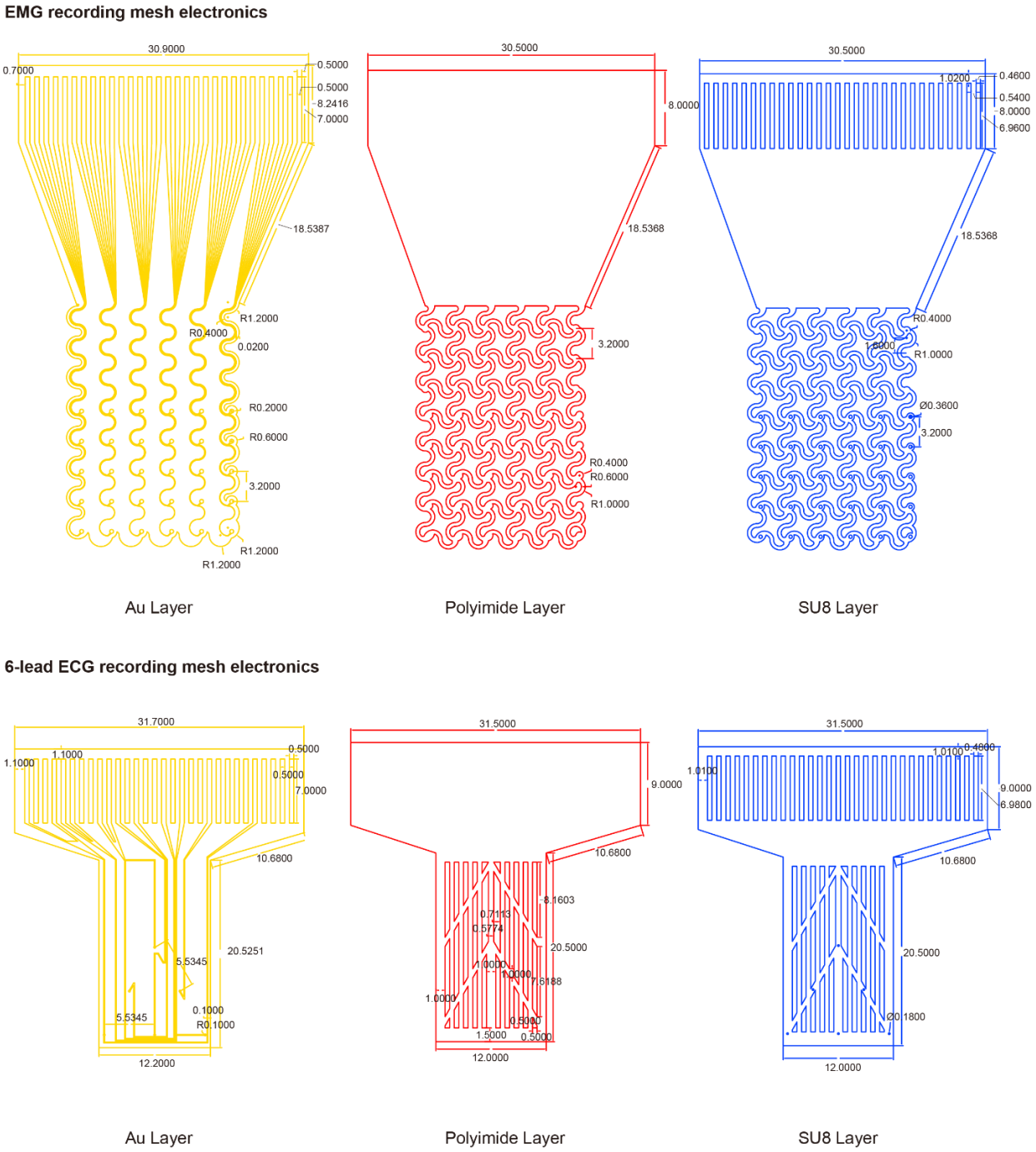

Figure 4-24 Mesh electronic design for EMG and ECG recording. Layer 1: Bottom polyimide as the supportive layer for the mesh device. Layer 2: Metal electrode layers for signal transduction. Layer 3: Top SU-8 as the encapsulation layer.

To demonstrate the ability of living hydrogel in facilitating bioelectronics recording, we interfaced the electrophysiology-based ABLE device with the skin on a rat's leg and recorded the EMG signals evoked by sciatic nerve stimulation (Figure 4-25).

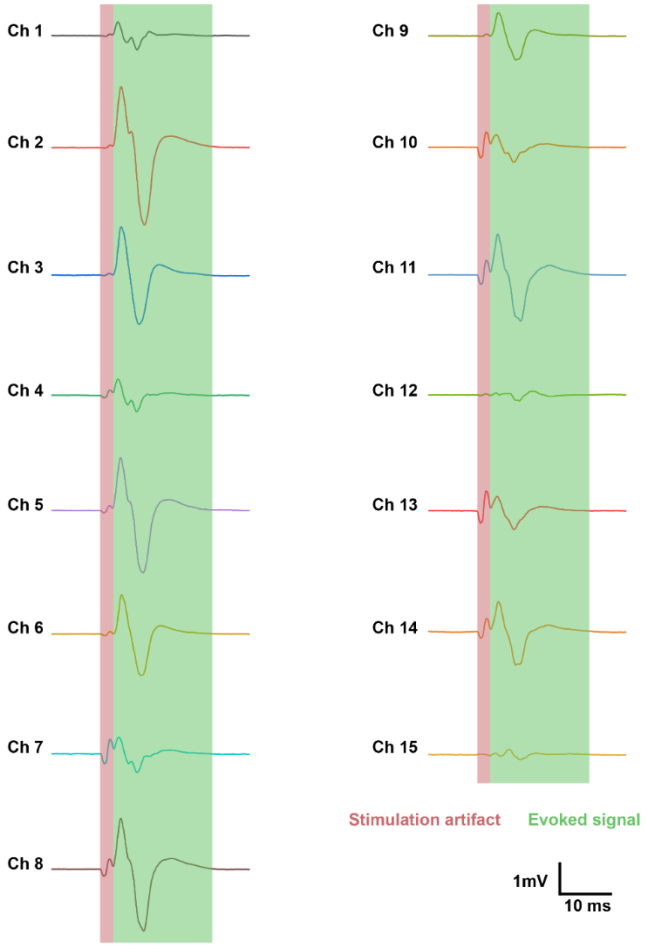

Figure 4-25 The electrical signals collected by each electrode in the hybrid electronics device with the living biointerface. The electrical signals in 15 channels (Ch) show the Electromyography (EMG) information at the surface of leg skin.

Notably, the ABLE device formed conformal and adhesive interfaces with the skin on the rat leg and recorded the EMG signals with an average signal-to-noise ratio (SNR) of 26.76 dB (Figure 4-26). Furthermore, given the stable and conformal biointerface the ABLE device resolved high

sEMG spatiotemporal intensity dynamics over an area of 16 × 12.8 mm. Instead to a gold biointerface (electronics without living hydrogel) recorded EMG signals with an SNR of 12.00 dB, indicating that the conformal nature of the ABLE facilitates electrophysiological signal transmission.

$$SNR_{\,dB} = 10\log_{10}(\frac{P_{signal}}{P_{noise}})$$

Figure 4-26 Spatial intensity map reveals the sEMG activity across the 15 electrical channels at the rat leg. Size of region: 16 mm (horizontal) × 12.8 mm (vertical). Comparison of signal-to-noise ratio (SNR) in gold bioelectronics biointerface versus living hydrogel coating indicated that living hydrogels-coated bioelectronics indicates that living hydrogels facilitate electrophysiological recording.

The living biointerface boosts the durability of bioelectronics, shown by a steady EMG signal over 4 hours without significant SNR loss (Figure 4-27). Long-term stability is essential for reliable bioelectronics recording, reducing the need for repeated surgical procedures, and thereby improving patient safety and comfort. Such stability ensures consistent signal capture, enhances therapeutic outcomes, and prevents the device from degrading.

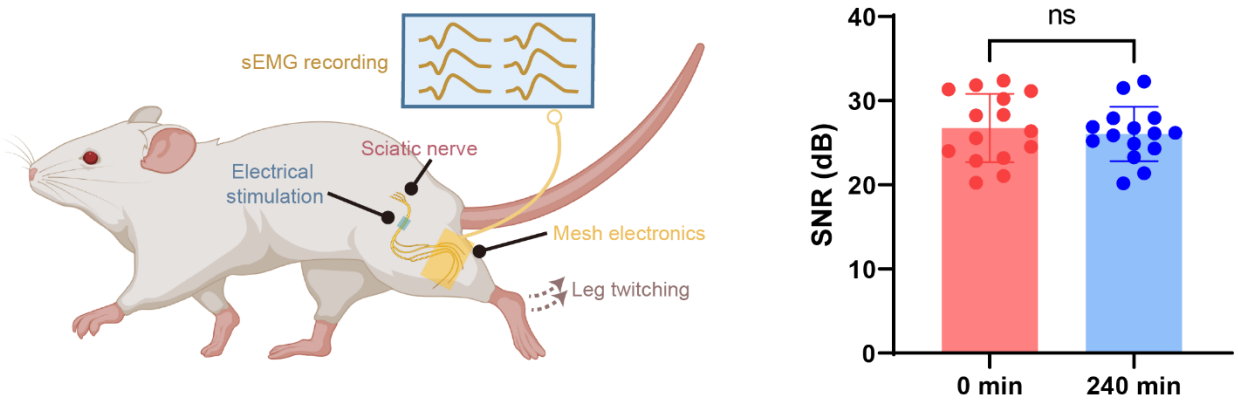

Figure 4-27 Signal-to-noise ratio (SNR) indicates that living mesh electronics could stably record the surface EMG signal for 240 minutes. P values are determined by paired t-test, two tailed.

4.2.4 Living bioelectronics applications

To demonstrate the utility of ABLE in complex disease, we applied the ABLE devices to a psoriasis mouse model. Psoriasis is a chronic inflammatory disease that impacts approximately 125 million people worldwide, with no complete cure[24]. Current treatment options often involve small-molecule drugs with potential systemic side effects. Here, we conducted a series of pre-clinical evaluations using ABLE in the imiquimod (IMQ)-induced psoriasis model[25]. This model is widely utilized in in vivo research due to its clinical and histological similarities to human psoriasis, including characteristic symptoms such as desquamation, thickening of the epithelial structure, skin inflammation, and dysregulated host skin microbiota[26]. The detail introduction of psoriasis disease will give in the next chapter. Here we only briefly show the therapeutic effect and biochemical properties of living materials in psoriasis disease.

To demonstrate the potential of ABLE in the skin inflammation diagnosis and treatment, we first fabricated a mesh electronics device with a spin-coated living interface for 6-lead surface electrocardiogram (sECG) recording (Figure 4-28).

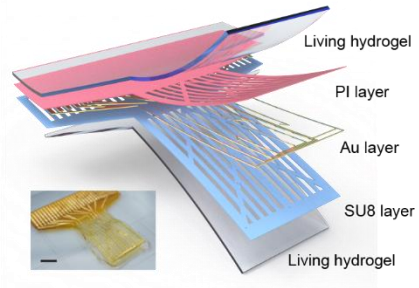

Figure 4-28 Schematic diagram and photograph show the structural configuration of the living hydrogel hybrid mesh electronics device for sECG recording. Scale bar, 5 mm.

Upon attachment to the chest area of healthy mice, the ABLE stably recorded the 6-lead ECG (I, II, III, aVL, aVR, and aVF) with an average SNR of 18.97 dB (Figure 4-29). In contrast, the ABLE recorded a significantly lower SNR of 7.96 dB in mice with psoriasis symptoms, mainly attributed to the thickening of the psoriasiform skin. Hence, alterations in recorded electrophysiological signals offer qualitative information in the detection of skin diseases.

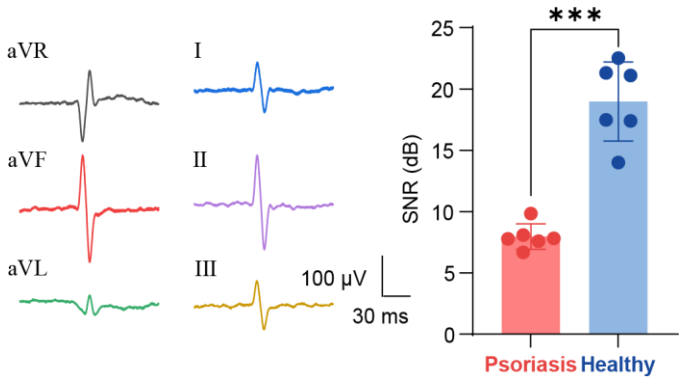

Figure 4-29 Representative 6-lead electrocardiogram signals reveal heart rhythm in I, II, III, aVL, aVR, and aVF leads. Living bioelectronics device reports lower SNR in ECG recording in psoriasiform skin compared to controls. Data are presented as mean values ± SD. n=6 for each group.

More importantly, ABLE will not induce undesired inflammatory skin responses but treating psoriasis inflammation. When the ABLE device was applied to psoriatic skin for 4 days, we found that the SNR of recorded ECG was largely enhanced (Day 0 vs Day 4 recording), indicating reduced psoriasis symptoms in the mouse skin (Figure 4-30). These results demonstrate how the ABLE system may be used to record electrophysiological signals while concurrently providing biochemical cues to regulate inflammatory skin diseases.

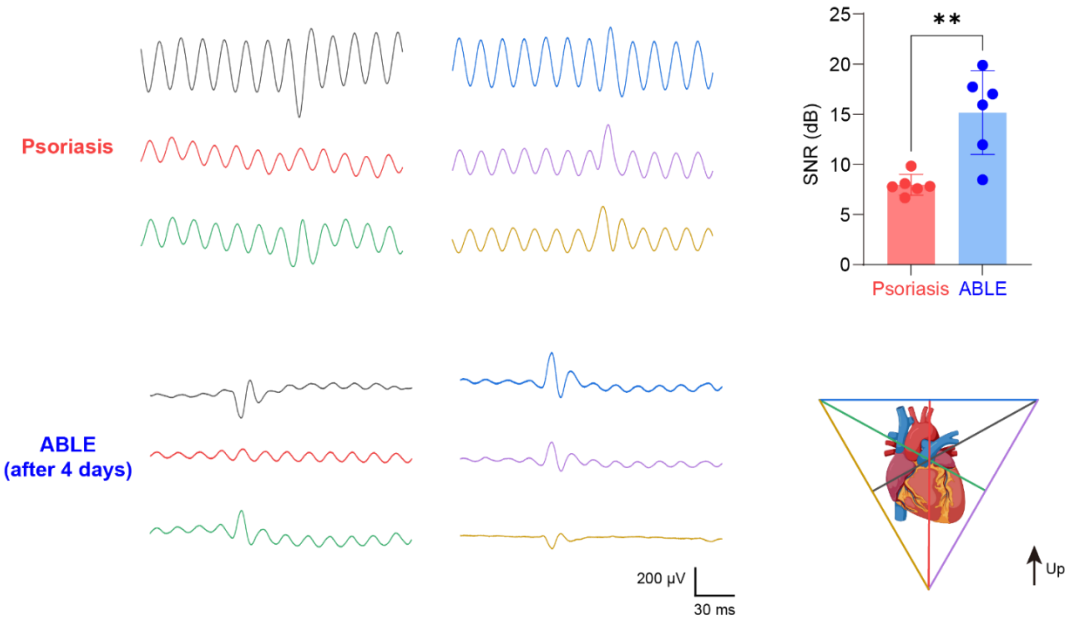

Figure 4-30 The 6-lead ECG signals acquired from each individual channel demonstrate a significant enhancement in signal-to-noise ratio (SNR) following a 4-day ABLE treatment period. P values are determined by paired t-test, two tailed. Data are presented as mean values ± SD. n=6 for each group.

4.3 Conclusion

In this chapter, we delved into the construction of living materials as a biointerfacial layer for bioelectronics. Using techniques derived from material science and engineering, we rationally designed a hydrogel matrix that supports the long-term sustainability of bacteria. While previous

efforts in creating living matrices often depended on empirical experiences, our approach was more systematic, inspired from the natural biofilm based on biomimetic principles. Through meticulous design and processing of starch granules, we were able to decipher the biochemical interactions between the material and bacteria. These techniques offer a blueprint for the design of future engineered living materials to sustain various bacterial systems.

Moreover, we showcased that the living hydrogel can deliver both bioelectrical and biomechanical properties essential for bioelectronics. The ionic-conductive nature of hydrogel enhances electrophysiological recordings in the pre-clinical animal model. Additionally, its viscoelastic properties, reminiscent of natural tissues, ensure a seamless integration between bioelectronics and biological tissues. Overall, our research introduces novel methods for crafting tissue-like biointerfaces for bioelectronics. Such advancements hold the potential to significantly elevate the performance and utility of contemporary bioelectronics in both disease diagnosis and treatment.

4.4 Experimental Methods

Synthesis of hydrogel composite. A starch gelatin hydrogel was prepared by mixing tapioca starch (15 wt%), gelatin (10 wt%), and deionized water or tryptic soy broth (TSB) medium (cat. no. 22092). The mixture was then heated in an oil bath at 80°C for 30 minutes to facilitate the gelatinization of starch. Subsequently, the hydrogel was transferred to a 4°C refrigerator for gelation. To create a living hydrogel, Staphylococcus epidermidis (S. epidermidis) was cultivated in TSB medium at 37°C until the optical density at 600 nm (OD600) reached a range of 2.80 to 3.00. Then, 1ml of cultured Staphylococcus epidermidis was aseptically added and vigorously mixed with the starch-gelatin hydrogel at 42 °C water bath. For the synthesis of granular starch-gelatin hydrogel, gelatin and TSB medium were mixed and heated at 80°C for 30 minutes. After

cooling the mixture in a 42°C water bath, tapioca starch was aseptically added. To synthesize polyacrylamide hydrogel, AA (3.5 wt%), APS (0.1 wt%) and MBAA (0.01 wt%) were mixed vigorously in deionized water. After 30 minutes, the accelerator TEMED (0.02 wt%) was added into the mixture and quickly mixed before pouring into acrylic molds for subsequent polymerization at room temperature.

Confocal laser scanning microscopy. Staphylococcus epidermidis was subjected to staining using the LIVE/DEAD BacLight Bacterial Viability Kit (Molecular Probes), following the guidelines provided by the manufacturer. The stained samples were then visualized using a Stellaris8 falcon WLL confocal microscope, equipped with a 63x objective. In the microscope images, live cells exhibited a green fluorescence (SYTO9), while dead cells appeared red (PI). To determine the percentage of viability, individual cells or colonies were threshold and counted using ImageJ software. For the reconstruction of Z-stack images, Imaris from Oxford Instruments was employed. To visualize the process of starch gelatinization, the reducing ends of tapioca starch were marked with 8-amino-1,3,6-pyrenetrisulfonic acid (APTS). The hydrogel was soaked in an APTS solution (20mM, mixed in 15% acetic acid), followed by the addition of 500mM sodium cyanoborohydride. This blend was incubated at 25°C for 15 hours, then rinsed five times with deionized water to remove any unattached dye. It was later suspended in 50% glycerol to deter water evaporation. Visualization was done using a Stellaris8 Falcon WLL confocal microscope with a 100x objective lens. The excitation was set at 488nm with a detection range of 500 to 580 nm. To visualize bacterial distribution within the hydrogel matrix, the APTS-marked hydrogel was heated to 42°C, and Staphylococcus epidermidis, stained with FM1-43 (5μM), was introduced. Post-solidification, image was captured on two separate channels. Acquired images were processed using ImageJ software and then reconstructed using Imaris by Oxford Instruments.

Polymer screening. To conduct the polymer biocompatibility test, a mixture was prepared by combining 3 ml of TSB containing Staphylococcus epidermidis with an OD600 of 0.25-0.30 and 1% w/v of polymers. The resulting polymer-bacteria suspension was then placed inside an orbital shaker and incubated at 37°C, shaking at a speed of 200 rpm for a duration of 3 hours. Before and after the incubation period, 100 µl of the suspension was sampled and mixed in a 1:1 ratio with the BacTiter-Glo™ Microbial Cell Viability Assay kit (Promega). The luminescence emitted by the samples was measured using a Synergy Neo HTS Plate Reader. The fold change in viability was determined by dividing the luminescence reading obtained after 3 hours of incubation by the luminescence reading obtained at 0 hours and further normalized by the control group without any polymers.

Long-term viability test. To monitor the long-term viability of *S. epidermidis* within the hydrogel phase, samples of starch gelatin hydrogel (granular and gelatinized) were collected at 0 hour and 96 hours. These samples were placed in glass vials and weighed. To dissolve the sampled hydrogel, 10 ml of PBS was added, and the vials were incubated at 42°C for 10 minutes. The resulting solution, containing the released bacteria, was mixed with the BacTiter-Glo™ Microbial Cell Viability Assay kit from Promega in a 1:1 ratio. The luminescence emitted by the samples was recorded using a Synergy Neo HTS Plate Reader. To obtain normalized viability measurements, the raw luminescence values were divided by the sampled mass of the hydrogel and further normalized by the viability measurement obtained at 0 hours, serving as the reference point.

Freeze-drying of the living hydrogel. An Eppendorf tube filled with a starch-gelatin hydrogel with live *S. epidermidis* was frozen in a dry ice/ethanol bath for 20 minutes. It was then subjected to freeze-drying in a FreeZone 4.5 Liter Benchtop Freeze Dryer at -43°C for a day, and later stored in a freezer set at -80°C. After 30 days, the dried hydrogel was rehydrated with 10ml of deionized

water and a sample was taken for viability measurements. This rehydrated mixture was allowed to sit at room temperature overnight for rejuvenation, and another sample was taken for viability measurements at 31 days. To dissolve the sampled hydrogel, 10 ml of PBS was added, followed by heating at 42°C for 10 minutes. The ensuing liquid, which contained the liberated bacteria, was combined at an equal ratio with the BacTiter-Glo™ Microbial Cell Viability Assay kit by Promega. Using a Synergy Neo HTS Plate Reader, the luminescence from the samples was measured. To obtain normalized viability measurements, the raw luminescence values were divided by the sampled mass of the hydrogel and further normalized by the viability measurement obtained at 0 hours, serving as the reference point.

Scanning Electron Microscope. A scanning electron microscope (SEM; Carl Zeiss, Merlin) was used to image the morphology of multiple samples, including S. epidermidis-encapsulated living hydrogels, porcine skin attached to living hydrogels and Au/PI film. Samples were fixed in 3% glutaraldehyde, followed by washing in DI water and dehydration with an increasing ethanol gradient. Samples were dried in a critical point dryer (Leica EM CPD300) and 8nm Pt/Pd coating was applied before imaging with the SEM at 10kV.

Transmission electron microscopy. S. epidermidis-encapsulated living hydrogel underwent freezing in a high-pressure freezer (Baltec HPM 010, Technotrade). Freeze substitution was employed for preservation, involving a gradual temperature change from -180°C to -50°C over a span of five days. This process utilized a solution of 0.25% glutaraldehyde and 0.1% urinal acetate (GA-UA) dissolved in acetone. Upon reaching -50°C, the specimens were rinsed thrice with anhydrous acetone and gradually permeated with increasing concentrations of Hm20 Lowicryl resin over a period of four days (25%, 50%, 75%, and finally 100%, each for 24 hours). Following this, the specimens were rinsed with fresh 100% Hm20 solution and dislodged from their holders.

Polymerization of the resins took place under UV radiation for 24 hours at room temperature. The Leica AFS system was employed to control temperatures throughout the processes of freeze substitution, Lowicryl embedding, and resin polymerization. Using an ultramicrotome (Leica UC6), the resin blocks were affixed and sliced. The slices were then moved onto copper slot grids coated with formvar. Imaging was carried out with the aid of a 300kv FEI Tecnai G2 F30 Super Twin Transmission Electron Microscope.

Bacterial motility test. To prepare the solution phase sample, SYTO9-stained S. epidermidis was resuspended in fresh TSB medium (OD600=1.0). For the gel phase sample, SYTO9-stained S. epidermidis was enclosed within a starch-gelatin hydrogel. A volume of 10 µl from either the liquid suspension or the starch-gelatin hydrogel was then added to a 50 mm glass-bottom dish and covered with a glass coverslip. To facilitate imaging, the glass-bottom dish was placed on an INUB-ONICS TOKAI HIT Standard Heating Stage Top Incubator (UNIV-D56) set to a temperature of 25°C. Using a Nikon Ti2 microscope with 488 nm excitation, a video of S. epidermidis was recorded. Subsequently, the video was analyzed using the TrackMate plugin in ImageJ. The average speed of individual cells was calculated by dividing the total displacement by the tracking time.

Electrical analysis. A layer of starch-gelatin hydrogel with a thickness of 2 mm was applied onto an electrode with a disinfection geometry. Subsequently, potentiostatic electrochemical impedance spectroscopy (PEIS) and cyclic voltammetry (CV) measurement were conducted using the electrochemical workstation (Biologic SP-200). The impedance measurement spanned a frequency range of 100 kHz to 1 Hz, utilizing a sinusoidal amplitude of 20 mV.

Mechanical analysis. A rotational ARES rheometer (TA Instruments) equipped with parallel plates was employed to evaluate the viscoelastic properties of the living hydrogel. To preserve the

hydration of the hydrogel, the samples were surrounded with water throughout the experiments. Prior to each measurement, a slight contact force was applied to ensure proper contact between the plates and samples. The samples were allowed to soak for 100 seconds, enabling relaxation and rebalancing within the surrounding environment. The shear modulus was determined by subjecting the samples to an oscillatory shear strain of 1% at a frequency of 1Hz, unless stated otherwise. The adhesion strength was tested using the standard tensile test (ASTM F2258) at the Zwick-Roell ZwickiLine Z0.5. All tests were conducted at a constant tensile speed of 50 mm/min.

Fourier-Transform Infrared Spectroscopy (FTIR). To investigate the molecular interaction between starch and gelatin macromolecules, the different hydrogel samples with D2O (Sigma Aldrich) was measured by the Shimadzu IRTracer-100 Fourier transform infrared spectrophotometer.

Rat in vivo electromyography (EMG) recording. An adult rat ranging between 12 and 24 weeks and inclusive of both genders, was deeply anesthetized using 2-4% isoflurane. Fur from the animal's hindquarters was removed using surgical clippers and depilatory cream. A midline incision was made in the skin, following which the fascial plane between the gluteus maximus and the anterior head of the biceps femoris was opened, thereby exposing the sciatic nerve. The nerve was gently drawn-out using sutures, and a flexible Ti-Au/Polyimide electrode (thickness 10 nm/200 nm/5 μm) was coiled around the nerve bundle for the purpose of electrical stimulation. Then the hydrogel-coated mesh electrode was adhered to the rat's leg to facilitate multi-channel EMG recordings in response to sciatic nerve stimulation. Electrical stimulation was performed using a 2 ms biphasic electrical current ranging from 100 to 800 μA, which elicited muscle movement. For the recording process, an Intantech RHD USB interface board and an RHD 16-channel bipolar-input recording headstage were employed. Signals were recorded at a rate of 20

kS s^{-1} within the 100-1000 Hz bandwidth. All signal-to-noise ratio (SNR) in this paper is defined as:

$$SNR_{dB} = 10\ log_{10}(\frac{P_{signal}}{P_{noise}})$$

Psoriasis model. Eight-week-old male C57BL/6, B6.129-Tlr2tm1Kir/J (TLR2 KO) mice were housed in groups of five mice per cage and acclimatized for 7 days before inclusion in the investigation. To induce psoriasiform dermatitis, the mice were shaved and topically applied with 5% IMQ cream (Perrigo) for 3 consecutive days unless otherwise noted. For the therapeutic experiments, living bioelectronics with or without living components were topically applied to mouse dorsal skin for skin sensing and therapy. Tegaderm (3 M™) or band-aid were then used to fix the position of bioelectronics. Dressing was changed every day during the daily skin information collection episodes. During the experiment, changes in skin psoriasiform information including erythema, induration, and desquamation were recorded daily. The mice were euthanized on the last day of the experiment and their skin and spleen were harvested. The histological evaluation of the tissue was also performed. The general psoriasis symptoms, including the redness, scaling, and thickness (induction) of murine skin, were evaluated to score the "Psoriasis severity index (PSI)", which assesses the severity of the induced erythema, desquamation, and induration of the psoriasis. Each parameter was measured on a scale of 0–4 (from none to the maximum damage). The sum of these four values was the value of the PSI index, with the maximum value of 12.

Murine in-vivo 6- lead electrocardiogram (ECG) recording. The procedure was carried out on an adult mouse, including both healthy individuals and those exhibiting psoriasis on the chest. The subjects were deeply anesthetized using 2-4% isoflurane. A 6-lead living hydrogel-hybrid mesh electrode was adhered to a specific area covering the mouse's chest, strategically aligned to

conform to the standard positions for frontal plane ECG leads (*I, II, III, aVR, aVL,* and *aVF*). The recording procedure employed an Intantech RHD USB interface board and an RHD 16-channel bipolar-input recording headstage. Signals were recorded at a rate of 20 kS s^{-1}, within the bandwidth range of 0.6 - 100 Hz.

4.5 References

1 Jiang, Y. W., Zhang, Z. T., Wang, Y. X., Li, D. L., Coen, C. T., Hwaun, E., Chen, G., Wu, H. C., Zhong, D. L., Niu, S. M., Wang, W. C., Saberi, A., Lai, J. C., Wu, Y. L., Wang, Y., Trotsyuk, A. A., Loh, K. Y., Shih, C. C., Xu, W. H., Liang, K., Zhang, K. L., Bai, Y. H., Gurusankar, G., Hu, W. P., Jia, W., Cheng, Z., Dauskardt, R. H., Gurtner, G. C., Tok, J. B. H., Deisseroth, K., Soltesz, I. & Bao, Z. N. Topological supramolecular network enabled high-conductivity, stretchable organic bioelectronics. *Science* **375**, 1411-1417, doi:10.1126/science.abj7564 (2022).

2 Boys, A. J., Carnicer-Lombarte, A., Gueemes-Gonzalez, A., van Niekerk, D. C., Hilton, S., Barone, D. G., Proctor, C. M., Owens, R. M. & Malliaras, G. G. 3D Bioelectronics with a Remodellable Matrix for Long-Term Tissue Integration and Recording. *Adv Mater* **35**, doi:10.1002/adma.202207847 (2023).

3 Inda-Webb, M. E., Jimenez, M., Liu, Q., Phan, N. V., Ahn, J., Steiger, C., Wentworth, A., Riaz, A., Zirtiloglu, T., Wong, K., Ishida, K., Fabian, N., Jenkins, J., Kuosmanen, J., Madani, W., McNally, R., Lai, Y., Hayward, A., Mimee, M., Nadeau, P., Chandrakasan, A. P., Traverso, G., Yazicigil, R. T. & Lu, T. K. Sub-1.4 cm(3) capsule for detecting labile inflammatory biomarkers in situ. *Nature*, doi:10.1038/s41586-023-06369-x (2023).

4 Nan, K., Feig, V. R., Ying, B. B., Howarth, J. G., Kang, Z. L., Yang, Y. Y. & Traverso, G. Mucosa-interfacing electronics. *Nat Rev Mater* **7**, 908-925, doi:10.1038/s41578-022-00477-2 (2022).

5 Wang, M. Q., Yang, Y. R., Min, J. H., Song, Y., Tu, J. B., Mukasa, D., Ye, C., Xu, C. H., Heflin, N., McCune, J. S., Hsiai, T. K., Li, Z. P. & Gao, W. A wearable electrochemical biosensor for the monitoring of metabolites and nutrients. *Nat Biomed Eng* **6**, 1225-1235, doi:10.1038/s41551-022-00916-z (2022).

6 Gao, Y. J., Nguyen, D. T., Yeo, T., Lim, S. B., Tan, W. X., Madden, L. E., Jin, L., Long, J. Y. K. N., Aloweni, F. A., Liew, Y. J. A., Tan, M. L., Ang, S. Y., Maniya, S. D. O., Abdelwahab, I., Loh, K. P., Chen, C. H., Becker, D. L., Leavesley, D., Ho, J. S. & Lim, C. T. A flexible multiplexed immunosensor for point-of-care in situ wound monitoring. *Sci Adv* **7**, doi:10.1126/sciadv.abg9614 (2021).

7 Ouyang, W., Lu, W., Zhang, Y. M., Liu, Y. M., Kim, J. U., Shen, H. X., Wu, Y. Y., Luan, H. W., Kilner, K., Lee, S. P., Lu, Y. S., Yang, Y. Y., Wang, J., Yu, Y. J., Wegener, A. J., Moreno, J. A., Xie, Z. Q., Wu, Y. X., Won, S. M., Kwon, K., Wu, C. S., Bai, W. B., Guo, H. X., Liu, T. L., Bai, H. D., Monti, G., Zhu, J., Madhvapathy, S. R., Trueb, J., Stanslaski, M., Higbee-Dempsey, E. M., Stepien, I., Ghoreishi-Haack, N., Haney, C. R., Kim, T. I., Huang, Y. G., Ghaffari, R., Banks, A. R., Jhou, T. C., Good, C. H. & Rogers,

J. A. A wireless and battery-less implant for multimodal closed-loop neuromodulation in small animals. *Nat Biomed Eng*, doi:10.1038/s41551-023-01029-x (2023).

8 Wang, C. H., Chen, X. Y., Wang, L., Makihata, M., Liu, H. C., Zhou, T. & Zhao, X. H. Bioadhesive ultrasound for long-term continuous imaging of diverse organs. *Science* **377**, 517-523, doi:10.1126/science.abo2542 (2022).

9 Yang, Q. S., Wei, T., Yin, R. T., Wu, M. Z., Xu, Y. M., Koo, J., Choi, Y. S., Xie, Z. Q., Chen, S. W., Kandela, I., Yao, S. L., Deng, Y. J., Avila, R., Liu, T. L., Bai, W. B., Yang, Y. Y., Han, M. D., Zhang, Q. H., Haney, C. R., Lee, K. B., Aras, K., Wang, T., Seo, M. H., Luan, H. W., Lee, S. M., Brikha, A., Ghoreishi-Haack, N., Tran, L., Stepien, I., Aird, F., Waters, E. A., Yu, X. G., Banks, A., Trachiotis, G. D., Torkelson, J. M., Huang, Y. G., Kozorovitskiy, Y., Efimov, I. R. & Rogers, J. A. Photocurable bioresorbable adhesives as functional interfaces between flexible bioelectronic devices and soft biological tissues. *Nat Mater* **20**, 1559-1570, doi:10.1038/s41563-021-01051-x (2021).

10 Rochford, A. E., Carnicer-Lombarte, A., Kawan, M., Jin, A. M. Y., Hilton, S., Curto, V. F., Rutz, A. L., Moreau, T., Kotter, M. R. N., Malliaras, G. G. & Barone, D. G. Functional neurological restoration of amputated peripheral nerve using biohybrid regenerative bioelectronics. *Sci Adv* **9**, doi:10.1126/sciadv.add8162 (2023).

11 Song, E. M., Xie, Z. Q., Bai, W. B., Luan, H. W., Ji, B. W., Ning, X., Xia, Y., Baek, J. M., Lee, Y. J., Avila, R., Chen, H. Y., Kim, J. H., Madhvapathy, S., Yao, K. M., Li, D. F., Zhou, J. K., Han, M. D., Won, S. M., Zhang, X. Y., Myers, D. J., Mei, Y. F., Guo, X., Xu, S., Chang, J. K., Yu, X. G., Huang, Y. G. & Rogers, J. A. Miniaturized electromechanical devices for the characterization of the biomechanics of deep tissue. *Nat Biomed Eng* **5**, 759-771, doi:10.1038/s41551-021-00723-y (2021).

12 Karin, M. & Clevers, H. Reparative inflammation takes charge of tissue regeneration. *Nature* **529**, 307-315, doi:10.1038/nature17039 (2016).

13 Tang, T. C., An, B. L., Huang, Y. Y., Vasikaran, S., Wang, Y. Y., Jiang, X. Y., Lu, T. K. & Zhong, C. Materials design by synthetic biology. *Nat Rev Mater* **6**, 332-350, doi:10.1038/s41578-020-00265-w (2021).

14 Rodrigo-Navarro, A., Sankaran, S., Dalby, M. J., del Campo, A. & Salmeron-Sanchez, M. J. N. R. M. Engineered living biomaterials. **6**, 1175-1190 (2021).

15 Zhou, T., Yuk, H., Hu, F. Q., Wu, J. J., Tian, F. J., Roh, H., Shen, Z. Q., Gu, G. Y., Xu, J. K., Lu, B. Y. & Zhao, X. H. 3D printable high-performance conducting polymer hydrogel for all-hydrogel bioelectronic interfaces. *Nat Mater* **22**, 895-902, doi:10.1038/s41563-023-01569-2 (2023).

16 Severn, M. M. & Horswill, A. R. Staphylococcus epidermidis and its dual lifestyle in skin health and infection. *Nat Rev Microbiol* **21**, 97-111, doi:10.1038/s41579-022-00780-3 (2023).

17 Sauer, K., Stoodley, P., Goeres, D. M., Hall-Stoodley, L., Burmolle, M., Stewart, P. S. & Bjarnsholt, T. The biofilm life cycle: expanding the conceptual model of biofilm formation. *Nat Rev Microbiol* **20**, 608-620, doi:10.1038/s41579-022-00767-0 (2022).

18 Baumgartner, M., Hartmann, F., Drack, M., Preninger, D., Wirthl, D., Gerstmayr, R., Lehner, L., Mao, G. Y., Pruckner, R., Demchyshyn, S., Reiter, L., Strobel, M., Stockinger, T., Schiller, D., Kimeswenger, S., Greibich, F., Buchberger, G., Bradt, E., Hild, S., Bauer, S. & Kaltenbrunner, M. Resilient yet entirely degradable gelatin-based biogels for soft robots and electronics. *Nat Mater* **19**, 1102-1109, doi:10.1038/s41563-020-0699-3 (2020).

19 O'Neill, E. C. & Field, R. A. Underpinning starch biology with in vitro studies on carbohydrate-active enzymes and biosynthetic glycomaterials. *Front Bioeng Biotech* **3**, doi:10.3389/fbioe.2015.00136 (2015).
20 Bertoft, E. Understanding Starch Structure: Recent Progress. *Agronomy-Basel* **7**, doi:10.3390/agronomy7030056 (2017).
21 Ratnayake, W. S., Jackson, D. S. J. J. o. a. & chemistry, f. Gelatinization and solubility of corn starch during heating in excess water: new insights. **54**, 3712-3716 (2006).
22 Lin, Y. L., Gao, X., Yue, J. P., Fang, Y., Shi, J. Y., Meng, L. Y., Clayton, C., Zhang, X. X., Shi, F. Y., Deng, J. J., Chen, S., Jiang, Y., Marin, F., Hu, J. T., Tsai, H. M., Tu, Q., Roth, E. W., Bleher, R., Chen, X. Q., Griffin, P., Cai, Z. H., Prominski, A., Odom, T. W. & Tian, B. Z. A soil-inspired dynamically responsive chemical system for microbial modulation. *Nat Chem* **15**, 119-128, doi:10.1038/s41557-022-01064-2 (2023).
23 Wang, S. J., Li, C. L., Copeland, L., Niu, Q. & Wang, S. Starch Retrogradation: A Comprehensive Review. *Compr Rev Food Sci F* **14**, 568-585, doi:10.1111/1541-4337.12143 (2015).
24 Greb, J. E., Goldminz, A. M., Elder, J. T., Lebwohl, M. G., Gladman, D. D., Wu, J. J., Mehta, N. N., Finlay, A. Y. & Gottlieb, A. B. Psoriasis. *Nature Reviews Disease Primers* **2**, 16082, doi:10.1038/nrdp.2016.82 (2016).
25 Liang, H. Y., Yan, Y. Z., Wu, J. J., Ge, X. F., Wei, L., Liu, L. X. & Chen, Y. M. Topical nanoparticles interfering with the DNA-LL37 complex to alleviate psoriatic inflammation in mice and monkeys. *Sci Adv* **6**, doi:10.1126/sciadv.abb5274 (2020).
26 Bracho-Sanchez, E., Rocha, F. G., Bedingfield, S. K., Partain, B. D., Macias, S. L., Brusko, M. A., Colazo, J. M., Fettis, M. M., Farhadi, S. A., Helm, E. Y., Koenders, K., Kwiatkowski, A. J., Restuccia, A., Morales, B. S., Wanchoo, A., Avram, D., Allen, K. D., Duvall, C. L., Wallet, S. M., Hudalla, G. A. & Keselowsky, B. G. Suppression of local inflammation via galectin-anchored indoleamine 2,3-dioxygenase. *Nat Biomed Eng*, doi:10.1038/s41551-023-01025-1 (2023).

Chapter 5. Living biointerface for skin inflammation management

5.1 Introduction

Psoriasis is a chronic skin inflammatory disease, impacting an estimated 125 million population worldwide[1]. Psoriasis is characterized as an autoimmune disorder and it presents both cutaneous and systemic manifestations, imposing significant detriments on patient quality of life and also posing a financial strain on the healthcare system[2]. The psoriasis symptoms are usually associated with the distressing physical symptoms (e.g., itching, pains), devasting psychological impact (e.g., anxiety, suicidal ideation, and experience feelings of shame), and chronic rheumatological and cardiovascular co-morbidities[3]. While there is no complete cure for psoriasis, there is an increasing interest in designing new treatments to manage and alleviate its symptoms[4]. Presently, small-molecule drugs, including acitretin and cyclosporine, are widely used as the therapeutic options[5]. However, the potential for systemic side effects, including teratogenic effects and nephrotoxicity, becomes a concern, especially with imprecise or excessive medication usage[6]. Moreover, patients with moderate to severe psoriasis often face the challenge of recurrent flare-ups, leading to frequent and costly inpatient care[7]. A significant advancement in the treatment landscape has been the advent of biologics, predominantly monoclonal antibodies that target proinflammatory cytokines[8]. These include those aimed at TNF-α, like infliximab; IL-17, such as ixekizumab, brodalumab, and secukinumab; and IL-23, including ustekinumab and guselkumab. While these biologics have offered transformative results for patients who don't benefit from for traditional treatments, their cost remains prohibitive[9]. At approximately $25,000 per year, biologics are nearly ten times the cost of conventional treatments, relegating them to the status of second-line therapies[7]. In light of these challenges, there remains a pressing need for innovative medications

and monitoring systems. Such advances could gauge treatment responses more accurately, setting the stage for a future where precision medicine plays a central role in psoriasis management.

In addition to the therapeutic challenges posed by psoriasis, there's a critical need for advanced monitoring systems to track disease progression[10]. Effective therapy with innovative treatments necessitates an accurate, precise, and consistent assessment of disease severity tailored to each individual[11]. Recognizing and addressing ineffective therapies early can prevent further escalation of the disease and reduce the unwarranted treatment costs. Therefore, the introduction of new techniques that seamlessly integrate innovative therapies with real-time disease progression monitoring holds immense potential[12]. Such integrated systems could revolutionize the management of skin inflammatory diseases, paving the way for a new era of telemedicine and point-of-care precision medicine.

Herein, wearable bioelectronics have become an emerging technique in disease management[13]. They are capable of capturing physiological signals[14], monitoring inflammation for diagnostic purposes[15], and even performing biological modulation for targeted treatments[16]. Nevertheless, traditional bioelectronics face a significant challenge: their restricted capability in modulating diseased tissue. While there have been instances where drug-free bioelectronics effectively managed electro-active tissues, such as in wound healing[17], they fall short when it comes to more complex diseases like skin inflammation. A significant portion of this limitation is attributed to the absence of important biochemical and biological properties in current bioelectronic devices. With the aid of living materials, we introduced in last chapter, in this chapter, we delve into the application of living bioelectronics in disease management. We will illustrate how these innovative devices can simultaneously monitor disease progression and provide timely medical interventions, showcasing their potential as integrated solutions in disease management.

5.2 Result and Discussion

5.2.1 Wearable bioelectronics design

To achieve the long-term monitoring for the skin inflammatory diseases, the wireless wearable bioelectronics is essential to provide real-time monitoring, feedback, and insights in a convenient and non-invasive manner. Thus, we created a battery-free, wireless flexible printed circuit board (FPCB). The FPCB-based ABLE can achieve comprehensive interplay between the three components (i.e., hydrogel, bacteria, electronics). It is capable of (1) wireless energy harvesting and data transfer; (2) real-time disease progress monitoring via skin impedance, humidity, and temperature sensing; and (3) on-demand bacterial disinfection. The FPCB is highly flexible and functions effectively as it bends to conform to the skin tissue (Figure 5-1).

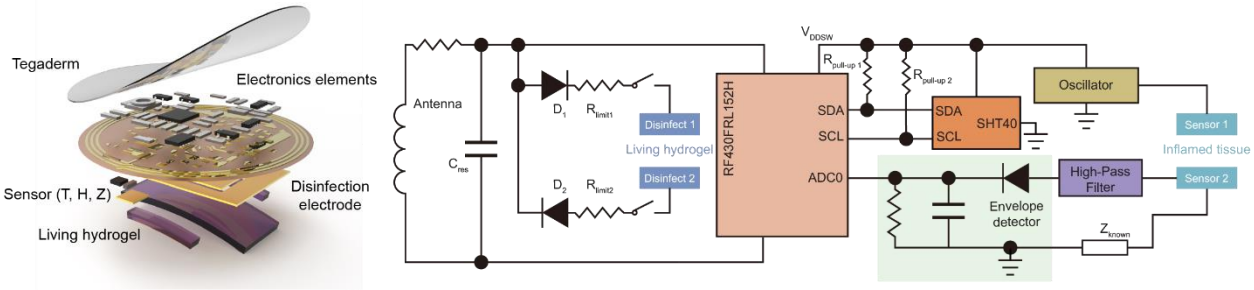

Figure 5-1 Schematic diagram shows the structural configuration of flexible printed circuit board (FPCB)-based ABLE. Circuit diagram of wireless bioelectronics for skin monitoring and living hydrogel modulation.

It integrates a near-field communication (NFC) transponder (RF430FRL152H) for radiofrequency (RF) energy harvesting and wireless data transfer following the ISO 15693 protocol (Figure 5-2).

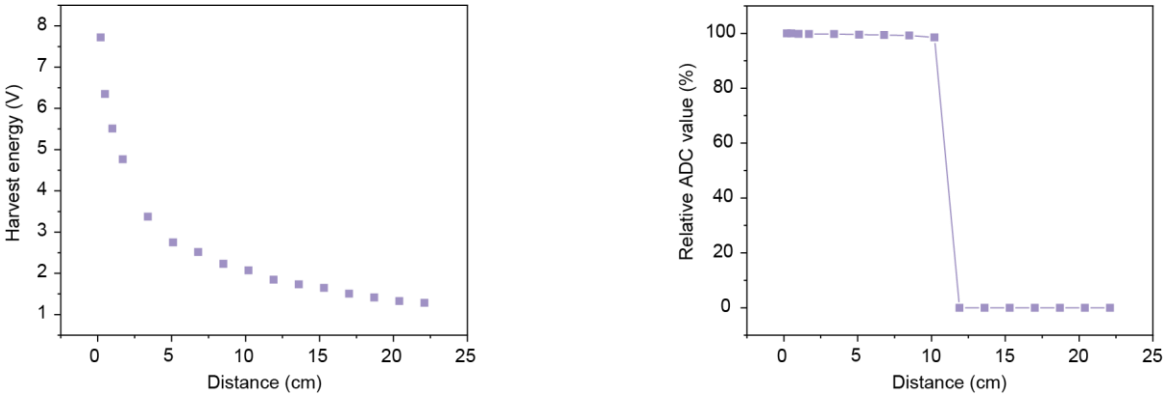

Figure 5-2 FPCB demonstrates the ability in wireless energy and data transition. Measured RF-harvested voltage is dependent on antenna–reader distance. Wireless communication functions well and stably when FPCB is 10 cm away from the external reader.

For comprehensive monitoring of inflammatory skin conditions, the FPCB incorporates an impedance sensor circuit (Figure 5-3) along with a commercialized temperature and humidity digital sensor (SHT40). In the impedance sensing methods, an oscillator produces a 32.768-kHz square-wave alternating current (AC) signal. This signal passes through both the skin and a known impedance component. By employing a voltage divider, the AC signal applied to this known impedance can mirror the wound's impedance. Any random direct current (DC) component within the oscillation signal is then eliminated via a high-pass filter (HPF). Subsequently, an envelope detector converts the amplitude of the AC signal to a DC voltage. This is then captured by the ADC0 channel within the RF430FRL152H transponder. Utilizing this method allows for continuous monitoring of skin impedance, which in turn indicates the status of skin inflammation.

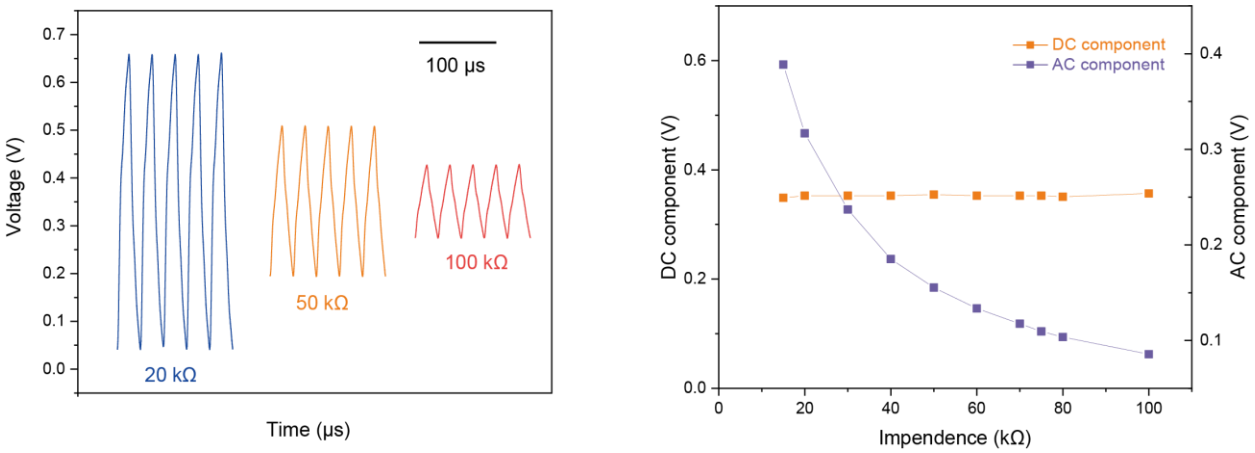

Figure 5-3 The voltage output in the impedance sensor, after passing through a high-pass filter, reveals a reduction in AC components for the higher impedance resistors. The DC components of the signals remain constant for all different impedance resistors.

The SHT40 sensor was chosen here because of its noise robustness, measurement repeatability, and low-power consumption (3.3 μW) due to its digital nature (Figure 5-4). The SHT4x is built on a newly optimized CMOSens® chip, which offers both reduced power consumption and enhanced accuracy specifications. With its extended supply voltage range of 1.08 V to 3.6 V, the SHT4x is ideally suited for mobile and battery-driven applications. Notably, the latest version to the date in humidity and temperature sensor technology is represented by the SHT45. This advanced sensor achieves a remarkable precision of ±1.0% RH for humidity and ±0.1°C for temperature. In our design, the SHT40 sensor was connected to the NFC transponder through the I2C protocol. The acquired sensing data can be wirelessly transferred and remotely analyzed to monitor disease recovery progress and provide information for bacterial modulation.

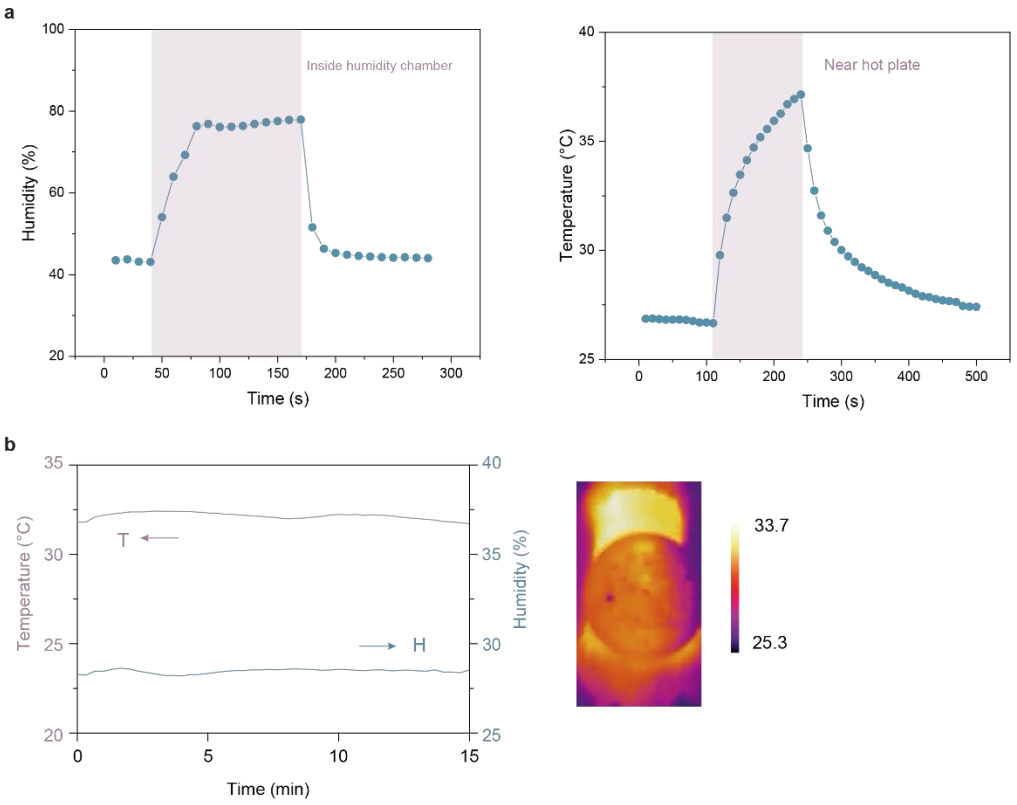

Figure 5-4 Validation experiments prove the FPCB has fast response to the environmental temperature and humidity variations. The FPCB detects environmental changes when it is placed inside a humidity chamber or brought into proximity with a hot plate. The FPCB with living interface can readily record the temperature and humidity information on the mice skin.

While application of living hydrogel in bioelectronics interfaces improved bioactivity for disease management, it presents practical challenges[18]. One major concern is that the S. epidermidis can proliferate and colonize on skin, leading to infections and the development of virulence factors[19]. Besides, current households are not equipped with proper biohazard containers to safely discard bacteria-laden materials[20]. Thus, our FPCB included two modulation electrodes with triggers for delivering electrical current in terminal disinfection. To maximize disinfection efficiency, we added a thin Au film to the back of the FPCB, which promotes reactive oxygen species (ROS)

generation in the hydrogels-electronics interface (Figure 5-5). Using bioelectronics for disinfection management, we can apply opportunistic pathogens (e.g., commensal bacteria) to the skin.

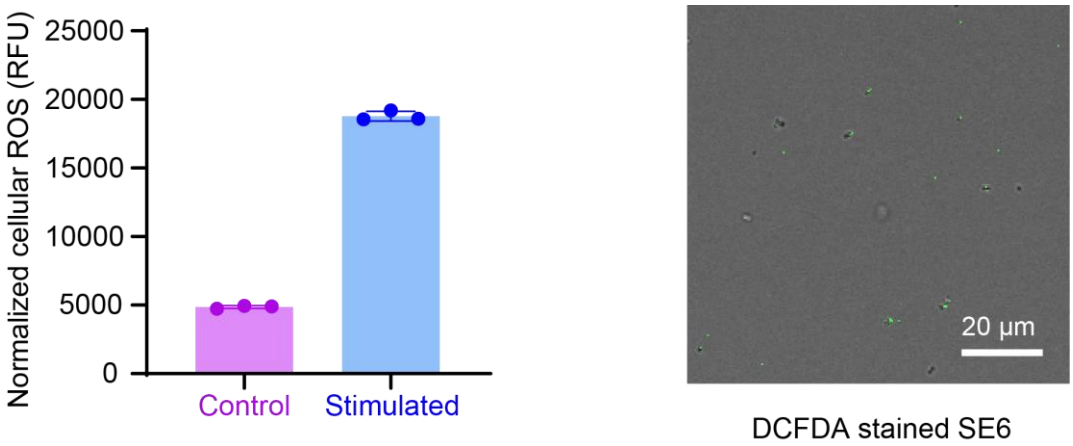

Figure 5-5 DCFDA/H2DCFDA staining of living material shows intracellular ROS level increase upon electrical field (EF) stimulation. Gelatin-encapsulated Staphylococcus epidermidis treated for 3.5V, 10 min shows about 4x higher intracellular ROS fluorescence intensity compared to unstimulated control, when normalized with % viability from LIVE/DEAD assay. Data are presented as mean values ± SD. n=3 for each group.

In preclinical assessments, open-field movement tests confirmed that the lightweight and wireless ABLE does not hinder mouse mobility (Figure 5-6). Furthermore, we validated the functionality of sensors attached to mouse dorsal skin during movement, confirming sensor reliability for research and data collection.

Figure 5-6 Living bioelectronics are lightweight and untethered with cable. (Left) The photograph shows the mice wearing living bioelectronics. (Middle) Representative moving trajectories of mice between the with device and without device group. (Right) The travel distance comparison indicates the living bioelectronics will not interfere with the motion of mice in the cage. Data are presented as mean values ± SD. n=4 for each group.

5.2.2 Living bioelectronics in skin inflammation management

Incorporating the FPCB circuit in the ABLE design, we can integrate disease monitoring with drug-free skin cellular modulation for disease treatment (Figure 5-7).

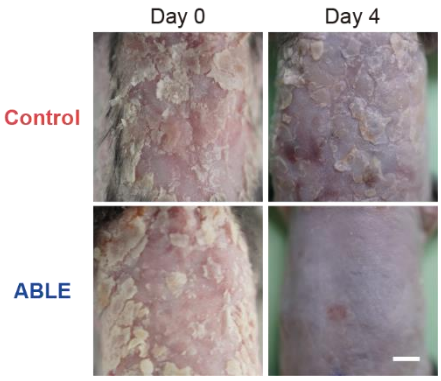

Figure 5-7 Representative photographs at Day 0 and Day 4 showing that the living bioelectronics treats psoriasis. Psoriasiform features including erythema, induration, and desquamation, are all significantly diminished. Scale bar, 5 mm.

The constant decrease in impedance recorded by ABLE during the recovery process aligns well with the psoriasis severity index (PSI) of the mice skin over 4 days (Figure 5-8). PASI is a widely-used tool in biomedical settings to determine the severity of psoriasis in human. It evaluates and scores the extent and severity of psoriatic lesions based on erythema (redness), induration (thickness), and desquamation (scaling). In mice model, the area is not a countable parameter, so we only use PSI score. Characteristic clinical symptoms of psoriasiform skin, including erythema, induration, and desquamation were all largely reduced after ABLE treatment, indicating how living biointerfaces can regulate the immune system.

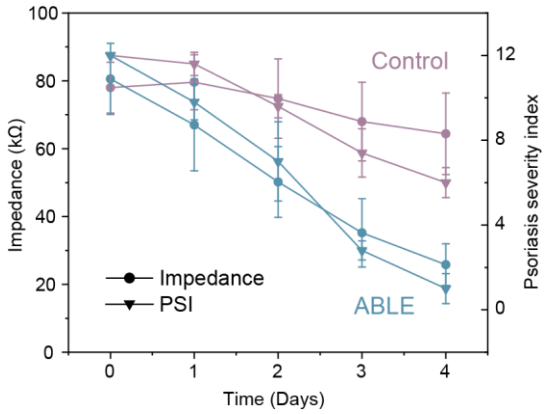

Figure 5-8 Impedance of psoriasis skin lesions, as measured using living bioelectronics, indicates recovery progress. Results align with the psoriasis severity index (PSI). Data are presented as mean values ± SD. n=5 for each group.

Humidity and temperature information over 4 days of treatment also provides essential information on the changing skin environments (Figure 5-9).

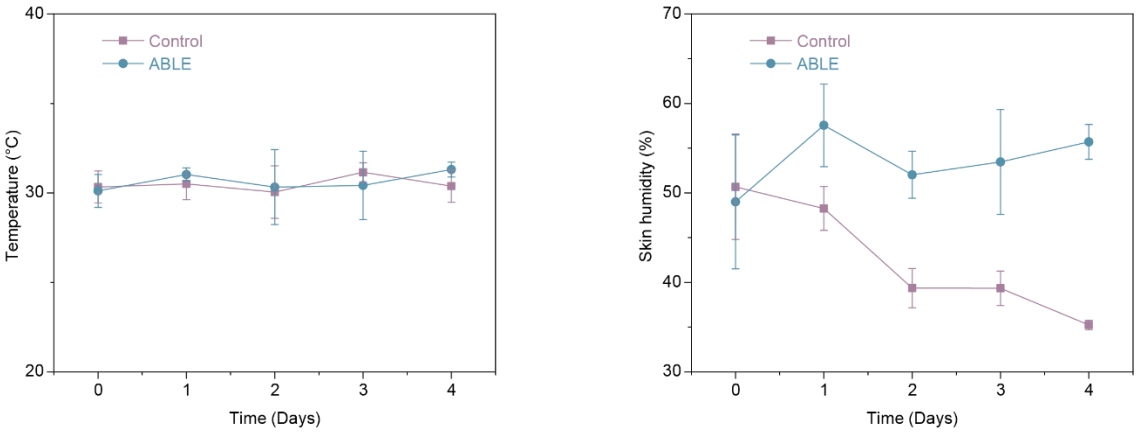

Figure 5-9 Temperature and humidity sensors monitor skin information during disease treatment. Data are presented as mean values ± SD. n=5 for each group.

Moreover, upon treatment completion, two disinfection electrodes positioned in the ABLE deliver direct current (DC) to the living hydrogel interface for 30 minutes of disinfection (Figure 5-10). This process effectively disinfects the bacteria present within the living interface, as supported by the confocal microscope imaging. This feature significantly reduces the biohazard risk associated with the living hydrogel, ensuring biosafety for both humans and the environment.

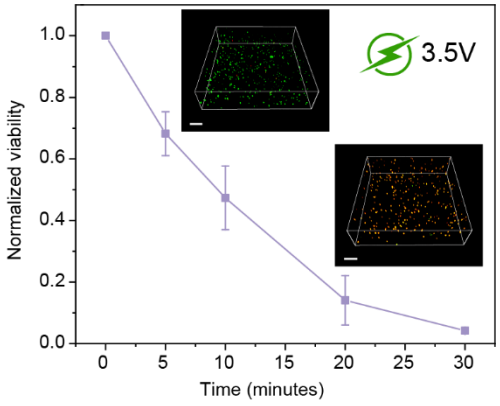

Figure 5-10 Disinfection electrodes on the living bioelectronics disinfect the living hydrogel through 3.5 V direct voltage within 30 minutes. Inner panel shows confocal images of living hydrogel before and after disinfection. Bacteria were stained with Baclight Live/Dead kit containing SYTO9/PI. Scale bar, 20 μm.

In addition to examining the impact of disinfection time on outcomes, we also explored the influence of applied voltage on the results (Figure 5-11). The figure illustrates that low voltages between 1.0-2.0V do not significantly disinfect bacteria. However, with higher voltages, bacteria are disinfected efficiently.

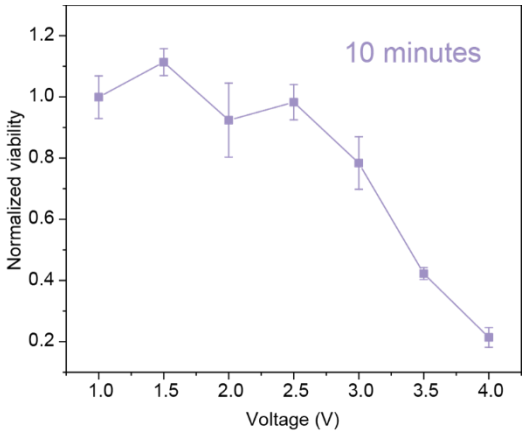

Figure 5-11 A higher voltage output demonstrates a faster disinfection efficiency for living bioelectronics. The disinfection time is set for 10 minutes. Data are presented as mean values ± SD. (n=3).

5.2.3 Histology and cytokine analysis

We next studied how the ABLE biochemically modulates the cellular environment in inflammatory skin conditions. Although the role of S. epidermidis in mediating skin homeostasis is widely known[21,22], there is minimal literature on its therapeutic effects in psoriasis, let alone translation to clinic. This gap in knowledge may be attributed to the scarcity of suitable housing matrices and accessible monitoring systems for systematic investigation of interactions between commensal bacteria and skin tissue[18]. The ABLE provides a regulatory platform for delving into these interaction mechanisms.

The spleen is an important component of the immune system, with critical roles in both innate and adaptive immunity. It functions to filter the blood, removing damaged or aged red blood cells and actively detects and responds to pathogens and other foreign elements. Variations in spleen weight, especially splenomegaly (an enlarged spleen), can signify different immunological conditions or diseases. Following our treatment using living bioelectronics, we observed a decrease in spleen weight by Day 4. This suggests that the ABLE can influence and modulate the entire immune system, as illustrated (Figure 5-12).

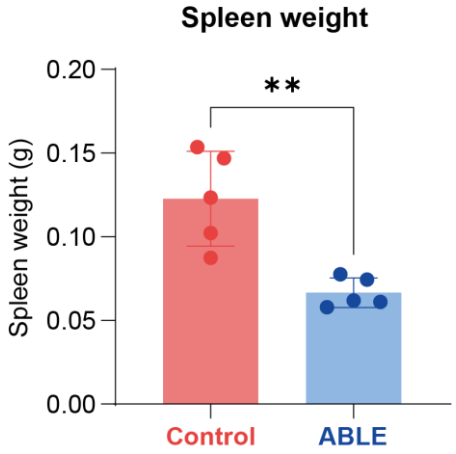

Figure 5-12 Living bioelectronics treatment reduced splenomegaly in psoriatic mice. Data are presented as mean values ± SD. n=4 for each group.

We subsequently employed Hematoxylin and eosin (H&E) staining to analyze the skin. This technique is widely used in histology, utilized to delineate the microscopic structures of tissues. Hematoxylin, a basic dye, colors cell nuclei blue, whereas eosin, an acidic counterpart, imparts a pink to red hue to the cytoplasm and extracellular matrix. This color differentiation distinctly outlines various cellular and extracellular components, rendering H&E staining invaluable in pathology, especially for diagnosing skin ailments. Notably, post-ABLE treatment, the H&E

staining revealed a marked decrease in epidermal thickening (hyperplasia), parakeratosis, and cutaneous inflammation in skin lesions (Figure 5-13 and Table 5-1).

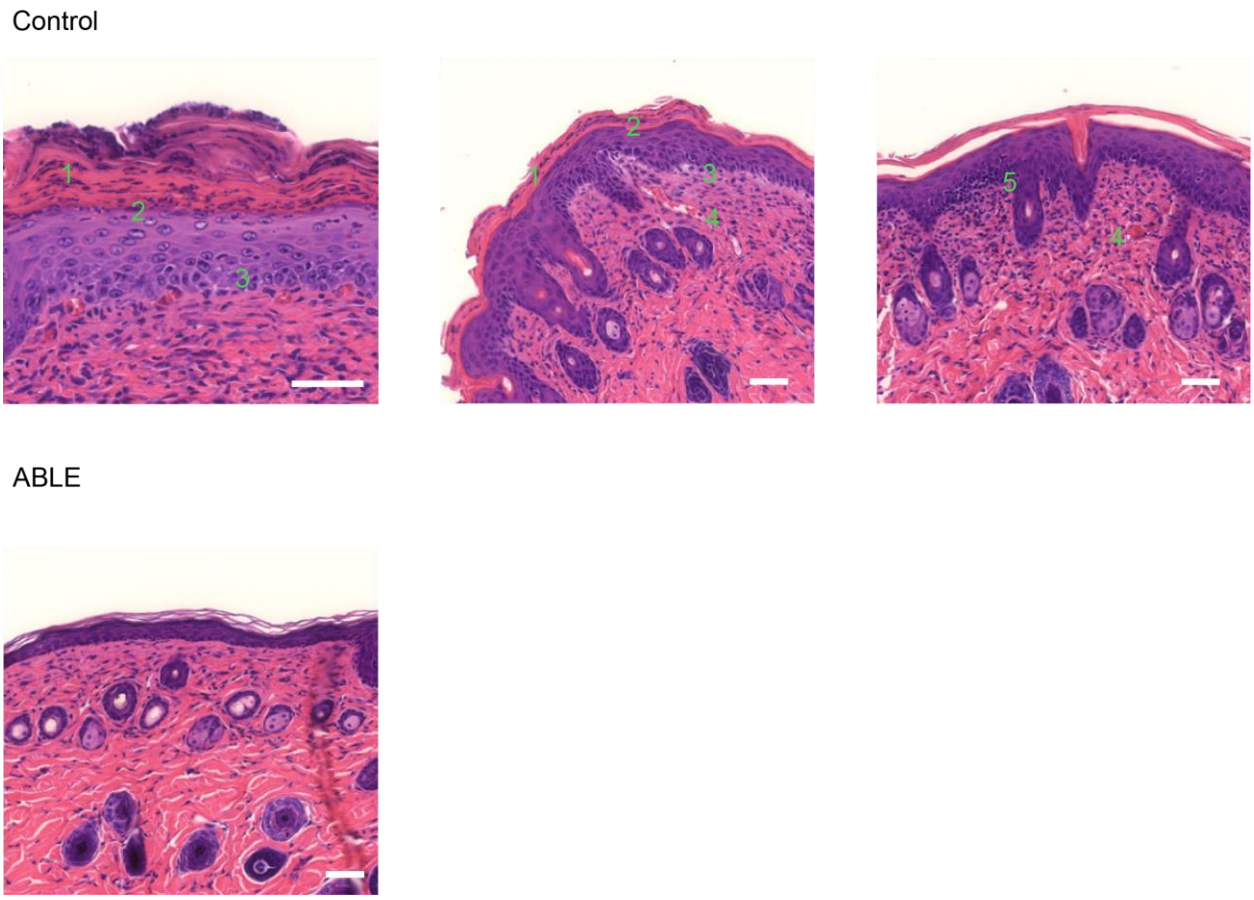

Figure 5-13 Histological assessment indicates that ABLE treatment significantly alleviated psoriatic features, in comparison to the control group. The psoriatic feature includes 1, parakeratosis; 2, loss of granular layer; 3, psoriasiform hyperplasia; 4, dilated blood vessels; 5, inflammation. Scale bar, 50 μm.

Histopathological characteristics of psoriasis	**Control**	**ABLE**
Psoriasiform hyperplasia	Moderate (5/5)	Barely seen (5/5)
Parakeratosis	Positive (5/5)	Negative (5/5)
Neutrophil in stratum corneum	Positive (5/5)	Negative (5/5)
Loss of granular layer	Discontinuously seen (5/5)	Negative (5/5)
Dilated capillaries	Universally positive (5/5)	Negative (5/5)

Table 5-1 Histopathological summary of the mice skin after ABLE treatments.

Note that the hydrogel matrix alone, when combined with the bioelectronics device (*i.e.*, the vehicle without the bacterial component), demonstrated limited therapeutic effects on psoriasis as shown in Figure 5-14. This is corroborated by the Psoriasis Severity Index (PSI) when compared to treatment with ABLE. Moreover, splenomegaly, resulting from abnormal immune system activities, persisted after the treatment in the vehicle group. Additionally, we conducted H&E histology to examine the pathology of the skin lesions. As depicted in Figure 5-14, epidermal thickening (hyperplasia), parakeratosis, and cutaneous inflammation remain evident in the skin lesions. This serves as an essential control, underscoring the significance of biogenic components in bioelectronics.

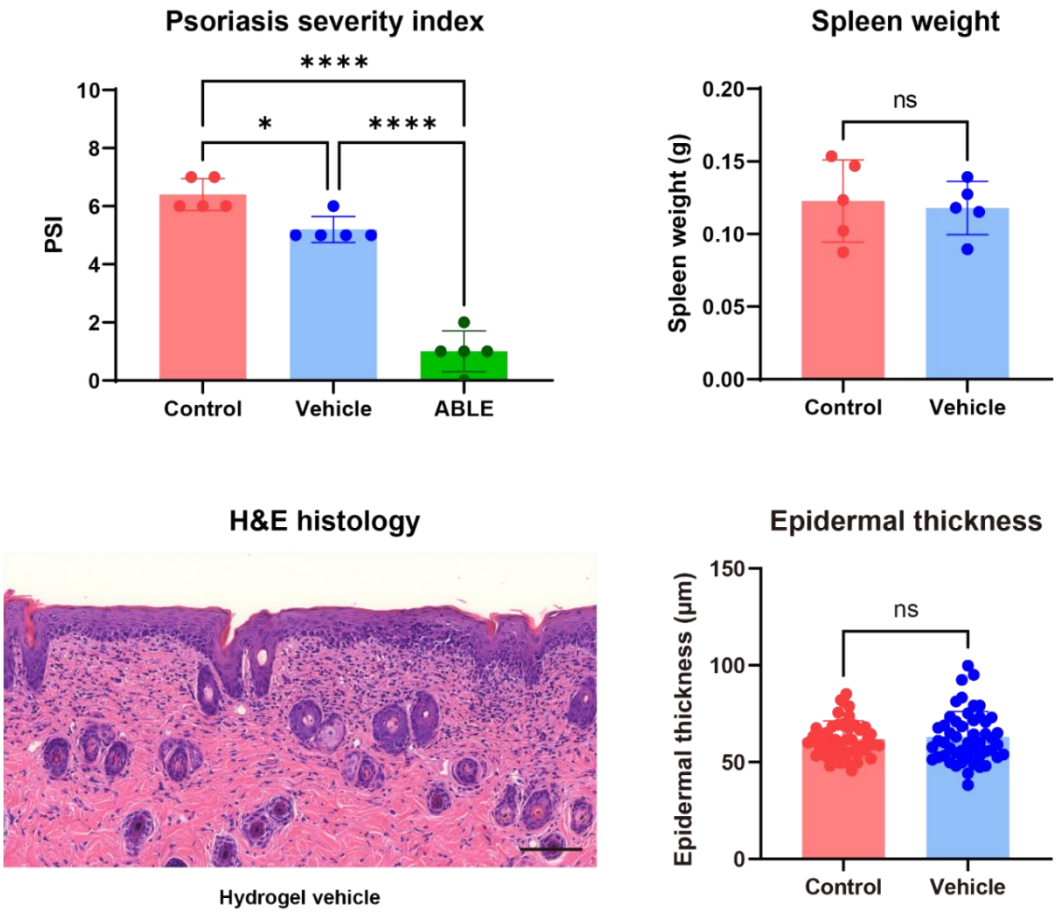

Figure 5-14 Hydrogel as the vehicle interface has limited therapeutic effect in treating psoriasis. Bioelectronics with non-living hydrogel matrix does not reduce the skin psoriasiform symptoms as indicated by psoriasis severity index (PSI). Besides, the symptoms regarding splenomegaly and psoriasiform hyperplasia still exist. Scale bar, 100 μm.

Then, to fully understand the immune environment under skin, we perform the immunohistochemistry analysis for the skin samples. Immunohistochemistry analysis (IHC) of Cytokeratin 14 and F4/80 demonstrated a notable decrease in dendritic cells and macrophages activities following ABLE treatment (Figure 5-15).

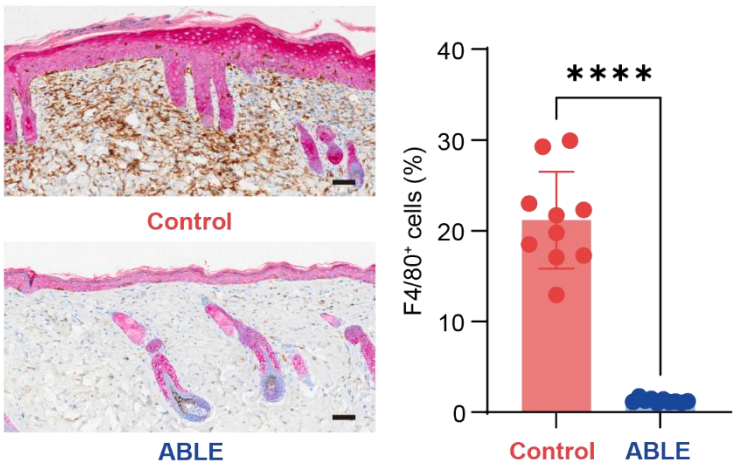

Figure 5-15 Representative dual-immunohistochemical images of Cytokeratin 14 and F4/80 staining indicate significantly decreased dendritic cells and macrophages in psoriatic skin lesions of ABLE-treated mice. Scale bar, 50 μm. Data are presented as mean values ± SD. n=10 for each group.

IHC of CD4 indicated a significant reduction of T helper cells (Figure 5-16). CD4 is a glycoprotein found on the surface of several cells, including T helper cells, monocytes, macrophages, and dendritic cells. In IHC, anti-CD4 antibodies target and detect the presence of these CD4-expressing cells within tissue samples. This detection is informative in the study and diagnosis of inflammatory diseases, allowing for a deeper understanding of the role T helper cells play in the disease's pathology.

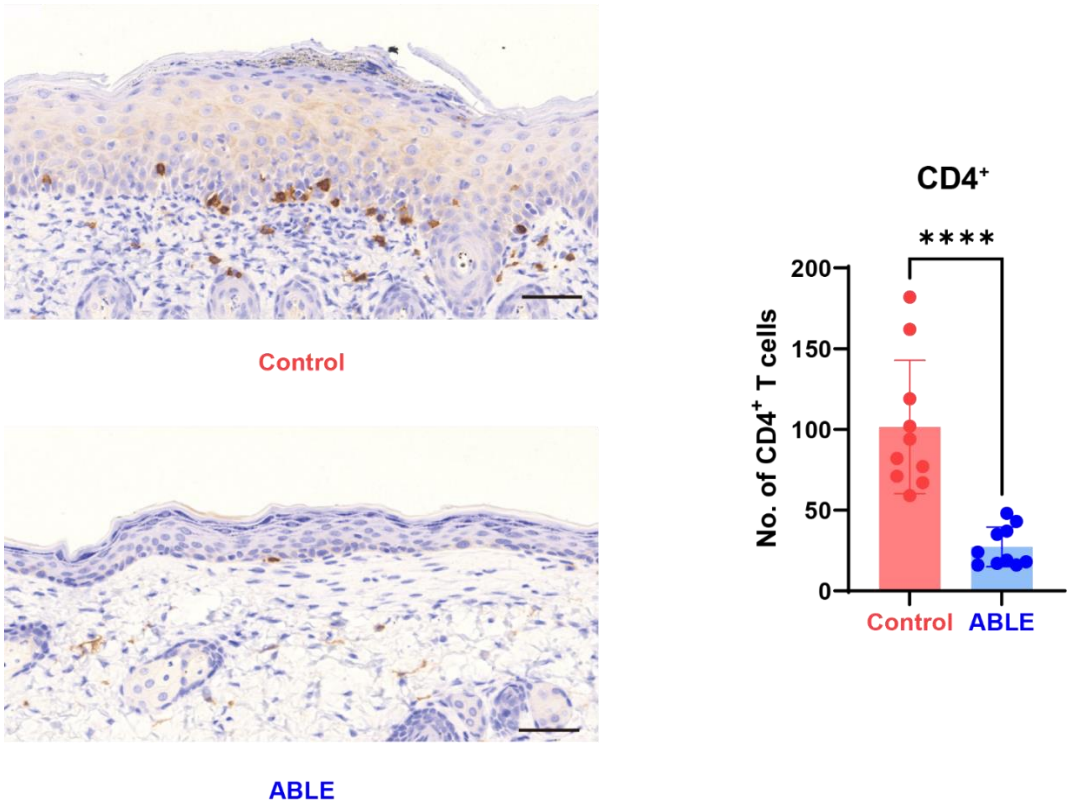

Figure 5-16 CD4 immunohistology images of skin tissue after ABLE treatment show that the ABLE treatment downregulated the number of cutaneous CD4$^+$ T helper cells during the recovery process. Scale bar, 50 µm.

Alongside CD4, IHC for CD8 revealed a marked decrease in T cytotoxic cells, as illustrated in Figure 5-17. CD8 is a glycoprotein expressed on the surface of cytotoxic T cells, also referred as CD8$^+$ T cells. Using anti-CD8 antibodies in immunohistochemistry enables the detection of these CD8-expressing cells under skin tissue. CD8 IHC is principally utilized to assess immune cell distribution in various inflammatory conditions, thereby facilitating a deeper understanding of the role cytotoxic T cells play in the autoimmune disease progression.

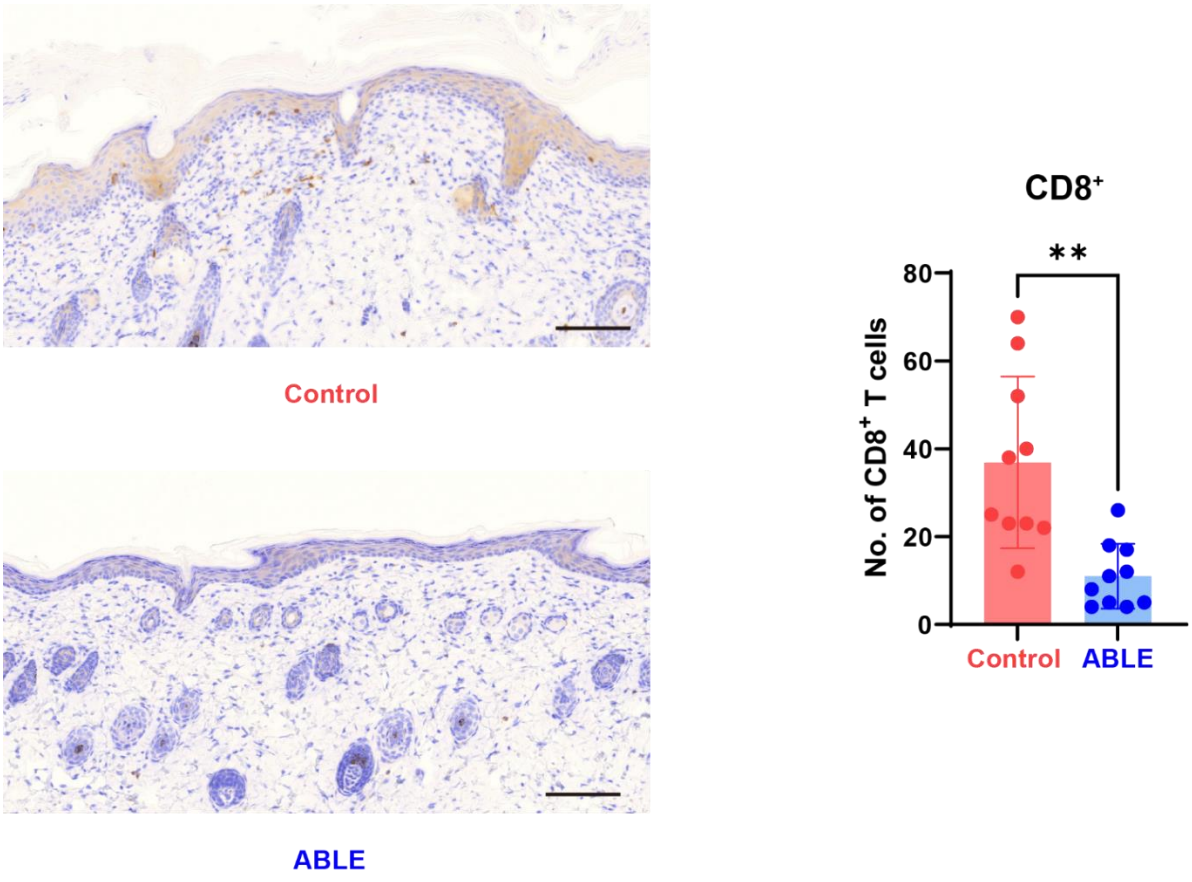

Figure 5-17 CD8 immunohistology images of skin tissue after ABLE treatment show that the ABLE treatment downregulated the number of cutaneous CD8$^+$ cytotoxic T cells during the recovery process. Scale bar, 100 µm.

Furthermore, immunostaining utilizing Ki-67 highlighted a decrease in epidermal proliferation (Figure 5-18). The Ki-67 protein is a nuclear protein intimately associated with cellular proliferation. It is present during all active cell cycle phases (G1, S, G2, and mitosis) but is conspicuously absent in dormant (G0) cells. As a result, Ki-67 is an invaluable marker for gauging the growth fraction of specific cell populations. The primary utility of Ki-67 IHC lies in its capacity to assist in diagnosis, provide prognostic evaluations, and guide therapeutic decision-making.

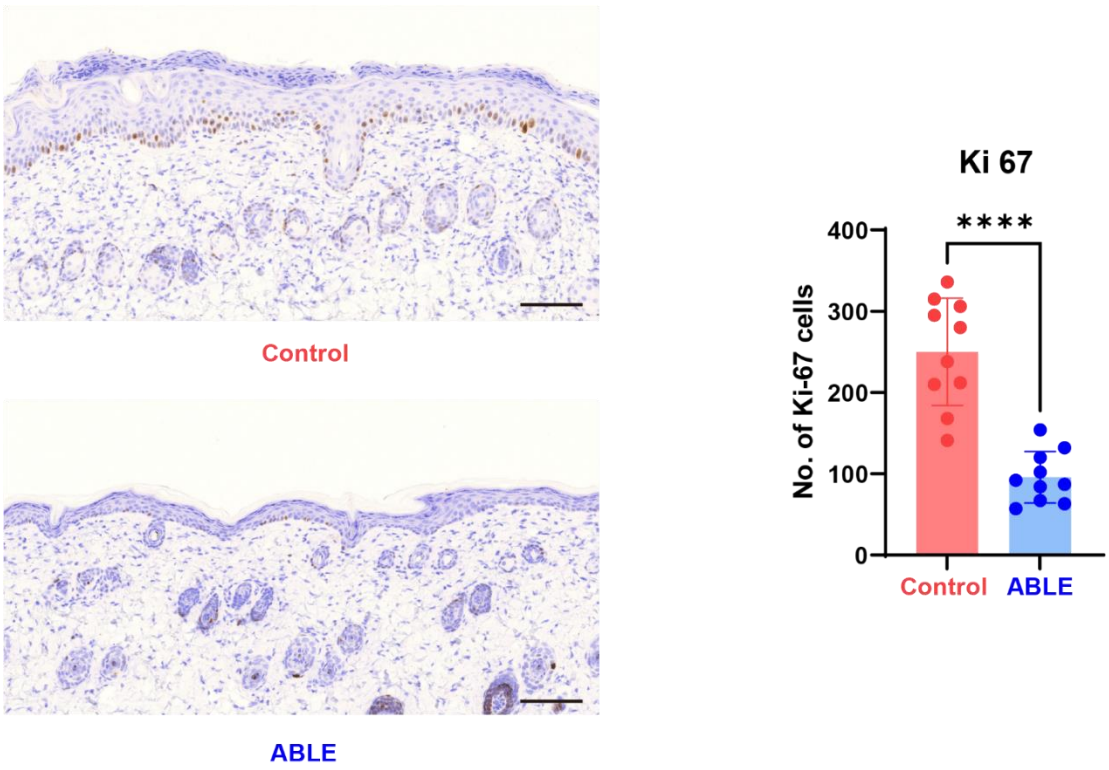

Figure 5-18 Ki-67 immunohistology images of skin tissue after ABLE treatment show that the ABLE treatment downregulated the expression level of Ki67 antigen in the basal layer of epidermis. Scale bar, 100 µm.

CD31 immunofluorescence staining revealed fewer dilated blood vessels in ABLE-treated samples after 4 days compared to controls (mice with IMQ-induced psoriasis, no treatment) (Figure 5-19). The CD31 protein, also known as platelet endothelial cell adhesion molecule-1 (PECAM-1), is predominantly expressed under the skin that form the linings of blood vessels. Owing to its specific expression in endothelial cells, CD31 IHC is primarily employed to study angiogenesis, the process of new blood vessel formation, and the progress of the injured or inflammatory disease. Monitoring angiogenesis is pivotal as it offers insights into tumor growth, invasion, and metastasis. This is crucial because tumors necessitate blood vessels for both growth and dissemination.

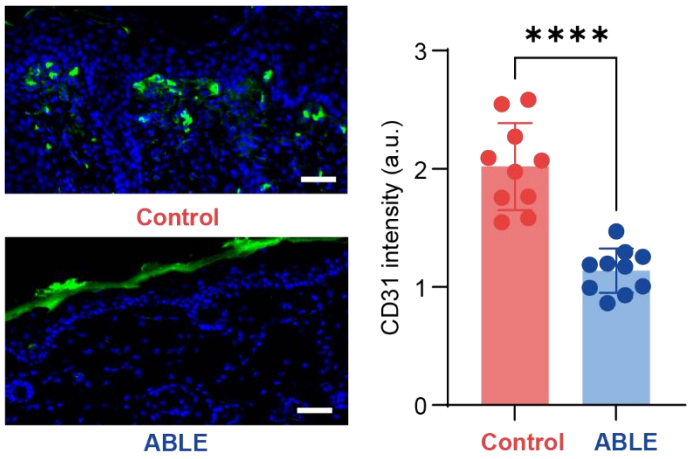

Figure 5-19 Representative immunofluorescent images of CD31 staining indicate significantly decreased blood vessel formation in skin lesions of ABLE-treated mice. False positive signals in the ABLE image are due to unspecified staining in the stratum corneum. Scale bar, 50 μm. Data are presented as mean values ± SD. n=10 for each group.

Cytokine analysis can provide the quantification and characterization of cytokines under skin. Cytokines are small protein molecules vital for cell signaling. These molecules are paramount in cellular communication, especially within the immune system. Encompassing interferons, interleukins, tumor necrosis factors, growth factors, and more, cytokines oversee a broad spectrum of biological functions in the body. These range from regulating inflammation and immune responses to guiding cell growth. Thus, we performed the cytokine analysis for our skin samples. Cytokine analysis showed reduced levels of inflammatory cytokines, with notable reductions in IL-17, IFN-γ, TNF-α, and IL-1, which play a crucial role in promoting recruitment of inflammatory cells to psoriatic plaque lesions, regulating keratinocyte proliferation, and disease development (Figure 5-20).

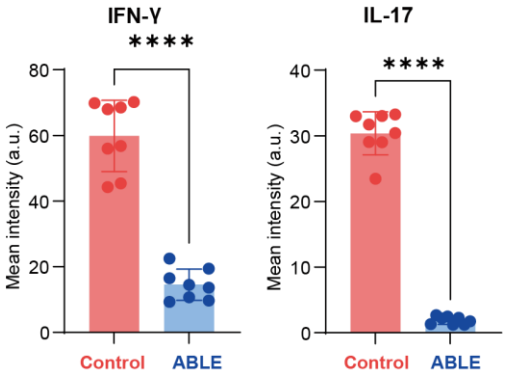

Figure 5-20 Cytokine analysis of the skin lesion indicates significant down regulation of IFN-γ and IL-17, which play an important role in inflammatory cell recruitment and regulate keratinocyte proliferation. Data are presented as mean values ± SD. n=8 for each group.

These findings collectively highlight the potential of living bioelectronics in modulating the inflammatory microenvironment and key aspects of psoriasis pathogenesis, including immune dysregulation, cellular proliferation, neovascularization, and cytokine-mediated inflammation. For a detailed cytokine analysis, we present the results of the interleukin family (Figure 5-21). The interleukin (IL) family encompasses a range of cytokines that have varied functions but are primarily centered on mediating interactions and facilitating communication between white blood cells. As the name suggests— "interleukin" translates to "between leukocytes" or white blood cells—these cytokines play pivotal roles in directing the immune system's reactions to both disease and injury. Furthermore, interleukins have the capability to either augment or diminish inflammation, underscoring their critical nature in immune responses.

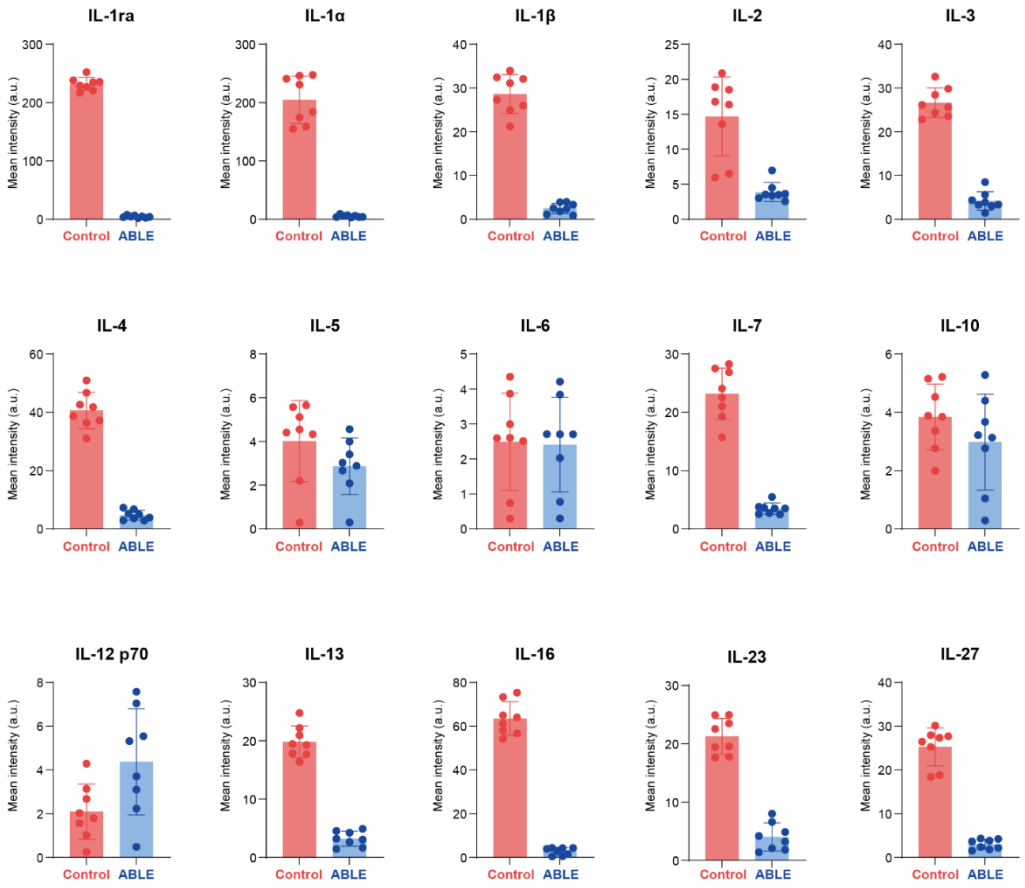

Figure 5-21 Cytokine analysis in psoriatic skin lesion reveals that the inflammation-related cytokines (IL family) are mostly down-regulated on Day 4 after ABLE treatment. Data are presented as mean values ± SD. n=8 for each group.

The rest important cytokine result is listed in Figure 5-22. They also give important information regarding the inflammatory status under the skin.

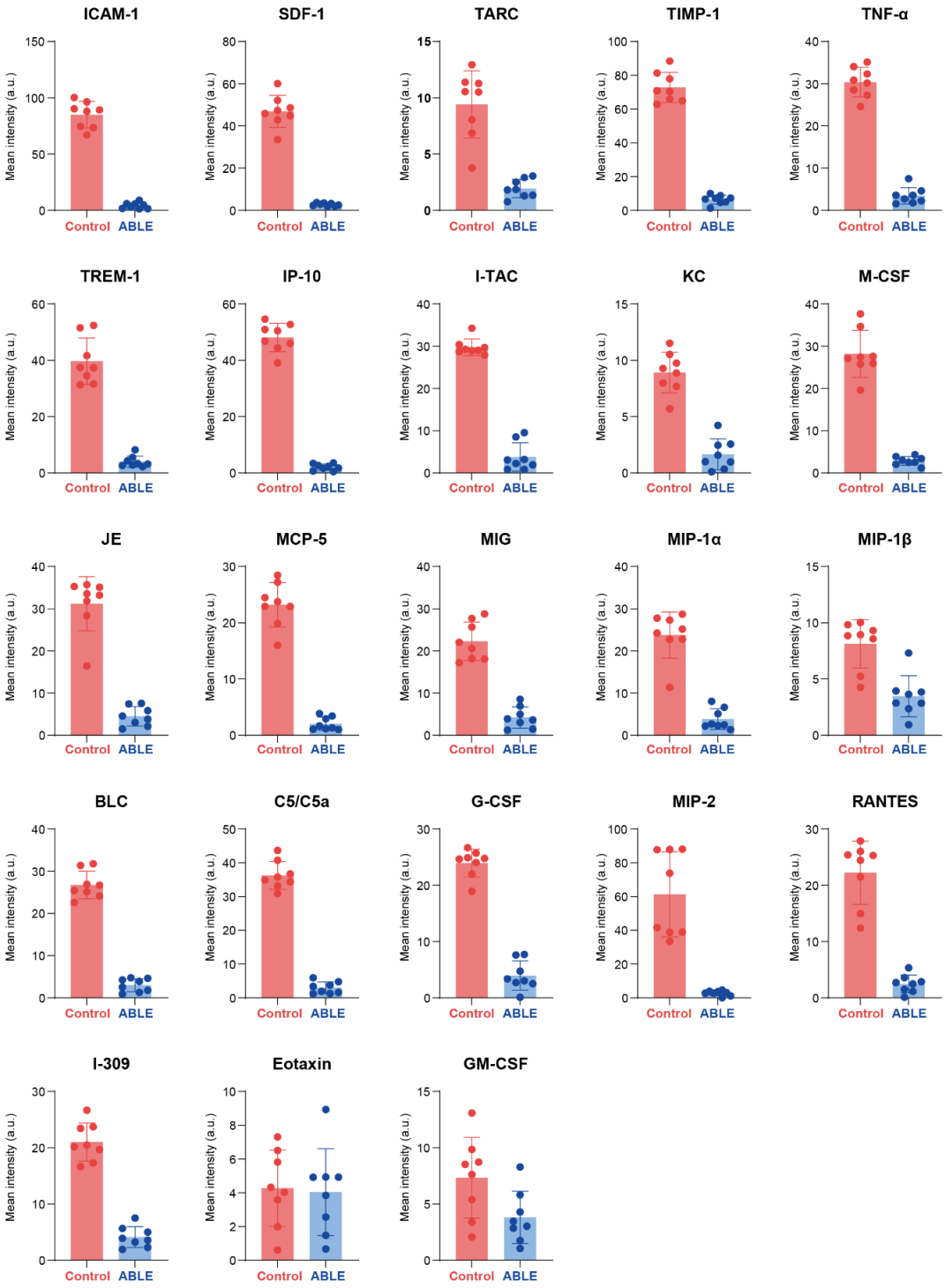

Figure 5-22 Cytokine analysis in psoriatic skin lesion reveals that the inflammation-related cytokines and chemokine (the rest) are mostly down-regulated after ABLE treatment on Day 4. Data are presented as mean values ± SD. n=8 for each group.

5.2.4 Skin microbiota and transcriptomics analysis

To gain further insight into ABLE modulation of skin microbiota, we conducted 16S ribosomal RNA gene sequencing analysis of the treated skin samples. 16S rRNA gene sequencing is a widely-used technique for identifying and differentiating bacteria within varied samples. By targeting the 16S rRNA gene, this method encompasses PCR amplification using specific primers, and then sequencing, typically via next-generation platforms. The obtained sequence data is then subjected to quality control, OTU picking, taxonomic assignment, and additional diversity analysis. This provides insights into microbial compositions on the skin community, potential links to diseases, and patterns in environmental distributions. Linear discriminant analysis Effect Size (LEfSe) results from our skin microbiota 16S rRNA results indicated that the ABLE effectively modulated the skin microbiota, inducing a transition from a psoriatic state to a healthier state (Figure 5-23).

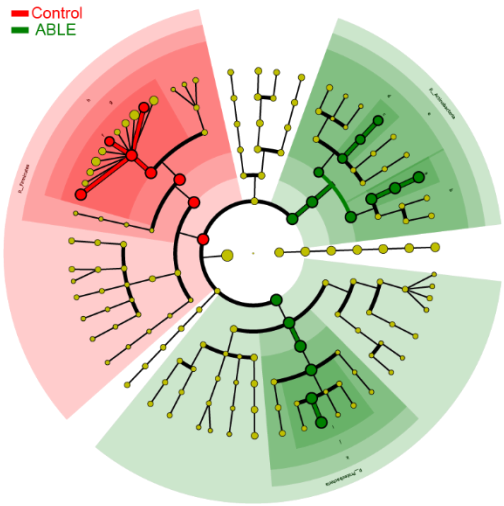

Figure 5-23 Linear discriminant analysis Effect Size (LEfSe) taxa analysis indicates altered bacterial diversity following ABLE treatment.

A Principal Coordinates Analysis (PCoA) plot of beta diversity showed that skin microbiota profiles in ABLE-treated mice were distinct from those in the control group, but quite close to those in healthy mice (Figure 5-24).

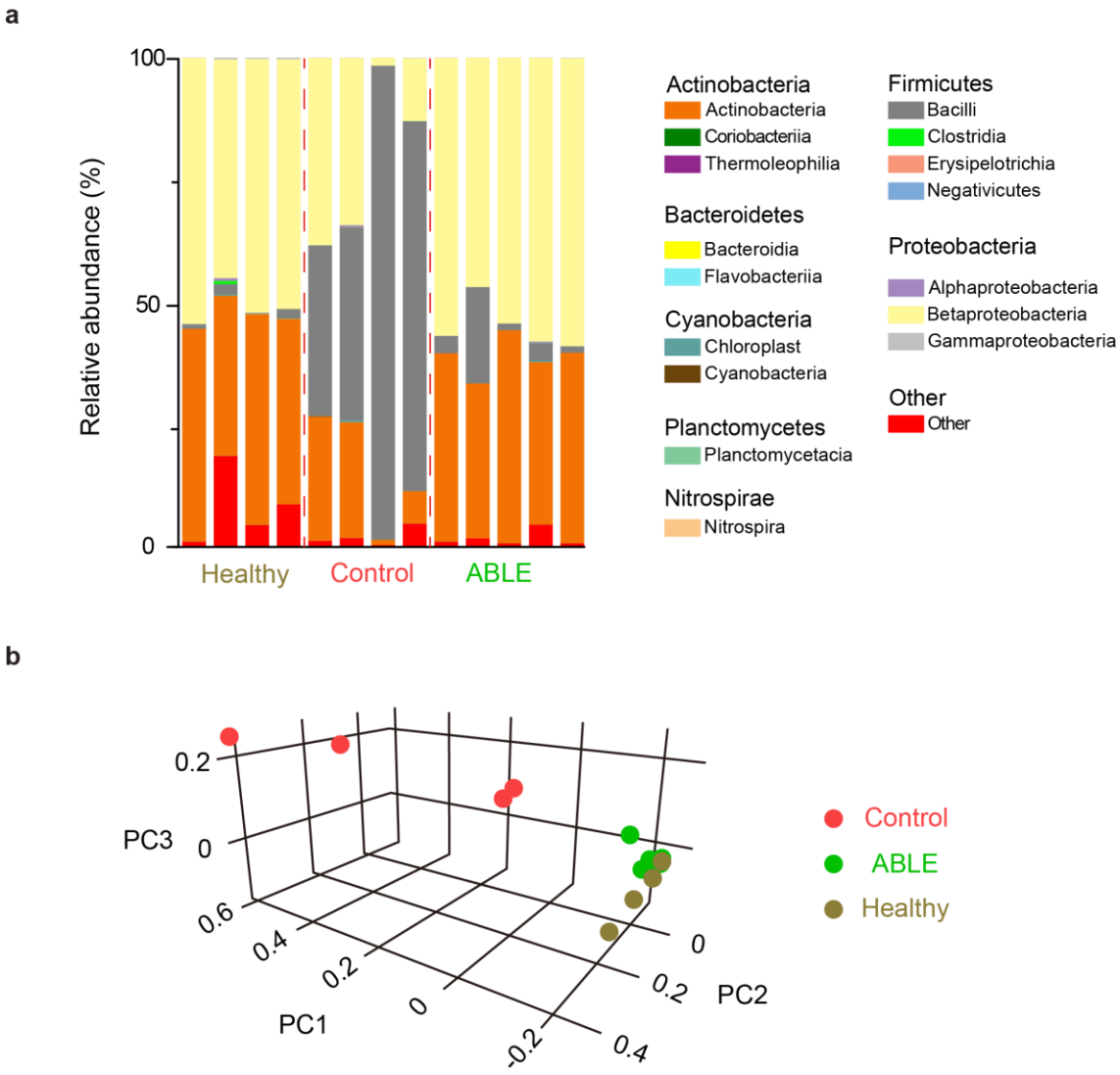

Figure 5-24 16S rRNA sequencing result indicates that the ABLE could modulate the skin microbiota towards healthy conditions. (a)Taxa composition plots illustrate the skin microbial compositions at different taxonomy levels from phylum to class. (b) Principal Coordinates Analysis (PCoA) plot of beta diversity revealed that ABLE-treated mice had distinct skin microbiota profiles from control group, but quite similar to healthy mice.

At the species level, we observed a low abundance of S. epidermidis on the skin, indicating low S. epidermidis related safety concern under the bioelectronics control. Furthermore, the abundance of Staphylococcus aureus, a species known to be associated with psoriasis progression35, was also significantly reduced (Figure 5-25).

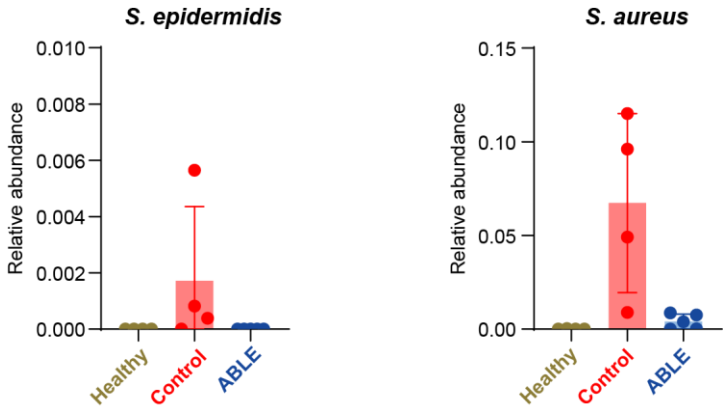

Figure 5-25 *S. epidermidis* is barely detected on skin during ABLE treatment. Relative abundance of Staphylococcus aureus is reduced after ABLE treatment. Data are presented as mean values ± SD. n>4 for each group.

We noticed that the abundance of other skin microbes, such as *Rhodococcus erythropolis* and *Delftia acidovorans*, was also significantly modulated by ABLE (Figure 5-26). The findings require further systematic investigation given the limited studies in past literature. Altogether, changes in bacterial abundance can probably be attributed to the mutual interactions between different bacterial species and Staphylococcus epidermidis[23].

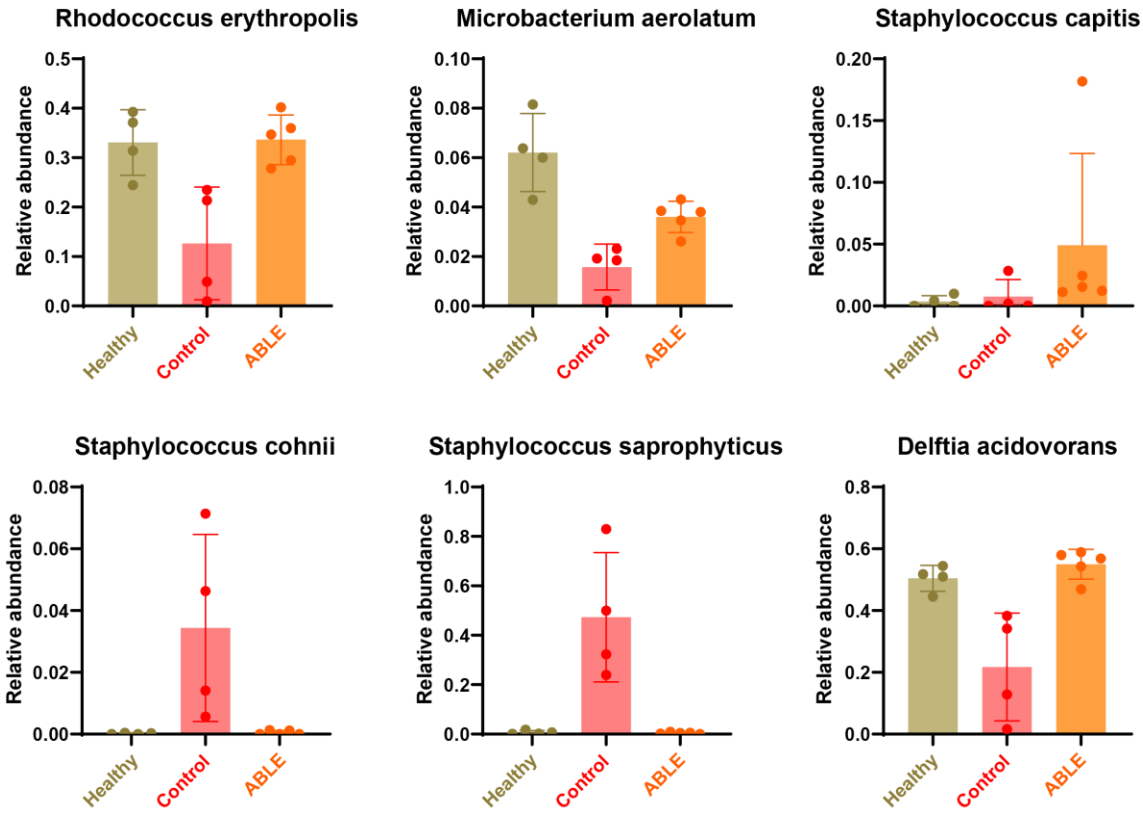

Figure 5-26 Living bioelectronics healthcare system modulates the relative abundance of various species of bacteria in skin microbiota. No statistical significance was found between the relative abundances of any groups. Data are presented as mean values ± SD. n>4 for each group.

We next sought to investigate the molecular mechanisms underlying ABLE-based regulation of the immune system and skin microbiota. Previous research has reported the inverse relationship between S. epidermidis and S. aureus, wherein S. epidermidis activates the host innate and adaptive immune system against S. aureus by the toll-like receptor 2 (TLR2) channel on dendritic cells. The TLR2 (Toll-like receptor 2) is a member of the Toll-like receptor (TLR) family, which plays a crucial role in the innate immune system. These receptors recognize distinct pathogen-associated molecular patterns (PAMPs) that are expressed on infectious agents and mediate the production of cytokines necessary for the development of effective immunity.

This knowledge prompted us to explore the therapeutic effect of ABLE in the TLR2-knockout mouse strain B6.129-Tlr2^{tm1Kir}/J. We found that ABLE treatment in TLR2-knockout mice did not result in the same therapeutic effects observed for wildtype mice, as determined by PSI (Figure 5-27).

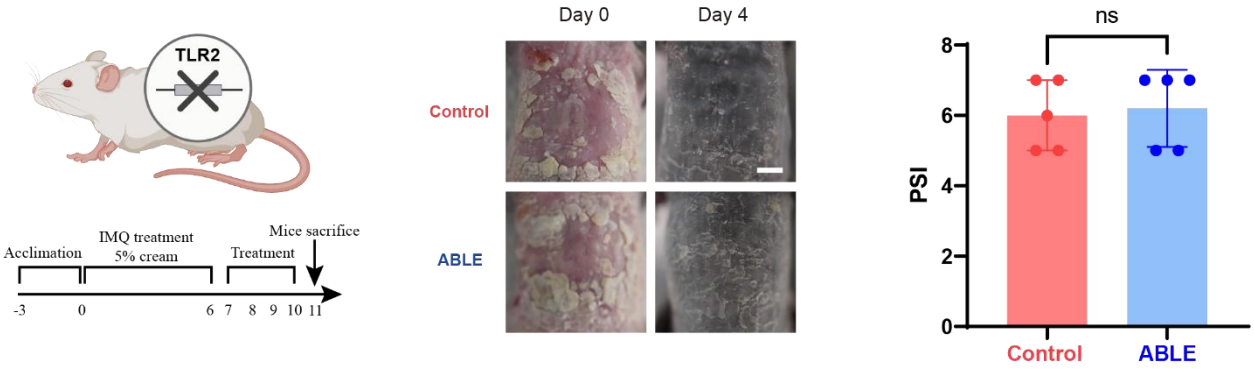

Figure 5-27 ABLE treatment didn't show therapeutic effects on psoriatic skin of TLR2 knockout (TLR2 KO) mice. (Left) schematic of the experimental design. (Middle) on Day 4 post ABLE treatment (ABLE), the psoriatic skin looks similar to the untreated control group (Control), in terms of the severity of psoriatic symptoms. This indicates no obvious therapeutic effects by ABLE. (Right) PSI score indicates that ABLE treatment didn't significantly alleviate psoriatic symptoms on Day 4.

The H&E analysis of skin tissue samples revealed that the ABLE treatment in TLR2 KO mice did not exhibit significant therapeutic effects when compared to the control groups, as depicted in Figure 5-28. Besides, key histological features in the H&E staining result, such as epidermal thickening (hyperplasia), parakeratosis, and cutaneous inflammation, still occurs in skin lesions.

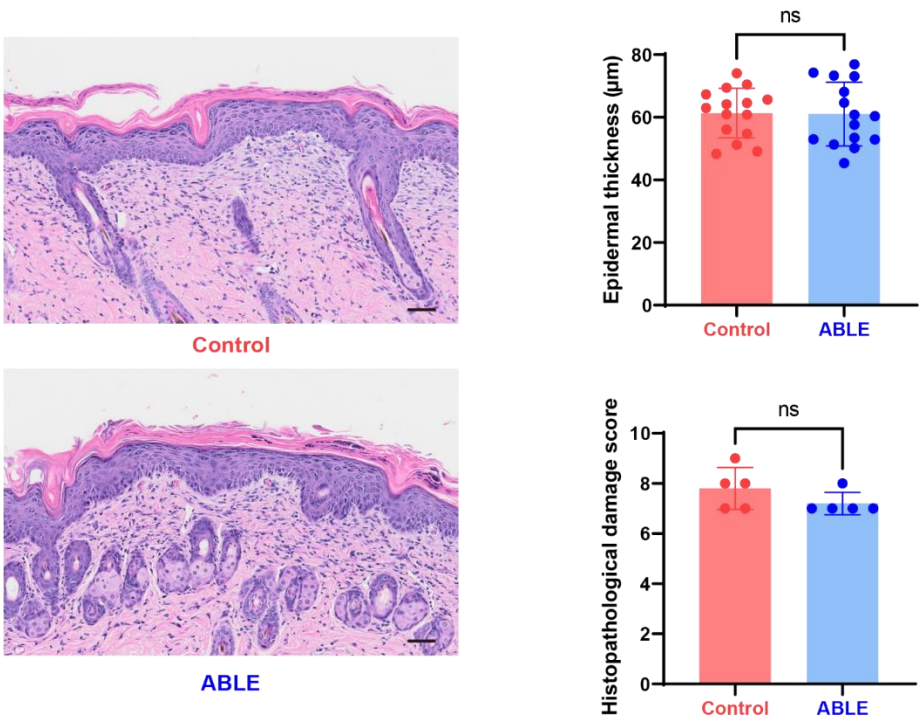

Figure 5-28 H&E histological analysis of psoriatic TLR2 KO skin. Neither histology and epidermal thickness didn't show significant difference between ABLE-treated (ABLE) and untreated psoriatic skin tissue (control) of TLR2 KO mice.

Additionally, CD4 and CD8 IHC showed the continued accumulation of T helper cells and T cytotoxic cells in the skin lesion (Figure 5-29). These results suggest that the efficacy of living bioelectronics in treating psoriasis may be dependent on the functionality of the TLR2 channel in immune cells. However, further investigations are needed to understand the underlying mechanisms.

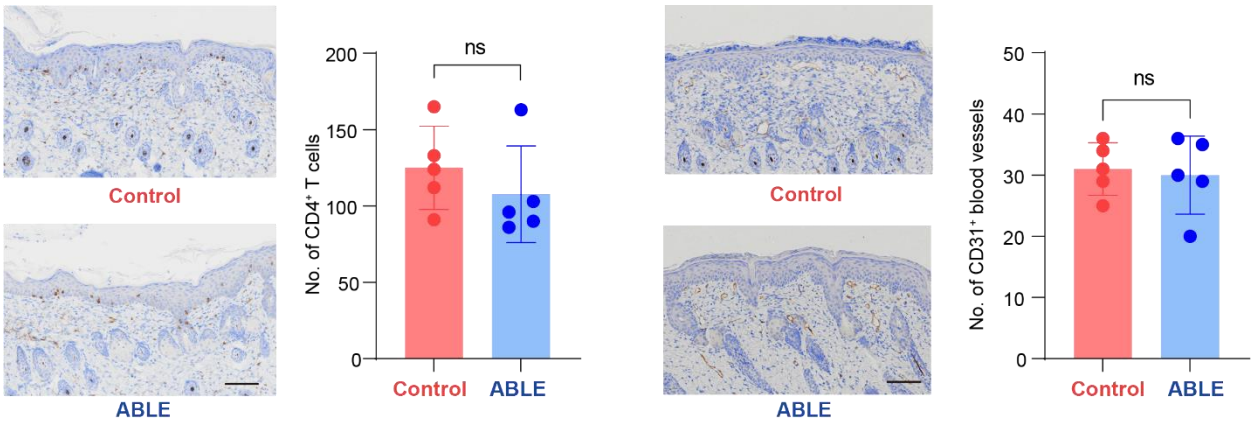

Figure 5-29 Immunobiological analysis of CD4$^+$ T cells and CD31$^+$ blood vessels didn't show significant difference between ABLE treated and untreated psoriatic skin of TLR2 KO mice. Scale bar, 50 µm.

RNA-sequencing (often referred to as transcriptomics) is a state-of-the-art technique designed to profile and quantify RNA molecules in a sample, offering an in-depth view of gene expression after specific treatment. This thorough examination of the transcriptome is important in biomedical research for a myriad of reasons. It facilitates differential gene expression analysis, shedding light on how genes vary in their expression in different conditions, such as in skin inflammatory diseases. Additionally, this technology is invaluable for genome annotation, decoding complex disease pathways, and pinpointing potential biomarkers. As a tool, RNA-seq is propelling the evolution of personalized medicine, enabling treatments to be crafted based on individual gene expression patterns. To fully understand the function of ABLE in psoriasis disease treatment, we performed transcriptomics. Specifically, bulk RNA-sequencing was conducted after 4 days of ABLE treatment. When comparing control treatment with ABLE treatment, we identified 1100 significantly altered genes, of which 695 were downregulated. Notably, ABLE exerted substantial regulatory effects on genes associated with psoriasis progression and pathogenesis (Figure 5-30), including genes pertinent to the innate immune response (e.g., Tlr2, Syk, Nod2), infiltration by

adaptive lymphocytes (e.g., Syk, Nlrp3), psoriatic epidermal hyperplasia (e.g., Epgn, Hbegf, JunB, Gpld1), skin inflammation (e.g., Ccl3, Cxcl2, S100a8), and angiogenesis (e.g., Hif1a, Ptgs1) (Figure 5-31).

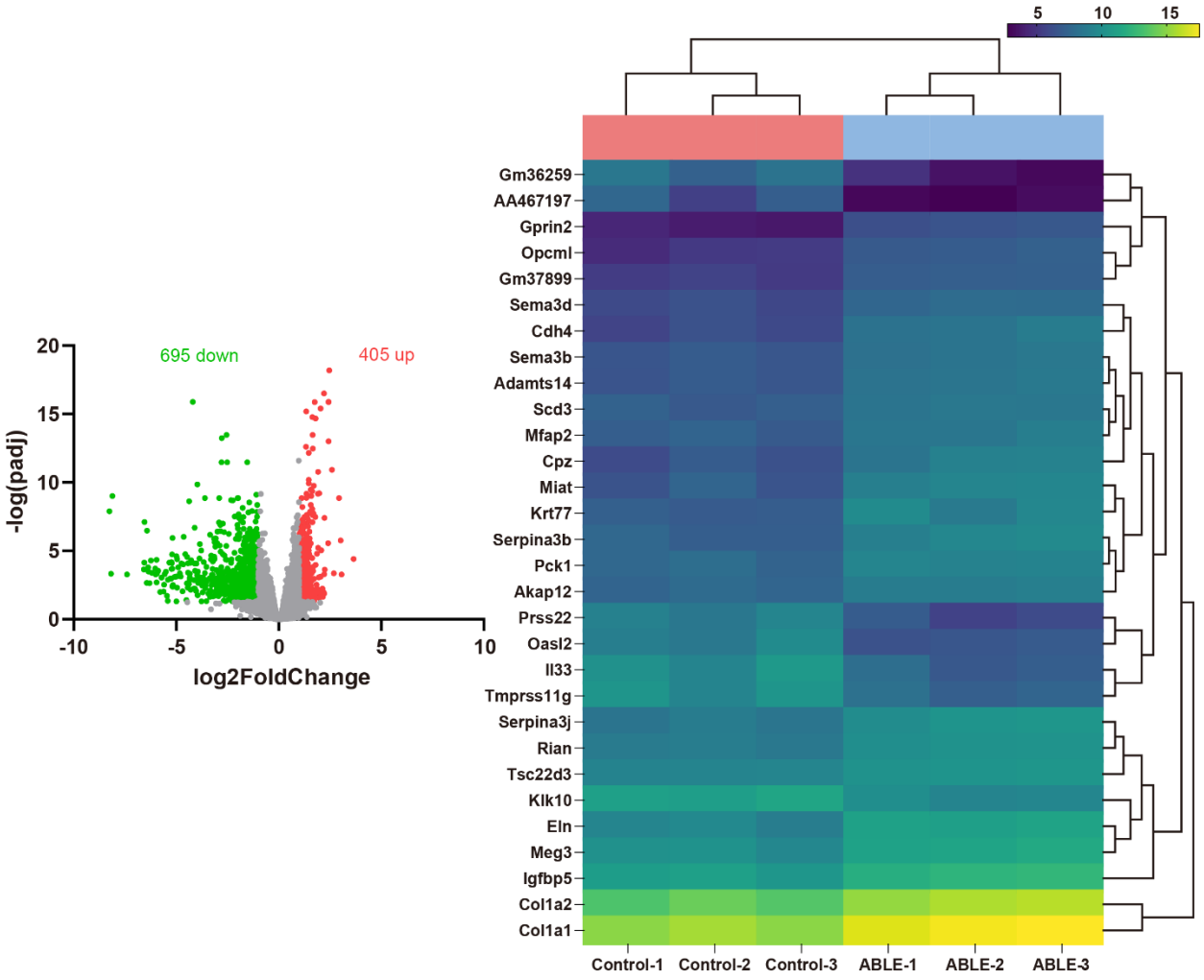

Figure 5-30 Comparison between control group and ABLE group indicates distinct transcriptome profiles. Volcano plot displays the gene expression profiles when comparing the control group with ABLE group. A bi-clustering heatmap was employed to visualize the expression profile of the top 30 differentially expressed genes. These genes were sorted based on their adjusted p-values, and their log2 transformed expression values.

Several pivotal genes are associated with the development of skin inflammation and psoriasis. We will expand our discussion here, starting with the Hypoxia-inducible factor-1 alpha (HIF1A). HIF1A is a transcription factor crucial for the cellular response to hypoxia, which refers to conditions of low oxygen levels. It is believed that HIF1A may play a significant role in the pathogenesis of psoriasis by promoting angiogenesis—the process of forming new blood vessels—as well as by exacerbating skin inflammation[24].

The NLRP3 is also believed to play a pivotal role in the pathogenesis of psoriasis. The inflammasome sensor proteins, NLRP-1 and NLRP-3, have been detected in psoriatic lesions, and certain polymorphisms of these proteins are linked with the disease. Furthermore, patients with psoriasis have been observed to possess elevated plasma levels of IL-1β and IL-18, which are generated by the inflammasome. This supports the idea that the NLRP3 is activated in these individuals[25].

NOD2 is a pivotal gene involved in the immune system's functionality. The protein encoded by this gene is active in various immune cells, especially dendritic cells. When activated, NOD2 fosters immunological tolerance to foreign antigens by stimulating the production of $CD103^+$ dendritic cells. Moreover, NOD2 activity can influence the outcomes of TLR signaling, thereby modifying the dendritic cell phenotype and function. This process in turn fosters the growth of T-helper type 2-like lymphocytes. Additionally, NOD2 activation in dendritic cells triggers the production of interleukin-23 (IL-23), which catalyzes an early mucosal T-helper 17 (Th17) cell response[26].

IL-17F is a member of the IL-17 cytokine family, and elevated levels of it have been detected in psoriatic lesions. While IL-17A, IL-17C, and IL-17F are all implicated in the pathogenesis of psoriasis, IL-17A was initially considered the predominant biologically active cytokine in this

context. However, subsequent findings have shown that IL-17F is also significantly over-expressed in the skin and synovial tissues of patients suffering from both psoriasis and psoriatic arthritis[27].

The Gpld1 gene, which encodes the enzyme glycosylphosphatidylinositol-specific phospholipase D1, is emerging as a notable gene in dermatological research. There is growing evidence to suggest its involvement in psoriasis disease. Furthermore, due to its potential role in these conditions, Gpld1 could serve as a valuable biomarker, offering insights into the severity of psoriasis in patients and helping gauge their response to treatments[28].

Syk (spleen tyrosine kinase) is believed to be implicated in the pathogenesis of psoriasis, particularly through its potential contribution to IL-17 production and its modulation of dendritic cell functions. IL-17, which Syk may help produce, stands out as a central mediator driving the progression of psoriasis. As such, targeting and inhibiting Syk presents a promising therapeutic avenue for addressing psoriasis-like inflammation[29].

Ptgs2, better known as cyclooxygenase-2 (COX-2), is an enzyme integral to the synthesis of prostaglandins, molecules heavily involved in inflammatory processes. Notably, Ptgs2 has been linked to the stimulation of keratinocyte proliferation, a defining characteristic of psoriasis. This association indicates that Ptgs2 might play a significant role in the excessive proliferation of keratinocytes commonly observed in psoriasis[30].

HIF1a, or hypoxia-inducible factor-1 alpha, is a transcription factor instrumental in guiding cellular reactions to conditions of low oxygen. HIF1a plays a pivotal role in the development of psoriasis mediated by Th17-driven inflammation. Besides, HIF1a is found to be upregulated in psoriasis, suggesting its involvement in the inflammation and aberrant cellular reactions characteristic of this condition[31].

S100a8 is a member of the S100 family, specifically the EF-hand Ca^{2+}-binding proteins, and its expression is notably heightened in psoriatic skin. Both S100a8 and S100a9 exhibit dual roles, functioning as both pro-inflammatory and anti-inflammatory agents. Interleukin 17 (IL-17) amplifies the expression of S100a8 and S100a9 during keratinocytes inflammatory reactions. Moreover, a transcriptome analysis comparing gene expressions in control samples with lesional and non-lesional skin from psoriasis patients revealed a notable down-regulation of S100a8 and S100a9 expression when subjected to IL-17-targeted therapy[32].

There are still many interesting genes closely related to the psoriasis development, which need more effort and pages for investigation.

Cuius rei demonstrationem mirabilem sane detexi hanc marginis exiguitas non caperet.

-Pierre de Fermat

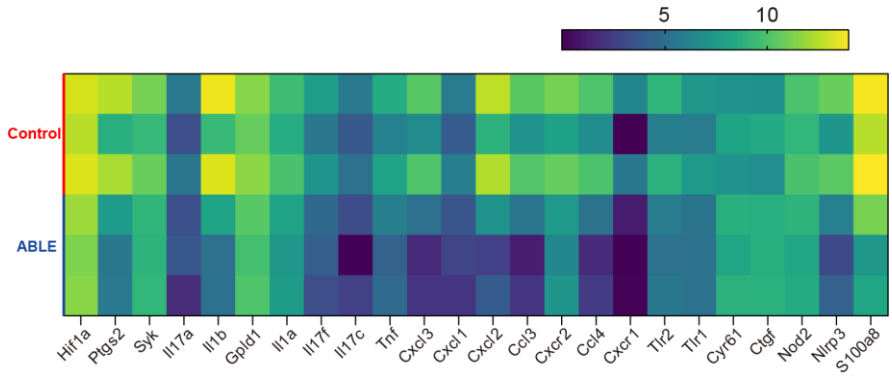

Figure 5-31 Heatmap shows expression profile of psoriasis-related genes. The genes list in the heatmap are all highly related to the development of the psoriasis disease.

Most of these psoriasis-related genes could be categorized into different gene ontology groups associated with immune and inflammatory processes (Figure 5-32).

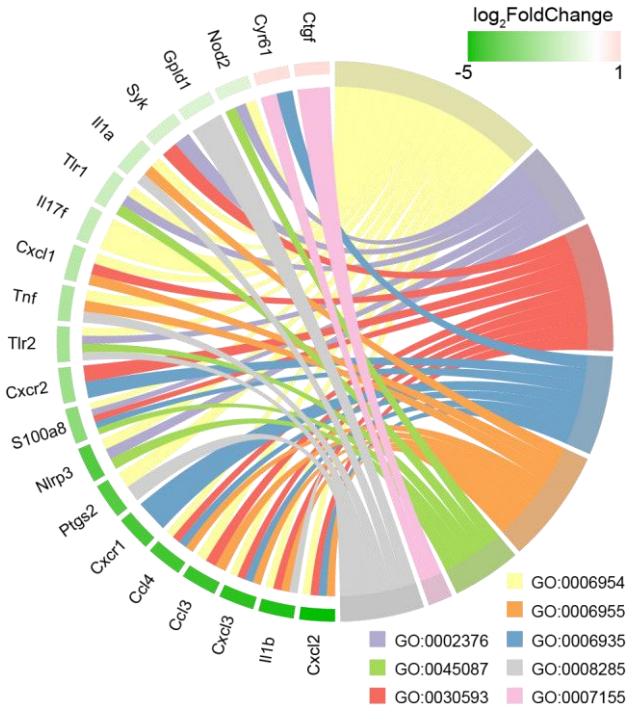

Figure 5-32 Gene ontology (GO) chord plot shows that several important psoriasis-related genes are categorized into different clusters.

Furthermore, a top 30 enriched gene ontology analysis of all significantly differentially expressed genes revealed enrichments in processes related to keratinization, keratinocyte differentiation, immune system functions, and inflammatory responses (Figure 5-33).

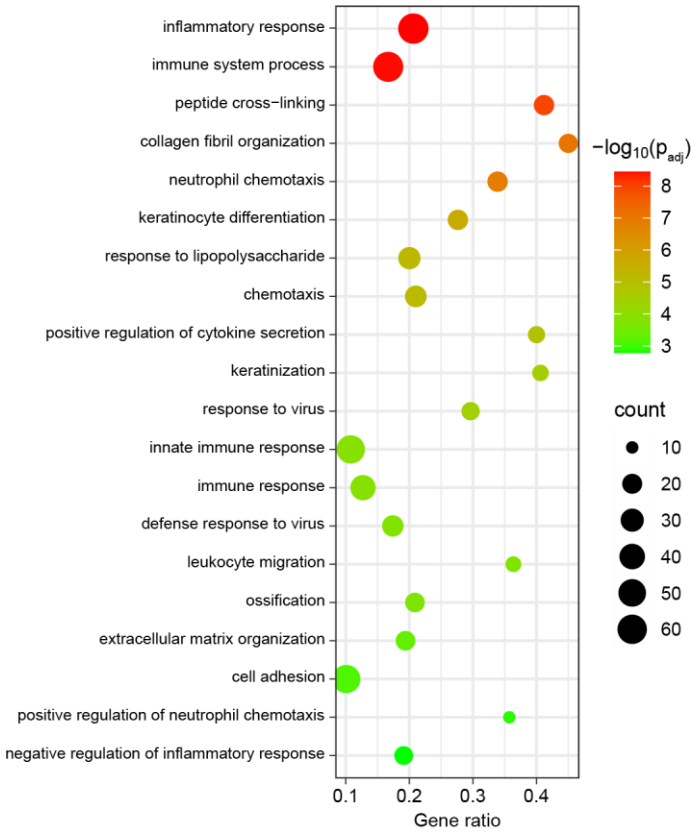

Figure 5-33 GO enrichment analysis of significantly differentially expressed genes between ABLE-treated and control groups shows that ABLE regulates biological processes related to immune response and keratinocytes.

Treatment with vehicle alone (ABLE without S. epidermidis) resulted in a substantially lower number of significantly modified genes (Figure 5-34). Additionally, both gene expression and gene ontology analysis indicated that vehicle treatment lacked involvement of gene related to inflammation and immune response. This observation underscores the pivotal role of the living components in the ABLE system in managing skin inflammation and facilitating therapeutic intervention via bioelectronics interfaces. Also, there is no significant difference between the control group and vehicle group based on the transcriptomics (Figure 5-35).

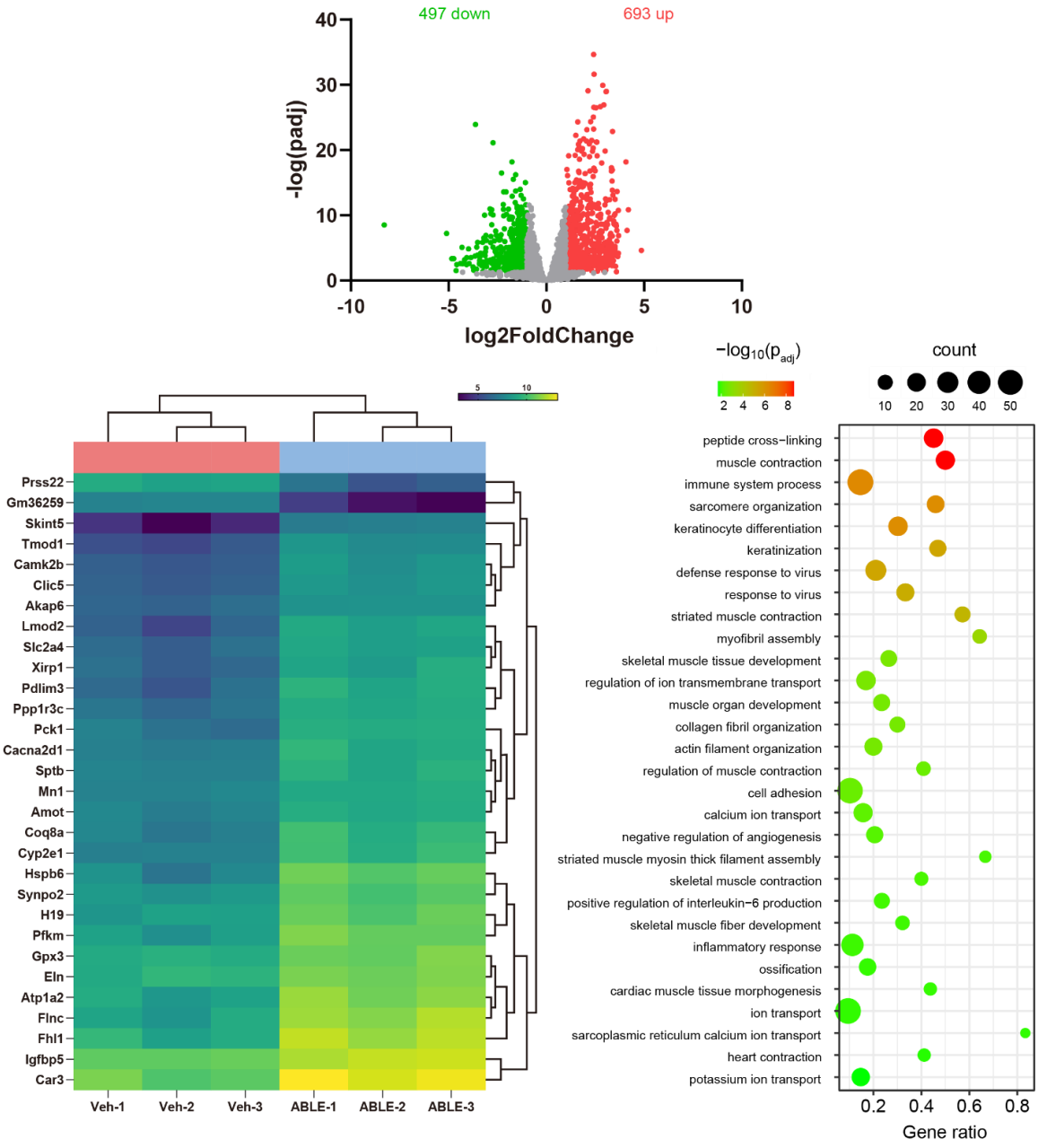

Figure 5-34 Comparison between vehicle group and ABLE group indicates distinct transcriptome profiles. Volcano plot displays the gene expression profiles when comparing the vehicle group with ABLE group. A bi-clustering heatmap was employed to visualize the expression profile of the top 30 differentially expressed genes. These genes were sorted based on their adjusted p-values, and their log2 transformed expression values. Gene ontology analysis reveals the regulatory impact of ABLE treatment on psoriasis-related processes, including immune response and keratinization.

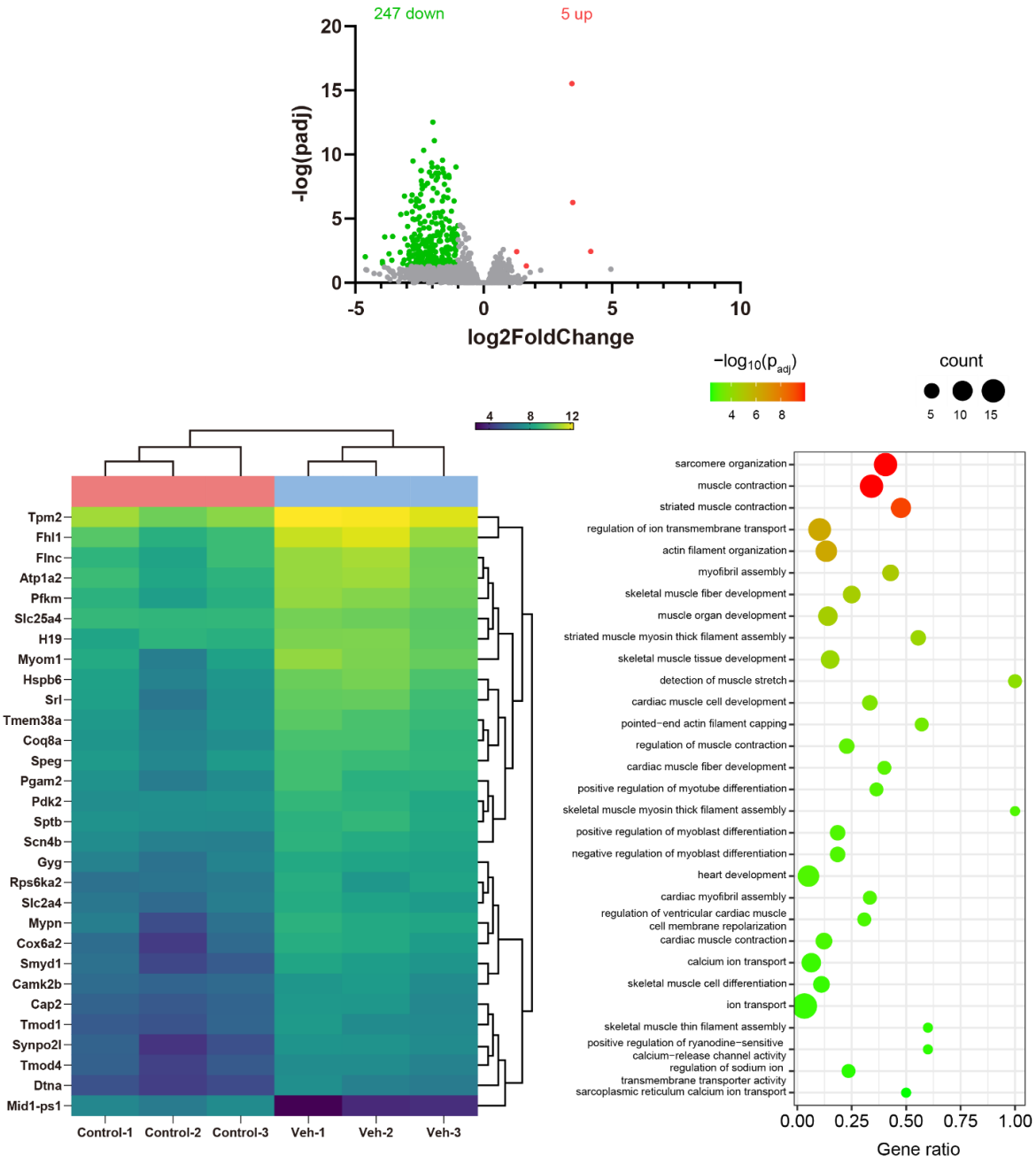

Figure 5-35 Comparison between control group and vehicle group indicates similar transcriptome profiles. Volcano plot displays the gene expression profiles when comparing the control group with vehicle group. A bi-clustering heatmap was employed to visualize the expression profile of the top 30 differentially expressed genes. These genes were sorted based on their adjusted p-values, and their log2 transformed expression values. Gene ontology analysis reveals vehicle group without living components cannot regulate inflammation and immune process.

Collectively, we found that ABLE significantly modulates the inflammatory environment in psoriasis (Figure 5-36). First, ABLE mitigates the expression of the Tlr2 gene, along with other genes pivotal to initiation of the innate immune response (e.g., Syk, Nod2). The importance of TLR2 in the therapeutic effect of ABLE in IMQ-induced psoriasis echoed across our transcriptome-level analysis and in TLR2-KO mice experiments. This result strongly suggests that ABLE biochemically inhibits activation of dendritic cells and macrophages. Second, ABLE treatment substantially mitigates infiltration of adaptive lymphocytes to skin lesions, as indicated by histology analysis and reduced expression levels of genes associated with lymphocyte infiltration (e.g., Syk, Nlrp3). Third, both mRNA and protein levels of key cytokines, including IL-17, TNF-α, and IL-1, were markedly diminished following ABLE treatment. Finally, genes associated with psoriatic epidermal hyperplasia (e.g., Epgn, Hbegf, JunB, Gpld1) and papillary vessel dilation and angiogenesis (e.g., Hif1a, ptgs1) exhibited downregulation following ABLE treatment. These findings are in harmony with the therapeutic effects observed at the histological tissue level. In summary, ABLE treatment demonstrates potent therapeutic effects on IMQ-induced murine psoriasis by impeding the activation of initiating dendritic cells and subsequently curbing the inflammatory phases intrinsic to psoriatic pathogenesis.

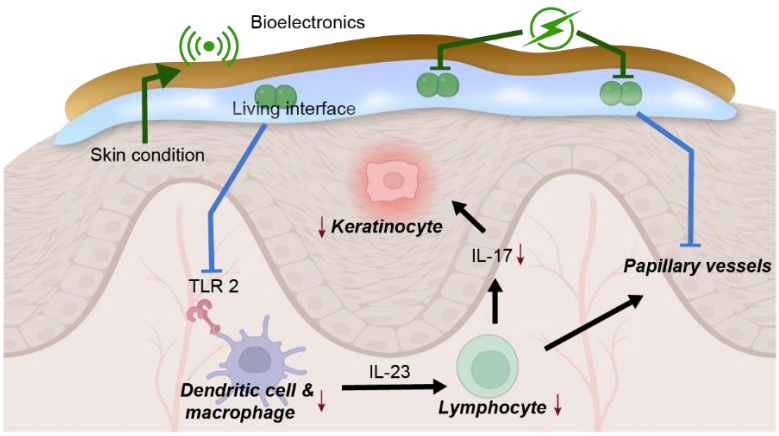

Figure 5-36 Proposed mechanism for ABLE-regulation of the inflammatory skin environment and therapeutic effect in IMQ-induced psoriasis.

5.3 Conclusion

In this research, we validated the efficacy of an integrated living biointerface-bioelectronics device, the ABLE, in the context of biomedical applications. Using the IMQ-induced psoriasis model, we demonstrate the potential for clinical adaptation of living bioelectronics devices that promote therapeutic effects via a living interface. The ABLE platform will advance telemedicine capabilities, furnishing healthcare professionals with enriched data for clinical diagnostics and prognosis. The commercial and therapeutic prospects of the ABLE platform for diverse inflammatory conditions are substantial.

The nexus between living materials and electrical systems presents new opportunities to explore the interplay between biological and nonbiological systems. Helminthic therapy involves the introduction of specific parasitic worms (e.g., helminths) into the human body as a therapeutic intervention for autoimmune diseases. This unconventional approach is based on the hygiene hypothesis. This theory posed that the increased incidence of modern autoimmune and inflammatory disorders can be attributed to our diminished exposure to infectious agents, such as

parasites, due to our increasingly sanitized living conditions. By reintroducing helminths, the goal is to recalibrate or modulate the immune system, potentially mitigating detrimental inflammation. Historically, humans have coexisted with various parasites, which likely influenced the evolution of our immune responses. For helminthic therapy, specific worm species like Necator americanus (hookworm) and Trichuris suis (pig whipworm) are chosen. These worms are preferred because they can provide potential therapeutic benefits without inducing severe diseases in humans. While Helminthic therapy offers apparent benefits in some autoimmune diseases, the lack of exhaustive studies has led to regulatory constraints. The advent of living bioelectronics paves the way for controlled studies into the dynamics between potentially deleterious organisms and human tissues. Future research investigations could explore electrical modulation of cellular metabolic pathways within the living hydrogel. Such investigation can cultivate precision in managing living entities during disease intervention, optimizing the benefits of living components while curtailing associated risks. More broadly, the potential of the ABLE platform extends beyond autoimmune diseases, offering promising avenues for tissue repair, regeneration, functional restoration, and rehabilitation medicine. Envisioning the broader spectrum, the ABLE platform has promising potential to integrate diverse bioelectronics for bioelectronic medicine applications.

It should also be noted that there is still a gap between research studies and real clinical applications. Diseases that develop in humans can be more complicated than any pre-clinical murine models, especially for chronic inflammatory diseases (Figure 5-37). The shorter lifespan of mice can lead to accelerated disease progression. Moreover, clinical translation faces more technical challenges, such as device adherence, skin irritation, and ethical concerns. Additionally, fundamental analysis, including simulation and omics analysis, can help us better understand the materials system and working process.

Figure 5-37 There is still long way for translation of current research techniques into clinical scenario.

As ABLE is a good proof of concept, there are still many challenges remaining for real clinical translation. This requires more efforts in the fields to solve these engineering problems.

5.4 Experimental Methods

Synthesis of hydrogel composite. A starch gelatin hydrogel was prepared by mixing tapioca starch (15 wt%), gelatin (10 wt%), and deionized water or tryptic soy broth (TSB) medium (cat. no. 22092). The mixture was then heated in an oil bath at 80°C for 30 minutes to facilitate the gelatinization of starch. Subsequently, the hydrogel was transferred to a 4°C refrigerator for gelation. To create a living hydrogel, Staphylococcus epidermidis (S. epidermidis) was cultivated in TSB medium at 37°C until the optical density at 600 nm (OD600) reached a range of 2.80 to

3.00. Then, 1ml of cultured Staphylococcus epidermidis was aseptically added and vigorously mixed with the starch-gelatin hydrogel at 42 °C water bath. For the synthesis of granular starch-gelatin hydrogel, gelatin and TSB medium were mixed and heated at 80°C for 30 minutes. After cooling the mixture in a 42°C water bath, tapioca starch was aseptically added. To synthesize polyacrylamide hydrogel, AA (3.5 wt%), APS (0.1 wt%) and MBAA (0.01 wt%) were mixed vigorously in deionized water. After 30 minutes, the accelerator TEMED (0.02 wt%) was added into the mixture and quickly mixed before pouring into acrylic molds for subsequent polymerization at room temperature.

Intracellular ROS assay. A 2 mm thick living hydrogel was placed onto the patterned disinfection electrodes. Subsequently, electrical stimulation was applied to the living hydrogel at a condition of 3.5 V for a duration of 10 minutes. Following the electrical stimulation, the samples were liquefied and then diluted 10-fold with phosphate-buffered saline (PBS) to ensure the complete release of bacterial cells. The released cells were washed once with PBS and resuspended in a staining solution obtained from the DCFDA/H2DCFDA - Cellular ROS Assay Kit (ab113851). The intracellular ROS level was measured using a Synergy Neo HTS Plate Reader. To standardize the raw fluorescence intensity, it was divided by the percentage viability determined using the LIVE/DEAD BacLight Bacterial Viability Kit.

Fabrication of the flexible printed circuit board. Custom-designed flexible printed circuit boards were manufactured by commercial vendors, such as PCBWay, in compliance with the ISO 9001 certificate. The electronic components integrated into the circuit boards included passive elements like capacitors, resistors, and diodes. Additionally, the boards had a temperature and humidity sensor (Sensirion, model no. 403-SHT40-AD1F-R2), an ISO 15693 sensor transponder with a programmable low-power microcontroller (Texas Instruments, model no.

RF430FRL152H), a crystal oscillator (Epson Timing, model no. SG-3030LC 32.7680KB6:PURE SN), and two operational amplifiers (STMicroelectronics, model no. TSV620AILT). All circuit components were soldered using lead-free no-clean solder (Chip Quik Inc., model no. Sn96.5Ag3Cu0.5 (96.5/3/0.5), melting point range of 217~220 °C)) through hot-air blowing. To optimize bacterial electrical modulation efficiency, two stimulation electrodes were patterned with 100 nm Au metal layers for bacterial disinfection electrode geometry or bacteria stimulation electrode geometry using an electron-beam evaporator (EvoVac, Angstrom Engineering). To prevent chronic electrochemical corrosion of the electrodes, silver/silver chloride (Ag/AgCl) conducting paste (Nagase ChemteX, model no. CI-4040) was applied and printed onto electrode area, followed by curing on a hot plate at 70 ℃ for 30 minutes. The original electrode area was subsequently encapsulated with an elastomeric polyurethane coating (Smooth-On, model no. Clear Flex 50) and cured at 70 °C for 30 minutes. The living hydrogel interface was positioned between the two disinfection electrodes, while the non-living hydrogel interface was placed separately on the two sensing electrodes.

Living hydrogel disinfection demonstration. The living hydrogel with S. epidermidis was first put onto disinfection electrodes and then the electrical potential was applied for the desired duration. Subsequently, a sample of the treated hydrogel was collected and measured inside a glass vial. The sampled hydrogel was dissolved by adding 10 ml of PBS and incubating the mixture at 42°C for 15 minutes. The resulting solution, containing the released bacteria, was combined with the BacTiter-Glo™ Microbial Cell Viability Assay kit (Promega) in a 1:1 ratio. Luminescence was measured using a Synergy Neo HTS Plate Reader. Concurrently, a control group sample was run in parallel, following an identical procedure, except without electric stimulation. The raw

luminescence data obtained was normalized by the sampled mass, and the differences between the control and treated groups were calculated to determine the normalized viability.

Open-field movement test. The open-field test was conducted to evaluate the moving behavior of mice with and without the living bioelectronics in a 30 × 18 cm2 open cage. Each group consisted of four mice, which were given the freedom to explore the area for a duration of 30 minutes. Throughout the test, the mice's moving activities were recorded using an overhead camera. The recorded videos were subsequently analyzed using a deep learning architecture (DeepLabCut, v2.3.5) to measure the total distances traveled by each group.

Psoriasis model. Eight-week-old male C57BL/6, B6.129-Tlr2tm1Kir/J (TLR2 KO) mice were housed in groups of five mice per cage and acclimatized for 7 days before inclusion in the investigation. To induce psoriasiform dermatitis, the mice were shaved and topically applied with 5% IMQ cream (Perrigo) for 3 consecutive days unless otherwise noted. For the therapeutic experiments, living bioelectronics with or without living components were topically applied to mouse dorsal skin for skin sensing and therapy. Tegaderm (3 M™) or band-aid were then used to fix the position of bioelectronics. Dressing was changed every day during the daily skin information collection episodes. During the experiment, changes in skin psoriasiform information including erythema, induration, and desquamation were recorded daily. The mice were euthanized on the last day of the experiment and their skin and spleen were harvested. The histological evaluation of the tissue was also performed. The general psoriasis symptoms, including the redness, scaling, and thickness (induction) of murine skin, were evaluated to score the “Psoriasis severity index (PSI)”, which assesses the severity of the induced erythema, desquamation, and induration of the psoriasis. Each parameter was measured on a scale of 0–4 (from none to the

maximum damage). The sum of these four values was the value of the PSI index, with the maximum value of 12.

Histology, immunohistochemistry, and immunofluorescence. For tissue histological analysis, Hematoxylin and eosin (H&E), and CD4, CD8, ki-67, CD31, CK14, F4/80 histological tissue sections were prepared and stained by the Human Tissue Resource Center at the University of Chicago. All the tissue histological results were analyzed by the CaseViewer software (3DHISTECH) and QuPath (0.4.0). The histological damage, including hyperplasia, parakeratosis, neutrophil infiltration, loss of granular layer, dilated capillaries, dermal inflammation on a scale of 0–4 (from none to the maximum damage, was scored based on the H&E-stained skin tissue sections. The sum of all above values was the value of the histological damage score. The thickness of the epidermal layer and the counting of IHC positive cells were analyzed through ImageJ.

Cytokine analysis. The Mouse Cytokine Array, Panel A (R&D Systems #ARY006) utilizes capture antibodies spotted onto a nitrocellulose membrane to allow high-throughput multi-analyte profiling of 40 cytokines, chemokines, and more in a single sample. For cytokine assays, fresh skin psoriatic skin tissues were harvested and homogenized in cold RIPA buffer. Subsequently, 200 μg of lysate was used for each array by following the manufacturers' instructions. Array images were collected and analyzed using the Bio-rad Gel Doc XR+ Imaging System.

Microbiome analysis. Three groups of mice (C57BL/6) were prepared for skin microbiome analysis: 1) The first group (Healthy) was healthy mice; 2) The second group (Control) was the mice with IMQ-induced psoriasis; 3) The third group was the mice with IMQ-induced psoriasis and treated with living bioelectronics for 4 days. Skin tissue samples from three different groups were collected and analyzed by the ZymoBIOMICS® Targeted 16S Sequencing Service (Zymo Research, Irvine, CA). DADA2 was used to infer unique amplicon sequence variants from raw

reads[33]. Chimeric sequences and potential sequencing errors were removed using the DADA2 pipeline. We used Uclust from Qiime version 1.9.1, a 16S database designed and curated as a reference, for taxonomy assignment. Linear discriminant analysis Effect Size (LEfSe) was used to identify taxonomies with significant abundance among different groups[34]. PCoA plots were performed using internal scripts. Quantitative real-time PCR was used to quantify the absolute abundance and the results were displayed as the number of gene copies.

RNA sequencing. Three groups of mice (C57BL/6) were prepared for transcriptome analysis: 1) The first group (Control/IMQ) was the mice with IMQ-induced psoriasis; 2) The second group was the mice with IMQ-induced psoriasis and treated with non-living ABLE (Vehicle); 3) The third group was the mice with IMQ-induced psoriasis and treated with ABLE for 4 days (ABLE). RNA extraction, library preparations and sequencing reactions were conducted at Azenta Life Sciences. Briefly, total RNA was extracted and treated with TURBO DNase (Thermo Fisher Scientific, Waltham, MA, USA) to remove DNA contaminants. rRNA depletion sequencing library was prepared by using QIAGEN FastSelect rRNA HMR Kit (Qiagen, Hilden, Germany). RNA sequencing library preparation used NEB Next Ultra II RNA Library Preparation Kit for Illumina by following the manufacturer's recommendations (NEB, Ipswich, MA, USA). The sequencing libraries were multiplexed and clustered on the Illumina NovaSeq instrument according to manufacturer's instructions. The samples were sequenced using a 2x150 Pair-End (PE) configuration. Raw sequence data (.bcl files) generated from Illumina NovaSeq was converted into fastq files and de-multiplexed using Illumina bcl2fastq program version 2.20. One mismatch was allowed for index sequence identification.

After demultiplexing, sequence data was checked for overall quality and yield. Then, raw sequence reads were trimmed to remove possible adapter sequences and nucleotides with poor quality using

Trimmomatic v.0.36. The reads were then mapped to the Mus musculus reference genome available on ENSEMBL using the STAR aligner v.2.5.2b. BAM files were generated as a result of this step. Unique gene hit counts were calculated by using feature Counts from the Subread package v.1.5.2. Only unique reads that fell within exon regions were counted.

After extraction of gene hit counts, the gene hit counts table was used for downstream differential expression analysis. Using DESeq2, a comparison of gene expression between the groups of samples was performed. The Wald test was used to generate P values and Log2 fold changes. Genes with adjusted P values < 0.05 and absolute log2 fold changes >1 were called as differentially expressed genes for each comparison. Gene ontology analysis was performed on the statistically significant set of genes by implementing the software GeneSCF. The goa_Mus musculus GO list was used to cluster the set of genes based on their biological process and determine their statistical significance. A PCA analysis was performed using the "plot PCA" function within the DESeq2 R package. The plot shows the samples in a 2D plane spanned by their first two principal components. The top genes, selected by highest row variance, were used to generate the plot.

5.5 References

1 Lebwohl, M. Psoriasis. *The Lancet* **361**, 1197-1204, doi:doi.org/10.1016/S0140-6736(03)12954-6 (2003).

2 Bowcock, A. M. & Krueger, J. G. Getting under the skin: The immunogenetics of psoriasis. *Nat Rev Immunol* **5**, 699-711, doi:10.1038/nri1689 (2005).

3 Kim, N., Thrash, B. & Menter, A. in *Seminars in cutaneous medicine and surgery*. 10-15 (WB Saunders).

4 Greb, J. E., Goldminz, A. M., Elder, J. T., Lebwohl, M. G., Gladman, D. D., Wu, J. J., Mehta, N. N., Finlay, A. Y. & Gottlieb, A. B. Psoriasis. *Nature Reviews Disease Primers* **2**, 16082, doi:10.1038/nrdp.2016.82 (2016).

5 Wang, Z. K., Sun, Y., Lou, F. Z., Bai, J., Zhou, H., Cai, X. J., Sun, L. B., Yin, Q. Q., Tang, S. B., Wu, Y., Fan, L., Xu, Z. Y., Wang, H., Hu, X. Y. & Wang, H. L. Targeting the transcription factor HES1 by L-menthol restores protein phosphatase 6 in keratinocytes in models of psoriasis. *Nat Commun* **13**, doi:10.1038/s41467-022-35565-y (2022).

6 Zhang, W. T., Chen, Y. X., Zhao, Z. J., Zheng, H. Q., Wang, S. Q., Liao, Z. Y., Sheng, T., Zhao, S., Hou, W. H., Yu, X. M., He, F., Yu, J. C., Zhang, Y. Q. & Gu, Z. Adoptive Treg therapy with metabolic intervention via perforated microneedles ameliorates psoriasis syndrome. *Sci Adv* **9**, doi:10.1126/sciadv.adg6007 (2023).
7 Hindelang, B., Nau, T., Englert, L., Berezhnoi, A., Lauffer, F., Darsow, U., Biedermann, T., Eyerich, K., Aguirre, J. & Ntziachristos, V. Enabling precision monitoring of psoriasis treatment by optoacoustic mesoscopy. *Sci Transl Med* **14**, doi:10.1126/scitranslmed.abm8059 (2022).
8 Warren, R. B., Gooderham, M., Burge, R., Zhu, B. J., Amato, D., Liu, K. H., Shrom, D., Guo, J. Y., Brnabic, A. & Blauvelt, A. Comparison of cumulative clinical benefits of biologics for the treatment of psoriasis over 16 weeks: Results from a network meta-analysis. *J Am Acad Dermatol* **82**, 1138-1149, doi:10.1016/j.jaad.2019.12.038 (2020).
9 Wagner, E. F., Schonthaler, H. B., Guinea-Viniegra, J. & Tschachler, E. Psoriasis: what we have learned from mouse models. *Nat Rev Rheumatol* **6**, 704-714, doi:10.1038/nrrheum.2010.157 (2010).
10 Madhvapathy, S. R., Wang, H. L., Kong, J., Zhang, M., Lee, J. Y., Park, J. B., Jang, H. Y., Xie, Z. Q., Cao, J. Y., Avila, R., Wei, C., D'Angelo, V., Zhu, J. S., Chung, H. U., Coughlin, S., Patel, M., Winograd, J., Lim, J. M., Banks, A., Xu, S., Huang, Y. G. & Rogers, J. A. Reliable, low-cost, fully integrated hydration sensors for monitoring and diagnosis of inflammatory skin diseases in any environment. *Sci Adv* **6**, doi:10.1126/sciadv.abd7146 (2020).
11 Spuls, P. I., Lecluse, L. L., Poulsen, M.-L. N., Bos, J. D., Stern, R. S. & Nijsten, T. How good are clinical severity and outcome measures for psoriasis?: quantitative evaluation in a systematic review. *J Invest Dermatol* **130**, 933-943 (2010).
12 Lim, C., Hong, Y. J., Jung, J., Shin, Y., Sunwoo, S. H., Baik, S., Park, O. K., Choi, S. H., Hyeon, T., Kim, J. H., Lee, S. & Kim, D. H. Tissue-like skin-device interface for wearable bioelectronics by using ultrasoft, mass-permeable, and low-impedance hydrogels. *Sci Adv* **7**, doi:10.1126/sciadv.abd3716 (2021).
13 Jiang, Y., Ji, S. B., Sun, J., Huang, J. P., Li, Y. H., Zou, G. J., Salim, T., Wang, C. X., Li, W. L., Jin, H. R., Xu, J., Wang, S. H., Lei, T., Yan, X. Z., Peh, W. Y. X., Yen, S. C., Liu, Z. H., Yu, M., Zhao, H., Lu, Z. C., Li, G. L., Gao, H. J., Liu, Z. Y., Bao, Z. A. & Chen, X. D. A universal interface for plug-and-play assembly of stretchable devices. *Nature* **614**, 456-462, doi:10.1038/s41586-022-05579-z (2023).
14 Guan, Y. S., Ershad, F., Rao, Z. Y., Ke, Z. F., Da Costa, E. C., Xiang, Q., Lu, Y. T., Wang, X., Mei, J. G., Vanderslice, P., Hochman-Mendez, C. & Yu, C. J. Elastic electronics based on micromesh-structured rubbery semiconductor films. *Nat Electron* **5**, 881-892, doi:10.1038/s41928-022-00874-z (2022).
15 Gao, Y. J., Nguyen, D. T., Yeo, T., Lim, S. B., Tan, W. X., Madden, L. E., Jin, L., Long, J. Y. K. N., Aloweni, F. A., Liew, Y. J. A., Tan, M. L., Ang, S. Y., Maniya, S. D. O., Abdelwahab, I., Loh, K. P., Chen, C. H., Becker, D. L., Leavesley, D., Ho, J. S. & Lim, C. T. A flexible multiplexed immunosensor for point-of-care in situ wound monitoring. *Sci Adv* **7**, doi:10.1126/sciadv.abg9614 (2021).
16 Park, J., Jin, K., Sahasrabudhe, A., Chiang, P. H., Maalouf, J. H., Koehler, F., Rosenfeld, D., Rao, S., Tanaka, T., Khudiyev, T., Schiffer, Z. J., Fink, Y., Yizhar, O., Manthiram, K. & Anikeeva, P. In situ electrochemical generation of nitric oxide for neuronal modulation. *Nat Nanotechnol* **15**, 690-697, doi:10.1038/s41565-020-0701-x (2020).

17 Jiang, Y. W., Trotsyuk, A. A., Niu, S. M., Henn, D., Chen, K., Shih, C. C., Larson, M. R., Mermin-Bunnell, A. M., Mittal, S., Lai, J. C., Saberi, A., Beard, E., Jing, S., Zhong, D. L., Steele, S. R., Sun, K. F., Jain, T., Zhao, E., Neimeth, C. R., Viana, W. G., Tang, J., Sivaraj, D., Padmanabhan, J., Rodrigues, M., Perrault, D. P., Chattopadhyay, A., Maan, Z. N., Leeolou, M. C., Bonham, C. A., Kwon, S. H., Kussie, H. C., Fischer, K. S., Gurusankar, G., Liang, K., Zhang, K. L., Nag, R., Snyder, M. P., Januszyk, M., Gurtner, G. C. & Bao, Z. N. Wireless, closed-loop, smart bandage with integrated sensors and stimulators for advanced wound care and accelerated healing. *Nat Biotechnol* **41**, 652-662, doi:10.1038/s41587-022-01528-3 (2023).

18 Tang, T. C., An, B. L., Huang, Y. Y., Vasikaran, S., Wang, Y. Y., Jiang, X. Y., Lu, T. K. & Zhong, C. Materials design by synthetic biology. *Nat Rev Mater* **6**, 332-350, doi:10.1038/s41578-020-00265-w (2021).

19 Otto, M. Staphylococcus epidermidis - the 'accidental' pathogen. *Nat Rev Microbiol* **7**, 555-567, doi:10.1038/nrmicro2182 (2009).

20 Rodrigo-Navarro, A., Sankaran, S., Dalby, M. J., del Campo, A. & Salmeron-Sanchez, M. Engineered living biomaterials. *Nat Rev Mater* **6**, 1175-1190 (2021).

21 Severn, M. M. & Horswill, A. R. Staphylococcus epidermidis and its dual lifestyle in skin health and infection. *Nat Rev Microbiol* **21**, 97-111, doi:10.1038/s41579-022-00780-3 (2023).

22 Linehan, J. L., Harrison, O. J., Han, S. J., Byrd, A. L., Vujkovic-Cvijin, I., Villarino, A. V., Sen, S. K., Shaik, J., Smelkinson, M., Tamoutounour, S., Collins, N., Bouladoux, N., Dzutsev, A., Rosshart, S. P., Arbuckle, J. H., Wang, C. R., Kristie, T. M., Rehermann, B., Trinchieri, G., Brenchley, J. M., O'Shea, J. J. & Belkaid, Y. Non-classical Immunity Controls Microbiota Impact on Skin Immunity and Tissue Repair. *Cell* **172**, 784-796, doi:10.1016/j.cell.2017.12.033 (2018).

23 Byrd, A. L., Belkaid, Y. & Segre, J. A. The human skin microbiome. *Nat Rev Microbiol* **16**, 143-155 (2018).

24 Zhu, W. J., Li, P., Wang, L. & Xu, Y. C. Hypoxia-inducible factor-1: A potential pharmacological target to manage psoriasis. *Int Immunopharmacol* **86**, doi:10.1016/j.intimp.2020.106689 (2020).

25 Verma, D., Fekri, S. Z., Sigurdardottir, G., Eding, C. B., Sandin, C. & Enerback, C. Enhanced Inflammasome Activity in Patients with Psoriasis Promotes Systemic Inflammation. *J Invest Dermatol* **141**, 586-595, doi:10.1016/j.jid.2020.07.012 (2021).

26 Prescott, D., Maisonneuve, C., Yadav, J., Rubino, S. J., Girardin, S. E. & Philpott, D. J. NOD2 modulates immune tolerance via the GM-CSF&-dependent generation of CD103+ dendritic cells. *Proc. Natl. Acad. Sci. U.S.A.* **117**, 10946-10957, doi:doi:10.1073/pnas.1912866117 (2020).

27 Iznardo, H. & Puig, L. Dual inhibition of IL-17A and IL-17F in psoriatic disease. *Ther Adv Chronic Dis* **12**, doi:10.1177/20406223211037846 (2021).

28 Ma, J., Liu, M. T., Wang, Y. C., Xin, C., Zhang, H., Chen, S. R., Zheng, X. D., Zhang, X. J., Xiao, F. L. & Yang, S. Quantitative proteomics analysis of young and elderly skin with DIA mass spectrometry reveals new skin aging-related proteins. *Aging-Us* **12**, 13529-13554, doi:DOI 10.18632/aging.103461 (2020).

29 Szilveszter, K. P., Nemeth, M. & Mocsai, A. Tyrosine Kinases in Autoimmune and Inflammatory Skin Diseases. *Front Immunol* **10**, doi:10.3389/fimmu.2019.01862 (2019).

30 Poumay, Y. & de Rouvroit, C. L. HB-EGF, the Growth Factor that Accelerates Keratinocyte Migration, But Slows Proliferation. *J Invest Dermatol* **132**, 2129-2130, doi:10.1038/jid.2012.225 (2012).
31 Rosenberger, C., Solovan, C., Rosenberger, A. D., Li, J. P., Treudler, R., Frei, U., Eckardt, K. U. & Brown, L. F. Upregulation of hypoxia-inducible factors in normal and psoriatic skin. *J Invest Dermatol* **127**, 2445-2452, doi:10.1038/sj.jid.5700874 (2007).
32 Liang, H. F., Li, J. Q. & Zhang, K. M. Pathogenic role of S100 proteins in psoriasis. *Front Immunol* **14**, doi:10.3389/fimmu.2023.1191645 (2023).
33 Callahan, B. J., McMurdie, P. J., Rosen, M. J., Han, A. W., Johnson, A. J. A. & Holmes, S. P. DADA2: High-resolution sample inference from Illumina amplicon data. *Nat Methods* **13**, 581-583, doi:10.1038/Nmeth.3869 (2016).
34 Segata, N., Izard, J., Waldron, L., Gevers, D., Miropolsky, L., Garrett, W. S. & Huttenhower, C. Metagenomic biomarker discovery and explanation. *Genome Biol* **12**, doi:10.1186/gb-2011-12-6-r60 (2011).

Chapter 6. In-situ formation of semiconductor biointerface for biomodulation

6.1 Introduction

Inorganic semiconductors showcase various good physical properties, allowing them to be crafted into device platforms suitable for multiple applications, including environment, energy, sustainability[1-3]. When you compare them with polymers and metals, semiconductors emerge as particularly well-suited for studies related to electronic and photonic biointerfaces[4,5]. This is because they have the flexibility to be designed into versatile devices like sensors, modulators, and switches, tailored with specific characteristics. A primary strength of these inorganic semiconductor devices is their capability to undergo processing on a large scale[6]. This is due to the presence of industrial technologies used in creating complementary metal–oxide–semiconductor (CMOS) circuits[7]. Moreover, devices made from inorganic semiconductors are recognized for their rapid response, ability to amplify signals, their multifaceted nature, and the capacity to handle multiple tasks[8]. They are also tolerant to errors, which makes them a perfect choice for studying the intricate dynamics present in biological entities[9]. Another noteworthy aspect is that these devices excel in capturing optical energy and changing it into other energy types, like electricity[10]. This ability is crucial for the functioning of small-sized wireless instruments[11]. Nonetheless, creating a consistent and integrated connection between the semiconductor and biological tissues is still a challenge[12]. The core of this issue lies in the differences in attributes, such as Young's modulus and surface properties, between conventional semiconductors and biological tissues[13]. Hence, fine-tuning the interaction with biological entities, especially smaller ones like bacteria, remains a work in progress.

Here, inspired by the nature biomineralization process, we proposed a new method by in-situ building a periplasmic semiconductor for biomodulation and sustainable applications (Figure 6-

1). The constructed semiconductors exhibit low crystallinity and are stabilized by the peptidoglycan matrix of periplasms, thus providing a softer bioelectrical interface with bacterial cells. As a demonstration, we introduced metal ions and cysteine to *Escherichia coli (E. coli)* culture to mineralize semiconductors such as cadmium sulfide (Figure 6-1), one of the most-studied optically-active materials[14], in the periplasm. The selection of *E. coli* was based on the fact that it is one of the most studied organisms on earth. A number of favorable characteristics, including genetic tractability, favorable growth conditions, well-characterized biochemistry and physiology, as well as the availability of genetic manipulation tools, make *E. coli* an ideal platform for developing the periplasmic biointerfaces. Notably, we have examined the ability of periplasmic semiconductor clusters to couple photosensitization with bacterial metabolism to enhance intracellular biosynthesis (Figure 6-1). Besides, we also found that the bacteria display a higher density of fimbriae (*i.e.,* microbial nanowires) following semiconductor cluster mineralization (Figure 6-1) and is capable of mineralizing multiple-metal-element to form 'high-entropy' semiconductor clusters. Furthermore, the production of periplasmic hybrids can be performed using either a flask culture or a continuous bioreactor, which has great potential for large-scale production. This emphasize that the biomodulation product could be used for low-cost and scale-up application, including water purification, manufacturing of living bioreactors, and artificial photosynthesis.

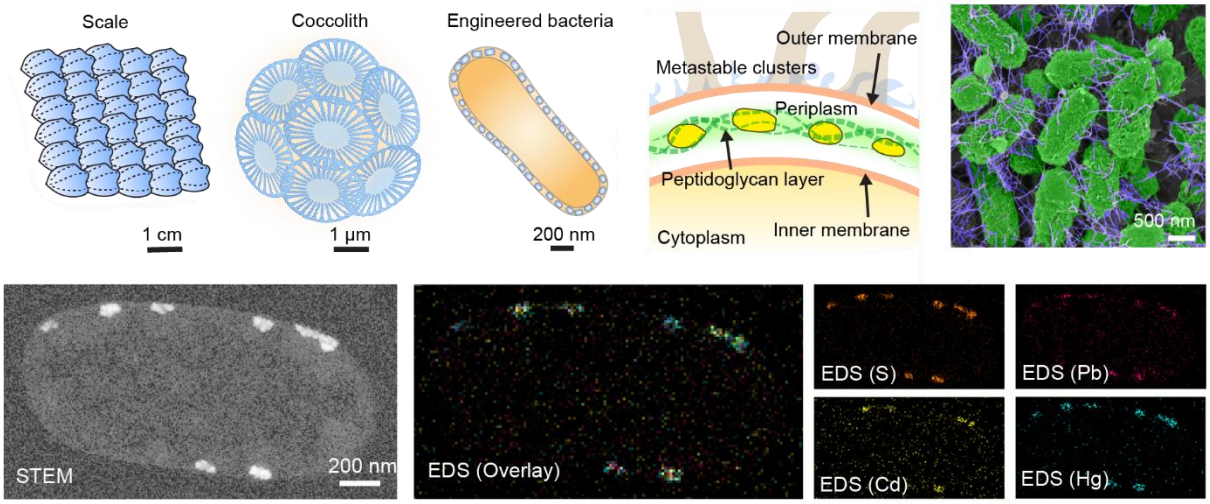

Figure 6-1 An illustration of aquatic and biomineralized soft-hard composites with a wide range of length scales and a variety of structures and functions. Examples include fish scales, coccoliths, and the proposed nanostructured 'exoskeletons' in the periplasm of gram-negative bacteria. The scale bars are only representative. Schematic illustrating the synthesis of semiconductor nanoclusters within the periplasm of gram-negative bacteria. The periplasm is the space between the inner membrane and the outer membrane. Electron and X-ray microscopy images of the biohybrids. Pseudo-colored scanning electron microscope (SEM) image showing E. coli (green) with extensive amounts of microbial nanowires (purple). Scanning transmission electron microscopy (STEM) image and energy dispersive X-ray spectroscopy (EDS) mapping showing bacterial cell can mineralize semiconductor clusters composed of multiple elements, including Cd, Pb, and Hg, within single bacterial cell.

6.2 Result and Discussion

6.2.1 Periplasmic biomineralization for biointerface formation

To in-situ form semiconductor biointerface, we first closely studied how the precursors will influence the bacteria. We first confirmed that *E. coli* growth in the M9 medium was significantly suppressed in the absence of cysteine at Cd^{2+} concentrations greater than 0.1 mM. This is reasonable since heavy metal ions such as Cd^{2+} could be toxic to bacterial cells. Note that this study utilized the minimal media (M9) due to its definite components, very low autofluorescence, and very low absorbance[15]. The bacteria, however, were able to tolerate concentrations of Cd^{2+} as

high as 0.3 mM in the presence of cysteine (1 mM) (Figure 6-2). The fact that cysteine may mitigate the cytotoxicity elicited by metal ions suggests that metal ions may be transformed into precipitates by cysteine.

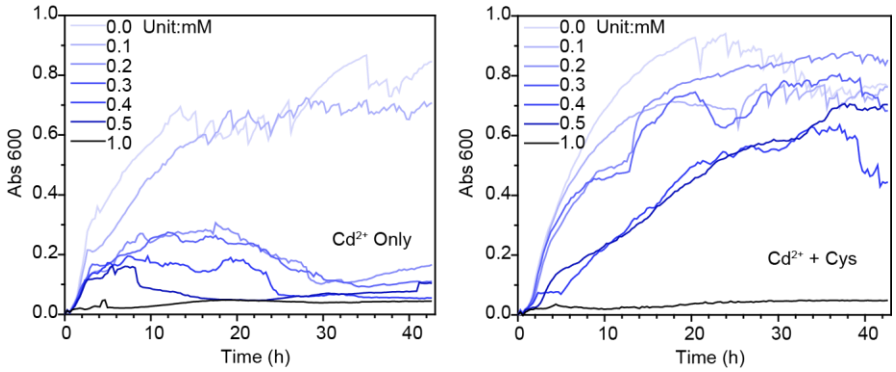

Figure 6-2 Optical density measurements showing that in the absence of Cys, E. coli growth is severely inhibited at Cd^{2+} concentrations > 0.1 mM. Optical density measurements showing that in the presence of Cys, E. coli cells can tolerate Cd^{2+} concentrations up to 0.3 mM with little adverse effect on growth. Lines in A and B represent the entire measured data set while dots are representative observations.

Using scanning transmission electron microscopy, we examined images of *E. coli* cells grown in a medium containing both Cd^{2+} and cysteine, and it showed a high density of biomineralization (Figure 6-3).

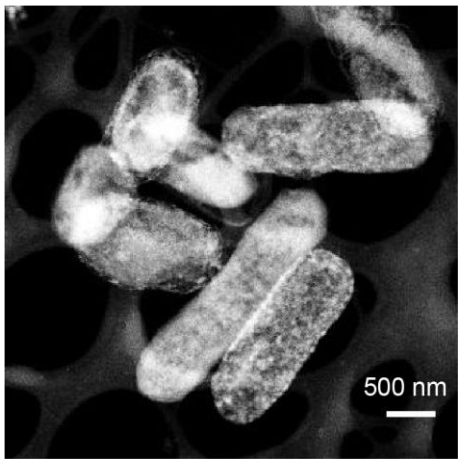

Figure 6-3 STEM image indicating the formation of biohybrids with mineralized aggregates. Scale bar, 500 nm.

The bacteria also grew a significant number of fimbriae over time, which is confirmed by time-lapse scanning electron microscope (SEM) images and the statistical analysis (Figure 6-4).

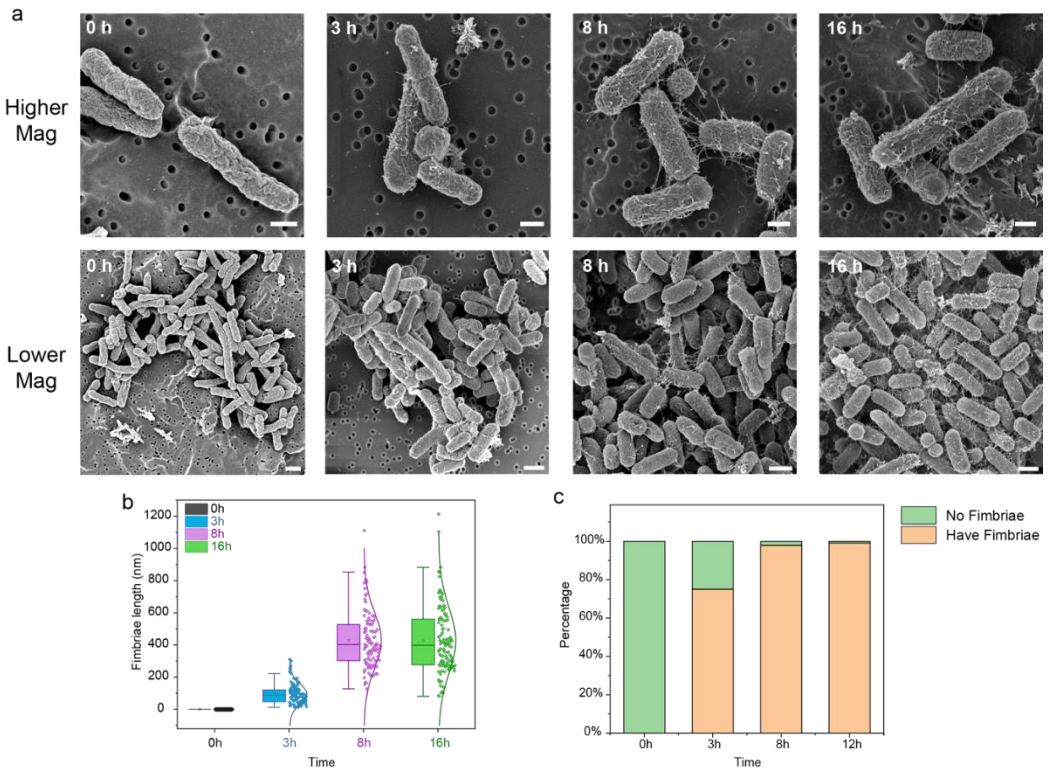

Figure 6-4 SEM images of bacteria incubated in Cd2+/Cys-containing medium at 0 h, 3 h, 8 h, and 16 h. (a) SEM images show the growth of microbial nanowires. Microbial nanowires begin

to form after ~ 3 h and reach maximum length at ~8 h. (b) The pili length at different time points. c) The percentage of bacterial cells developed with pili at different time points. The boxes represent the 25th, 50th (median) and 75th percentiles of the data; the whiskers represent the lowest (or highest) datum within 1.5× interquartile range from the 25th (or 75th) percentile (n>100). Scale bars, 500 nm for higher magnifications and 1 μm for lower magnifications. More than ten images from higher and lower magnifications (over 50 cells from each group) and quantified the length of pili and the percentage of cells developed pili over a period of time.

To verify that the formation of the semiconductor biointerface results from the utilization of cysteine and cadmium salt precursors, we conducted experiments with a control group. In the absence of cysteine or Cd^{2+}, no biomineralization or fimbriae formation was observed (Figure 6-5).

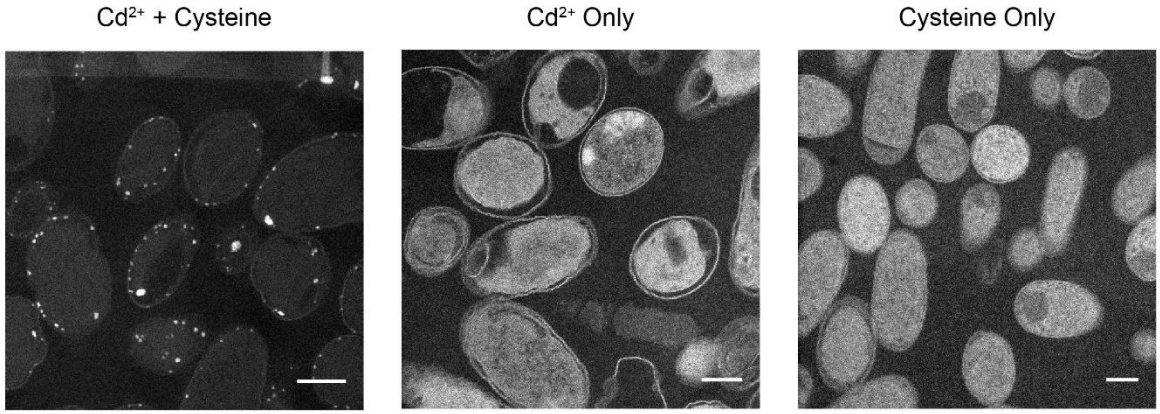

Figure 6-5 Cross-sectional TEM images of E. coil under different culture conditions show that both Cd^{2+} and cysteine are necessary for nanocluster biomineralization. Cd^{2+} only and cysteine only culture conditions will not induce biomineralization. Scale bar, 500 nm.

Furthermore, we used inductively coupled plasma mass spectrometry (ICP-MS) to study the metal ion removal (Figure 6-6).

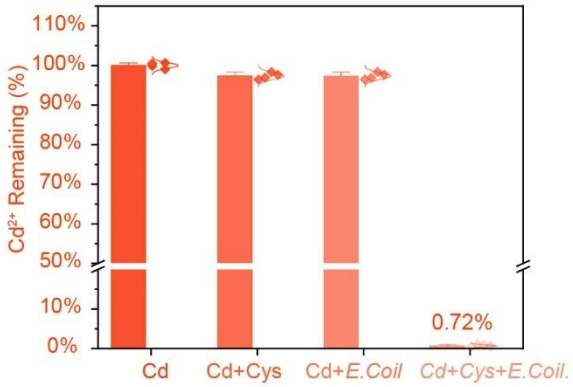

Figure 6-6 The E. coli flask culture can remove heavy metals with cysteine at very high efficacy with the presence of cysteine. Plots of the remaining Cd2+metal ions (percentages) in medium after flask culture treatment under varying culture conditions indicate that with cysteine and E. coli, the flask culture can achieve high removal efficiency.

With only cysteine or *E. coli* present, heavy metals were hardly removed. However, in the presence of both cysteine and *E. coli*, 99.28% of Cd^{2+} were eliminated. These results suggest that the metal ions were actively removed from the media in the presence of cysteine and were utilized by the bacteria for biomineralization. Metal ions, cysteine and bacteria are all essential for this process.

While STEM suggested biomineralization in the aggregate form, we cannot exclude the possibility of metal ions being immobilized at the molecular level within the cells. To check the chemical composition of the semiconductor inside the bacteria, we employed synchrotron-based, 3D X-ray fluorescence tomography on supercritical-dried biohybrids, a method sensitive enough to establish position correlations between various elements (Figure 6-7).

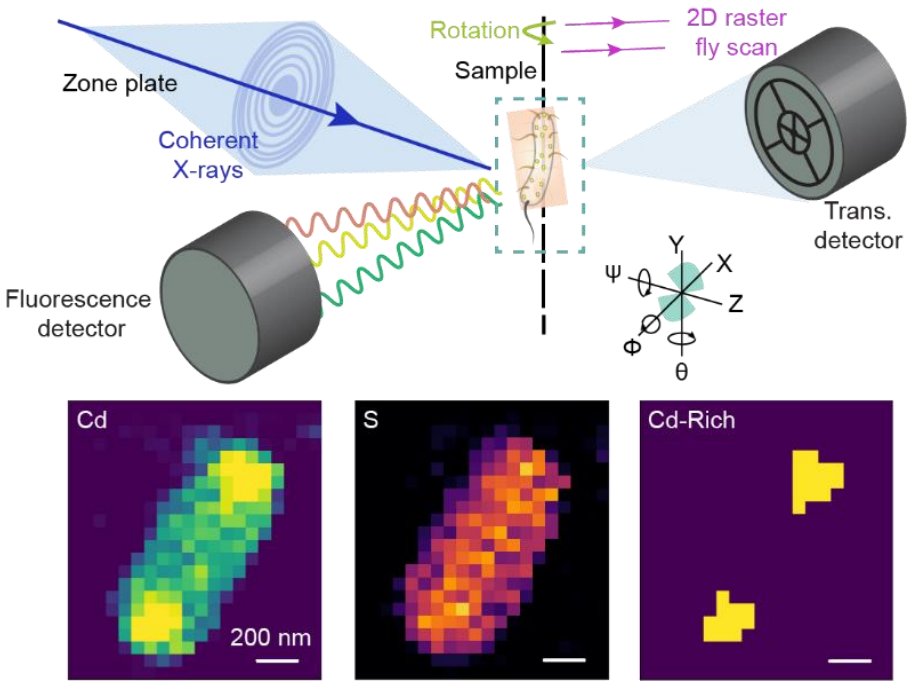

Figure 6-7 Schematic of the synchrotron-based, 3D X-ray fluorescence tomography experiment. Using a zone plate, a monochromatized X-ray beam is focused on the sample. While the sample is raster scanned, X-ray fluorescence spectra are recorded, forming 2D elemental maps and 3D reconstructions in tomography mode. Using a quadrant photodiode, differential phase contrast images are generated from transmission signals. Selected slice of the 3D X-ray fluorescence tomography reconstruction showing the presence of both the Cd and S elements within an intact bacterial cell. In each virtual slice, Cd-rich regions are identified when pixel intensity is beyond 2 times of standard deviation from the mean in each virtual slice. Scale bar, 200 nm.

Different direction images of 3D X-ray fluorescence tomography are shown in Figure 6-8.

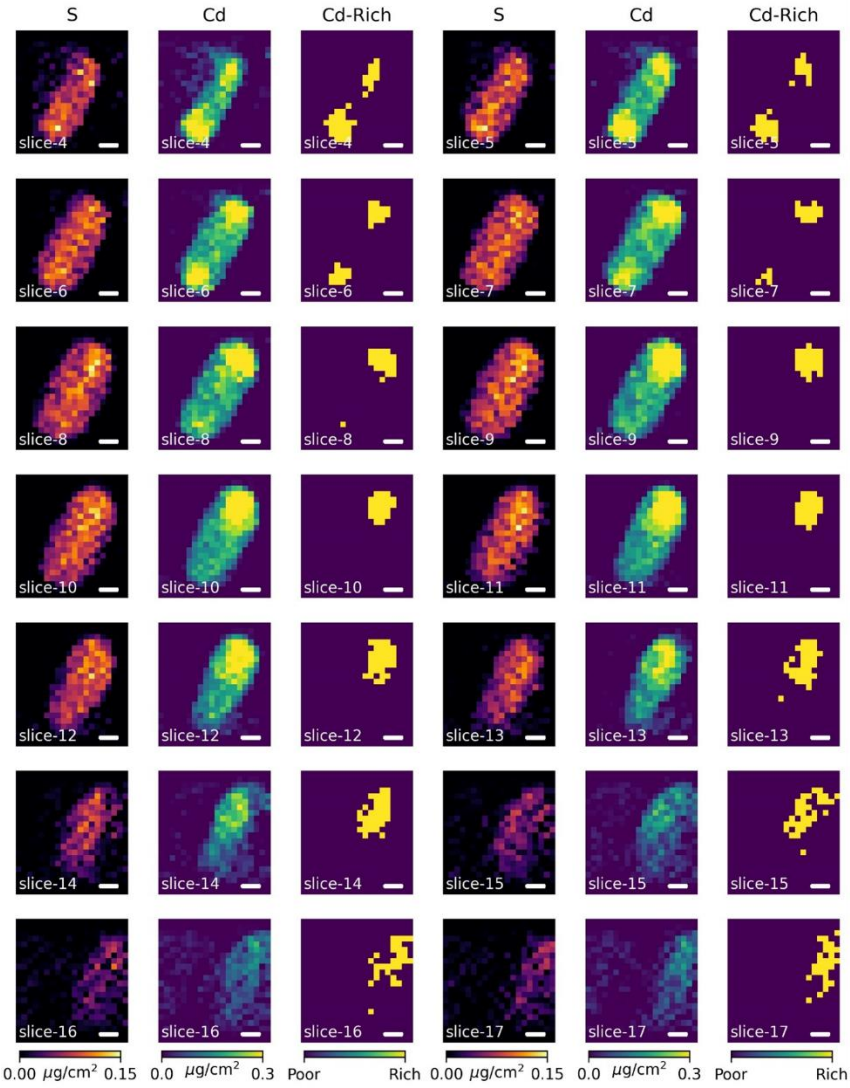

Figure 6-8 Spatial distribution of S and Cd in virtual cross-sectional slices after 3D tomography reconstruction. Cd-rich regions are identified when the pixel intensity is beyond 2 times of standard deviation from the mean in each virtual slice. Scale bar, 200 nm.

The following observations were noteworthy. Firstly, the results confirmed the presence of Cd and S elements within the cell, indicating the efficient uptake of Cd^{2+} and likely the cysteine by *E. coli*. Second, after determining a threshold for Cd/S rich regions (*i.e.*, areas with pixel intensity beyond 2 times of standard deviation from the mean in each virtual slice), we found a tendency for Cd/S rich areas to be located in the outer regions of the bacteria, possibly associated with periplasm- or

cell wall-bound aggregates. Third, the estimated molar ratio (Figure 6-9) of Cd/S in the Cd/S rich region is 1.02, whereas that in the Cd/S poor region is 0.573. Since the Cd/S rich region is located near the cell periphery, we believe biomineralization is less likely to occur in the cytoplasm, even though immobilized Cd^{2+} might exist there.

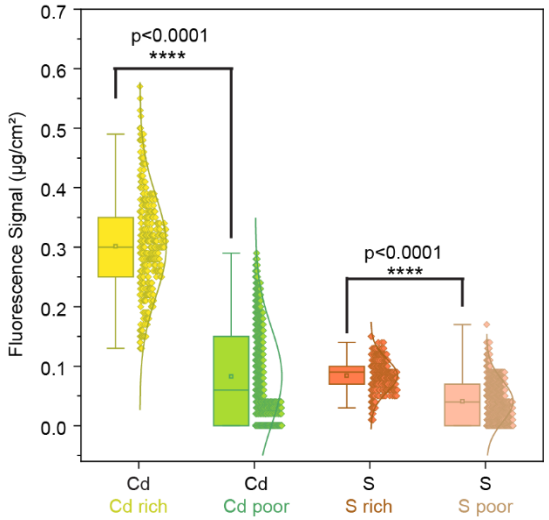

Figure 6-9 Boxplot showing the correlation between the distributions of Cd and S in 3D reconstruction slices. Boxes bind interquartile range (IQR) divided by the median.

6.2.2 Semiconductor biointerface characterization

To more clearly discern the location of the Cd/S aggregates near the bacterial peripherals, we prepared cross-sectional samples of biohybrids through micro-toming. STEM images of cross-sectional samples revealed that the biomineralized Cd/S aggregates had an average size of ~ 29.3 nm, and they were primarily located between the inner membranes (IM) and outer membranes (OM), which correspond to periplasmic space (Figure 6-10).

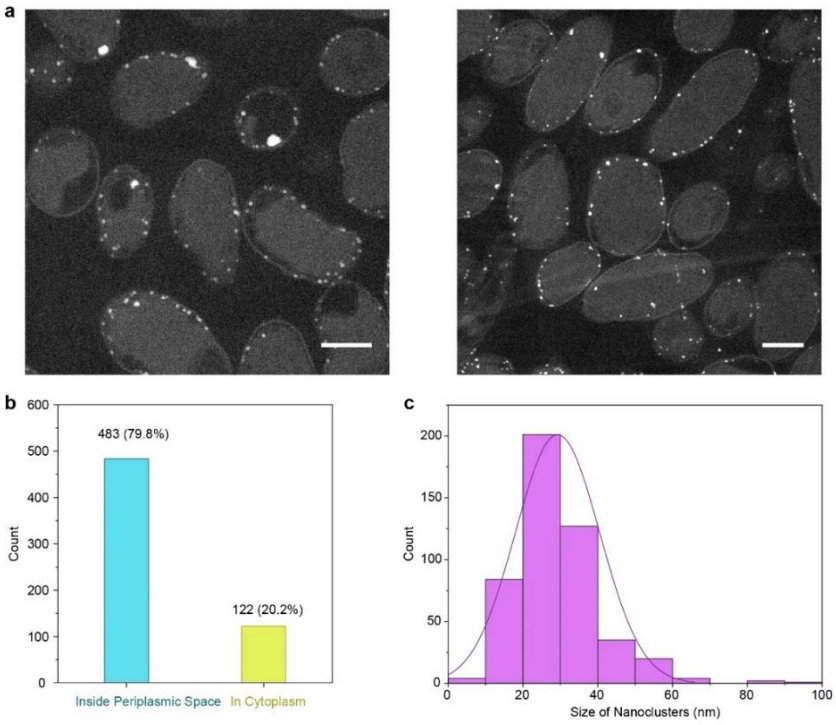

Figure 6-10 The biomineralized nanoclusters are mainly located in the periplasmic space. (a) Cross-sectional STEM images showed most of the nanoclusters are located in the periplasmic space. Scale bar, 500 nm. (b) Statistical analysis further confirmed that 483 out of 605 particles (79.8%) were located between the inner and outer membranes with clear boundaries. It is noteworthy that we only defined those particles as being within the periplasmic space. However, for E. coli, the periplasmic space could occupy up to 40% of the cell volume. Therefore, the percentage within periplasmic space might be underestimated. (c) The CdS nanoclusters in the bacterial cells have an average size of 29.3 nm based on cross-sectional STEM images. The size distribution corresponds to over 400 nanoclusters.

STEM energy dispersive spectroscopy (STEM-EDS) mapping showed that the aggregates were composed of Cd and S elements, whose locations are highly correlated. STEM images and selective area electron diffraction (SAED) of the individual Cd/S aggregates show low crystallinity or almost amorphous structures (Figure 6-11), suggesting that the building blocks of biominerals are nanoclusters.

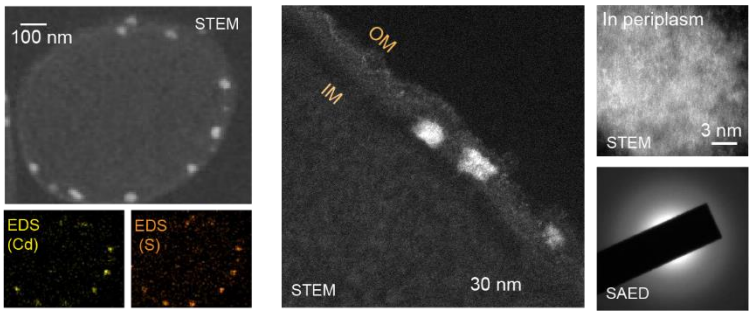

Figure 6-11 Zoom-in STEM images and selected area electron diffraction (SAED) showing the aggregates display low crystallinity and are nanoclusters. Scale bar, 30 nm, and 3 nm.

Furthermore, after collecting the aggregates by cell lysis and centrifugation, we found that the biominerals dissociated into smaller particles with an average size of ~ 6.02 nm (Figure 6-12), suggesting that the associations between the nanoclusters in the periplasm are largely due to the peptidoglycan matrix (i.e., the biomineralization template).

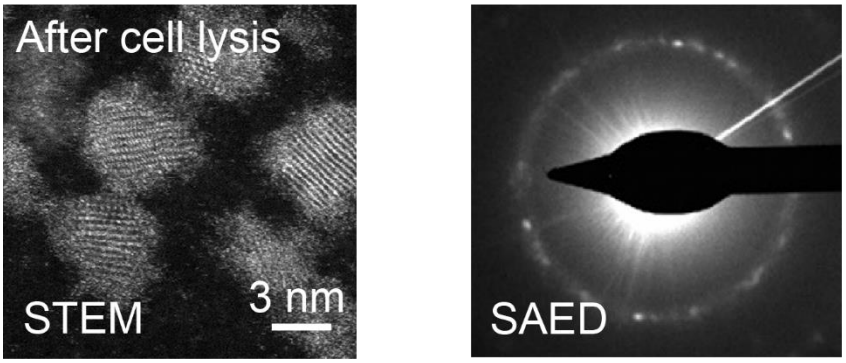

Figure 6-12 STEM image and SAED of the minerals (with TEM) after cell lysis and particle extraction, showing smaller particle sizes and improved crystallinity. Scale bar, 3 nm.

The similar methods could also be used to generate other semiconductors such as lead sulfide (PbS) and mercury sulfide (HgS), we also used similar methods to measure their size and crystallinity (Figure 6-13).

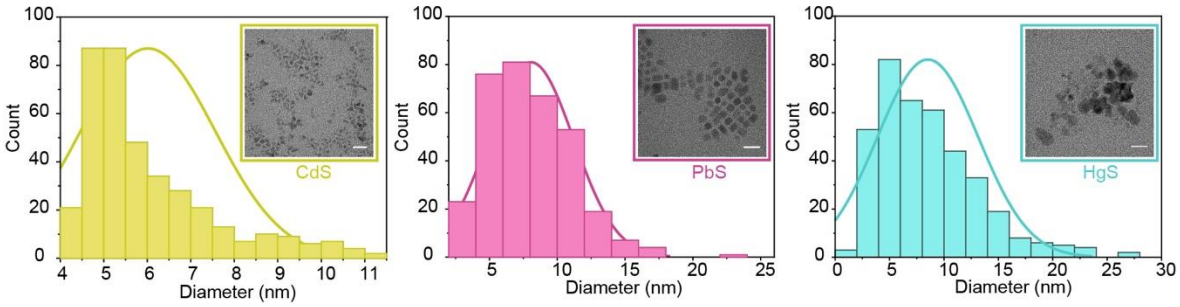

Figure 6-13 Histograms showing the diameter distribution of CdS, PbS and HgS nanoparticles after extraction from the biohybrid. The CdS, PbS, and HgS nanoparticles have diameters of 6.02 ± 1.55 nm, 8.06 ± 3.15 nm, and 8.52 ± 4.65 nm, respectively (n>300). The corresponding inset TEM images show the morphology of the small nanoparticles. Scale bar, 20 nm.

Notably, the removal of the periplasmic components from the aggregates increases the crystallinity and forms Zincblende-phase crystallites (Figure 6-14), likely through oriented attachment or other non-classical crystallization pathways[16].

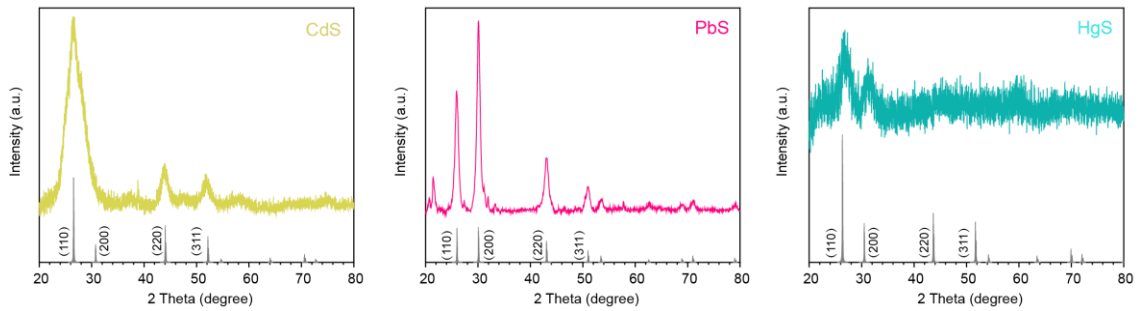

Figure 6-14 XRD confirms the crystal structures of the CdS, PbS, and HgS nanoparticles after extraction from the biohybrid.

These observations, in conjunction with the Cd/S ratio provided by X-ray fluorescent tomography, indicate that CdS is the primary material mineralized in the periplasm. The CdS nanoclusters in

bacteria give the biohybrids fluorescence properties, as indicated by fluorescence imaging and micro-spectrofluorometry measurements from a few cells. Biohybrids show a defect-dominant fluorescence spectrum, characterized by a broad distribution of emissions around ~700 nm, that differs significantly from the band edge emission of bulk CdS (i.e., ~510 nm). Taken together, these results suggest that CdS nanoclusters mineralized in the periplasm are metastable and mainly disordered and defect-rich aggregates (Figure 6-15).

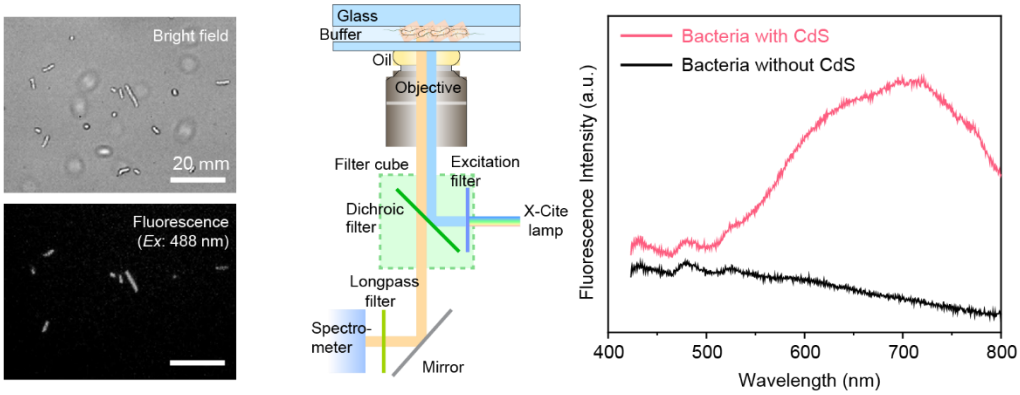

Figure 6-15 Bright-field and fluorescence optical microscopy images of the biohybrids, excitation wavelength, 488 nm. Scale bar, 20 μm. UV-induced micro-spectrofluorometry spectra showing that the bacteria with CdS nanoclusters have defect-dominant fluorescent properties with a broad emission peak.

6.2.3 Transcriptomic analysis

To probe the potential cellular processes, we performed a transcriptomic study on Cd^{2+}/cysteine-treated E. coli samples (with CdS nanocluster formation) and the control Cd^{2+}-treated E. coli samples (without CdS nanocluster formation) (Figure 6-16).

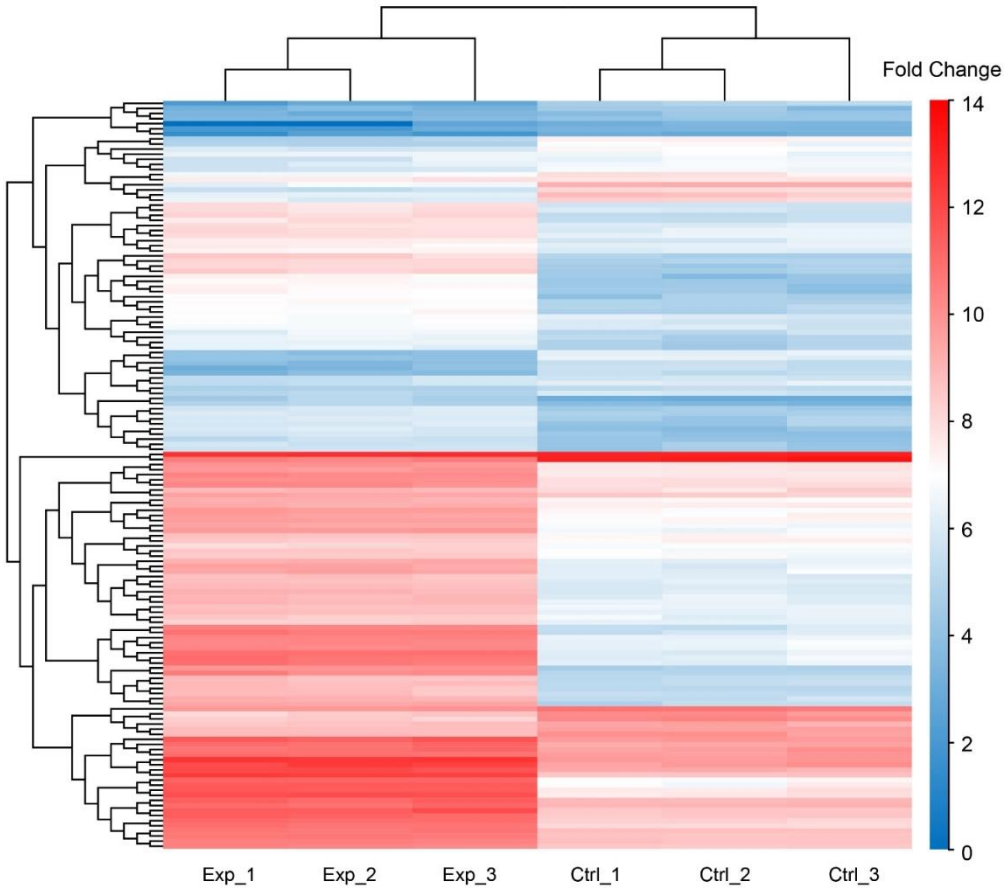

Figure 6-16 Hierarchical clustering analysis of RNA-Seq differential expression data in three individual control group samples treated with Cd^{2+} only and experimental group samples treated with Cd^{2+} and cysteine.

We found that several key genes encoding cysteine desulfhydrase, including cysK, dcyD, cysM, metB, metC, and sufS, were up-regulated in Cd^{2+}/cysteine-treated samples compared to Cd^{2+}-treated samples (Figure 6-17).

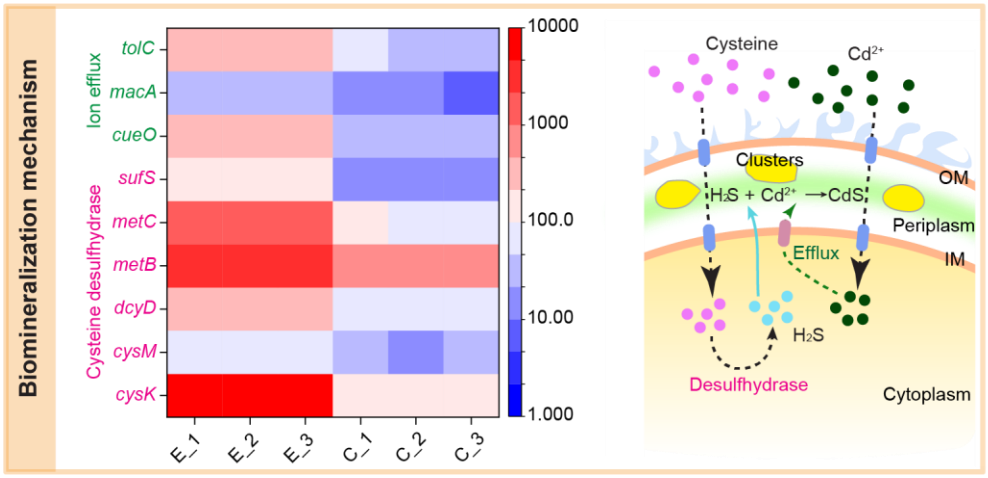

Figure 6-17 Heatmap of transcriptomic study confirming the upregulation of genes encoding cysteine desulfhydrase and ion efflux pumps. E_1, E_2, and E_3 represent three independent experimental groups, while C_1, C_2, and C_3 are the control groups. The number of the color bar represents fragments per kilobase of exon per million mapped fragments (FPKM).

The cysK, dcyD, cysM, and metC genes are directly involved in different biological pathways that convert cysteine into hydrogen sulfide (H_2S) (Figure 6-18).

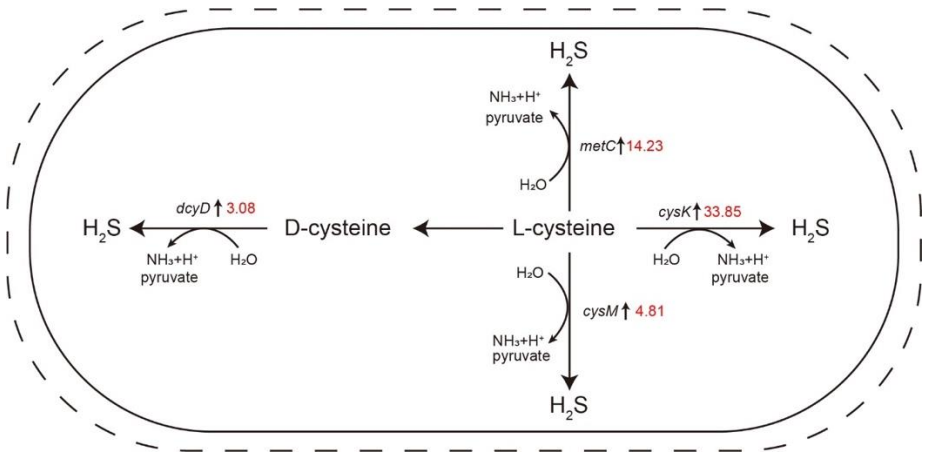

Figure 6-18 Multiple biological pathways to metabolize cysteine into H2S. Cysteine could be metabolized through different biological pathways, and we discovered the up-regulation of several genes in Cd^{2+} and cysteine-treated samples that are directedly related to H2S synthesis, including cysK, dcyD, cysM, and metC, in comparison with Cd^{2+} treated samples.

The up-regulation of efflux-related genes, including tolC, cueO, and macA (Figure 6-19), suggested the efflux of Cd^{2+} into the periplasmic space following uptake by the E. coli cells[17,18].

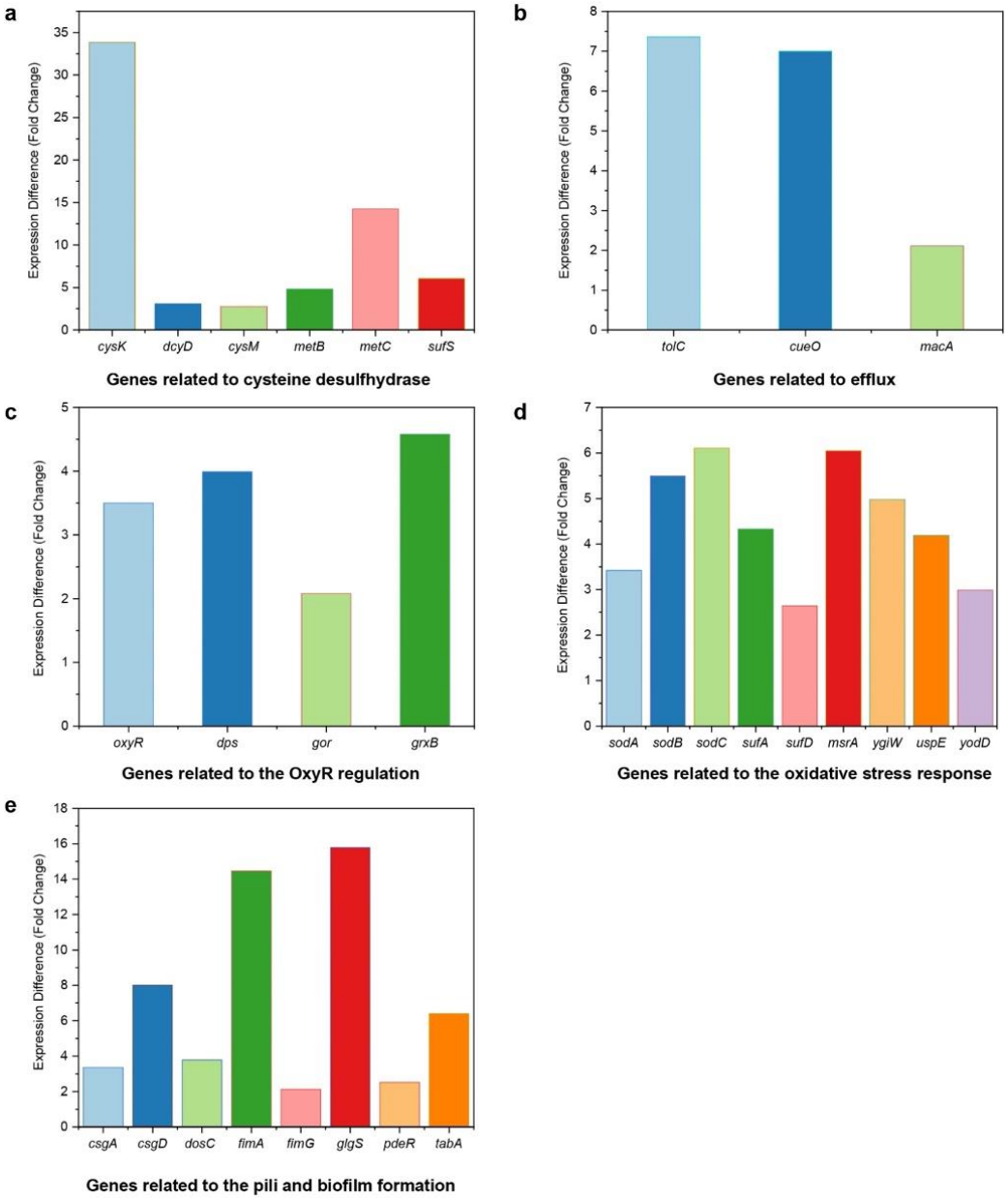

Figure 6-19 Up-regulation of different genes related to the biomineralization process. (a) Multiple cysteine desulfhydrase genes, including cysK (+33.85), dcyD (+3.08), cysM (+2.76), metB (+4.81), metC (+14.23), sufS (+6.05), were up-regulated in Cd^{2+} and cysteine treated E. coli

cells compared to those treated with Cd^{2+} only. (b) Multiple efflux-related genes, including tolC (+7.36), cueO (+7.00), and macA (+2.11), were up-regulated in Cd^{2+} and cysteine treated E. coli cells compared to those treated with Cd^{2+} only, indicating the efflux of Cd^{2+} into the periplasmic space. (c) Multiple OxyR-related genes, including oxyR (+3.50), dps (+3.99), gor (+2.08), grxB (+4.58), were up-regulated in Cd^{2+} and cysteine treated E. coli cells compared to those treated with Cd^{2+} only, suggesting that the synthesized CdS nanoparticles contribute to the induced oxidative stress in the E.coli cells. (d) Multiple oxidative stress response-related genes, including sodA (+3.42), sodB (+5.50), sodC (+6.11), sufA (+4.33), sufD (+2.64), msrA (+6.05), ygiW (+4.98), uspE (+4.19), and yodD (+2.99), were up-regulated in Cd^{2+} and cysteine treated E. coli cells compared to those treated with Cd^{2+} only, suggesting the E. coli cells were under increased oxidative stress during the nanoparticle and microbial nanowires formation. (e) Multiple oxidative stress response-related genes, including csgA (+3.36), csgD (+8.02), dosC (+3.78), fimA (+14.46), fimG (+2.13), glgS (+15.79), and tabA (+6.40), were up-regulated in Cd^{2+} and cysteine treated E. coli cells compared to those treated with Cd^{2+} only.

H_2S is highly lipophilic molecule and freely penetrate cell membrane[19]. Therefore, the reaction of H_2S and Cd^{2+} to precipitate CdS nanoclusters would be mainly confined to the periplasmic space; this is further supported by the up-regulation of multiples genes encoding proteins that are typically located in the periplasmic space (Figure 6-20).

H_2S can react with Cd^{2+} to precipitate CdS particles in various biological systems, such as bacteria[20], yeast[21], and fungi[22]. Given the fact that bacteria must be metabolically active for the biomineralization to occur and the transcriptomic results, we conclude in this case that 1) the cysteine is converted into H_2S through desulfhydrase; 2) Cd^{2+} may enter the cell and even reach the cytoplasm, but they mainly interact with H_2S to form CdS nanoclusters within the periplasmic space due to the efflux.

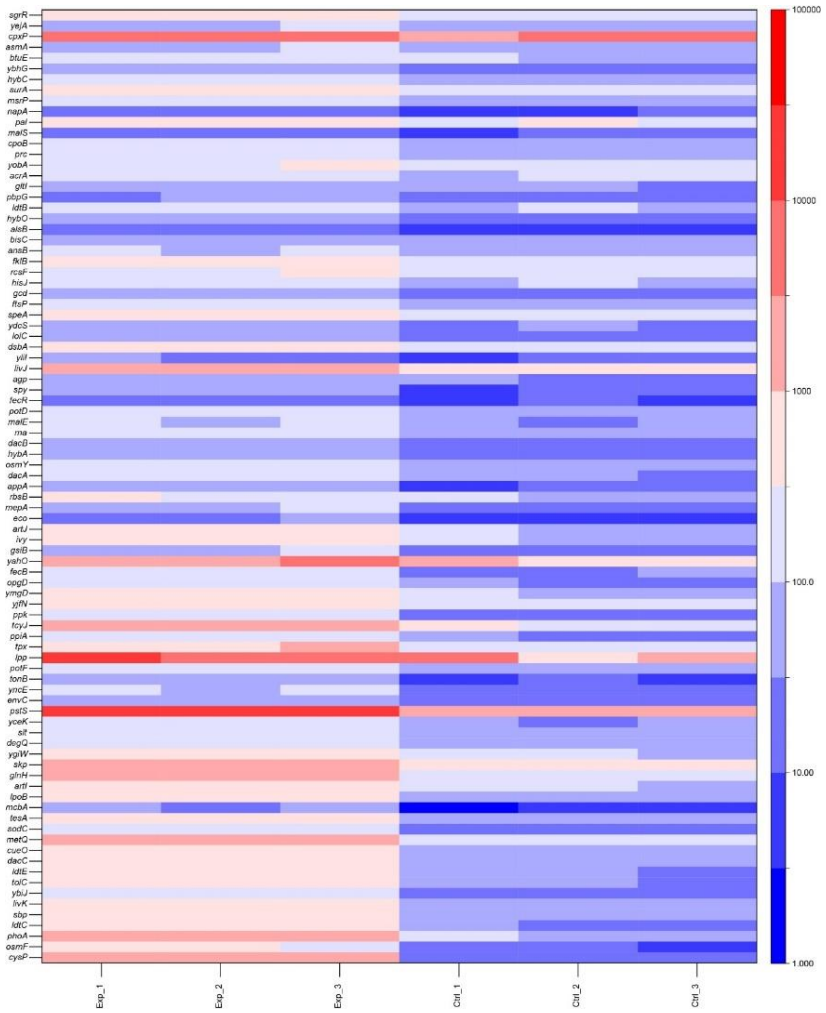

Figure 6-20 Heatmap illustrating the up-regulation of genes encoding proteins located in the periplasmic space. The data indicate that the synthesis of CdS nanoclusters in the periplasmic space may also upregulate protein expression in the periplasmic space.

Also, we discovered that the formation of CdS could induce high oxidative stress, as evidenced by the up-regulation of dps, gor, grxB, and oxyR genes under the OxyR regulon as well as multiple oxidative stress-responsive genes, including msrA, sodA, sodB, sodC, sufA, sufD, uspE, ygiW, and yodD. The induced oxidative stress could induce the fimbria and pili formation, as confirmed with the major fimbrial subunit gene fimA (14.46 fold) and major curli subunit gene csgA (3.36 fold), corresponding to the microbial nanowire formation.

6.2.4 Application in water purification and microbial modulation

Along with the semiconductor formation process, the heavy metal is also moved from the water. This suggests the potential sustainable application. The bacteria could use the wastewater for generating semiconductor biointerface for biofuel production. To further investigate this, we use the flask culture to further extend the biomineralization using different metal ions (Figure 6-21). The bacteria can utilize most of Cd^{2+} (99.28%), Pb^{2+} (94.72%), and Hg^{2+} (95.68%) within 24 hours, and the concentrations of metals can be as high as 0.3 mM. Using cross-sectional STEM images and EDS maps, we confirmed the presence of PbS and HgS aggregates with the bacteria. As we observed for metastable CdS, these biosynthetic PbS and HgS aggregates can also be extracted from the periplasm and transformed into crystalline and smaller nanocrystals.

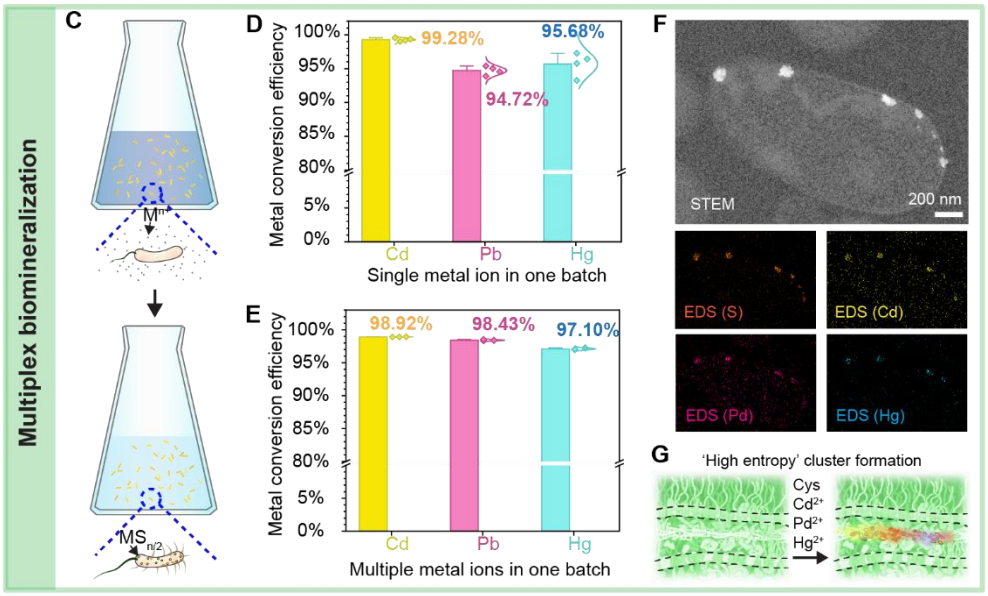

Figure 6-21 Schematic showing that *E. coli* can utilize different heavy metals (M^{n+}), including Cd^{2+}, Pb^{2+}, and Hg^{2+}, from flask cultures to form metal sulfides. Plot summarizing individual heavy metal ion removal upon biomineralization. The metal conversion rates of Cd^{2+}, Pb^{2+} and Hg^{2+} (0.3 mM each) are 99.28%, 94.72%, and 95.68%, respectively. The data points represent mean ± s.d. (n=4). Plot illustrating the simultaneous removal of heavy metal ions upon multiplex biomineralization. The metal conversion rates of Cd^{2+}, Pb^{2+} and Hg^{2+} (0.1 mM each) are 98.91%, 98.43%, and 97.10%, respectively. Data points represent mean ± s.d. (n=4). STEM image and EDS map showing *E. coli* can biosynthesize $Cd_xPb_yHg_zS$ (x + y + z ~ 1), as the locations for different elements are highly correlated in space. Scale bar, 200 nm. Schematic showing a process of forming 'high entropy' nanoclusters through periplasm-supported biomineralization.

Besides single-metal-element sulfides formation, we also explored multiplex biomineralization. At 0.1 mM of individual ion concentration, 98% of Cd^{2+}, 98% of Pb^{2+}, and 97% of Hg^{2+} can be simultaneously removed from the mixture within 24 hours. The slight difference in removal efficiency between Cd^{2+}, Pb^{2+} and Hg^{2+} may be due to the different affinity of *E.coli* cells for each metal ion[23]. Besides flask culture, we have also constructed replaceable membranes that contain living bacteria and filter membranes and mounted them onto a 3D printed bioreactor for continuous processing (Figure 6-22).

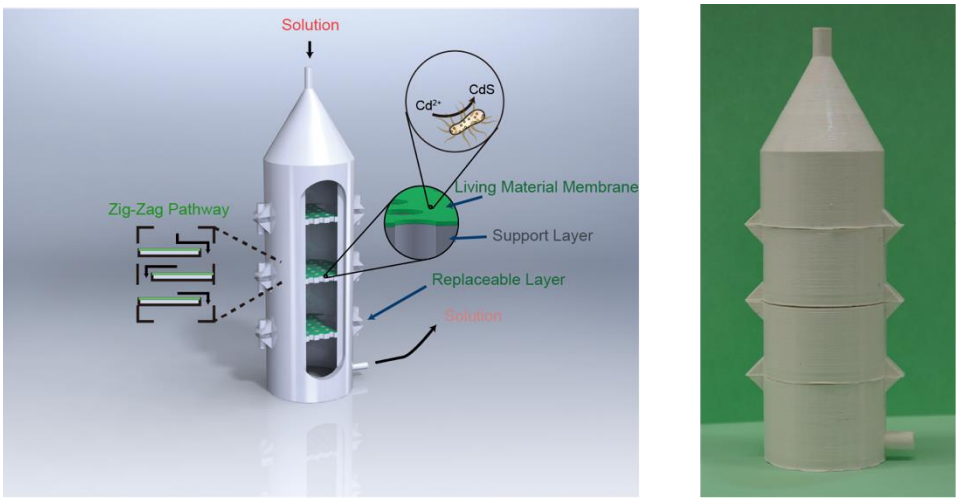

Figure 6-22 Continuous bioprocessing reactor for biohybrids synthesis. The design of the reactor and the zoom-in images show the utilization of the living material membrane with a zig-zag pathway to induce biohybrids synthesis in a continuous manner. Left: Schematic; Right: a photograph of the actual reactor.

The bioreactor was supplied with 200 mL of M9 medium containing Cd^{2+}, Pb^{2+}, and Hg^{2+} (0.1 mM each), and Cd^{2+} and Pb^{2+} had already reached 79.1% and 91.2% utilization efficiency after 2 hours, respectively. After 24 hours, the metal conversation rate of Cd^{2+}, Pb^{2+}, and Hg^{2+} reached 98.7%, 98.1%, and 87.3%, respectively. Without further optimization, this small living composite membrane (diameter: 25 mm) could process up to 200 mL of medium for biomineralization. The continuous system may be further scaled up and integrated with programmable and self-regulating systems for application in modulation biointerface and synthetic biology[24] (Figure 6-23).

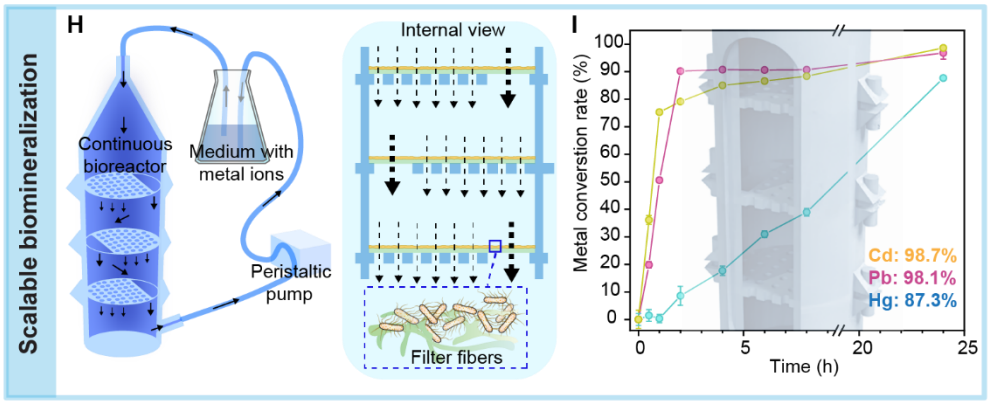

Figure 6-23 Schematic illustrating biomineralization over a replaceable living membrane, composed of *E. coli* and filter paper, in a continuous bioprocessing reactor. The solid or dashed arrows suggest the flow pattern throughout the bioreactor and its accessories. The green matrix beneath the bacteria is filter. (**I**) Plot showing the metal conversion of Cd^{2+}, Pb^{2+} and Hg^{2+} in the continuous bioprocessing reactor. The semi-transparent background shows the actual 3D design of the bioreactor.

The transcriptomic studies, in addition to revealing the potential role of cysteine desulfhydrase, show the upregulation of dehydrogenase genes in the presence of periplasmic CdS, including expression of formate dehydrogenases, NADH dehydrogenases, glyceraldehyde-3-phosphate dehydrogenases, pyruvate oxidase, D-lactate dehydrogenase, and glucose dehydrogenase, as well as upregulation of terminal reductases and oxidases genes (Figure 6-24). Moreover, periplasmic CdS biomineralization also resulted in the upregulation of 7 out of 8 ATP synthase subunit genes, including *atpA*, *atpC*, *atpD*, *atpE*, *atpF*, *atpG*, and *atpH*. Based on these up-regulations, an accelerated bacterial respiratory efficiency and a higher rate of ATP synthesis may be possible. Nanocrystalline CdS is known to produce photoelectrons in bilayer lipid membranes[25]. Given that the metastable CdS nanoclusters remain optically active and are physically close proximity to the electron transfer chain (which is located within the inner membrane of *E. coli*), we next explored the possibility of optically modulating microbial processes using the periplasmic biointerfaces.

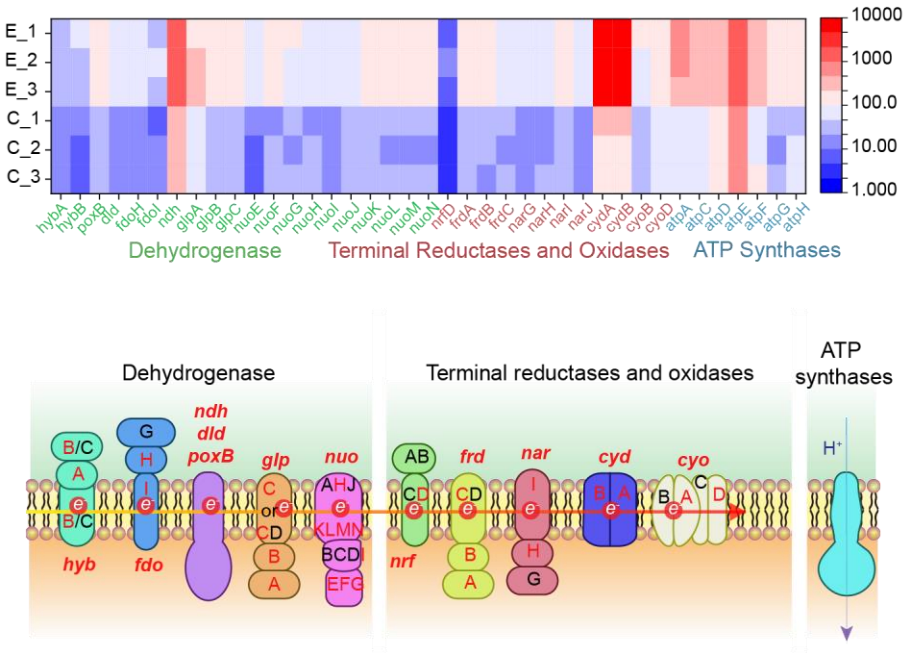

Figure 6-24 A heat map from transcriptomic analysis indicates that CdS biomineralization up-regulates genes related to the electron transport chain, including dehydrogenases, terminal reductases and oxidases, and ATP synthases. Schematic showing the electron transport chain with up-regulated genes highlighted in red letters. The red arrow indicates the direction of electron transport, while the purple arrow indicates proton transport.

Next, we will demonstrate that those in-situ formed biointerfaces could modulate the bacteria functionality and metabolism with the light stimulation. We incubated *E. coli* with *in situ* synthesized CdS nanoclusters under light illumination. We found that ATP level in *E. coli* under light was 8.1-times that of the dark condition. Repeating the same experiment in *E. coli* without CdS nanocluster mineralization, the ATP level under light was only 1.4 times that of the dark condition. This benchmark experiment suggested that the CdS nanoclusters may contribute to accelerated bacterial respiration and ATP level (Figure 6-25).

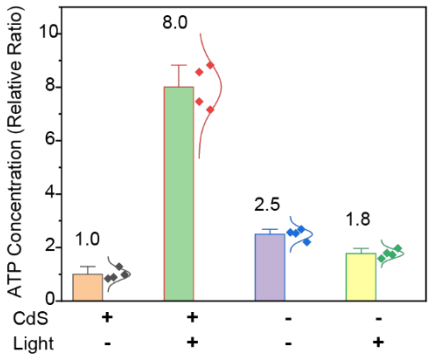

Figure 6-25 Production of ATP in *E. coli* cells with biomineralized CdS nanoclusters under light is 8.1-times of the ATP production in cells in dark. Data points represent mean ± s.d. (n=4). P values (< 0.001) are determined by unpaired two-tailed t-test.

Bioproduction is dependent upon the intracellular supply of ATP. Hence, establishing a cell factory that enhances ATP level under artificially controlled conditions is a promising strategy for improving bioproduction yields. To this end, we use the production of malate as a test system to determine whether our biohybrids can enhance biosynthesis under light stimulation. Malate is a four-carbon dicarboxylic acid identified as an optimal building block that could be derived from biomass[26], and it is widely used in fine chemical synthesis precursors and food industry additive[27]. The reductive tricarboxylic acid pathway utilizes ATP to generate malate[28]. Specifically, increasing ATP levels may activate the enzymes phosphoenolpyruvate synthase (PPS) and pyruvate carboxylase (PC), which would then redirect carbon flux from pyruvate to malate. The CdS nanocluster biomineralization increases the malate production from 1.87 mg/L to 12.10 mg/L under light stimulation, while the biomass of flask cultures (optical density of 600 nm, OD_{600}) is similar. However, the control bacterial group without CdS nanocluster does not have statistically significant differences in malate production with and without light stimulation (Figure 6-26). Cysteine alone cannot enhance malate bioproduction with light stimulation, either. The results suggest that semiconductor-based bio-interfaces in periplasm could be used for artificial

photosynthesis. The fact that the semiconductor nanoclusters are defect-rich and metastable suggests that modulation biointerfaces may not necessarily need high-quality components if efficient coupling can be achieved (in this case, via the periplasmic *in-situ* biomineralization). As opposed to discarding the defect-rich (*i.e.*, low-grade) biomineralized semiconductors along with their cellular hosts, the biohybrid can be utilized for artificial photosynthesis in a sustainable manner.

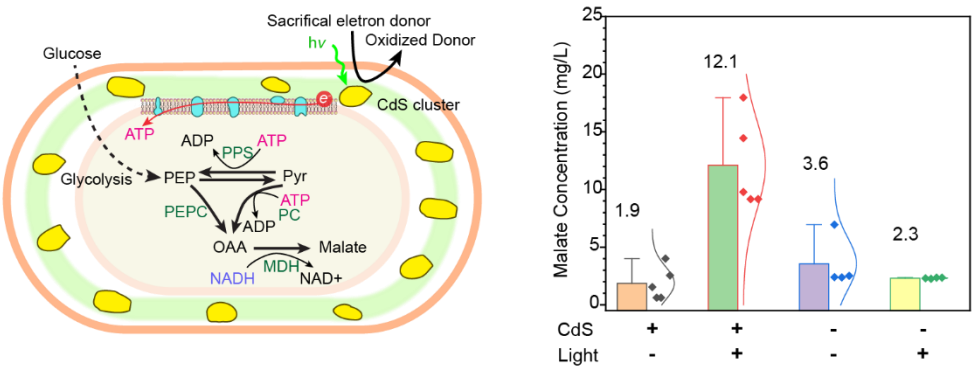

Figure 6-26 Schematic of an artificial power system derived from biohybrids to assist ATP production and speed up the production of high-value biochemicals (*e.g.*, malate). Production of malate in E. coli with CdS nanoclusters increases from 1.87 mg/L (in dark) to 12.1 mg/L (under light). Data points represent mean ± s.d. (n=5). P values (< 0.001) are determined by unpaired two-tailed t-test. E. coli without CdS nanoclusters produces no significant difference in malate production in light or in dark.

6.3 Conclusion

The intersection of materials science, semiconductor-enabled technologies, and synthetic biology is likely to become a major focus of research in the coming years, as it offers new opportunities for addressing pressing sustainability challenges[29,30]. We demonstrate in this study that the periplasm can biomineralize metastable semiconductor nanoclusters for biomodulation and wastewater treatment. This process is scalable and can be applied to the construction of a

continuous bioreactor based on living materials for multiplex conversion. Under light stimulation, the metastable semiconductor nanoclusters could couple with the electron transport chain to increase ATP level and enhance malate production. By using the biohybrid for artificial photosynthesis, we do not have to discard the defect-rich (*i.e.*, low-grade) biomineralized semiconductors with their cellular hosts. The current demonstration of semiconductor-based biointerfaces in the periplasm and the use of hybrid living materials provide a new path toward programmable, adaptable, and defect-tolerant systems where existing cellular chassis and a wide range of nanocluster-cell combinations can be used. Incorporating semiconductors, additional genetic tools, and existing microbial models, periplasmic biohybrid platforms will enable the multilevel sustainability in a cost-effective manner.

6.4 Experimental Methods

Growth of *E. coli* with CdS Nanoclusters and Microbial Nanowires Formation. *E. coli* were cultured overnight in LB medium at 37 °C. Then 1% bacterial culture was inoculated in 50 mL fresh LB medium and grown at 37 °C for ~3 h to an OD600 of ~0.6. The cells were centrifuged and resuspended in modified M9 medium containing 1 g/L NH_4Cl, 0.5 g/L NaCl, 10.99 g/L Tris-HCl buffer (pH 7.5), 340 mg/L thiamine, 0.4% (v/v) glycerol, 4 g/L glucose, 2 mM $MgSO_4$, and 0.1 mM $CaCl_2$. In a typical experiment, the *E. coli* cells were inoculated at 37 °C and 0.3 mM $CdCl_2$ and 1 mM cysteine were added to the culture. The samples were collected for electron imaging, X-ray imaging, RNA sequencing, and intracellular ATP measurement at specific time points.

Growth of *E. coli* with Different Concentrations of $CdCl_2$. *E. coli* were cultured overnight in LB medium at 37 °C. Then 1% bacterial culture was transferred to 50 mL fresh LB medium and

grown at 37 °C for ~3 h. Cells were centrifuged and resuspended in a modified M9 medium to an OD600 of ~0.1. The *E. coli* cells were cultured in a 96-well plate reader with/without 1 mM cysteine and $CdCl_2$ at concentrations of 0.0, 0.1, 0.2, 0.3, 0.4, 0.5, and 1.0 mM. The growth of *E. coli* cells was determined according to the absorbance at 600 nm.

Critical Point Drying (CPD). To image the bacterial samples using an electron microscope or X-ray characterization in a vacuum environment, we firstly performed critical point drying to dehydrate the bacterial samples. The bacterial sample was first fixed using 3% glutaraldehyde in PBS at 4^{o}C overnight. These samples were then sequentially submerged into an ethanol series (30%, 50%, 70%, 80%, 90%, 96%, and 100%) at 25 ^{o}C for 10 minutes each to remove the water content. A critical point dryer (Leica EM CPD300) was used to dry the samples with supercritical carbon dioxide (304.13 K, 73.8 bar). Carbon dioxide was injected at low speed with a delay of 120 s, and it exchanged ethanol at speed 3 for 14 cycles.

Scanning Electron Microscopy (SEM). Bacterial samples or biofilm samples were dried by CPD and then imaged using SEM (Carl Zeiss, Merlin). All samples were coated with a conductive layer of 10 nm thick platinum/palladium coating by sputter coating (Agar AGB7341) before SEM imaging at an acceleration voltage of 2 kV. For each sample, a minimum of 10 measurements were taken to confirm the repeatability of the experiments.

X-Ray Fluorescence Microscopy and Tomography. Synchrotron-based X-ray fluorescence microscopy and tomography were performed at the Bionanoprobe (BNP) located at beamline 9-ID-B of the Advanced Photon Source at Argonne National Laboratory to characterize the spatial distribution of CdS nanocluster in the bacterial cells. Bacterial cells with CdS nanocluster were first fixed with 3% glutaraldehyde and then immersed with a series of ethanol solutions (30%, 50%, 70%, 80%, 90%, 96%, and 100%). A critical point dryer (Leica EM CPD300) was used to

fully dry the bacterial cells for X-ray imaging. X-ray photons of 10.5 keV were focused using zone plate optics onto a sample with a focal size of ~80 nm. The sample was raster scanned through the focused X-ray beam in a fly-scan mode with a step size of 60 nm and 50 ms dwell time per pixel. A full spectrum was collected at each pixel to construct two-dimensional (2D) elemental maps of a single bacterial cell. A series of such 2D projections were acquired while the sample rotated around a vertical axis from -68° to 63° with respect to the incident X-ray beam with a 1° increment to form a three-dimensional (3D) tomography dataset. Per-pixel spectrum fitting and quantification were performed using MAPS software on each projection. An AXO standard thin film (AXO products, Dresden, Germany) was used for elemental concentration calibration. Prior to performing a 3D volume reconstruction, the quantitative 2D maps were further segmented using k-means clustering analysis to extract features of interest. Tomography reconstruction was done using the gridrec algorithm in an open-source software named TomoPy.

Transmission Electron Microscopy and Scanning Transmission Electron Microscopy. The particle suspension was dropped onto copper grids (Ted Pella Inc., Lacey Formvar/Carbon, 200 meshes) and imaged on TEM FEI 30 with 300 kV acceleration voltage in the Advanced Electron Microscopy Facility at the University of Chicago after it was thoroughly dried. After CPD treatment, bacterial samples were dropped onto copper grids. The sample was imaged under FEI F30 with 300 kV acceleration voltage and JEOL JEM-ARM200CF with 200 kV acceleration voltage in the Electron Microscopy Core at the University of Illinois at Chicago in STEM mode. For bacterial cross-sectional samples, bacterial cells were collected and fixed with glutaraldehyde and paraformaldehyde. The sample was then stained with uranyl acetate, followed by dehydration, infiltration, and polymerization. 90 nm thick sections were prepared with Leica EM UC6. Bacterial cross-sectional samples were also imaged under FEI F30 with 300 kV acceleration voltage and

JEOL JEM-ARM200CF with 200 kV acceleration voltage in the Electron Microscopy Core at the University of Illinois at Chicago in STEM mode. Energy-dispersive x-ray spectroscopy (EDS) mapping was collected with JEOL JEM-ARM200C in STEM mode. For each sample, more than 10 imaging measurements were performed to confirm the repeatability of the experiments.

Fluorescence Microscopy and Microspectrofluorometry. Following bacterial cell culture with or without CdS, bacterial cells are centrifuged and resuspended in a new M9 solution to maintain the same fluorescent background. A drop of bacterial suspension was then transferred to the microscope slide and sealed with a glass coverslip and microscope nail polish (Fisher Scientific) to prevent the evaporation of buffer. The fluorescent images of bacteria with CdS were taken with a Nikon eclipse Ti2 inverted microscope with the excitation light at 488 nm. Microspectrofluorometry of bacterial culture was performed on an inverted microscope (Olympus IX71) using an UPlanFL100x/1.30 (Olympus) oil lens. A fluorescent X-Cite lamp (120PC Q, Lumen Dynamics) was used as a light source for excitation. U-MNUA2 filter cube with BP360-370 excitation filter and DM400 dichroic, but without emission filter was used for spectrum recording. Residual scattering of excitation wavelength has been filtered out using GG400 colored glass filter (400 nm, longpass, FGL400S, Thorlabs) before analysis in the spectrometer. Spectra were recorded using a Fergie spectrometer and LightField software (Princeton Instruments). The spectra were corrected post-measurement for detector quantum efficiency, and dichroic mirror and longpass filter transmissions using data obtained from technical specifications.

Biomineral Extraction. *E. coli* were cultured with different metallic ions and the bacterial cells were harvested after 24 h. The cells were concentrated by centrifugation and resuspended in DI water. Cell lysis was performed via sonication in an ice bath for 2 h with a probe sonicator (Sonics Ultrasonic Vibra Cell) under pulse mode. The sample was centrifuged at 13000 rpm for 1 h to

collect the particles. Further surface chemical modification was applied to further disperse the biosynthesized nanoparticles. In a typical experiment, the particles were resuspended with 5 mg/mL Li_2S/ formamide solution and sonicated for 15 mins to obtain a uniform solution. Then 50 mg/mL didodecyldimethylammonium bromide (DDAB)/toluene was added to the top of the solution with continuous stirring. After the overnight reaction, the DDAB-modified nanoparticles were collected from the top layer of the solution (oil layer) and washed with acetone and ethanol three times to remove the excessive DDAB. The dispersion was then centrifuged at 10 000 rpm for 10 min and redispersed in toluene. The nanoparticles were collected for transmission electron microscopy, scanning transmission electron microscopy, and x-ray powder diffraction.

X-Ray Powder Diffraction (XRD). The extracted nanoparticle solution was drop cast on silica substrates as a thin film. Wide-angle powder X-ray diffraction patterns were collected using a Bruker D8 diffractometer with a Cu Kα X-ray source operating at 40 kV and 40 mA.

RNA Extraction and RNA-Seq Analysis. Cells were cultured in 0.3 mM $CdCl_2$ with/without 1 mM cysteine following the cultivation method described above and collected after 6 h. The total RNA was extracted using the TRIzol™ Reagent (Invitrogen, catalog number: 15596026), and the quality was determined using the Agilent 2100 Bioanalyzer (Agilent RNA 6000 Nano Kit). The rRNA was removed using I Ribo-Zero™ Magnetic Kit (Epicenter). The RNA was sheared and reverse transcribed using random primers to obtain cDNA which was used for library construction. Libraries were run on a BGISEQ-500 (BGI). All RNA-seq experiments were performed in biological triplicates from distinct samples.

Flask Culture for Multi-Element Sulfide Biosynthesis. *E. coli* were cultured overnight in LB medium at 37°C. Then 1% bacterial culture was further transferred to fresh LB medium and grown at 37°C for about 3 h. Cells were centrifuged and resuspended with a modified M9 medium to an

OD600 of ~0.6. The bacterial culture was grown at 37°C with various metal ions ($CdCl_2$, $HgCl_2$, $PbCl_2$) at a concentration of 0.1 mM with/without 1 mM cysteine. After 12 h, the cells pellets were collected for nanoparticle analysis, and the supernatants were collected for inductively coupled plasma to evaluate the removal efficiency.

Inductively Coupled Plasma Mass Spectrometry (ICP-MS). After incubating the bacteria in M9 minimal medium in the presence of heavy metal ions for different times, the heavy metal concentrations were characterized by inductively coupled plasma (Agilent 700). The bacterial suspension is centrifuged at 13000 rpm for half an hour, and the supernatant is collected for ICP measurement. High purity concentrated nitric acid (TraceSELECT™, 68 w/w%) was used to digest the sample and then further diluted by deionized (DI) water to the proper concentrations. A multielement standard solution (Sigma-Aldrich 51844) was used as the standard for all analyses. Four standard samples were prepared, with concentrations of 0 ppm, 1 ppm, 5ppm, and 25 ppm for each element (Cd and Pb) being analyzed. These standards have the same concentration of nitric acid as the samples. For the analyses of the Hg atoms, 12.5 v/v% of 400 ppm gold (III) chloride trihydrate solution was also added to both standard solution and samples to stabilize Hg atoms during the measurement. All the experiments were repeated at least three times to confirm the repeatability of the experiments.

Continuous Bioprocessing Reactor. Continuous bioprocessing systems are composed of a replaceable living material membrane, a tower bioreactor, and a cyclic pumping system. The living material membrane was composed of *E. coli* biofilm on the filter membrane. Specifically, *E. coli* were cultured overnight in LB medium at 37°C. Then 1% bacterial culture was further transferred to a 50 mL fresh LB medium and grown at 37°C for about 3 h. Cells were harvested from shake flask cultures at an OD600 of ~ 0.6. The cell culture was drop cast on a filter membrane (0.22 μm

MCE membrane, MF-Millipore), and gently vacuum filtrated to leave a layer of cells on the membrane. The membrane was later transferred onto an LB agar plate and grown at 30°C for 48 h. The biofilm, together with the filter membrane, served as the living material membrane. The tower bioreactor comprises three portions, and each of them was printed with 3D printing (Ultimaker 3). The living membrane was integrated into the bioreactor before assembling. The structure of the bioreactor. The cyclic pump system was composed of a pump (Fisherbrand Variable-Flow Peristaltic Pumps, 13-876-2) and silicone tubes (Cole-Parmer, 06422-074) to cyclic the fluids in the bioreactor. Solution samples containing Cd^{2+}, Pb^{2+}, and Hg^{2+} with 0.1 mM each were pumped inside the bioreactor and cycled at 37 ^{o}C. We sampled the cyclic solution at different time points, followed by centrifugation to collect the supernatant for ICP-MS measurements to determine the metal conversion efficiency.

Intracellular ATP Assay in *E. coli* Cells. *E. coli* were cultured and resuspended with a modified M9 medium. 0.3 mM $CdCl_2$ and 1 mM cysteine were added to the culture, and the culture was grown at 37 °C in a shaker at 220 rpm with and without light stimulation (light intensity: 6.25 mW/cm^2). The same experiment was repeated for cell cultures without the addition of $CdCl_2$ and cysteine. Intracellular ATP levels in the cells were measured using the Promega ATP assay kit. Specifically, we collected 2 mL of bacterial culture medium and resuspended it in 0.2 mL of distilled water. Samples were boiled at 95 ^{o}C for 5 min to deactivate ATPases, and the supernatant was collected for ATP measurement. ATP measurement was conducted by following the manufacturer's instructions. Meanwhile, the intracellular protein concentrations of the collected bacterial samples were measured using a Thermo BCA assay kit. ATP reading values were adjusted by protein concentrations to avoid loading amount variance. The intracellular ATP levels were presented as in fold changes compared to samples without light stimulation.

Detection of Malate. *E. coli* were cultured overnight in LB medium at 37 °C. Then 1% bacterial culture was inoculated in fresh LB medium and grown at 37 °C for ~3 h to an OD600 of ~0.6. Cells were centrifuged and resuspended in a modified M9 medium to an OD600 of ~0.5, then 0.3 mM $CdCl_2$ and 1 mM cysteine were added. The *E. coli* cells were cultured in a photoreaction flask at 37 °C at 220 rpm with and without light stimulation (light intensity: 6.25 mW/cm^2). After 24 h cultivation, the supernatant was filtered and detected by high-performance liquid chromatography (Agilent 1260 Infinity II). Malate was determined with an Aminex HPX-87H column (300 × 7.8 mm, Bio-Rad) at a wavelength of 210 nm. The mobile phase was 5 mM H_2SO_4, and the flow rate was 0.6 mL/min.

6.5 References

1 Jiang, Y. W. & Tian, B. Z. Inorganic semiconductor biointerfaces. *Nat Rev Mater* **3**, 473-490, doi:10.1038/s41578-018-0062-3 (2018).

2 Ning, C. Z., Dou, L. T. & Yang, P. D. Bandgap engineering in semiconductor alloy nanomaterials with widely tunable compositions. *Nat Rev Mater* **2**, doi:10.1038/natrevmats.2017.70 (2017).

3 Reiss, P., Carrière, M., Lincheneau, C., Vaure, L. & Tamang, S. Synthesis of Semiconductor Nanocrystals, Focusing on Nontoxic and Earth-Abundant Materials. *Chem Rev* **116**, 10731-10819, doi:10.1021/acs.chemrev.6b00116 (2016).

4 Rivnay, J., Inal, S., Collins, B. A., Sessolo, M., Stavrinidou, E., Strakosas, X., Tassone, C., Delongchamp, D. M. & Malliaras, G. G. Structural control of mixed ionic and electronic transport in conducting polymers. *Nat Commun* **7**, doi:10.1038/ncomms11287 (2016).

5 Xu, J., Wang, S. H., Wang, G. J. N., Zhu, C. X., Luo, S. C., Jin, L. H., Gu, X. D., Chen, S. C., Feig, V. R., To, J. W. F., Rondeau-Gagne, S., Park, J., Schroeder, B. C., Lu, C., Oh, J. Y., Wang, Y. M., Kim, Y. H., Yan, H., Sinclair, R., Zhou, D. S., Xue, G., Murmann, B., Linder, C., Cai, W., Tok, J. B. H., Chung, J. W. & Bao, Z. N. Highly stretchable polymer semiconductor films through the nanoconfinement effect. *Science* **355**, 59-64, doi:10.1126/science.aah4496 (2017).

6 Yao, J., Yan, H. & Lieber, C. M. A nanoscale combing technique for the large-scale assembly of highly aligned nanowires. *Nat Nanotechnol* **8**, 329-335, doi:10.1038/Nnano.2013.55 (2013).

7 Abbott, J., Ye, T. Y., Qin, L., Jorgolli, M., Gertner, R. S., Ham, D. & Park, H. CMOS nanoelectrode array for all-electrical intracellular electrophysiological imaging. *Nat Nanotechnol* **12**, 460-466, doi:10.1038/Nnano.2017.3 (2017).

8 Walter, M. G., Warren, E. L., McKone, J. R., Boettcher, S. W., Mi, Q. X., Santori, E. A. & Lewis, N. S. Solar Water Splitting Cells. *Chem Rev* **110**, 6446-6473, doi:10.1021/cr1002326 (2010).
9 Strukov, D. B. & Likharev, K. K. Defect-tolerant architectures for nanoelectronic crossbar memories. *J Nanosci Nanotechno* **7**, 151-167, doi:10.1166/jnn.2007.013 (2007).
10 Tian, B. Z., Zheng, X. L., Kempa, T. J., Fang, Y., Yu, N. F., Yu, G. H., Huang, J. L. & Lieber, C. M. Coaxial silicon nanowires as solar cells and nanoelectronic power sources. *Nature* **449**, 885-U888, doi:10.1038/nature06181 (2007).
11 Mathieson, K., Loudin, J., Goetz, G., Huie, P., Wang, L. L., Kamins, T. I., Galambos, L., Smith, R., Harris, J. S., Sher, A. & Palanker, D. Photovoltaic retinal prosthesis with high pixel density. *Nat Photonics* **6**, 391-397, doi:10.1038/Nphoton.2012.104 (2012).
12 Elnathan, R., Barbato, M. G., Guo, X., Mariano, A., Wang, Z., Santoro, F., Shi, P., Voelcker, N. H., Xie, X., Young, J. L., Zhao, Y., Zhao, W. & Chiappini, C. Biointerface design for vertical nanoprobes. *Nat Rev Mater* **7**, 953-973, doi:10.1038/s41578-022-00464-7 (2022).
13 Ledesma, H. A., Li, X. J., Carvalho-de-Souza, J. L., Wei, W., Bezanilla, F. & Tian, B. Z. An atlas of nano-enabled neural interfaces. *Nat Nanotechnol* **14**, 645-657, doi:10.1038/s41565-019-0487-x (2019).
14 Cestellos-Blanco, S., Zhang, H., Kim, J. M., Shen, Y. X. & Yang, P. D. Photosynthetic semiconductor biohybrids for solar-driven biocatalysis. *Nat Catal* **3**, 245-255, doi:10.1038/s41929-020-0428-y (2020).
15 Pardee, A. B., Jacob, F. & Monod, J. The genetic control and cytoplasmic expression of "Inducibility" in the synthesis of β-galactosidase by E. coli. *Journal of Molecular Biology* **1**, 165-178, doi:doi.org/10.1016/S0022-2836(59)80045-0 (1959).
16 De Yoreo, J. J., Gilbert, P. U. P. A., Sommerdijk, N. A. J. M., Penn, R. L., Whitelam, S., Joester, D., Zhang, H. Z., Rimer, J. D., Navrotsky, A., Banfield, J. F., Wallace, A. F., Michel, F. M., Meldrum, F. C., Cölfen, H. & Dove, P. M. Crystallization by particle attachment in synthetic, biogenic, and geologic environments. *Science* **349**, doi:10.1126/science.aaa6760 (2015).
17 Riahi, S. & Rowley, C. N. Why Can Hydrogen Sulfide Permeate Cell Membranes? *Journal of the American Chemical Society* **136**, 15111-15113, doi:10.1021/ja508063s (2014).
18 Nies, D. H. Efflux-mediated heavy metal resistance in prokaryotes. *Fems Microbiol Rev* **27**, 313-339, doi:10.1016/S0168-6445(03)00048-2 (2003).
19 Mathai, J. C., Missner, A., Kügler, P., Saparov, S. M., Zeidel, M. L., Lee, J. K. & Pohl, P. No facilitator required for membrane transport of hydrogen sulfide. *P Natl Acad Sci USA* **106**, 16633-16638, doi:10.1073/pnas.0902952106 (2009).
20 Bang, S. W., Clark, D. S. & Keasling, J. D. Engineering Hydrogen Sulfide Production and Cadmium Removal by Expression of the Thiosulfate Reductase Gene (phsABC) from Salmonella enterica Serovar Typhimurium in Escherichia coli. *Appl Environ Microb* **66**, 3939-3944, doi:Doi 10.1128/Aem.66.9.3939-3944.2000 (2000).
21 Sun, G. L., Reynolds, E. E. & Belcher, A. M. Using yeast to sustainably remediate and extract heavy metals from waste waters. *Nat Sustain* **3**, 303-311, doi:10.1038/s41893-020-0478-9 (2020).
22 Reyes, L. R., Gómez, I. & Garza, M. T. J. I. J. o. G. N. B. Biosynthesis of cadmium sulfide nanoparticles by the fungi Fusarium sp. **1**, B90-B95 (2009).

23 Hui, C. Y., Guo, Y., Yang, X. Q., Zhang, W. & Huang, X. Q. Surface display of metal binding domain derived from PbrR on specifically increases lead(II) adsorption. *Biotechnol Lett* **40**, 837-845, doi:10.1007/s10529-018-2533-4 (2018).
24 Lu, L., Guest, J. S., Peters, C. A., Zhu, X. P., Rau, G. H. & Ren, Z. J. Wastewater treatment for carbon capture and utilization. *Nat Sustain* **1**, 750-758, doi:10.1038/s41893-018-0187-9 (2018).
25 Baral, S. & Fendler, J. H. Cadmium-Sulfide Mediated Photoelectric Effects in Bilayer Lipid-Membranes. *Journal of the American Chemical Society* **111**, 1604-1614, doi:DOI 10.1021/ja00187a012 (1989).
26 Werpy, T. & Petersen, G. Top value added chemicals from biomass: volume I--results of screening for potential candidates from sugars and synthesis gas. (National Renewable Energy Lab.(NREL), Golden, CO (United States), 2004).
27 Chen, X. L., Xu, G. Q., Xu, N., Zou, W., Zhu, P., Liu, L. M. & Chen, J. Metabolic engineering of Torulopsis glabrata for malate production. *Metab Eng* **19**, 10-16, doi:10.1016/j.ymben.2013.05.002 (2013).
28 Jiang, Y., Zheng, T., Ye, X., Xin, F., Zhang, W., Dong, W., Ma, J. & Jiang, M. Metabolic engineering of Escherichia coli for L-malate production anaerobically. *Microb Cell Fact* **19**, 165, doi:10.1186/s12934-020-01422-0 (2020).
29 Chen, A. Y., Deng, Z., Billings, A. N., Seker, U. O., Lu, M. Y., Citorik, R. J., Zakeri, B. & Lu, T. K. Synthesis and patterning of tunable multiscale materials with engineered cells. *Nat Mater* **13**, 515-523, doi:10.1038/nmat3912 (2014).
30 Gilbert, C., Tang, T. C., Ott, W., Dorr, B. A., Shaw, W. M., Sun, G. L., Lu, T. K. & Ellis, T. Living materials with programmable functionalities grown from engineered microbial co-cultures. *Nat Mater* **20**, 691-700, doi:10.1038/s41563-020-00857-5 (2021).

Afterword

"*Ad astra per aspera*". As I reach the end of this thesis, I reminded of the journey that led me to this point. The research process has been both challenging and rewarding, and I would like to take a moment to reflect on some key aspects of this journey.

For a long time, I have believed that what I have pursued here is a Doctor of Philosophy rather than a Doctor of Chemistry or Doctor of Science. What I want to emphasize here is that the knowledge and skillset I have acquired in this journey serve merely as a carrier or a tangible representation of the abstract philosophy and methodology. This academic odyssey has been not only about the accumulation of scientific and technical knowledge, but more about embracing the understanding of the world, guided by philosophical inquiry and critical thought. Thus, instead of discussing all the research findings presented in this thesis, I would like to reflect on the three lessons I learned during my Ph.D., which, to me, may be more important than the data shown in the previous chapters.

The first is independence. Research independence means having the capacity to go off and work on your own ideas. Waiting for or relying on the senior input does not really facilitate progress in innovative research; instead, it leads to a diminishing of your passions or a loss of directions. It is about sculpting your own unique career trajectory and establishing a personal style of research taste, rather than passively traversing a path meticulously laid out by others.

The second is collaboration. While it might seem antithetical to the first, collaboration emerges as an indispensable force especially in the interdisciplinary field where I am working on. Independence does not imply being insulated or isolated from your surroundings, your colleagues, and your sponsors; rather, it calls for a judicious balance. The capabilities in fostering collaborations and seamlessly integrating resources largely determine the potential impact and

reach of the work. It is through this collaboration in multiple realms that we propel the frontiers of knowledge forward, crafting a legacy of innovation and discovery.

The third is dialectic (I am not sure whether it is a right description in English). The beauty lies in its inherent uncertainty: you are working on something that can be right or wrong, or even no answers, or even "not even wrong". Research is, at its core, an exploration into somethings that no one has ever been explored before. In facing novel ideas and arguments, it is essential to encapsulate the intricate dance between conflicting ideas in minds and accept that we may not be able to find clear and definitive answers, or simple and clear-cut solutions. Thus, take any challenges and attack from the outsides as a crucible for refining your thoughts and strengthen your logics.

It was the best of times; it was the worst of times. Five years have unfolded in a swift, encapsulating both the zeniths of triumph and the nadirs of struggle. In the meanwhile, there are numerous changes happens in my life simultaneously. From the international environments and the COVID-19 pandemic to the rise of artificial intelligence (*e.g.*, ChatGPT), these formidable forces have reshaped my way of thinking, my lifestyle, and my aspiration. It is also inevitable presented significant challenge to me. What lies ahead on my path? What is my destiny? However, to wander is not to be lost. As I believed that PhD is a good starting point for my life, allowing me to establish a small barrier of knowledge even in a world dominated by information overload and media omnipresence. It has equipped me with the tools to carve out a niche of knowledge that only belongs to me.

I appreciate having the time and space to reflect on my journey so far here. Overall, The Ph.D. journey is like a storm, when it comes to a real end now, when all the trials now behind me, I do

not remember how I make it through and how I managed to survive. But one thing is for sure that I am not the same person who walked in. That's what my Ph.D. all about.

Wish in the future, on a peaceful afternoon, when I open this thesis again, I would still find my thinking here is inspiring.

Jiuyun Shi

December 6, 2023

In GCIS, Campus of The University of Chicago